frontiers | Research Topics

Combining computational and experimental approaches to characterize ion channels and transporters

Edited by
Christoph Fahlke, Han Sun, Walter Sandtner,
Klaus Schicker and Jan-Philipp Machtens

Published in
Frontiers in Physiology

ISSN 1664-8714
ISBN 978-2-8325-4004-6
DOI 10.3389/978-2-8325-4004-6

About Frontiers

Frontiers is more than just an open access publisher of scholarly articles: it is a pioneering approach to the world of academia, radically improving the way scholarly research is managed. The grand vision of Frontiers is a world where all people have an equal opportunity to seek, share and generate knowledge. Frontiers provides immediate and permanent online open access to all its publications, but this alone is not enough to realize our grand goals.

Frontiers journal series

The Frontiers journal series is a multi-tier and interdisciplinary set of open-access, online journals, promising a paradigm shift from the current review, selection and dissemination processes in academic publishing. All Frontiers journals are driven by researchers for researchers; therefore, they constitute a service to the scholarly community. At the same time, the *Frontiers journal series* operates on a revolutionary invention, the tiered publishing system, initially addressing specific communities of scholars, and gradually climbing up to broader public understanding, thus serving the interests of the lay society, too.

Dedication to quality

Each Frontiers article is a landmark of the highest quality, thanks to genuinely collaborative interactions between authors and review editors, who include some of the world's best academicians. Research must be certified by peers before entering a stream of knowledge that may eventually reach the public - and shape society; therefore, Frontiers only applies the most rigorous and unbiased reviews. Frontiers revolutionizes research publishing by freely delivering the most outstanding research, evaluated with no bias from both the academic and social point of view. By applying the most advanced information technologies, Frontiers is catapulting scholarly publishing into a new generation.

What are Frontiers Research Topics?

Frontiers Research Topics are very popular trademarks of the *Frontiers journals series*: they are collections of at least ten articles, all centered on a particular subject. With their unique mix of varied contributions from Original Research to Review Articles, Frontiers Research Topics unify the most influential researchers, the latest key findings and historical advances in a hot research area.

Find out more on how to host your own Frontiers Research Topic or contribute to one as an author by contacting the Frontiers editorial office: frontiersin.org/about/contact

Combining computational and experimental approaches to characterize ion channels and transporters

Topic editors

Christoph Fahlke — Julich Research Center, Helmholtz Association of German Research Centres (HZ), Germany

Han Sun — Leibniz-Institut für Molekulare Pharmakologie (FMP), Germany

Walter Sandtner — Medical University of Vienna, Austria

Klaus Schicker — Medical University of Vienna, Austria

Jan-Philipp Machtens — Molecular and Cell Physiology, Institute of Biological Information processing, Julich Research Center, Helmholtz Association of German Research Centres (HZ), Germany

Citation

Fahlke, C., Sun, H., Sandtner, W., Schicker, K., Machtens, J.-P., eds. (2023). *Combining computational and experimental approaches to characterize ion channels and transporters*. Lausanne: Frontiers Media SA. doi: 10.3389/978-2-8325-4004-6

Table of contents

frontiers | Frontiers in Physiology

TYPE Editorial
PUBLISHED 08 November 2023
DOI 10.3389/fphys.2023.1320336

OPEN ACCESS

EDITED AND REVIEWED BY
Mary Hongying Cheng,
University of Pittsburgh, United States

*CORRESPONDENCE
Christoph Fahlke,
c.fahlke@fz-juelich.de

RECEIVED 12 October 2023
ACCEPTED 27 October 2023
PUBLISHED 08 November 2023

CITATION
Fahlke C, Machtens J-P, Sandtner W, Schicker K and Sun H (2023), Editorial: Combining computational and experimental approaches to characterize ion channels and transporters.
Front. Physiol. 14:1320336.
doi: 10.3389/fphys.2023.1320336

Editorial: Combining computational and experimental approaches to characterize ion channels and transporters

Christoph Fahlke[1]*, Jan-Philipp Machtens[1], Walter Sandtner[2], Klaus Schicker[2] and Han Sun[3,4]

[1]Institute of Biological Information Processing, Molekular- und Zellphysiologie (IBI-1), Forschungszentrum Jülich, Jülich, Germany, [2]Center of Physiology and Pharmacology, Medical University of Vienna, Vienna, Austria, [3]Leibniz-Forschungsinstitut für Molekulare Pharmakologie (FMP), Berlin, Germany, [4]Institute of Chemistry, Technical University of Berlin, Berlin, Germany

KEYWORDS

ion channels, ion transporter, computational biology, kinetic modeling, molecular dynamics simulation

Editorial on the Research Topic
Combining computational and experimental approaches to characterize ion channels and transporters

Electrical signaling plays a major role in a variety of cellular functions. It is fast, well suited for coding information and is—because of the low dielectric constant of biological membranes—very energy-efficient. In living systems, ion channels and transporters determine electrical signals in a cooperative fashion. Transporters generate ion gradients, and ion channels utilize these gradients by mediating large ion fluxes that quickly charge the membrane capacitor and change voltages across the membrane. The importance of ion channels in excitable tissues has been known for many decades. The invention of patch clamping made a broad variety of cells accessible to cell electrophysiology; such experiments demonstrated the importance of electrical signaling also in many non-excitable cells over the human body.

Because of their widespread importance, ion channels and transporters have been intensively studied in the recent past. Currently, we have reached a solid understanding of the function of many ion channels and transporters, and we possess knowledge of the three-dimensional structures for most of them. Simultaneously, computational biology tools now enable us to link structure dynamics to transport functions. This rapid progress in understanding these class of membrane proteins prepares us for the next step, to use channel and transport function to predict ion concentrations and membrane potentials in cell organelles and cell compartments, towards an atomistic understanding of cell function.

To link channel and transporter structure to protein function and even more to the behavior of subcellular and cellular systems, experiments need to be combined with computational approaches. Our Research Topic *Combining Computational and Experimental Approaches to Characterize Ion Channels and Transporters*, has the aim to present recent progress and findings achieved through the application of such a combination. It encompasses eight publications that combine experiments and computational work to describe the function of various ion channels and transporters.

The mini-review by Hendriks et al. summarizes recent insights into the cation selectivity in ion channels. They describe multiple structures with distinct selectivity filter conformations that were discovered recently using a combination of structural biology, spectroscopic, and computational methods. Yüksel et al. combine atomistic MD simulation and electrophysiology for a better understanding of channel gating in HCN channels. They uncouple a linker region from the channel core by inserting one to five glycine residues. These modifications already abolish modulation by cAMP upon insertion of one glycine. In addition they accelerate activation kinetics. Simulations demonstrate increased mobility of the linker and the cyclic nucleotide-binding domains (CNBD) as well as destabilization of the channel gate. In HCN channels, hyperpolarizing voltage and cAMP binding are integrated by a mechanical continuum between the voltage sensor and the CNBD. This allows for the transmitting information to the periphery of the channel, thereby bypassing the pore. Gabriel et al. study ion binding within the selectivity filter of K^+ channels using high bandwidth single channel recording and the blocker tetrapropylammonium. The authors determine voltage-dependent ion occupation probabilities by using a kinetic model of single-channel currents recorded in the absence of the blocker and extract release rate constants of the blocker from these data.

Five publications address transporters, and all of them describe transporter function with the help of kinetic models. Shi et al. focus on transporters that accumulate neutral and cationic amino acids in a Na^+ and Cl^- dependent manner. Their analysis shows that the substrate turnover rate of this transporter is faster than for other SLC6 transporters, including the closely related glycine transporters. Whereas substrate translocation is fast (i.e., in sub-millisecond range), Na^+ binding to the empty transporter is slow and possibly the rate-limiting partial reaction.

Walter Sandtner's group explored how substrate concentrations on extra- and intracellular membrane sides can exert evolutionary pressure on the operating mode of a transporter (Schicker et al.). Their approach uses microscopic rate constants, which parameterize the kinetic models of solute carriers, to describe transporter function by analytical descriptors such as K_M and V_{max} for substrate transport. They hypothesize that the outcome of evolutionary adaptation must maximize substrate uptake rate at prevailing conditions and use an optimization algorithm to search for the microscopic rate constants, which yielded the largest possible value for the substrate uptake rate. This approach provided novel insights into how evolution may have shaped solute carrier function. In another study, the same group explored the general properties of allosteric modulation of solute carriers (Boytsov et al.). For this purpose, they use transition state theory and linear free energy relationships (LFER) to provide a theoretical framework for allosteric solute carrier modulation. Suslova et al. combine fast substrate application and kinetic modeling to understand the kinetic basis of gain-of-anion channel changes of the glial glutamate transporter EAAT1 in the pathomechanism in episodic ataxia (Winter et al., 2012; Kovermann et al., 2020). In this work, they also establish a method for statistical testing of fit parameters in kinetic transporter modeling. Barta et al. analyze how passive movements of transport substrates and ions affect secondary active transport. For this, they use a continuum mathematical model of liposomes with and without the sodium glucose transporter 1 (SGLT1) to assign water conductive states to the transport cycle and to improve the interpretation of substrate accumulation data in liposome systems.

Our Research Topic illustrates the potential of combining experiments and computational approaches. It shows how experiments can verify the results of molecular simulations and inspire new simulation studies. In addition, it demonstrates the usefulness of kinetic modeling for describing the mechanistic basis of secondary active transport and for discovering general principles of their function. Lastly, it provides an example how computational approaches that describe more complex experimental systems, i.e. liposomes, can significantly improve the interpretability of the obtained results. We are confident that computational approaches will be increasingly employed in membrane physiology and biophysics, and that we will see many contributions with a similar set of methods in the near future.

Author contributions

CF: Writing–original draft, Writing–review & editing. J-PM: Writing–review & editing. WS: Writing–original draft, Writing–review & editing. KS: Writing–review & editing. HS: Writing–original draft, Writing–review & editing.

Conflict of interest

The authors declare that the research was conducted in the absence of any commercial or financial relationships that could be construed as a potential conflict of interest.

The author(s) declared that they were an editorial board member of Frontiers, at the time of submission. This had no impact on the peer review process and the final decision.

Publisher's note

References

Kovermann, P., Untiet, V., Kolobkova, Y., Engels, M., Baader, S., Schilling, K., et al. (2020). Increased glutamate transporter-associated anion currents cause glial apoptosis in episodic ataxia 6. *Brain Commun.* 4 (2), fcaa022. doi:10.1093/braincomms/fcaa022

Winter, N., Kovermann, P., and Fahlke, C. (2012). A point mutation associated with episodic ataxia 6 increases glutamate transporter anion currents. *Brain* 135 (11), 3416–3425. doi:10.1093/brain/aws255

frontiers in Physiology

ORIGINAL RESEARCH
published: 29 October 2021
doi: 10.3389/fphys.2021.737834

Asymmetric Interplay Between K^+ and Blocker and Atomistic Parameters From Physiological Experiments Quantify K^+ Channel Blocker Release

*Tobias S. Gabriel[1], Ulf-Peter Hansen[2], Martin Urban[3], Nils Drexler[4], Tobias Winterstein[1], Oliver Rauh[1], Gerhard Thiel[1], Stefan M. Kast[3] and Indra Schroeder[1,4]**

[1] Plant Membrane Biophysics, Technische Universität Darmstadt, Darmstadt, Germany, [2] Department of Structural Biology, Christian-Albrechts-Universität zu Kiel, Kiel, Germany, [3] Physikalische Chemie III, Technische Universität Dortmund, Dortmund, Germany, [4] Institute of Physiology II, University Hospital Jena, Friedrich Schiller University Jena, Jena, Germany

OPEN ACCESS

Edited by:
Klaus Schicker,
Medical University of Vienna, Austria

Reviewed by:
Fan Yang,
Zhejiang University, China
Jan-Philipp Machtens,
Zelluläre Biophysik (ICS-4), Institut für Komplexe Systeme,
Forschungszentrum Jülich, Germany

***Correspondence:**
Indra Schroeder
indra.schroeder@med.uni-jena.de

Specialty section:
This article was submitted to Membrane Physiology and Membrane Biophysics, a section of the journal Frontiers in Physiology

Received: 07 July 2021
Accepted: 04 October 2021
Published: 29 October 2021

Citation:
Gabriel TS, Hansen U-P, Urban M, Drexler N, Winterstein T, Rauh O, Thiel G, Kast SM and Schroeder I (2021) Asymmetric Interplay Between K^+ and Blocker and Atomistic Parameters From Physiological Experiments Quantify K^+ Channel Blocker Release. Front. Physiol. 12:737834. doi: 10.3389/fphys.2021.737834

Modulating the activity of ion channels by blockers yields information on both the mode of drug action and on the biophysics of ion transport. Here we investigate the interplay between ions in the selectivity filter (SF) of K^+ channels and the release kinetics of the blocker tetrapropylammonium in the model channel Kcv_{NTS}. A quantitative expression calculates blocker release rate constants directly from voltage-dependent ion occupation probabilities in the SF. The latter are obtained by a kinetic model of single-channel currents recorded in the absence of the blocker. The resulting model contains only two adjustable parameters of ion-blocker interaction and holds for both symmetric and asymmetric ionic conditions. This data-derived model is corroborated by 3D reference interaction site model (3D RISM) calculations on several model systems, which show that the K^+ occupation probability is unaffected by the blocker, a direct consequence of the strength of the ion-carbonyl attraction in the SF, independent of the specific protein background. Hence, Kcv_{NTS} channel blocker release kinetics can be reduced to a small number of system-specific parameters. The pore-independent asymmetric interplay between K^+ and blocker ions potentially allows for generalizing these results to similar potassium channels.

Keywords: selectivity filter, ion binding, blocker kinetics, 3D RISM, extended beta distributions, viral potassium channels, carbonyl-ion interaction

INTRODUCTION

Ion channels are crucial for many cellular functions and therefore important drug targets (Ashcroft, 2006; Bernard and Shevell, 2008; Fernández-Ballester et al., 2011; Bagal et al., 2013). A major class of drugs for potassium (K^+) channels are pore blockers that bind in the aqueous cavity between selectivity filter and intracellular pore entrance. Many of these molecules are either positively

charged (Sánchez-Chapula et al., 2002) or bind with a positively charge moiety oriented towards the selectivity filter (Bucchi et al., 2013; Du et al., 2014). Examples are the heart rate-reducing agent ivabradine for HCN channels (Bucchi et al., 2013), and drugs blocking hERG channels either as a desired effect (e.g., the antiarrhythmic ranolazine, Du et al., 2014) or as an unwanted side effect, like Chloroquine (Sánchez-Chapula et al., 2002). Due to the structural conservation within the superfamily of cation-selective channels, similar findings have been reported for other channels, e.g., a block of Na_V channels by different anticonvulsants and anesthetics (Tikhonov and Zhorov, 2017). To facilitate the development of new compounds, a profound understanding of the molecular interactions between the blocker, the channel protein, and the permeating ions is essential.

Decades of research with pore blockers (Armstrong and Hille, 1972; Villarroel et al., 1988; Choi et al., 1993; Jara-Oseguera et al., 2007; Piechotta et al., 2011) have contributed to a detailed understanding of the channels' structure and dynamics including the insight that mutual interactions between blocker and permeating ions are crucial for blocker binding/release kinetics. Two examples are the release of a positively charged blocker from TRPV (Jara-Oseguera et al., 2007) and MthK (Posson et al., 2013) channels, which is in both cases accelerated via the electrostatic repulsion by nearby cations.

However, a quantitative model for blocker release kinetics in a K^+ channel that explicitly considers the distinct population states in the selectivity filter (SF) is still missing. To this end, it is necessary to measure the voltage-dependent rate constants of blocker release, and to determine the occupation probabilities of the ion binding sites in the SF. So far, these ion occupation probabilities can only be provided by computational modeling via MD simulations (Roux, 2005; Köpfer et al., 2014), liquid state theory (Kast et al., 2011), or experimentally by X-ray crystallography (Morais-Cabral et al., 2001; Yohannan et al., 2007), though only under non-physiological conditions and in most cases without the crucial voltage dependency. Considering the uncertainties of the underlying model assumptions (Roux, 2005; Köpfer et al., 2014; Rauh et al., 2018), ion distributions should ideally be determined experimentally under the same physiological conditions employed in the blocking experiments.

Here we apply methods developed previously (Rauh et al., 2018), which allow for determining the required voltage-dependent ion occupation probabilities of the individual binding sites in the SF of a K^+ channel from experimental open-state data. This was achieved by a global fit of single-channel current-voltage relationships and gating kinetics in the SF of a model K^+ channel (Kcv_{NTS}, Rauh et al., 2018) using an appropriate flux model (Roux, 2005) from the MD simulation literature. From the rate constants of ion hopping in this model, the desired voltage-dependent ion occupancies of the binding sites in the SF can be calculated.

Combined with a kinetic model of blocker release that depends on these calculated local SF occupancies obtained from *open-state* kinetic constants we end up with a quantitative expression for the voltage-dependent kinetic release constant. This model requires only two adjustable parameters that can be taken from experimental data on the voltage dependency of blocker release under symmetric ionic conditions, as exemplified for Kcv_{NTS} blocked by tetrapropylammonium (TPrA). The robustness of the expression is corroborated in two ways. First, the model is shown to be also applicable quantitatively to recordings under asymmetric bath conditions. Second, we validate the assumption that the presence of the blocker has no effect on SF populations and, therefore, does not influence the free energy surface governing the kinetic constants of K^+ transport. Such an insensitivity of the SF populations to the presence of blockers has already been found in several studies of crystal structures (Faraldo-Gómez et al., 2007; Yohannan et al., 2007; Lenaeus et al., 2014). Here, we provide further evidence from calculations using the three-dimensional reference interaction site model (3D RISM) integral equation theory. This approach provides ion and solvent populations for a given SF structure including permeating ions and the charged blocker. The results obtained for a variety of filter structures, including a maximally reduced system comprising only the canonical SF of K^+ channels, show conclusively that neither the blocker nor the protein environment affect SF occupancies. This can be traced back to the peculiar nature of K^+ SF energetics. Hence, the combined experimental and computational data uncover an asymmetric interplay between the blocker and K^+ ions in the filter which allows for transferring independently gathered open-state kinetic data to a blocking kinetics model, a key result of the present work. In this context, the term "asymmetry" does of course not mean a violation of force balance between interacting partners, but compactly describes the apparent strong effect of filter ion confinement to decouple occupancies from the blocker ion presence, facilitating the construction of a kinetic model in which the blocker simply switches off certain ion transitions in the flux model.

The K^+ channel Kcv_{NTS} used for the experimental studies represents the pore module of all K^+ channels, including the canonical SF sequence. Hence, we expect that the robust observation of ion/blocker asymmetry from the maximally reduced computational model translates to other K^+ channels. Together with the abstraction of blocker release kinetics to only two system-specific parameters, this implies that the phenomenon of asymmetric filter ion/blocker interplay may also hold for mammalian K^+ channels where this insight may ultimately improve the possibilities of rational drug design.

MATERIALS AND METHODS

In vitro Protein Expression and Purification

The Kcv_{NTS} protein was expressed *in vitro* and purified as described previously (Rauh et al., 2017b). Briefly, the gene of Kcv_{NTS} (Greiner, 2011; Jeanniard et al., 2013) was cloned into a pEXP5-CT/TOPO®-vector (Invitrogen, Karlsbad, CA, United States), the fusion of the His tag coded for in the plasmid was prevented by inserting a stop codon.

In vitro expression of the channel protein was performed with the MembraneMax™ *HN* Protein Expression Kit (Invitrogen) following the manufacturer's instructions. During the expression

procedure, the Kcv_{NTS} proteins were directly embedded into nanolipoproteins (NLPs), containing multiple His-tags (Katzen et al., 2008). This allows the purification of the native Kcv_{NTS} protein by metal chelate affinity chromatography. Purification was done on a 0.2 mL HisPur™ Ni-NTA spin column (Thermo Fisher Scientific, Waltham, MA, United States). To improve the reconstitution efficiency into the bilayer (Winterstein et al., 2018), neither the washing nor the elution solutions contained salts. The column was washed three times with two resin-bed volumes of 20 mM imidazole to remove unspecific binders. The Kcv_{NTS}-containing NLPs were eluted in three fractions (200 μL each) with 250 mM imidazole.

Lipid Bilayer Experiments

Planar lipid bilayer experiments at room temperature (20-25°C) were performed on a vertical bilayer setup (IonoVation, Osnabrück, Germany) as described previously (Braun et al., 2013). Briefly, 1,2-diphytanoyl-*sn*-glycero-3-phosphocholine (DPhPC, Avanti Polar Lipids, Alabaster, AL, United States) bilayers were formed using the pseudo painting/air bubble technique (Braun et al., 2014). One of the elution fractions was diluted in 250 mM imidazole solution by a factor of 1000 to 100000. For reconstitution of the channel, a small amount (1-3 μL) of the diluted NLP/Kcv_{NTS}-conjugates was added directly below the bilayer in the *trans* compartment with a bent Hamilton syringe.

Both the *cis* and *trans* compartment were filled with 100 mM KCl plus 10 mM HEPES adjusted to pH 7.0 with KOH. The correct insertion of the protein and its orientation was tested by short voltage pulses utilizing asymmetry of the apparent IV curves of Kcv channels (Gazzarrini et al., 2009). The *trans* compartment was grounded and membrane voltages were applied to the *cis* compartment. Positive currents in the graphs correspond to outward currents in the *in vivo* situation.

Constant voltages between +160 mV and −160 mV in steps of 20 mV were applied for 1 or 2 min. The single-channel current was measured via Ag/AgCl electrodes connected to the headstage of a patch-clamp amplifier (L/M-EPC-7, List-Medical, Darmstadt and Axopatch 200B, Molecular Devices). In order to prevent electromagnetic interference from outside sources, the amplifier and the 16-bit A/D converter were connected via an optical link. Currents were filtered with a 1-kHz 4-pole Bessel filter and digitized with a sampling frequency of 5 kHz (LIH 1600, HEKA Elektronik, Lambrecht, Germany). TPrA concentration was changed by replacing an appropriate amount of the solution in the *cis* (=cytosolic) chamber by a 1, 10, or 100 mM TPrA stock solution and thorough mixing. All blocker stock solutions contained 100 mM KCl plus 10 mM HEPES, pH was adjusted to 7.0 with KOH.

For the experiments with 500 mM external KCl, an appropriate amount of a KCl stock solution (3M KCl, 10 mM HEPES, pH 7.0) was added to the *trans* (=external) recording chamber after the reconstitution of a single channel. In these experiments, agar bridges (3M or 500 mM KCl, 1.5% agarose) were used for both electrodes.

Determination of I_{true} and the Rate Constants of Fast Gating From Extended Beta Distribution Analysis

If the rate constants of blocking or flickering are higher than the bandwidth of the low-pass filter of the experimental set-up, the related changes in current are strongly attenuated. In other words, neither the individual gating transitions, nor the true open channel current, I_{true}, can be directly observed. However, the attenuated flickering still causes "excess noise" (Heinemann and Sigworth, 1991; Schroeder, 2015), which results in broadened, non-Gaussian peaks in the amplitude histograms (**Supplementary Figure S1**). From these curves, the hidden gating parameters can be extracted by extended beta distribution analysis (Schroeder, 2015; Rauh et al., 2017a, 2018). The simulation algorithm for the generation of artificial time series of current and the equations for the calculation of amplitude histograms from these time series are given in Albertsen and Hansen (1994), Schroeder and Hansen (2006). The theoretical histograms were fitted to the measured ones by a simplex algorithm (Caceci and Cacheris, 1984).

The fitting strategies have also been described elsewhere (Schroeder and Hansen, 2009; Schroeder, 2015). Here, it is important to note, that simulation is done in continuous time and includes the same baseline noise as the experiment and a digital representation of the jump-response of the 4th-order Bessel filter used for the experiments. Details of the application of this analysis to fast gating in Kcv_{NTS} have been described previously (Rauh et al., 2017a).

The fit and calculation of confidence intervals in **Figure 3D** was done with Mathematica.

Computational Details

Structure Preparation

The protein structure of the KcsA-Fab-TBA complex (pdb code: 2HVK, Yohannan et al., 2007) was directly obtained from the protein data bank (PDB). For 3D RISM calculations only the chain consisting of the KcsA channel (chain C) and TBA (residue TBA) were used. Based on the geometric data provided in the pdb file a complete tetrameric structure was generated. All ions and water molecules were deleted, whereas for studying the effect of K^+ at position S4 on blocker energetics the respective ion was retained at the crystallographic position. Missing protein protons were added by VMD PSFGEN plugin (Humphrey et al., 1996). All titratable residues remained in the standard ionization state. Missing TBA protons were added by "reduce" (Case et al., 2016). For the reduced template model, only the filter carbonyls (residues 74 to 79) and the TBA molecule from 2HVK were retained. All other reduced models (KcsA 1K4C, Zhou et al., 2001); KirBac3.1 3ZRS, (Bavro et al., 2012); and Kcv_{PBCV-1}, (Tayefeh et al., 2009; Hoffgaard et al., 2015) were prepared similarly by aligning the filter structures to 2HVK by VMD (Humphrey et al., 1996) and keeping the TBA atom positions at the 2HVK reference values.

Reference Interaction Site Model Calculations

All RISM calculations were performed using software developed in our laboratory. For the RISM calculations models for 1 M KCl and pure water were used, applying the TIP3P water model (Jorgensen et al., 1983) with modified Lennard-Jones parameters for water of σ = 0.4 Å, ε = 0.0459 kcal mol^{-1} and ion parameters taken from CHARMM (Beglov and Roux, 1994). To derive the individual solvent susceptibilities 1D RISM calculations on a logarithmic grid ranging from $5.98{\cdot}10^{-3}$ Å to 164.02 Å with a total of 512 points were carried out. The solvent density of 0.0333295 Å^{-3} for pure water and 0.0323666 Å^{-3} for 1 M KCl at 298.15 K were used. For both solvents a dielectric permittivity of 78.4 was applied. All 3D RISM calculations were performed on a 100 Å × 100 Å × 144 Å grid with a spacing of 0.4 Å using the 3rd order Partial Series Expansion (PSE-3) closure (Kast and Kloss, 2008). 3D RISM equations were solved applying a maximum residual norm of direct correlation functions between successive steps of 10^{-4} as a convergence criterion. Solute-solvent interactions were modeled by the sum of Lennard-Jones (LJ, using standard Lorentz-Bertelot mixing rules) and Coulomb interactions. CHARMM27 (MacKerell et al., 1998) LJ parameters and partial charges for the protein were used. The partial charges of TBA were calculated using antechamber (Case et al., 2016) with AM1-BCC charges. TBA LJ parameters were obtained from general amber force field GAFF (Wang et al., 2004), see **Supplementary Table S2**. The calculations with reduced filter charges were performed by halving the carbonyl atom charges while keeping the total charge of the protein constant. This leads to a partial charge of the carbonyl C atom from original 0.51 to 0.255 and the carbonyl O atom from −0.51 to −0.255 e (**Supplementary Table S3**). Radial integration was performed based on grid data sliced by applying the HOLE algorithm (Smart et al., 1996). All parameters and structures of reduced filter models are collected in **Supplementary Tables S2-S7**, structures and parameters are also available in machine-readable format.

For computing the excess chemical potential change upon blocker release of 2HVK with and without an explicitly placed K^+ at S4, we subjected four systems: (i) isolated channel, (ii) channel with K^+, (iii) channel with TBA, and (iv) channel with TBA plus K^+ to 3D RISM calculations in modified SPC/E water. For these calculations a quantitatively optimized solvation free energy model based on the partial molar volume (PMV) and net charge correction is available from our earlier work (Tielker et al., 2018, 2021). Following the strategy described there for pure force field-based 3D RISM calculations the parameters for scaling the PMV and the net charge term were c_V = −0.09982 kcal mol^{-1} Å^{-3} and c_q = −15.66344 kcal mol^{-1} e^{-1}.

RESULTS AND DISCUSSION

Electrophysiological Measurements of Blocking by Tetrapropylammonium

In previous studies we have used the analysis of excess noise in the model channel Kcv_{NTS} for understanding the mechanism of fast gating in the SF and for determining the voltage-dependent occupation of the K^+ binding sites in the SF (Rauh et al., 2018). Here, we employ the same analysis for a better understanding of mutual interactions between the pore blocker TPrA and ions in the SF. It is well established that quaternary ammonium ions occlude the selectivity filter from the cytosolic side (Faraldo-Gómez et al., 2007; Lenaeus et al., 2014; **Figure 1E**). Because of the strong conservation of the canonical selectivity filter sequence throughout potassium channels in all realms of life (Heginbotham et al., 1994; **Figure 1D**), it is expected that the observed effects ought to be fairly similar throughout the whole K^+ channel family.

Under control conditions (**Figure 1A**), the time series of current in the Kcv_{NTS} channel display the typical high open probability with some short closures at positive voltages. At negative voltages, the current becomes increasingly noisy ("flickering," with excess noise, Heinemann and Sigworth, 1991) due to a fast gating process in the SF (Rauh et al., 2017a, 2018). Averaging over these events makes the apparent (average) current I_{app} smaller than the actual open-channel current I_{true} (Schroeder, 2015).

At moderate TPrA concentrations (0.1 mM, **Figure 1B**), I_{app} is slightly decreased, and some flickering and increased open-channel noise occurs at positive voltages indicating fast blocking events that are not directly resolved. Higher TPrA concentrations (**Figure 1C**) further decrease the apparent current at positive voltages. At negative voltages, the effect is much smaller. This is expected, since the positively charged blocker has to diffuse against the inward flow of K^+ ions, and it is influenced by interaction with an increasing ion population in the SF close to the blocker as shown below.

Evaluation of the Rate Constants of Fast Blocking by Fitting Amplitude Histograms

The TPrA-induced increase in open-channel noise can be exploited to extract the rate constants of blocking. The amplitude histograms (**Supplementary Figure S1**) are fitted with an adequate Markov model (**Figure 2A**). The model for gating of Kcv_{NTS} in the absence of a blocker (Schroeder, 2015; Rauh et al., 2017a, 2018) is extended by a fourth non-conducting state (B = blocked) to account for TPrA-induced block; the related rate constants are named k_{OB} and k_{BO}. k_{BO} is equivalent to k_{off}^{O} as it describes blocker dissociation in the open channel. This simplified model, in which the blocker interacts only with the open state, is justified since blocking events in single-channel recordings are only obtained for the open channel, in line with the 3D RISM calculations below that only consider structural information for the interaction of the blocker with the open channel. Any blocking events, which may occur while one of the intrinsic gates (S, M, F) is closed, do not contribute to the recorded single-channel currents and hence do not add to the amplitude histograms (**Supplementary Figure S1**). For the same reason they also do not occur in the model of **Figure 2A**. Any additional state-dependent rate constants of blocking would only be relevant if the blocker interferes with the intrinsic gates. A detailed discussion of this possibility is presented in the

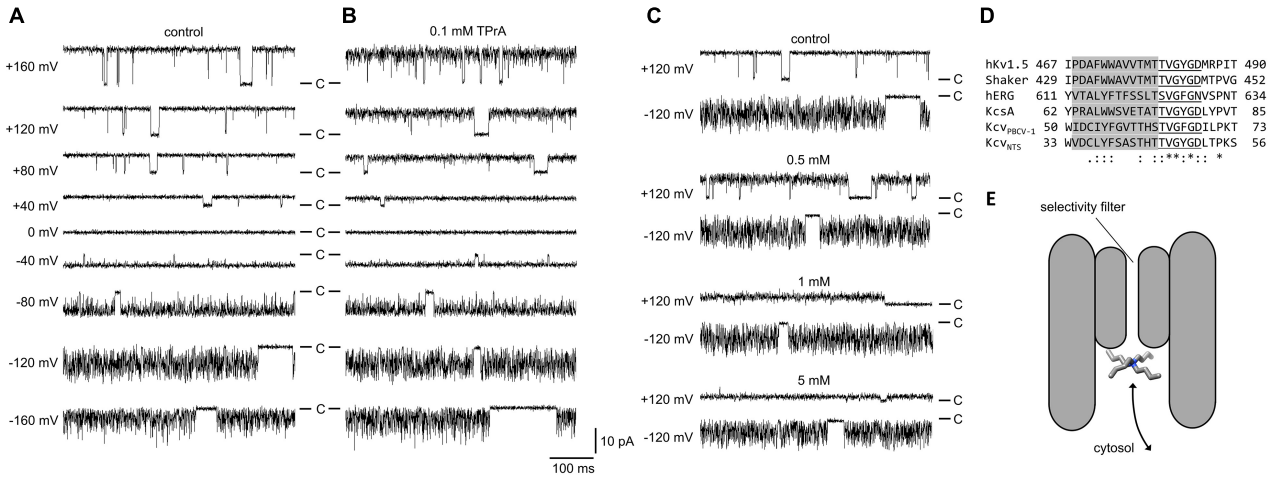

FIGURE 1 | Block of single-channel currents in Kcv$_{NTS}$ in DPhPC membranes by cytosolic TPrA. **(A,B)** Representative time series measured in symmetrical 100 mM KCl at different membrane voltages between +160 mV and −160 mV **(A)** without TPrA and **(B)** with 0.1 mM TPrA. **(C)** Time series measured in different concentrations of TPrA at +120 and −120 mV. The scale bar refers to all three panels in this figure. C marks the closed state. The data for ±120 mV without TPrA are displayed in both **(A,C)**. **(D)** Alignment of the pore loop of two viral K^+ channels (Kcv$_{NTS}$, Rauh et al., 2017b), the one used in this study, and Kcv$_{PBCV-1}$ (Tayefeh et al., 2009), a bacterial K^+ channel (KcsA, UniProtKB/Swiss-Prot: P0A334.1) and three eukaryotic potassium channels (*Shaker*, GenBank: CAA29917.1, hERG, GenBank: BAA37096.1, and human Kv1.5, NCBI Reference Sequence: NP_002225.2). Sequence conservation (*identity, : conservative,. semi-conservative) was calculated with the Clustal Omega Webapp. The selectivity filter sequence is underlined, the pore helix is shaded in gray. **(E)** Schematic illustration of the blocking process, the binding site is only accessible from the cytosolic pore entrance.

Supplementary Information (**Supplementary Figure S4**), which concludes that the influence of these secondary effects on the determination of the average rate constant k_{off}^{O} is in this case so small that it can be ignored. Consequently, we use the simplified Markov model in **Figure 2A** for determining the rate constant $k_{off}^{O} = k_{BO}$ of blocker release in the open channel. As we here deal with the rate constant of blocker release, details of blocker binding k_{OB} (**Figures 2C,D**) are discussed in the **Supplementary Material** (Equations S2, S3).

Figure 2B shows that k_{off}^{O} does not depend on TPrA concentration. This is not surprising because the dissociation of the blocker from its binding site in the channel cavity should not depend on the blocker concentration in the cytosol. Thus, the complete curve of the voltage dependency of k_{off}^{O} can be composed from the contributions of the different TPrA concentrations. The strong overlap of data points at voltages more positive than -80 mV justifies this procedure (**Figure 2B**). The data underpin the choice of TPrA for these experiments as its voltage-dependent rate constants of binding and unbinding (between 7000 s^{-1} and 700000 s^{-1}) are in a temporal range that is completely covered by our fast gating analysis (Schroeder, 2015). This is not the case for other QA blockers we tested.

Correlating Voltage Dependence of the Rate Constant of Blocker Dissociation With Ion Occupation Probability in S4

Since S4 is the ion binding site nearest to the blocker it is expected that its occupation probability P(S4) dominates the repulsion of the blocker. Thus, determination of P(S4) is required for the development of a quantitative model, which describes its effect on the rate constant k_{off}^{O} of blocker dissociation. In a previous study (Rauh et al., 2018), it has been shown that the "soft knock-on" model of ion transport in the selectivity filter (**Figure 3A**) as developed from MD simulations (Roux, 2005) is adequate for describing ion hopping in the open Kcv$_{NTS}$ channel. In contrast, the alternative "direct knock-on" model (Köpfer et al., 2014; Mironenko et al., 2021) was unable to describe the experimental data of Kcv$_{NTS}$ for the K^+ concentrations and membrane voltages used in the previous (Rauh et al., 2018) and present study, and is thus not further considered here. This does not imply that the direct knock-on model does not apply to ion channels especially as crystallographic support for a hard knock-on model has been provided (Langan et al., 2018) by anomalous X-ray diffraction studies of ion transport in K^+ channels. However, it may suggest that different models apply to different channels. The rate constants for **Figure 3A** have been obtained from a global fit of IV curves and the voltage dependency of k_{OM}, the rate constant of channel closure of the sub-millisecond gating in the SF, measured in symmetric 100 mM K^+ (activity 77 mM) (Rauh et al., 2018). From these rate constants, the occupation probability curves P_1 to P_5 (**Figure 3A**) are calculated for the unblocked state (**Figure 3B**). The respective equations and parameters are reported in the **Supplementary Material**.

An important premise of the calculation of P(S4) in the blocked state is the insensitivity of the crucial rate constants of ion hopping (**Figure 3A**) to the blocker. The analysis of the crystal structure of KcsA (Faraldo-Gómez et al., 2007; Yohannan et al., 2007; Lenaeus et al., 2014) shows that the blocker does indeed not influence the ion distribution in the filter. This implies that the rate constants of ion hopping in **Figure 3A**, the determinants of voltage-dependent ion distribution, are not

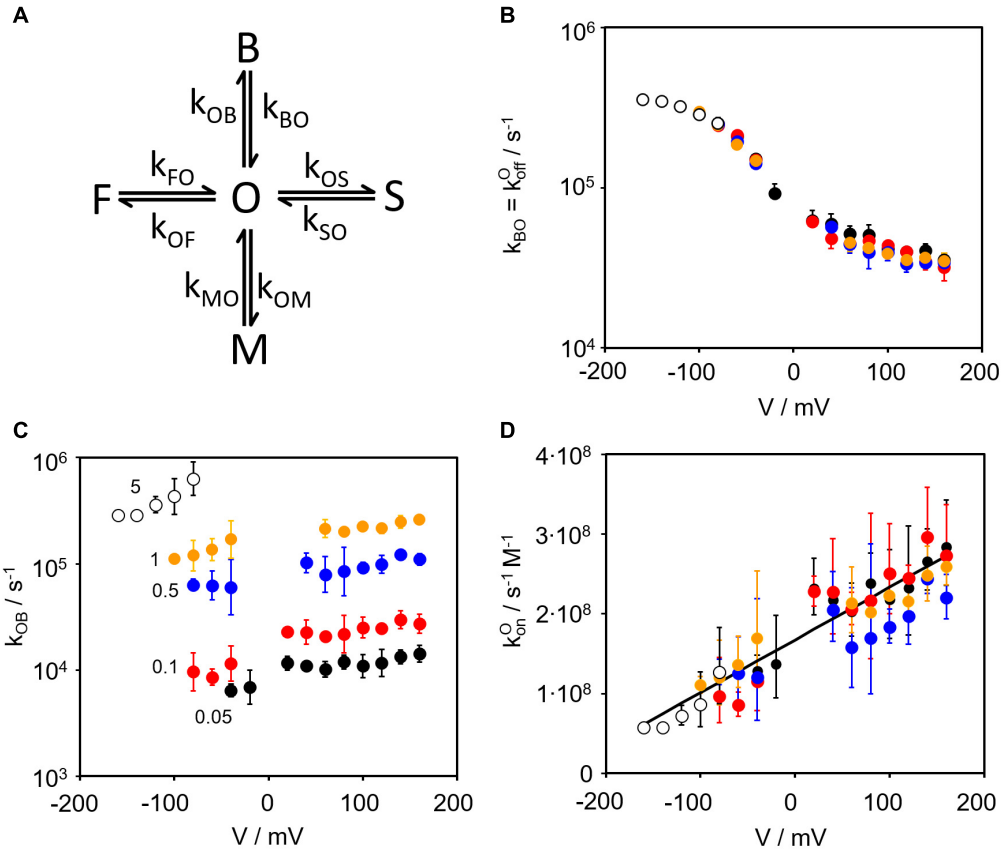

FIGURE 2 | Kinetics of the TPrA block. **(A)** Kinetic Markov model used for the fits of the amplitude histograms (**Supplementary Figure S1**). The states O (open) and F, M, S (three closed states of different dwell times) are those used previously in the 4-state model of gating in the unblocked Kcv_{NTS} (Rauh et al., 2017a, 2018). The blocked state B is introduced by the blocker TPrA. **(B)** Voltage dependence of the rate constant $k_{BO} = k^O_{off}$ measured at cytosolic TPrA concentrations of 0.05 mM ●, 0.1 mM ●, 0.5 mM ●, 1 mM ●, and 5 mM ○. **(C)** Voltage dependence of $k_{OB} = k^O_{on}$[TPrA] measured at the same concentrations as k_{BO}, **(D)** Voltage dependence of k^O_{on} as determined by dividing k_{OB} by the concentration of TPrA in mol. Data points are the geometric mean of 3 to 4 individual channels, error bars represent the geometric standard deviation. Some data points around 0 mV are missing because of insufficient signal-to-noise ratio.

affected by the blocker. These findings are further validated by 3D RISM calculations below. While both the crystal structures and 3D RISM calculations consider the situation at 0 mV, we show in the **Supplementary Material** that the rate constants of ion hopping are not affected by the blocker even under the action of non-zero membrane voltage.

For the calculation of P(S4) in the presence of the blocker, three rate constants are set to zero (crossed-out in red in **Figure 3A**). Binding and release of the K^+ ion at the cytosolic side is no longer possible, since the blocker occupies the required place of the cavity ion ($k_{12} = k_{21} = 0$). With a similar rational also $k_{32} = 0$ because the ion in S4 in state 3 (P_3) cannot leave into the cavity. In the KcsA structure (Faraldo-Gómez et al., 2007; Yohannan et al., 2007; Lenaeus et al., 2014) there is no space between S4 and the binding site of TPrA (see also inset in **Figure 4A**). The other rate constants in **Figure 3A** are assumed to be unchanged, as mentioned above and discussed in the **Supplementary Material**.

With these reasonable assumptions, the occupation probabilities of the states in the model in **Figure 3A** can be calculated from the rate constants of the open channel by Eq. S5.

The ion occupation probability of binding site S4 near the blocker includes all states with an ion in S4 resulting in:

$$P(S4) = P_3 + P_4 + P_5 \quad (1)$$

P_m is the probability of state m in **Figure 3A** and P(S4) the occupation probability of S4. These probabilities are shown in **Figure 3B** for the open unblocked channel and in **Figure 3C** for the blocked channel. State 2 is not occupied at all in the blocked channel, a trivial consequence of setting k_{32} and k_{12} to zero. Furthermore, the voltage dependence of P(S4) is drastically altered by the blocker (in contrast to the individual ion-hopping rate constants, except those being set to zero). This is because opening the cycle between P_1 and P_2 eliminates micro-reversibility. This does not matter at 0 mV because there is no net current. The inset in **Figure 3C** shows the values for the open and blocked channel taken from **Figures 3B,C** at 0 mV. The ion occupation probabilities P_3, P_4, and P_5 are virtually unchanged by the blocker at 0 mV. Only the probability P_1 is slightly increased since this state now has absorbed P_2, but this

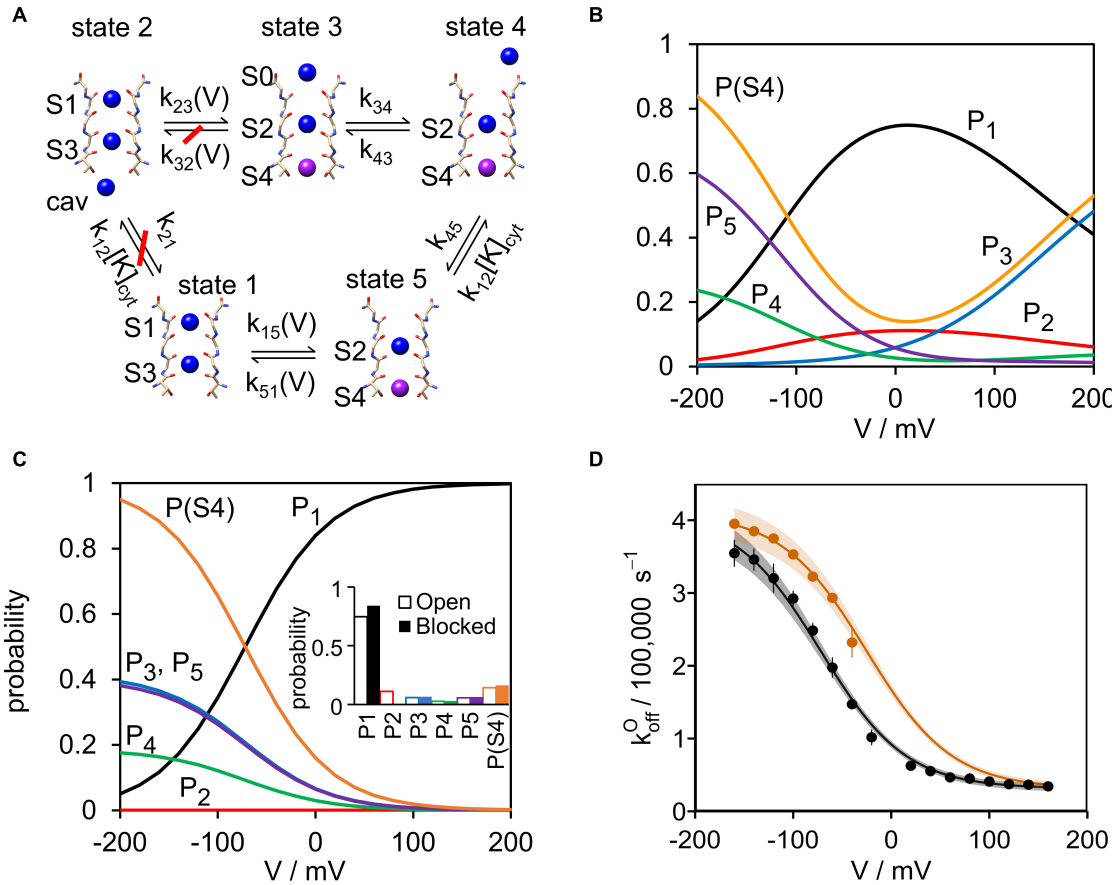

FIGURE 3 | Relating the voltage dependence of the rate constant of blocker release in the open state (k_{off}^{O}) to the ion distribution at S4 adjacent to the binding site of the blocker. **(A)** 5-state model of ion hopping (Roux, 2005) with the rate constants k_{ij} (i, j = 1 to 5) obtained from the previous analysis (Rauh et al., 2018). Numerical values for the rate constants are given in **Supplementary Table S1 (B,C)**. The probabilities P_m (m = 1 to 5) of the occurrence of the states 1 to 5 in the model of Roux (2005) calculated from Eqs. S4 to S9 for the case **(B)** that the channel is open and not blocked (redrawn from the original data of Rauh et al., 2018) and **(C)** that the channel is blocked ($k_{12} = k_{21} = k_{32} = 0$). P(S4) is the probability that there is an ion in binding site S4 (purple in panel **A**) close to the binding site of the blocker. According to panel **(A)**, $P(S4) = P_3 + P_4 + P_5$. The inset shows the probabilities for the open and blocked channel at 0 mV, as taken from panels **(B,C)**. **(D)** Comparison of the measured k_{off}^{O} with the values predicted by Eq. 4 based on P(S4). Black line: Fit of the experimentally determined k_{off}^{O} (black circles, pooled from all TPrA concentrations) with 100 mM symmetric KCl. Parameters a and b were free fit parameter in Eq. 3. Orange line: Prediction of Eq. 3 for 100 mM cytosolic and 500 mM external KCl. Parameters a and b were taken from the symmetric fit. Orange circles: experimentally determined k_{off}^{O} (with 5 mM TPrA). Data points show mean and standard deviation, shaded areas depict 99% confidence intervals.

does not affect P(S4). This is in line with the observation that filter population in crystal structures, and in our 3D RISM calculation, which are both without voltage, are unchanged by QA blockers (Faraldo-Gómez et al., 2007; Yohannan et al., 2007; Lenaeus et al., 2014).

Visual comparison of **Figures 2B**, **3C** already suggests that the voltage dependence of k_{off}^{O} and P(S4) are very similar. Their perfect coincidence (**Figure 3D**) corroborates the following model: After the blocker has bound, the ion distribution adopts a new steady or quasi-stationary state on the ns-time scale, since the transition time of a single ion is about 10 ns. This steady state lasts for an average time of $1/k_{off}^{O}$ (about 3 μs) until the blocker no longer withstands the electrostatic repulsion and leaves the binding site.

It is obvious from the model of ion-hopping (**Figure 3A**) that the ion occupation of S2, P(S2), is identical to P(S4). In the following equations, we nevertheless use P(S4) because of two arguments: 1. S2 is further away from the binding site of the blocker. Thus, its contribution to the repulsive force is expected to be small 2. P(S2) and P(S4) have the same voltage dependency. Thus, replacing P(S4) by $P(S4) + \text{const}^{*}P(S2)$ would merely lead to a slightly different constant pre-factor plus an additional fitting parameter in Eq. 3 without any influence on the core message of this investigation. It may be considered whether other K^{+} binding sites could have a similar effect as S2 and S4. **Figure 3A** shows that the alternatives P(S1) and P(S3) related to states 1 and 2. The probability of state 2 ($P2$) is zero and $P1$ has the opposite voltage dependency as k_{off}^{O} (**Figure 3C**).

Therefore, the causal relationship between k_{off}^{O} and P(S4) can be described by a weighted superposition of two different scenarios namely blocker release depending on the absence or

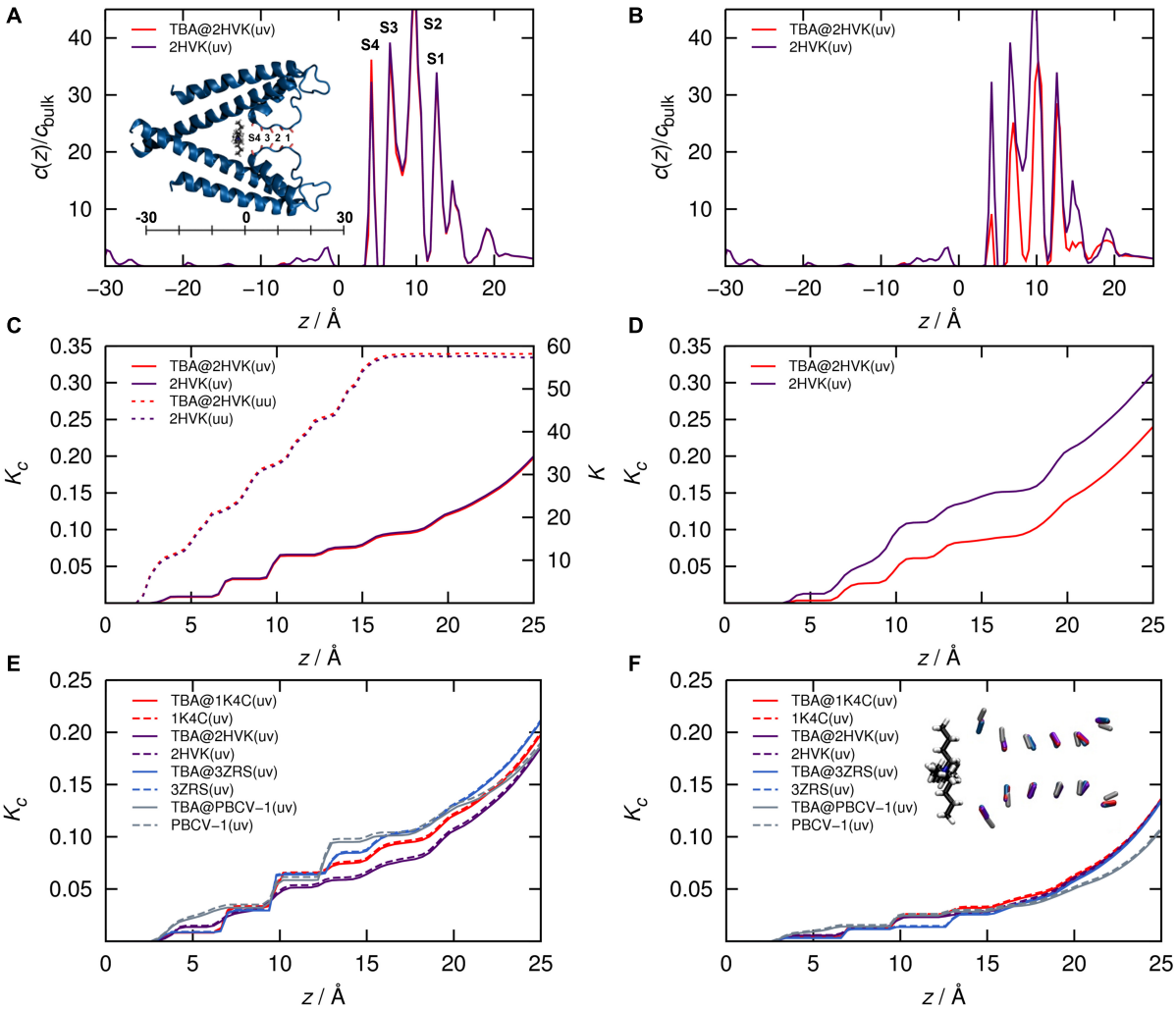

FIGURE 4 | (A,B) K^+ ion concentration profiles and **(C,D)** cumulative equilibrium constants as function of channel length coordinate z starting from the origin as shown in the inset in **(A)** from finite concentration (1 M, *uv*, solid lines) and infinite dilution (single hydrated ion, *uu*, dashed lines) 3D RISM calculations of KcsA (pdb code 2HVK) with (red) and without (purple) TBA placed in the cavity. **(E,F)** cumulative results for four reduced models with and without TBA comprising isolated carbonyl cages for KcsA (2HVK, Yohannan et al., 2007, crystalized with TBA and 1K4C (Zhou et al., 2001) crystalized without TBA), KirBac3.1 (3ZRS, Bavro et al., 2012) and the computationally determined filter model of Kcv_{PBCV-1} (Tayefeh et al., 2009; Hoffgaard et al., 2015). **(A,C,E)** from calculations with original force field, **(B,D,F)** with down-scaled filter carbonyl charges leading to halved local dipole moments. The inset in panel **(A)** represents the full 2HVK system in cartoon representation. The inset in panel **(F)** shows a superposition of all reduced filter carbonyl groups in the same color code as the curves.

presence of a K^+ ion in S4. This leads to the following Eyring-type expression for the total rate constant in the form of:

$$k_{\text{off}}^{\text{O}} = k_{\text{off},0}^{\text{O}}(1 - P(S4))\exp(-\Delta G_0/kT)$$
$$+k_{\text{off},0}^{\text{O}}P(S4)\exp(-\Delta G_{\text{ion}}/kT) \quad (2)$$

Here ΔG_0 and ΔG_{ion} are the free energy barriers that the blocker needs to overcome in order to leave its binding site in the absence (ΔG_0) or presence (ΔG_{ion}) of an ion in S4, respectively; k and T have their usual thermodynamic meaning. ΔG_0 and ΔG_{ion} are assumed to be independent of voltage. Voltage predominantly influences local ion occupancies, i.e., P(S4). The pre-factor $k_{\text{off},0}^{\text{O}}$ could in principle depend on voltage or the voltage-dependent ion population for example via structural rearrangements at the inner mouth, which are energetically coupled to the filter configuration. However, we approximate the pre-factors with and without blocker as identical as they measure the effective curvature of the blocker free energy surface; the latter is governed by the channel structure and determines the intrinsic blocker dynamics. This should be largely unaffected when the overall structure remains essentially unaltered by the filter ions (Faraldo-Gómez et al., 2007); see also the similar discussion related to 3D RISM calculations below.

For our model, we also ignore the direct influence of the electric field on measured blocker dissociation. It has been shown that about 80-90% of the transmembrane voltage decays

over the range of the selectivity filter (Jiang et al., 2002; Contreras et al., 2010; Andersson et al., 2018). This assumption is further corroborated by 3D RISM calculations (see below) that demonstrate that the energetic effect of typical electrostatic potential variations on singly charged ions are much smaller than the binding free energy change exerted by an ion placed at S4 on the blocker.

We therefore assume that all terms in Eq. 2 with exception of $P(S4)$ are voltage-independent. They can be merged into constant factors, which simplifies Eq. 2 to the form used for fitting voltage dependency of the measured values of k_{off}^{O} (**Figure 3D**):

$$k_{off}^{O} = a(1 - P(S4)) + cP(S4) = a + bP(S4) \quad (3)$$

This equation provides an excellent fit of k_{off}^{O} in symmetric 100 mM KCl (**Figure 3D**) with the following fit parameters:

$$a = k_{off,0}^{O} \exp(-\Delta G_0/kT) = 31\,400 \pm 1\,700\ s^{-1}, \text{ and}$$

$$b = c - a = k_{off,0}^{O}\left[\exp(-\Delta G_{ion}/kT) - \exp(-\Delta G_0/kT)\right]$$

$$= 378\,600 \pm 8\,600\ s^{-1}.$$

This model equation is the principal result of the present work: It demonstrates that blocker release kinetics can be fully described by two system-specific parameters of ion/blocker interaction, a and b, or equivalently a and c. a and c represent the blocker dissociation rate constants for the two aforementioned scenarios where binding site S4 is empty or occupied, respectively.

To further test this causal relationship between $P(S4)$ and k_{off}^{O} the two parameters a and b were used for experiments with asymmetric KCl solutions. To this end, we measured k_{off}^{O} of the TPrA block with 500 mM KCl on the external side and 100 mM KCl on the cytosolic side. Guided by the experience from measurements in symmetrical 100 mM KCl (**Figure 2**), we applied TPrA at a concentration of 5 mM. This assures blocking events at the critical range at negative voltages between −160 mV and −40 mV. These data cover the interesting region of the voltage dependency of k_{off}^{O} which is necessary for a comparison with the data from symmetrical 100 mM KCl.

The orange curve in **Figure 3D** shows excellent agreement within the confidence bands between measured values of k_{off}^{O} and those predicted from the ion hopping model with $P(S4)$ for an external K^+ concentration of 500 mM. It is important to emphasize that a and b were not fitted to the asymmetric data but taken from the results in symmetric solutions. $P(S4)$ was calculated for 500 mM external K^+ from the rate constants of ion hopping (**Figure 3A**) using the **Supplementary Eqs. S5-S9**.

The fact that the parameters a and b, determined for symmetrical KCl, also match the data from asymmetrical recordings confirms our model assumptions. The results in **Figure 3D** verify previous suggestions (Jara-Oseguera et al., 2007; Posson et al., 2013) that the rate constant of blocker release k_{off}^{O} is determined by the electrostatic repulsion of the positively charged blocker by the K^+ ions in site S4.

Since $k_{off,0}^{O}$ is unknown we can only estimate the relative change of the Eyring barrier, $\Delta\Delta G$, which is caused by the presence of the ion. The $\Delta\Delta G$ value can be obtained from the relation between a and c of Eq. 4 and the coefficients in Eq. 3 resulting in:

$$\Delta G_{ion} - \Delta G_0 = \Delta\Delta G = -\ln(1 + \frac{b}{a})\, kT \quad (4)$$

With the values of a and c given above we can calculate an effective $\Delta\Delta G = -2.6 \pm 0.15\ kT$.

Estimating the Influence of the Blocker on the Ion Distributions in the Selectivity Filter

A crucial assumption in the comparison between the voltage dependencies of k_{off}^{O} and ion occupation in S4 is that the blocker does not influence the relevant rate constants of ion hopping in the model of **Figure 3A**. Thus, we determined the impact of the blocker on filter occupancies using the crystal structure of KcsA in complex with tetrabutylammonium (TBA, pdb code 2HVK, Yohannan et al., 2007; **Figure 4A**, inset). This corresponds to the "closed" KcsA structure, which at a first glance seems to be inadequate, since here we block the open Kcv_{NTS}. However, in the "closed" KcsA channel only the bundle crossing gate is closed while the SF is open (Cuello et al., 2017), and that is exactly what we need to represent the Kcv_{NTS}. Because of the absence of a cytosolic gate in Kcv_{NTS} (Rauh et al., 2017b) the closed KcsA bundle crossing is of no concern as we only deal with the SF. Thus, the KcsA structure is a valid model system for interpreting the experimental data from Kcv_{NTS} in a structure/function context due to the similar SF and overall pore architecture of both channels.

The KcsA template structure was exposed to aqueous KCl solutions for 3D RISM calculations (Kast et al., 2011) in the presence and absence of blocker without changing the structure. This is in line with the apparent insensitivity of the pore structure to the blocker (Guo and Lu, 2001; Jara-Oseguera et al., 2007; Lenaeus et al., 2014). 3D RISM theory (Beglov and Roux, 1996, 1997; Kovalenko and Hirata, 1998) yields the approximate equilibrium distribution of solvent atoms and ions around (and inside) a molecule, from which ion occupancy measures can be computed in two different ways: a partitioning constant K_c (mass action law) and a thermodynamic binding constant K at infinite dilution. Details are discussed in the **Supplementary Material**.

Results for calculations with and without TBA (the latter obtained by removing TBA coordinates from the pdb structure) are shown along with a cartoon of the channel model in **Figure 4A**. The results with the original force field charges clearly corroborate the underlying hypothesis: The population of filter K^+ ions (in local concentration and the cumulative scale) and in both the finite concentration and infinite dilution setup (**Figures 4A,C**), are largely unaffected by TBA in its blocking site.

The situation only changes as soon as we (unphysically) scale the charges of the filter carbonyl ions to exhibit a local dipole moment of 50% of the original (**Figures 4B,D**): Only under this artificial condition the absolute filter population of K^+ ions decreases after placing TBA close to the exit of the SF. This indicates that the SF is remarkable in the context of protein/K^+ ion interactions; its architecture and electrostatic energy landscape is responsible for the apparent population

decoupling. In other words, the ions in the filter do not "feel" the presence of a blocker ion.

To test whether this finding from the KcsA structure can be extrapolated to the experimental data from Kcv_{NTS} in particular, and all K^+ channels with this type of SF in general we also calculated the blocker effect on K^+ ion occupancies in maximally reduced channel models. These contain only the isolated carbonyl groups of the SF; all atoms representing the protein background are removed. Analogous calculations as in **Figure 4A** were done for two reduced template structures of KcsA (2HVK and 1K4C) as well as on two further isolated filters from KirBac and Kcv_{PBCV-1} (**Figures 4E,F**). TBA was placed in the same position relative to the SF, which corresponds essentially to the closest possible distance between blocker and filter. In this way, we examined the upper limit of the blocker effect on the filter ions. Results for full carbonyl charges and corresponding halved dipole moments are shown in the bottom row of **Figure 4**. Notably, despite modest structural diversity of the model filters (see inset in **Figure 4F**), the calculations confirm the independence of the occupation of K^+ in the SF on the presence of the blocker. Worth noting is that the relative effect of halving the dipole moments is, different from the results in the full protein, practically negligible in the isolated carbonyl cages. This means that the protein environment actually counteracts the strongly attractive carbonyl forces exerted on the K^+ ions. Conversely, this result further emphasizes the dominant role of the filter carbonyl geometry and electrostatics for controlling the K^+ occupation probability. The data again confirm our basic premise that blocker kinetics can be derived from equilibrium ion concentrations determined from the blocker-free channel pore.

For the preceding analysis of the functional data in the context of the filter structure it is important to note that the ion concentration profile can be interpreted as the effective single-ion free energy landscape in the mean field of all ions, which are on average present in a structurally averaged SF. This energy landscape, which is seen by the ions, hence determines the rate constants of ion hopping. Therefore, when the concentration profile is unchanged, we can assume that the hopping kinetics are also unchanged (except of course for those transitions that are made impossible by the blocker). In this context it is plausible to assume that quasi-stationary concentration profiles at a given voltage will remain unaffected by the blocker even under an external potential due to the strong electrostatic carbonyl-ion interactions, though we are not able to quantitatively model such a system on the basis of an equilibrium theory such as 3D RISM.

Furthermore, 3D RISM calculations allow for an analytically computable estimation of the excess chemical potential, μ^{ex}, of molecular structures in solution (Kast and Kloss, 2008; Tielker et al., 2018, 2021), which can be used to check model assumptions. One interesting case is to study the impact of an explicitly placed K^+ ion at position S4 in the reference KcsA channel structure. Results for the isolated protein, channel with K^+ at S4, channel with TBA, and channel with both, K^+ and TBA are −16925.01 (KcsA), −16580.38 (KcsA-K^+), −16920.37 (KcsA-TBA), −16747.73 (KcsA-TBA-K^+) kJ/mol, respectively. Together with the direct TBA-K^+ interaction energy taken from the force field of ΔE = 243.34 kJ/mol we obtain for an approximation to the relative blocker release free energy between K^+-loaded and free structure a value of:

$$\begin{aligned}&\mu^{ex}(\mathrm{KcsA}-\mathrm{K}^+)-\mu^{ex}(\mathrm{KcsA}-\mathrm{TBA}-\mathrm{K}^+)\\&-[\mu^{ex}(\mathrm{KcsA})-\mu^{ex}(\mathrm{KcsA}-\mathrm{TBA})]-\Delta E\\&=-71.34\ \mathrm{kJ/mol}\end{aligned}\tag{5}$$

Although we ignored thermal fluctuations in this simple model, rigid body cancelation allows at least for estimating the order of magnitude of the explicit ion effect. Clearly, the presence of an explicit ion strongly disfavors blocker binding. This energetic effect is much larger than that from external voltage. Even if we assume a 100 mV drop over the distance between S4 and blocker site (which is in practice much smaller), this would amount to only roughly 9.6 kJ/mol, i.e., a value much smaller than the direct interaction effect. This corroborates the assumption that a direct influence of membrane voltage on the blocker can be ignored for our model in Eqs. 2, 3.

Given the magnitude of the observed free energy change, one might ask how the relatively small ion modulation of the relative barriers of $\Delta\Delta G = -2.6\ kT$ (ca. –6.4 kJ/mol) from Eq. 4 comes about. Here, we have to consider that an explicit ion lifts both, the absolute magnitudes of free energies in the bound minima and the transition states. The small $\Delta\Delta G$ therefore implies the change of energetic *distance* between transition and bound states. This merely means that the transition state feels less repulsive interaction with the S4 ion than the bound state. Mechanistically, this implies that the transition state is located farther away from the S4 ion than the bound state, which is of course plausible.

CONCLUSION

The experimental results culminating in **Figure 3D** as well as the calculations in **Figure 4** have important consequences for understanding the mutual interactions between blocker and channel proteins: The excellent fit verifies in quantitative terms the assumption (Heginbotham and Kutluay, 2004; Jara-Oseguera et al., 2007; Posson et al., 2013) that an ion close to the bound blocker is responsible for releasing the latter from its binding site. Our data now identify the K^+ ion in binding site S4 (possibly with a smaller contribution by the S2 ion) in the selectivity filter as the relevant repulsing ion. The occupation of this site determines in quantitative terms blocker dissociation.

The good agreement between experimental kinetic analysis in the Kcv_{NTS} channel and calculations on the structurally similar channel KcsA, which was crystallized in the presence of a blocker, reveals a surprising feature at the atomic level: Even though the electrostatic interaction/repulsion between blocker and K^+ ions is symmetric, the strong affinity between the filter carbonyl groups and K^+ ions basically "shields" the latter in a kinetic sense from any impact by the blocker ion even at close proximity by preserving filter ion occupancies. The population dynamics in the filter is therefore a consequence of the protein environment, and dominantly controlled by the specific ion-carbonyl interactions alone.

As a signature of this phenomenon, the occupation probability of the binding site in the SF in vicinity to the blocker (P(S4), Eq. 2) can be correctly determined from the rate constants of ion hopping (k_{ij} in **Figure 3A**). The latter were obtained from experimental data of the open channel (Rauh et al., 2018), using a global fit of IV curves and the voltage dependence of the rate constant of channel closing.

All these results corroborate the power of using excess noise analysis of electrophysiological recordings together with model-based analysis (Rauh et al., 2018) to test predictions from structural data and computational modeling. The fact that SF populations are unaffected by the blocker ion, irrespective of the exact filter geometry and the molecular features of the remaining protein, prompt further-reaching speculations: a direct consequence of these results is that functional data measured in the absence of the blocker and the respective rate constants suffice as input for quantifying the population variable in the kinetic release model. The presence of the blocker can then be simply modeled by setting rate constants of impossible pathways to zero, leaving only two adjustable parameters that completely describe the blocker release under diverse bath conditions. Because of the conserved pore architecture, it is tempting to predict that these features are transferable to other K^+ channels. This can be tested in future work, along with a development of a similar model for blocker binding, to close the gap to a general quantitative blocking/unblocking model approach, that will be helpful in rational drug design for K^+ channel targets.

DATA AVAILABILITY STATEMENT

The software for the 3D RISM calculations has been developed in our laboratory and can be made available for collaboration purposes on request. The program "bownhill" for extended beta distribution analysis as well as the source code is available on request from the corresponding author.

AUTHOR CONTRIBUTIONS

TG, TW, ND, and OR performed the experiments. MU performed the 3D RISM calculations. GT designed the research. SMK designed the research, analyzed the 3D RISM results, and wrote the manuscript. U-PH and IS designed the research, analyzed the data, and wrote the manuscript. All authors contributed to the article and approved the submitted version.

FUNDING

The work has been supported by the Deutsche Forschungsgemeinschaft (DFG, German Research Foundation), research grant HA 712/14-3 to U-PH and Heisenberg Fellowship SCHR 1467/4-1 and FOR 2518 (DynIon, SCHR 1467/6-1) to IS, and under Germany's Excellence Strategy – EXC-2033 – 390677874 – RESOLV – to SMK, and the European Research Council (NoMAGIC) under Grant Agreement No 695078 to GT.

ACKNOWLEDGMENTS

We thank the ITMC of TU Dortmund for computational support, and Christian Chodun and Nicolas Tielker for calibration of the free energy model for 3D RISM calculations.

SUPPLEMENTARY MATERIAL

The Supplementary Material for this article can be found online at: https://www.frontiersin.org/articles/10.3389/fphys.2021.737834/full#supplementary-material

REFERENCES

Albertsen, A., and Hansen, U.-P. (1994). Estimation of kinetic rate constants from multi-channel recordings by a direct fit of the time series. *Biophys. J.* 67, 1393–1403.

Andersson, A. E. V., Kasimova, M. A., and Delemotte, L. (2018). Exploring the viral channel Kcv_{PBCV-1} function via computation. *J. Membr. Biol.* 251, 419–430.

Armstrong, C. M., and Hille, B. (1972). The inner quaternary ammonium ion receptor in potassium channels of the node of Ranvier. *J. Gen. Physiol.* 59, 388–400.

Ashcroft, F. M. (2006). From molecule to malady. *Nature* 440, 440–447. doi: 10.1038/nature04707

Bagal, S. K., Brown, A. D., Cox, P. J., Omoto, K., Owen, R. M., Pryde, D. C., et al. (2013). Ion channels as therapeutic targets: a drug discovery perspective. *J. Med. Chem.* 56, 593–624. doi: 10.1021/jm301433

Bavro, V. N., De Zorzi, R., Schmidt, M. R., Muniz, J. R. C., Zubcevic, L., Sansom, M. S. P., et al. (2012). Structure of a KirBac potassium channel with an open bundle crossing indicates a mechanism of channel gating. *Nat. Struct. Mol. Biol.* 19, 158–164. doi: 10.1038/nsmb.2208

Beglov, D., and Roux, B. (1994). Finite representation of an infinite bulk system: solvent boundary potential for computer simulations. *J. Chem. Phys.* 100, 9050–9063. doi: 10.1063/1.466711

Beglov, D., and Roux, B. (1996). Solvation of complex molecules in a polar liquid: an integral equation theory. *J. Chem. Phys.* 104, 8678–8689. doi: 10.1063/1.471557

Beglov, D., and Roux, B. (1997). An integral equation to describe the solvation of polar molecules in liquid water. *J. Phys. Chem. B* 101, 7821–7826.

Bernard, G., and Shevell, M. I. (2008). Channelopathies: a review. *Pediatr. Neurol.* 38, 73–85. doi: 10.1016/j.pediatrneurol.2007.09.007

Braun, C. J., Baer, T., Moroni, A., and Thiel, G. (2014). Pseudo painting/air bubble technique for planar lipid bilayers. *J. Neurosci. Methods* 233, 13–17. doi: 10.1016/j.jneumeth.2014.05.031

Braun, C. J., Lachnit, C., Becker, P., Henkes, L. M., Arrigoni, C., Kast, S. M., et al. (2013). Viral potassium channels as a robust model system for studies of membrane-protein interaction. *Biochim. Biophys. Acta* 1838, 1096–1103. doi: 10.1016/j.bbamem.2013.06.010

Bucchi, A., Baruscotti, M., Nardini, M., Barbuti, A., Micheloni, S., Bolognesi, M., et al. (2013). Identification of the molecular site of ivabradine binding to HCN4 channels. *PLoS One* 8:e0053132. doi: 10.1371/journal.pone.0053132

Caceci, M. S., and Cacheris, W. P. (1984). Fitting curves to data - The simplex algorithm is the answer. *BYTE* 5, 340–362.

Case, D. A., Ben-Shalom, I. Y., Brozell, S. R., Cerutti, D. S., Cheatham, T. E. III, Cruzeiro, V. W. D., et al. (2016). "AMBER 2016," in *Proceedings of the NIC Symposium 2016*, Jülich.

Choi, K., Mossman, C., Jeffrey, A., and Yellen, G. (1993). The internal quaternary ammonium receptor site of *Shaker* potassium channels. *Neuron* 10, 533–541.

Contreras, J. E., Chen, J., Lau, A. Y., Jogini, V., Roux, B., and Holmgren, M. (2010). Voltage profile along the permeation pathway of an open channel. *Biophys. J.* 99, 2863–2869. doi: 10.1016/j.bpj.2010.08.053

Cuello, L. G., Cortes, D. M., and Perozo, E. (2017). The gating cycle of a K^+ channel at atomic resolution. *eLife* 6:e28032. doi: 10.7554/eLife.28032

Du, C., Zhang, Y., El Harchi, A., Dempsey, C. E., and Hancox, J. C. (2014). Ranolazine inhibition of hERG potassium channels: drug-pore interactions and reduced potency against inactivation mutants. *J. Mol. Cell. Cardiol.* 74, 220–230. doi: 10.1016/j.yjmcc.2014.05.013

Faraldo-Gómez, J. D., Kutluay, E., Jogini, V., Zhao, Y., Heginbotham, L., and Roux, B. (2007). Mechanism of intracellular block of the KcsA K^+ channel by tetrabutylammonium: insights from X-ray crystallography, electrophysiology and replica-exchange molecular dynamics simulations. *J. Mol. Biol.* 365, 649–662. doi: 10.1016/j.jmb.2006.09.069

Fernández-Ballester, G., Fernández-Carvajal, A., González-Ros, J. M., and Ferrer-Montiel, A. (2011). Ionic channels as targets for drug design: a review on computational methods. *Pharmaceutics* 3, 932–953. doi: 10.3390/pharmaceutics3040932

Gazzarrini, S., Kang, M., Abenavoli, A., Romani, G., Olivari, C., Gaslini, D., et al. (2009). *Chlorella* virus ATCV-1 encodes a functional potassium channel of 82 amino acids. *Biochem. J.* 420, 295–303. doi: 10.1042/BJ20090095

Greiner, T. (2011). *Characterization of Novel Potassium Transport Proteins from Chlorella* Viruses. Ph.D. thesis. Darmstadt: Technische Universität Darmstadt.

Guo, D., and Lu, Z. (2001). Kinetics of inward-rectifier K^+ channel block by quaternary alkylammonium ions: dimension and properties of the inner pore. *J. Gen. Physiol.* 117, 395–405.

Heginbotham, L., and Kutluay, E. (2004). Revisiting voltage-dependent relief of block in ion channels: a mechanism independent of punchthrough. *Biophys. J.* 86, 3663–3670. doi: 10.1529/biophysj.103.039412

Heginbotham, L., Lu, Z., Abramson, T., and MacKinnon, R. (1994). Mutations in the K^+ channel signature sequence. *Biophys. J.* 66, 1061–1067.

Heinemann, S. H., and Sigworth, F. J. (1991). Open channel noise. VI. Analysis of amplitude histograms to determine rapid kinetic parameters. *Biophys. J.* 60, 577–587.

Hoffgaard, F., Kast, S. M., Moroni, A., Thiel, G., and Hamacher, K. (2015). Tectonics of a K^+ channel: the importance of the N-terminus for channel gating. *Biochim. Biophys. Acta Biomembr.* 1848, 3197–3204. doi: 10.1016/j.bbamem.2015.09.015

Humphrey, W., Dahlke, A., and Schulten, K. (1996). VMD - visual molecular dynamics. *J. Mol. Graph.* 14, 33–38.

Jara-Oseguera, A., Islas, L. D., García-Villegas, R., and Rosenbaum, T. (2007). On the mechanism of TBA block of the TRPV1 channel. *Biophys. J.* 92, 3901–3914. doi: 10.1529/biophysj.106.102400

Jeanniard, A., Dunigan, D. D., Gurnon, J. R., Agarkova, I. V., Kang, M., Vitek, J., et al. (2013). Towards defining the chloroviruses: a genomic journey through a genus of large DNA viruses. *BMC Genomics* 14:158. doi: 10.1186/1471-2164-14-158

Jiang, Y., Lee, A., Chen, J., Cadene, M., Chait, B. T., and MacKinnon, R. (2002). The open pore conformation of potassium channels. *Nature* 417, 523–546. doi: 10.1038/417523a

Jorgensen, W. L., Chandrasekhar, J., Madura, J. D., Impey, R. W., and Klein, M. L. (1983). Comparison of simple potential functions for simulating liquid water. *J. Chem. Phys.* 79:926. doi: 10.1063/1.445869

Kast, S. M., and Kloss, T. (2008). Closed-form expressions of the chemical potential for integral equation closures with certain bridge functions. *J. Chem. Phys.* 129:236101. doi: 10.1063/1.3041709

Kast, S. M., Kloss, T., Tayefeh, S., and Thiel, G. (2011). A minimalist model for ion partitioning and competition in a K^+ channel selectivity filter. *J. Gen. Physiol.* 138, 371–373. doi: 10.1085/jgp.201110694

Katzen, F., Fletcher, J. E., Yang, J.-P., Kang, D., Peterson, T. C., Cappuccio, J. A., et al. (2008). Insertion of membrane proteins into discoidal membranes using a cell-free protein expression approach. *J. Prot. Res.* 7, 3535–3542.

Köpfer, D. A., Song, C., Gruene, T., Sheldrick, G. M., Zachariae, U., and De Groot, B. L. (2014). Ion permeation in K^+ channels occurs by direct Coulomb knock-on. *Science* 346, 352–355. doi: 10.1126/science.1254840

Kovalenko, A., and Hirata, F. (1998). Three-dimensional density profiles of water in contact with a solute of arbitrary shape: a RISM approach. *Chem. Phys. Lett.* 290, 237–244.

Langan, P. S., Vandavasi, V. G., Weiss, K. L., Afonine, P. V., el Omari, K., Duman, R., et al. (2018). Anomalous X-ray diffraction studies of ion transport in K^+ channels. *Nat. Commun.* 9:4540. doi: 10.1038/s41467-018-06957-w

Lenaeus, M. J., Burdette, D., Wagner, T., Focia, P. J., and Gross, A. (2014). Structures of KcsA in complex with symmetrical quaternary ammonium compounds reveal a hydrophobic binding site. *Biochemistry* 53, 5365–5373. doi: 10.1021/bi500525s

MacKerell, A. D. J., Bashford, D., Bellott, M., Dunbrack, R. L. J., Evanseck, J. D., Field, M. J., et al. (1998). All-atom empirical potential for molecular modeling and dynamics studies of proteins. *J. Phys. Chem. B* 5647, 3586–3616.

Mironenko, A., Zachariae, U., de Groot, B. L., and Kopec, W. (2021). The persistent question of potassium channel permeation mechanisms. *J. Mol. Biol.* 433:167002. doi: 10.1016/j.jmb.2021.167002

Morais-Cabral, J. H., Zhou, Y., and MacKinnon, R. (2001). Energetic optimization of ion conduction rate by the K^+ selectivity filter. *Nature* 414, 37–42. doi: 10.1038/35102000

Piechotta, P. L., Rapedius, M., Stansfeld, P. J., Bollepalli, M. K., Erhlich, G., Andres-Enguix, I., et al. (2011). The pore structure and gating mechanism of K2P channels. *EMBO J.* 30, 3607–3619. doi: 10.1038/emboj.2011.268

Posson, D. J., McCoy, J. G., and Nimigean, C. M. (2013). The voltage-dependent gate in MthK potassium channels is located at the selectivity filter. *Nat. Struct. Mol. Biol.* 20, 159–166. doi: 10.1038/nsmb.2473

Rauh, O., Urban, M., Henkes, L. M., Winterstein, T., Greiner, T., Van Etten, J. L., et al. (2017b). Identification of intra-helical bifurcated H-bonds as a new type of gate in K^+ channels. *J. Am. Chem. Soc.* 139, 7494–7503. doi: 10.1021/jacs.7b01158

Rauh, O., Hansen, U.-P., Mach, S., Hartel, A. J. W., Shepard, K. L., Thiel, G., et al. (2017a). Extended beta distributions open the access to fast gating in bilayer experiments - assigning the voltage-dependent gating to the selectivity filter. *FEBS Lett.* 591, 3850–3860. doi: 10.1002/1873-3468.12898

Rauh, O., Hansen, U.-P., Scheub, D. D., Thiel, G., and Schroeder, I. (2018). Site-specific ion occupation in the selectivity filter causes voltage-dependent gating in a viral K^+ channel. *Sci. Rep.* 8:10406. doi: 10.1038/s41598-018-28751-w

Roux, B. (2005). Ion conduction and selectivity in K^+ channels. *Annu. Rev. Biophys. Biomol. Struct.* 34, 153–171. doi: 10.1146/annurev.biophys.34.040204.144655

Sánchez-Chapula, J. A., Navarro-Polanco, R. A., Culberson, C., Chen, J., and Sanguinetti, M. C. (2002). Molecular determinants of voltage-dependent human ether-a-go-go related gene (HERG) K^+ channel block. *J. Biol. Chem.* 277, 23587–23595. doi: 10.1074/jbc.M200448200

Schroeder, I. (2015). How to resolve microsecond current fluctuations in single ion channels: the power of beta distributions. *Channels* 9, 262–280. doi: 10.1080/19336950.2015.1083660

Schroeder, I., and Hansen, U.-P. (2006). Strengths and limits of Beta distributions as a means of reconstructing the true single-channel current in patch clamp time series with fast gating. *J. Membr. Biol.* 210, 199–212.

Schroeder, I., and Hansen, U.-P. (2009). Using a five-state model for fitting amplitude histograms from MaxiK channels: beta-distributions reveal more than expected. *Eur. Biophys. J.* 38, 1101–1114. doi: 10.1007/s00249-009-0515-0

Smart, O. S., Neduvelil, J. G., Wang, X., Wallace, B. A., and Sansom, M. S. P. (1996). HOLE: a program for the analysis of the pore dimensions of ion channel structural models. *J. Mol. Graph.* 14, 354–360. doi: 10.1016/S0263-7855(97)00009-X

Tayefeh, S., Kloss, T., Kreim, M., Gebhardt, M., Baumeister, D., Hertel, B., et al. (2009). Model development for the viral Kcv potassium channel. *Biophys. J.* 96, 485–498. doi: 10.1016/j.bpj.2008.09.050

Tielker, N., Eberlein, L., Güssregen, S., and Kast, S. M. (2018). The SAMPL6 challenge on predicting aqueous pK^a values from EC-RISM theory. *J. Comput. Aided. Mol. Des.* 32, 1151–1163. doi: 10.1007/s10822-018-0140-z

Tielker, N., Eberlein, L., Hessler, G., Schmidt, K. F., Güssregen, S., and Kast, S. M. (2021). Quantum–mechanical property prediction of solvated drug molecules: What have we learned from a decade of SAMPL blind prediction challenges? *J. Comput. Aided. Mol. Des.* 35, 453–472. doi: 10.1007/s10822-020-00347-5

Tikhonov, D. B., and Zhorov, B. S. (2017). Mechanism of sodium channel block by local anesthetics, antiarrhythmics, and anticonvulsants. *J. Gen. Physiol.* 149, 465–481. doi: 10.1085/jgp.201611668

Villarroel, A., Alvarez, O., Oberhauser, A., and Latorre, R. (1988). Probing a Ca^{2+}-activated K^+ channel with quaternary ammonium ions. *Pflügers Arch. Eur. J. Physiol.* 413, 118–126.

Wang, J., Wolf, R. M., Caldwell, J. W., Kollman, P. A., and Case, D. A. (2004). Development and testing of a general amber force field. *J. Comput. Chem.* 25, 1157–1174. doi: 10.1002/jcc.20035

Winterstein, L.-M., Kukovetz, K., Rauh, O., Turman, D. L., Braun, C. J., Moroni, A., et al. (2018). Reconstitution and functional characterization of ion channels from nanodiscs in lipid bilayers. *J. Gen. Physiol.* 150, 637–646.

Yohannan, S., Hu, Y., and Zhou, Y. (2007). Crystallographic study of the tetrabutylammonium block to the KcsA K^+ channel. *J. Mol. Biol.* 366, 806–814. doi: 10.1016/j.jmb.2006.11.081

Zhou, Y., Morais-Cabral, J. H., Kaufman, A., and MacKinnon, R. (2001). Chemistry of ion coordination and hydration revealed by a K^+ channel-Fab complex at 2.0 A resolution. *Nature* 414, 43–48. doi: 10.1038/3510 2009

Conflict of Interest: The authors declare that the research was conducted in the absence of any commercial or financial relationships that could be construed as a potential conflict of interest.

Publisher's Note: All claims expressed in this article are solely those of the authors and do not necessarily represent those of their affiliated organizations, or those of the publisher, the editors and the reviewers. Any product that may be evaluated in this article, or claim that may be made by its manufacturer, is not guaranteed or endorsed by the publisher.

frontiers in Physiology

ORIGINAL RESEARCH
published: 16 November 2021
doi: 10.3389/fphys.2021.777050

Pre-steady-state Kinetic Analysis of Amino Acid Transporter SLC6A14 Reveals Rapid Turnover Rate and Substrate Translocation

*Yueyue Shi, Jiali Wang, Elias Ndaru and Christof Grewer**

Department of Chemistry, Binghamton University, Binghamton, NY, United States

SLC6A14 (solute carrier family 6 member 14) is an amino acid transporter, driven by Na^+ and Cl^- co-transport, whose structure, function, and molecular and kinetic mechanism have not been well characterized. Its broad substrate selectivity, including neutral and cationic amino acids, differentiates it from other SLC6 family members, and its proposed involvement in nutrient transport in several cancers suggest that it could become an important drug target. In the present study, we investigated SLC6A14 function and its kinetic mechanism after expression in human embryonic kidney (HEK293) cells, including substrate specificity and voltage dependence under various ionic conditions. We applied rapid solution exchange, voltage jumps, and laser photolysis of caged alanine, allowing sub-millisecond temporal resolution, to study SLC6A14 steady state and pre-steady state kinetics. The results highlight the broad substrate specificity and suggest that extracellular chloride enhances substrate transport but is not required for transport. As in other SLC6 family members, Na^+ binding to the substrate-free transporter (or conformational changes associated with it) is electrogenic and is likely rate limiting for transporter turnover. Transient current decaying with a time constant of <1 ms is also observed after rapid amino acid application, both in forward transport and homoexchange modes, indicating a slightly electrogenic, but fast and not rate-limiting substrate translocation step. Our results, which are consistent with kinetic modeling, suggest rapid transporter turnover rate and substrate translocation with faster kinetics compared with other SLC6 family members. Together, these results provided novel information on the SLC6A14 transport cycle and mechanism, expanding our understanding of SLC6A14 function.

Keywords: membrane transporter, SLC6A14, $ATB^{0,+}$, electrophysiology, rapid kinetics, laser-photolysis, molecular physiology

OPEN ACCESS

Edited by:
Han Sun,
Leibniz-Institut für Molekulare Pharmakologie (FMP), Germany

Reviewed by:
Cesare Indiveri,
University of Calabria, Italy
Michael L. Jennings,
University of Arkansas for Medical Sciences, United States

****Correspondence:***
Christof Grewer
cgrewer@binghamton.edu

Specialty section:
This article was submitted to Membrane Physiology and Membrane Biophysics, a section of the journal Frontiers in Physics

Received: *14 September 2021*
Accepted: *15 October 2021*
Published: *16 November 2021*

Citation:
Shi Y, Wang J, Ndaru E and Grewer C (2021) Pre-steady-state Kinetic Analysis of Amino Acid Transporter SLC6A14 Reveals Rapid Turnover Rate and Substrate Translocation. Front. Physiol. 12:777050. doi: 10.3389/fphys.2021.777050

INTRODUCTION

Plasma membrane amino acid transporters move amino acids across the lipophilic membrane bilayer into the cell (Zafra and Gimenez, 1986; Reyes et al., 2009; Wang et al., 2018), providing nutrients for many essential biological processes, such as protein and nucleotide synthesis, mammalian target of rapamycin (mTOR) signaling, and cell metabolism. Amino acid transporters

belong to several families of solute carrier (SLC) proteins and are differentiated by sequence similarity, substrate specificity, ion dependency, and transporter mechanism (Broer and Gether, 2012; Schaller and Lauschke, 2019), which contribute to various aspects of transporter function and regulation. Amino acid transporter SLC6A14 belongs to the Solute Carrier 6 (SLC6) family, which consists of 20 membrane transporters in the human genome. It is also known as $ATB^{0,+}$ derived from transport selectivity for neutral amino acids, denoted by "0" and cationic amino acids denoted by "+." SLC6A14 is a unidirectional transporter, in which amino acid transport is coupled to Na^+ and Cl^- co-transport, with broad substrate selectivity (Sloan and Mager, 1999; Ugawa et al., 2001; Le Guellec et al., 2021), including all neutral and cationic amino acids. It was also identified as a β-alanine carrier (Bhutia et al., 2015). The SLC6 family transporters are subdivided into four branches, based on sequence similarity, which are monoamine transporters, GABA transporters and amino acid transporters (I) and (II) (Page, 1996; Notredame et al., 2000; Broer and Gether, 2012). The amino acid SLC6 transporters from subfamily (I) transport glycine (GlyT1/SLC6A9, GlyT2/SLC6A5), proline (PROT/SLC6A7) and neutral/cationic amino acids ($ATB^{0,+}$/ SLC6A14). Amino acid transporter subfamily (II) comprised nutrient amino acid transporters SLC6A15-20 (Pramod et al., 2013; Rudnick et al., 2014; Coothankandaswamy et al., 2016).

The crystal structure of a bacterial homolog of SLC6 bacterial leucine transporter, LeuT (Yamashita et al., 2005), and a drosophila dopamine transporter (Penmatsa et al., 2013), as well as biochemical research (Kristensen et al., 2011), provided a foundation of structural and functional properties of SLC6 family members. While no crystal structure is known for SLC6A14, a homology model based on *Drosophila melanogaster* sodium-dependent DAT was published (Palazzolo et al., 2019), and another model is available from the AlphaFold server (Jumper et al., 2021). In contrast to the structure, the SLC6A14 functional properties have been investigated in more detail. SLC6A14 amino acid transport is dependent on Na^+ and Cl^-, with a proposed stoichiometry of 2:1:1 (Na^+: amino acid: Cl^-; Nakanishi et al., 2001; Umapathy et al., 2004; Karunakaran et al., 2011). Therefore, amino acid transport is electrogenic and associated with transport current, which was measured in *Xenopus* oocytes.

Amino acid transporter SLC6A14 has been cloned from human and rat tissues (Sloan and Mager, 1999; Nakanishi et al., 2001; Ugawa et al., 2001; Umapathy et al., 2004). SLC6A14 is highly expressed in lung, intestine, and other tissues such as pituitary, colon, and mammary gland. SLC6A14 is proposed to be upregulated in several cancers with the purpose of delivering amino acid nutrients into the cells, including colorectal cancer (Gupta et al., 2005), cervical cancer (Gupta et al., 2006), estrogen receptor positive breast cancer (Karunakaran et al., 2011; Schaller and Lauschke, 2019), and pancreatic cancer (Penheiter et al., 2015; Coothankandaswamy et al., 2016). The inhibition of SLC6A14 decreases the proliferation of tumor cells either with shRNA-mediated gene silencing or using α-methyl-L-tryptophan as an inhibitor *in vitro* and *in vivo* (Karunakaran et al., 2008; Babu et al., 2015). Therefore, SLC6A14 has great potential for further investigation as a drug target for cancer treatment.

Currently, the details of the transport mechanism of SLC6A14, as well as kinetic parameters, such as turnover rate, are unknown. Here, we expressed SLC6A14 in human embryonic kidney (HEK) cells to investigate substrate specificity under different ionic conditions, as well as the voltage dependencies of individual steps in the transport cycle. We further applied laser pulse photolysis with a caged amino acid, to investigate its functional and kinetic properties in steady state and pre-steady state. Consistent with other SLC6 family members, binding of extracellular Na^+ is a major contributor to transporter voltage dependence and limiter of the turnover rate (Hilgemann and Lu, 1999; Mennerick et al., 1999; Sloan and Mager, 1999; Grewer et al., 2000b, 2012; Watzke et al., 2001; Zhang et al., 2007; Wang et al., 2021). The anion effect, however, is more subtle, with Cl^- not being required for, but facilitating transport kinetically. Turnover rate was found to be one of the fastest in the SLC6 family.

MATERIALS AND METHODS

Cell Culture and Transfection

Human embryonic kidney 293 (HEK293, American Type Culture Collection CRL-1573) cells were cultured in DMEM prepared with 45 g/L fetal bovine serum (FBS), 4.5 g/L of penicillin, L-glutamine sodium pyruvate, and non-essential amino acid mix (Gibco) in the fully humidified incubator with constant temperature of 37°C and 5% carbon dioxide. Cell cultures were transiently transfected with wild-type SLC6A14 and YFP cDNAs (Genecopoeia, TakaraBio) using jet-PRIME transfection reagent followed by the protocol supplied by POLYPLUS-Transfection. Cells were incubated for 20–30 h after transfection and ready for electrophysiology technique.

Electrophysiological Techniques

The whole-cell recording configuration was used to perform electrophysiological experiments. The external buffer solutions used to measure the transport current were prepared in 140 mM NaCl, NaMes, NaI or NaGluconate, 2 mM $MgCl_2$ or $Mg(gluconate)_2$, 2 mM $CaCl_2$/ CaMes/$Ca(gluconate)_2$, and 10 mM HEPES in pH 7.40. When changing the anion at 140 mM Na^+, their respective salts were used, i.e., NaCl for Cl^-, and NaI for I^-, or a 140 mM NaOH solution was titrated with gluconic acid or methanesulfonic acid. The internal buffer KMes/ KSCN/ KGluconate were prepared from 130 mM KMes or KSCN or KGluconate, 2 mM $MgCl_2$ or $Mg(gluconate)_2$, 10 mM EGTA, and 10 mM HEPEs, pH 7.40, as published earlier (Grewer et al., 2001). To analyze anion effects in SLC6A14 transporters, currents at different extracellular or intracellular anion compositions, including various external or internal buffers, were recorded, respectively. Whole-cell recordings method were conducted in similar fashion as in previous publications (Wang et al., 2019; Grewer et al., 2000b; Wang et al., 2020). The glass patch pipettes back-filled with internal buffer (open pipette resistance of 3–7 MΩ) were used to establish a seal with the

cell membrane (resistance in the 500 MΩ to GΩ range). After establishing the whole cell recording mode using voltage pulses and/or suction, currents associated with the SLC6A14 amino acid transporter were recorded with an Adams & List EPC7 patch-clamp amplifier and digitized using a Molecular Devices Digidata A/D converter connected to a computer.

Voltage Jump Experiments

Voltage jumps (−100 to +60 mV) were performed on SLC6A14-expressing cells to perturb the electrogenic substrate (alanine) transport steady state, or the equilibria associated with partial reactions, such as Na^+ binding. To determine Na^+-dependent SLC6A14 currents, control currents were recorded in the presence of various Na^+ concentrations and subtracted from the substrate-induced currents. 5, 70,140 mM Na^+ solutions were made from 140 mM NaCl and NMGCl buffers and the cells were immersed in NMGMes bath. To determine anion effects on SLC6A14, control currents were recorded in the presence of external buffers containing various anion concentrations and subtracted from the substrate-induced currents. In addition, α-Methyl-Tryptophan was used as an inhibitor for subtracting unspecific currents. Capacitive transient compensation and series resistance compensation of up to 80% were achieved with EPC7 amplifier. Clampfit (Molecular Devices) was used to do subtraction of non-specific transient currents.

Rapid Solution Exchange and Laser Photolysis of Caged-Compounds

Rapid solution exchange (time resolution 100–200 ms) was performed by means of a quartz tube (opening diameter 350 μM) positioned at 0.5 mM to the cell. The solution flowed to the opening of the tube with the linear flow rate of 5–10 cm/s. Laser-pulse photolysis experiment were performed as described in detail previously (Niu et al., 1996; Grewer et al., 2001; Watzke et al., 2001; Tao et al., 2006; Wang et al., 2021). Photolysis of caged compounds was activated with a light flash (355 nm, 8 ns, frequency-tripled Minilite II, Continuum), which was delivered from a quartz fiber (diameter 365 μM), and placed in front of the cell at a distance of 300 μM. With laser light intensities of 500–840 mJ/cm^2, saturated free alanine or serine could be released, as tested in comparison with steady-state currents elicited by a known concentration of alanine, as described previously (Grewer et al., 2001). Data were recorded using pClamp6 software (Axon Instruments), digitized with a sampling rate of 1 kHz (solution exchange) or 25 kHz (laser photolysis and voltage jump) and low-pass filtered at 3–10 kHz.

Piezo-Based Solution Switching

Fast solution exchanges were applied using the setup SF-77B (Warner Instruments, LLC, MA, United States), allowing a time resolution in the 10–20 ms range (details can be found in the manufacturer's manual). The experiments were tested under forward transport conditions, extracellular with 140 mM NaCl, intracellular with 130 mM KMes. Five mM of alanine was rapidly applied through a theta capillary glass tubing (TG200-4, OD = 2.00 mM, ID = 1.40 mM, Warner Instruments, LLC, MA, United States), currents were recorded using pClamp software and analyzed in Origin software.

Data Analysis

All data are shown as mean ± SD, collected from recordings of 8–10 cells. For statistical analysis, paired two-tailed *t* tests were used in Microcal Origin software. To determine substrate K_m values, non-linear curve fitting was used with a Michaelis-Menten-like equation, $y = I_{max} * [substrate]/(K_m + [substrate])$ built in the Origin software least-squares-fitting package.

Nonlinear regression fits of laser-pulse photolysis experimental results were performed in Clampfit software (Axon Instruments) using the following equations. The pre-steady-state transport currents (in the absence of SCN^-) were fitted with a sum of two exponential functions and a steady-state current component: $I = I1 \cdot \exp(-t/\tau rise) + I2 \cdot \exp(-t/\tau decay1) + ISS$. Here, I is the current amplitude, τ the time constant, and t the time.

Synthesis of Caged Alanine

The caged alanine was synthesized according to the following procedures, as illustrated in the reaction scheme 1 (**Figure 1**).

Tert-butyl-2-bromo-2-(2-nitrophenyl)acetate (1). General synthesis of this intermediate was performed as described previously (Grewer et al., 2001).

2-(tert-butoxy)-1-(2-nitrophenyl)-2-oxoethyl (tert-butoxycar bonyl) alaninate (2). A mixture of N, N-diisopropylethylamine (204 mg, 1.58 mmol, 5 equi.), tert-butyl-2-bromo-2-(2-nitrophenyl)acetate (1) (100 mg, 0.316 mmol, 1 equi.) and tert-butoxycarbonyl alanine (65.8 mg, 0.348 mmol, 1,1 equi. (3) were weighed into an oven-dried round bottom flask. Acetone was added through a syringe into the flask purged with N_2 gas and the solution was refluxed at 60°C. The reaction mixture was stirred overnight and monitored by thin-layer chromatography (TLC) to reach completion. Subsequently, all contents were washed twice with sodium bicarbonate, twice with water. The organic layer was dried over sodium sulfate and filtered. The filtrate was concentrated *in vacuo* and product was purified using silica gel chromatography (0–25% ethyl acetate in hexane) to obtain a pure oil. 1H NMR (400 MHz, CDCl3) δ 8.03 (dd, J = 8.4, 2.0 Hz, 1H), 7.75–7.61 (m, 2H), 7.54 (ddd, J = 9.9, 6.8, 3.7 Hz, 1H), 6.79 (d, J = 15.5 Hz, 1H), 5.09 (s, 1H), 4.42 (dd, J = 47.5, 8.5 Hz, 1H), 1.58–1.49 (m, 2H), 1.45 (s, 1H), 1.40 (dd, J = 12.4, 7.3 Hz, 18H).

2-(alanyloxy)-2-(nitrophenyl) acetic acid (4). The protected compound (2) (72 mg, 0.17 mmol, 1.0 equi.) and Dithiothreitol (DTT; 52 mg, 0.34 mmol, 2 equi.) were weighed into an oven-dried round bottom flask. Trifluoroacetic acid (0.42 ml, 5.4 mmol, 32 equi.) was added dropwise under N_2 gas using syringe and cooled to 0°C to room temperature. The reaction mixture was stirred for 46 h which monitored by TLC (20–40% MeOH in DCM). TFA was removed under high vacuum and the mixture was concentrated *in vacuo*. The desired product was purified as a white solid through trituration in chilled diethyl ether and confirmed by TLC (20–40% MeOH in DCM). The stock solution in external buffer was prepared for further laser experiments.

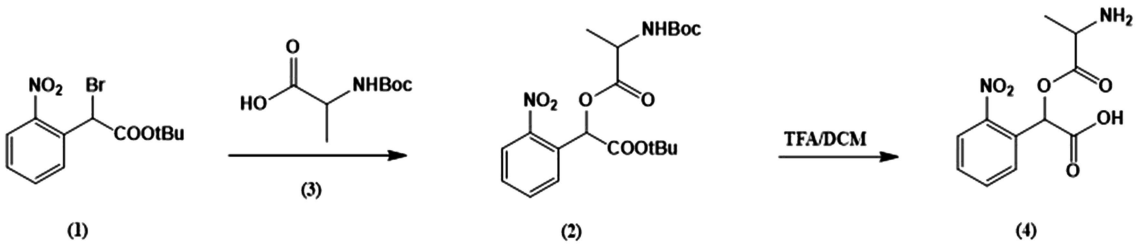

FIGURE 1 | Synthesis scheme of caged alanine.

RESULTS

Amino Acid Substrate Selectivity in SLC6A14

The objective of this work was to determine the functional properties of SLC6A14 by electrophysiology in a cell system that allows control of the ionic composition of solutions on both sides of the membrane. A conceptual transport cycle for SLC6A14 is shown in **Figure 2A**. To obtain the details of kinetic properties, we selected HEK293 cells to transiently over-express SLC6A14 cDNA and then voltage clamped the cells in the whole-cell recording mode. In contrast to previously-used *Xenopus* oocyte system, the intracellular solution can be manipulated through the ionic composition of the patch-clamp pipette in whole cell recordings of HEK293 cells. To compare the transport specificity of SLC6A14 with respect to different amino acids in HEK cells with respect to previously published data from the *Xenopus* oocyte system (Sloan and Mager, 1999; Nakanishi et al., 2001; Ugawa et al., 2001; Hatanaka et al., 2004; Karunakaran et al., 2008), cells were voltage clamped at 0 mV and solutions were applied to cells using a fast solution exchange setup. As expected from the electrogenicity of SLC6A14, extracellular application of the prototypical amino acid alanine resulted in inward currents (typical current recordings are shown in **Figure 2B**). Non-transfected cells did not show any currents induced by alanine (**Figure 2C**). Inward currents increased with increasing alanine concentrations (**Figures 2B**,**D**). These currents are expected to be caused by the stoichiometric, net ionic charge movement of Na^+ into the cell, while being co-transported with the neutral amino acid molecule and Cl^-. Typical dose response curves for L-alanine and L-serine as substrates are shown in **Figure 2D** with 140 mM NaCl external and 130 mM KMes internal buffers. After fitting to a Michaelis–Menten equation, the K_m for substrate Ala and Ser were determined to be 210 ± 40 μM and 320 ± 60 μM, respectively. Other amino acids' apparent affinity was tested in the same way, and the results are summarized in **Figure 2E**. Trp, Leu, Met, and Phe showed the highest apparent affinities (**Supplementary Table S1**) while Ala, Ser, Val, and Cys had intermediate level K_m values. In contrast, the basic amino acids, Arg and Lys, together with Gly and Asn had the lowest apparent affinities in the >350 μM range (**Figure 2E**, **Supplementary Table S1**). Amino acids with negatively-charged side chain did not elicit currents. In addition, aspartate at a concentration up to 500 μM, was unable to block alanine-induced transport current (200 μM), indicating that acidic amino acids are not recognized by the SLC6A14 binding site. Overall, aromatic amino acids with hydrophobic side chain have higher apparent affinities. Absolute currents magnitudes were analyzed at 2 mM substrate concentration and shown in **Figure 2F**. This concentration was chosen because it is close to saturating for most but the lowest affinity substrates. From comparison of these currents' magnitudes, the lower affinity amino acids Arg and Gly induced the largest currents. These results are generally consistent with those from the literature (Sloan and Mager, 1999; Ugawa et al., 2001; Karunakaran et al., 2008; Fairweather et al., 2021), although the exact apparent K_m values are slightly different, as is often the case when comparing results from mammalian cell lines to those from *Xenopus* oocytes.

Extracellular Chloride is not Required for, but Enhances Substrate Transport

To test the effect of anions on SLC6A14 transporter properties, we used whole-cell recording method with external and internal buffers containing various types of anions. Upon applying the amino acid from the extracellular side, inward currents were activated with or without extracellular or intracellular Cl^- (**Figures 3A**, **B**). When extracellular Cl^- was replaced with large, organic anions that are typically not known to interact with Cl^- binding sites (Sloan and Mager, 1999; Nakanishi et al., 2001; Hatanaka et al., 2004), such as Mes^- and $Gluconate^-$ ($Gluc^-$), inward current was reduced, but not abolished (**Figure 3D**). However, the apparent affinity for the amino acid substrate was reduced, in particular in the presence of extracellular $Gluconate^-$ (**Figure 3C**). Then, we analyzed the [Cl^-] dependence of transport current at a saturating concentration of alanine (**Figures 3E–G**). This is done by monitoring the inward current of alanine in presence of increasing concentration of Cl^-. When we selected different anions to replace Cl^-, Mes^-, and $Gluc^-$ showed different effects. The Michaelis constant (K_m) for Cl^- in presence of $NaGluc^-$ was 5.1 ± 2.4 mM and for NaMes was 3.8 ± 1.6 mM. The result from **Figure 3E** show that even with 0 mM concentration of external Cl^-, inward currents were still generated by alanine application in the presence Mes^- or $Gluconate^-$.

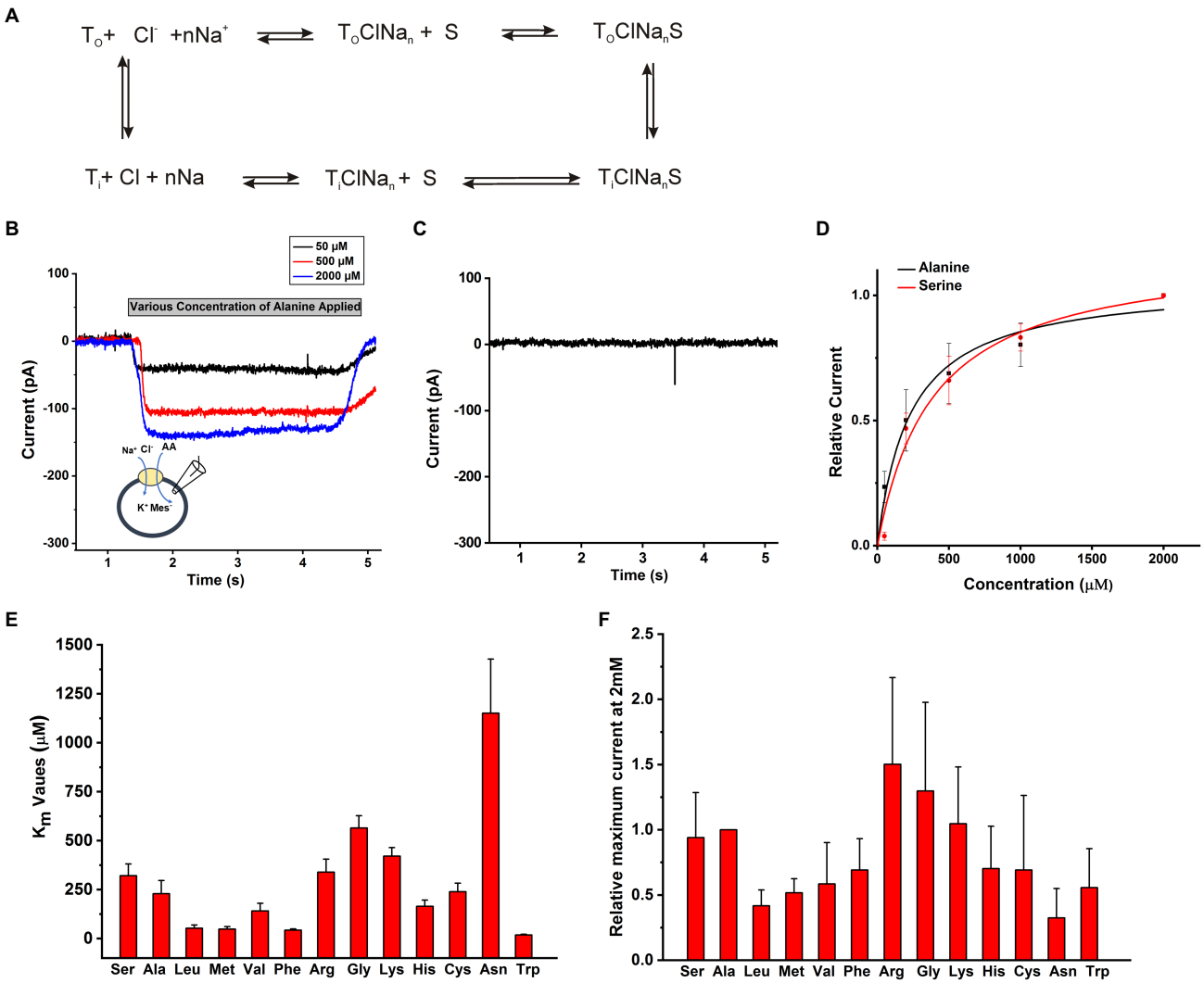

FIGURE 2 | Amino acid substrate selectivity. **(A)** A conceptual transport cycle of SLC6A14. **(B)** Typical electrophysiological recordings of concentration-dependent alanine-induced currents under forward transport conditions (140 mM NaCl as external buffer and 130 mM KMes as internal buffer). The time of application of substrate is indicated by the grey bar. Due to slight variations in the rate of flow in each tube for solution exchange, and the response time of the pinch valves, there is some variation in the onset of the current signal for each concentration. **(C)** An example trace of 200 μM alanine on HEK cells not expressing SLC6A14. **(D)** Alanine and serine dose response curves. The black (alanine) and red (serine) lines represent the best non-linear least squares fit to a Michaelis–Menten-like equation with apparent K_m value of 210 ± 40 μM for alanine and 320 ± 60 μM for serine. **(E)** Apparent K_m values for various amino acids. **(F)** Inward transport currents (realive to alanine) at 2 mM concentration of amino acid. The membrane potential was 0 mV in all experiments.

SLC6A14 Amino Acid Transport Is Na^+ Dependent

SLC6A14 was reported as a sodium and chloride co-transporter with a Na^+:Cl^- stoichiometry of 2:1 (Nakanishi et al., 2001; Umapathy et al., 2004; Karunakaran et al., 2011). To test this hypothesis, we analyzed the [Na^+] dependence of transport currents at a saturating concentration of alanine. An example of representative currents is shown in **Figure 4A**, with currents showing strong [Na^+] dependence with constant alanine and being virtually eliminated in the absence of sodium (replaced with NMG^+). The Na^+ dependence could be fitted using a Hill equation with a Hill coefficient of 1.96 ± 0.3, as expected for the 2:1 Na^+ to substrate stoichiometry (**Figure 4B**). The apparent affinity for sodium was K_m = 32.2 ± 4.3 mM, shown in **Figure 4B**. Together, these results confirm SLC6A14 to be a Na^+-dependent amino acid symporter.

Voltage Dependence of SLC6A14 Currents

To determine the voltage dependence of alanine transport, we measured currents after jumping the voltage from 0 mV to a range from −100 mV to +60 mV (voltage protocol shown in **Figure 5A**, top). Currents in the absence of alanine were then subtracted from currents in the presence of alanine to generate the amino acid-specific signal. As shown in **Figure 5A**, a voltage-jump to negative potentials induced a rapid transient current, followed by relaxation to a steady-state inward transport

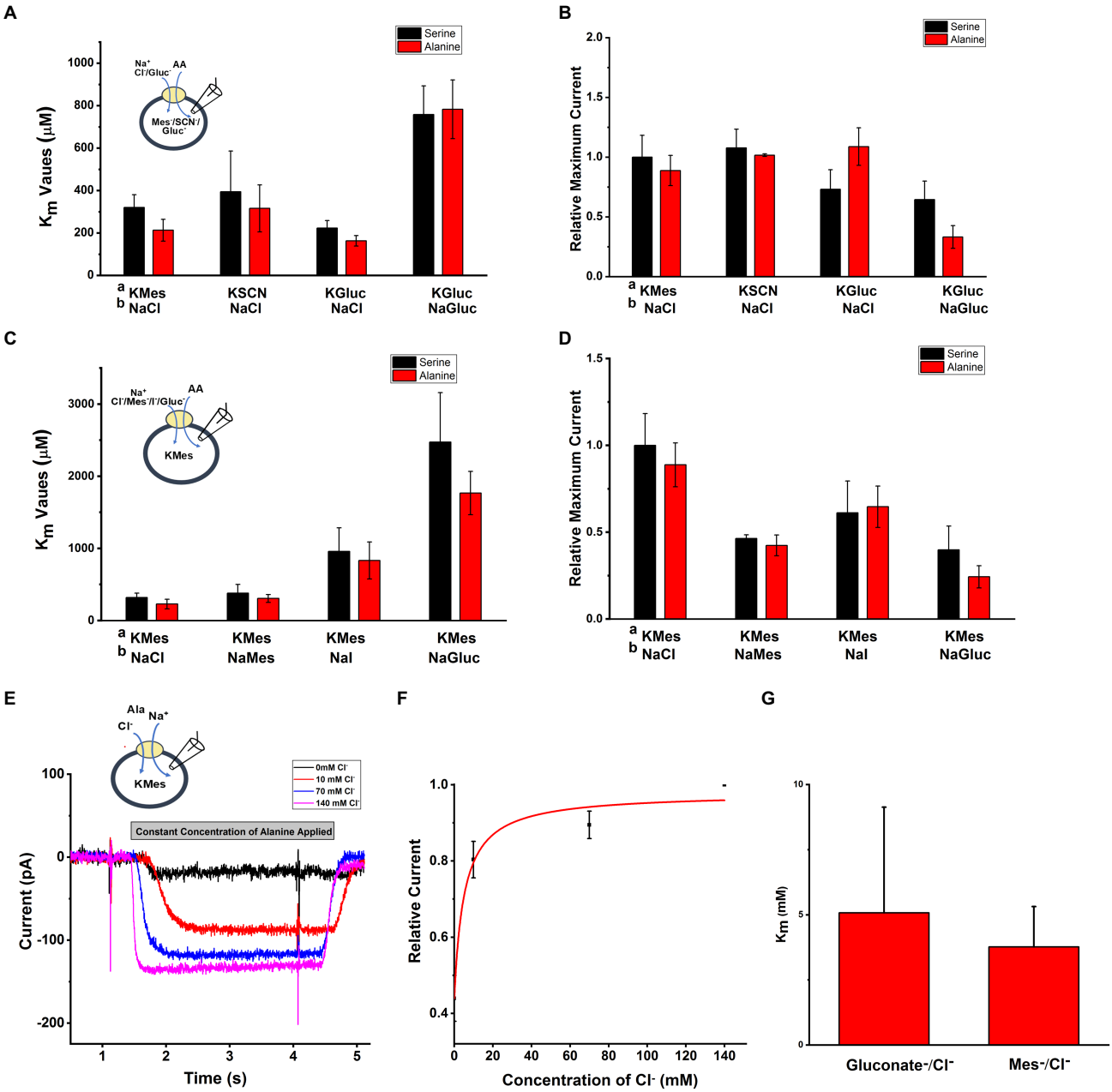

FIGURE 3 | Anion effect on alanine and serine transport currents. a Intracellular buffer; b extracellular buffer. **(A)** Apparent affinities for alanine or serine at different anionic conditions at the intracellular side. Internal anion concentration was 130 mM. The extracellular solution contained 140 mM NaCl, except for one experiment external NaGluc. **(B)** Current induced by alanine and serine (2 mM concentration) under the same conditions as in **(A)**. **(C)** Apparent affinities for alanine or serine when varying the anion at the extracellular side. **(D)** Inward current induced by alanine and serine (2 mM concentration) under the same conditions as in **(C)**. **(E)** Typical electrophysiological recordings of alanine-induced currents at increasing concentrations of cloride (NaGluc replacing NaCl). The alanine concentration was kept the same at 2 mM. **(F)** Dose response curve for chloride with K_m of 5.1 ± 2.4 mM. **(G)** Apparent K_m for Cl^- with replacement by either Mes^- or $Gluc^-$. The voltage was 0 mV in all experiments.

current. This steady-state current relaxed to baseline upon jumping the voltage back to 0 mV. The voltage dependence of the steady-state transport current was analyzed by subtracting current records during a series of voltage jumps in the presence of inhibitor α-Methyl-Tryptophan from corresponding currents in the presence of alanine only. As shown in **Figure 5B**, the relative transport current increased almost linearly with more negative membrane potential at 140 and 70 mM extracellular $[Na^+]$. In contrast, transport current was almost absent at positive potentials in the presence of low Na^+ concentration (5 mM), but increased exponentially at negative membrane potentials, suggesting a voltage dependence of the K_m for Na^+

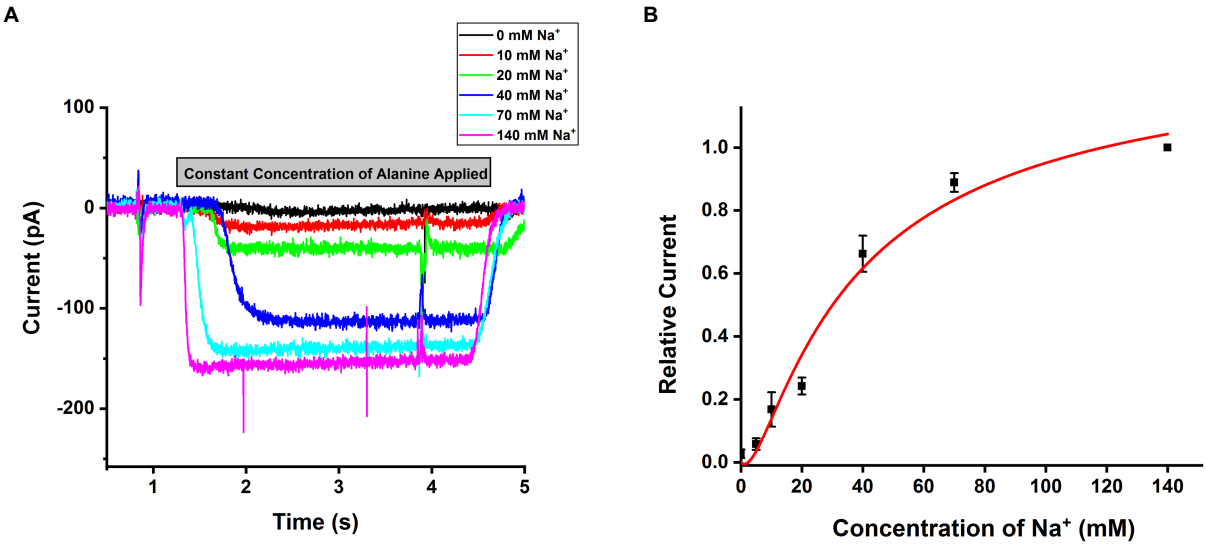

FIGURE 4 | Na^+ dependence of alanine mediated SLC6A14 transport currents. **(A)** Typical alanine-induced transport currents (2 mM alanine) at varying Na^+ concentrations (replaced by NMG^+). The internal buffer contained 130 mM KMes. **(B)** Na^+ dose response curve under the same conditions as in **(A)**. The results were fitted using the Hill equation (solid line). The fit parameters were $K_m = 32.2 \pm 4.3$ mM, and $n = 1.96$. The voltage was 0 mV in all experiments.

(higher apparent affinity at negative voltage and lower affinity at positive voltage), as expected if Na^+ binding is electrogenic, as is the case in other SLC6 family members (Jiang et al., 2005; Erdem et al., 2019).

Next, we further analyzed voltage dependence of transport current in the presence of different extracellular anions, as shown in **Figure 5C**. These results confirm the previous observations at 0 mV, namely that Cl^- is not required for amino acid transport process, but that it promotes transport currents at all membrane potentials. Interestingly, the voltage dependence in the presence of iodide is much weaker than with the other anions (**Figure 5C**). These results could indicate that a voltage-independent step becomes rate limiting in the presence of I^-.

To determine the relative charge movement of the transient current induced by the voltage jumps, we integrated the area of inward-directed transient current over time, which is shown in **Figure 5D**. No matter whether hyperpolarizing and depolarizing voltage pulses were applied, the charge movement induced by initiating the voltage jump (on charge) was equivalent to the charge movement after returning to the original potential (off charge). When plotting charge-voltage relationship in **Figure 5E**, we observed that the relative charge movement saturated at negative potential (< −80 mV) and increased steeply in the range of −40 mV to +40 mV. The Q-V curve was fitted using a Boltzmann-like function with a midpoint potential of 0.11 mV and slope factor of 50.6 V^{-1}.

In other SCL6 members, pre-steady state charge movement was observed in the absence of substrate and is thought to be related to Na^+ binding (Mager et al., 1996; Hilgemann and Lu, 1999; Erdem et al., 2019). In order to isolate transient charge movement in the absence of substrate, we applied the SLC6A14 blocker, α-Methyl-Tryptophan, to analyze the current induced by voltage jump without back-ground current. In this experiment, the voltage dependence of the transport current was analyzed by subtracting current records during a series of voltage pulses in the presence of α-Methyl-Tryptophan from corresponding currents in the absence of α-Methyl-Tryptophan to strongly inhibit transporter to eliminate any back-ground current effect. An example trace of transient current induced by voltage jumps at 140 mM NaMes condition is shown in **Figure 6A**. The transient current is Na^+ dependent, because it is eliminated in the presence of 140 mM NMGCl as shown in **Figure 6B**. The current decayed with a time constant of 7.1 ± 1.0 ms at 0 mV, and the decay is accelerated at negative membrane potentials. The charge-voltage relationship, obtained by integrating the current, is plotted using a Boltzmann-like function with a midpoint potential of 13.5 mV and slope factor of 35.2 V^{-1} in **Figure 6C**, pointing to a valence of 0.9 for the underlying electrogenic process. The charge movement starts to saturate at negative −100 mV membrane potentials. Overall, these results are compatible with voltage-dependent Na^+ binding step(s), or conformational changes associated with them, for example, a potential redistribution of the inward-outward-facing equilibrium of the empty transporter. **Figure 6D** shows the dependence of the rate constant for the transient current decay as a function of the voltage. As expected for a reversible, electrogenic reaction, the rate constant increases at both positive and negative voltages, and displays a minimum at −40 mV.

Pre-steady-state Currents in Response to Rapid Application of Alanine Through Photolysis of Caged Alanine

Previously, SLC6A14 pre-steady-state currents could not be measured in response to the application of alanine, due to limitations in the rate of solution exchange when using

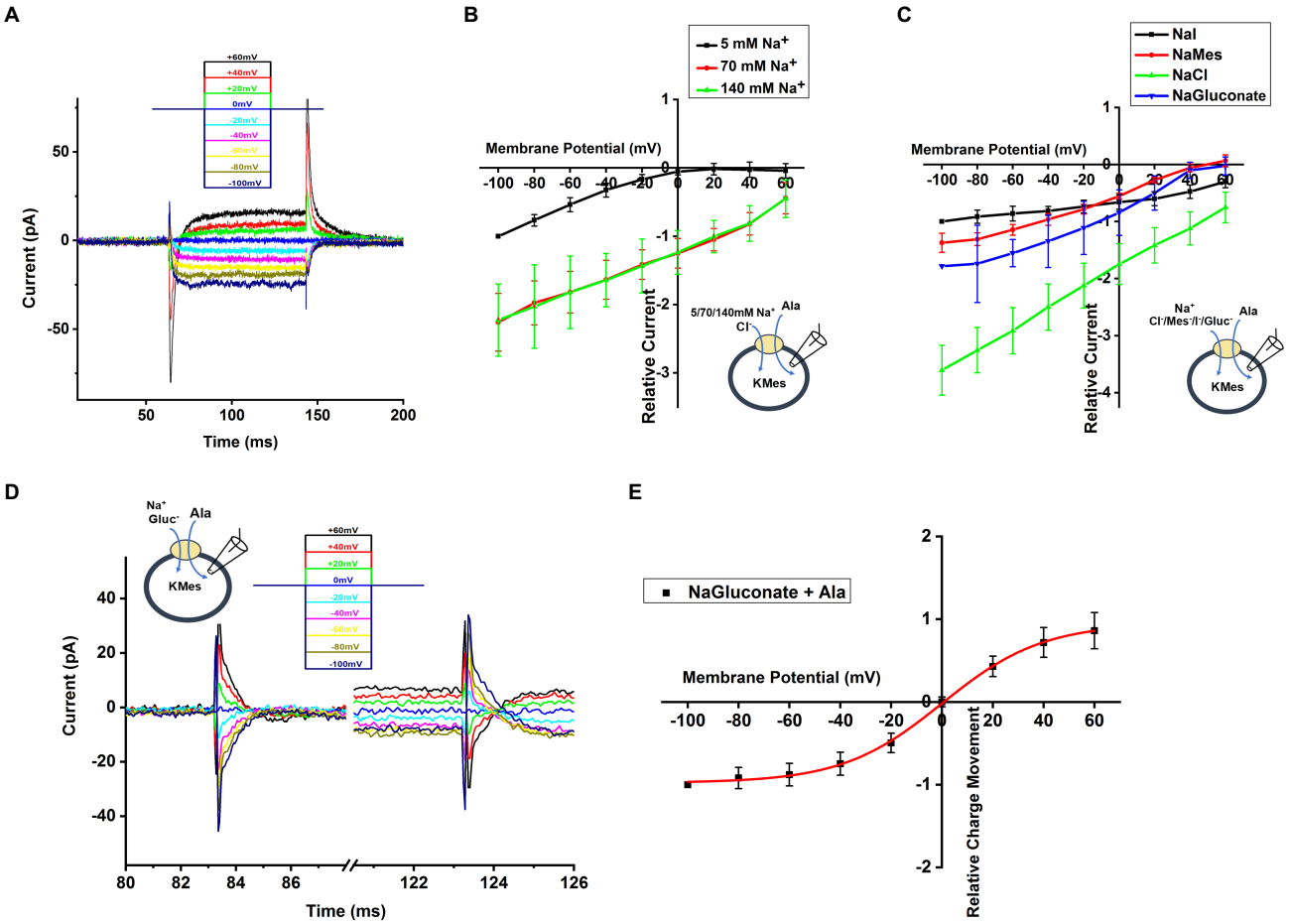

FIGURE 5 | Voltage Dependence of SLC6A14 currents. **(A)** Typical transport current recordings at different membrane potentials, ranging from −100 mV to 60 mV in the presence of 130 mM of intracellular KMes and 10 mM alanine in the external buffer (140 mM NaCl). The voltage jump protocol is illustrated in the inset (top). **(B)** Voltage dependence of relative transport currents as a functiom of the external [Na^+]. The concentration of 2 mM alanine was kept constant. Specific currents were calculated after subtraction of currents in the presence of inhibitor α-Methyl-Tryptophan, to eliminate background currents. All currents were normalized to the current induced at 5 mM Na^+ at −100 mV. **(C)** Currents similar as in **(B)**, but with different anions in the extracellular solution. **(D)** Voltage dependence of the transient current component. **(E)** Integration of the transient current results in the transient charge movement, relative to the charge movement at −100 mV.

Xenopus oocytes (Sloan and Mager, 1999; Nakanishi et al., 2001; Ugawa et al., 2001; Umapathy et al., 2004; Karunakaran et al., 2008, 2011), due to their large diameter of approximately 1 mM. To circumvent this problem, we synthesized caged alanine (see synthesis scheme, **Figure 1**) as a tool to rapidly liberate free alanine through flash photolysis, allowing the detection of early steps in the amino acid transport cycle. We first examined the effect of the caged compound on SLC6A14 transporter steady-state currents, showing no change of the magnitude of alanine-induced inward current with or without caged alanine, suggesting that the compound is biologically inert with respect to the SLC6A14 transporter. We observed small inward current before light activation of caged alanine, which contributed to small inward background currents caused by a background of free alanine in the caged compound, either from the purification protocol, or through some spontaneous hydrolysis of caged alanine (<50 µM).

After photolysis with a brief laser flash, a pre-steady-state inward current was observed, which rapidly decayed to the steady state within less than 10 ms (**Figure 7A**) under forward transport conditions (intracellular KMes). Using a sum of two exponential components and a steady state for fitting, time constants of 0.16 ms (rising phase) and 0.40 ms (decaying phase) were observed at 2 mM caged alanine, as shown in **Figure 7B**. The liberated alanine concentration was estimated to about 300 µM, not a saturating concentration, but one that is $>K_m$.

We also used a piezo-driven rapid solution exchange device to test the recovery of the current using paired pulses, as well as the rate constant of current decay upon alanine removal, as a potential determinant of the turnover rate. As shown in **Figure 7C**, despite its 10–20 ms time resolution, the method was unable to resolve the transient current and the recovery rate in time, most likely due to the very rapid transporter kinetics. However, from the deactivation of the current after alanine removal, a decay rate of 19 ± 5 ms was determined.

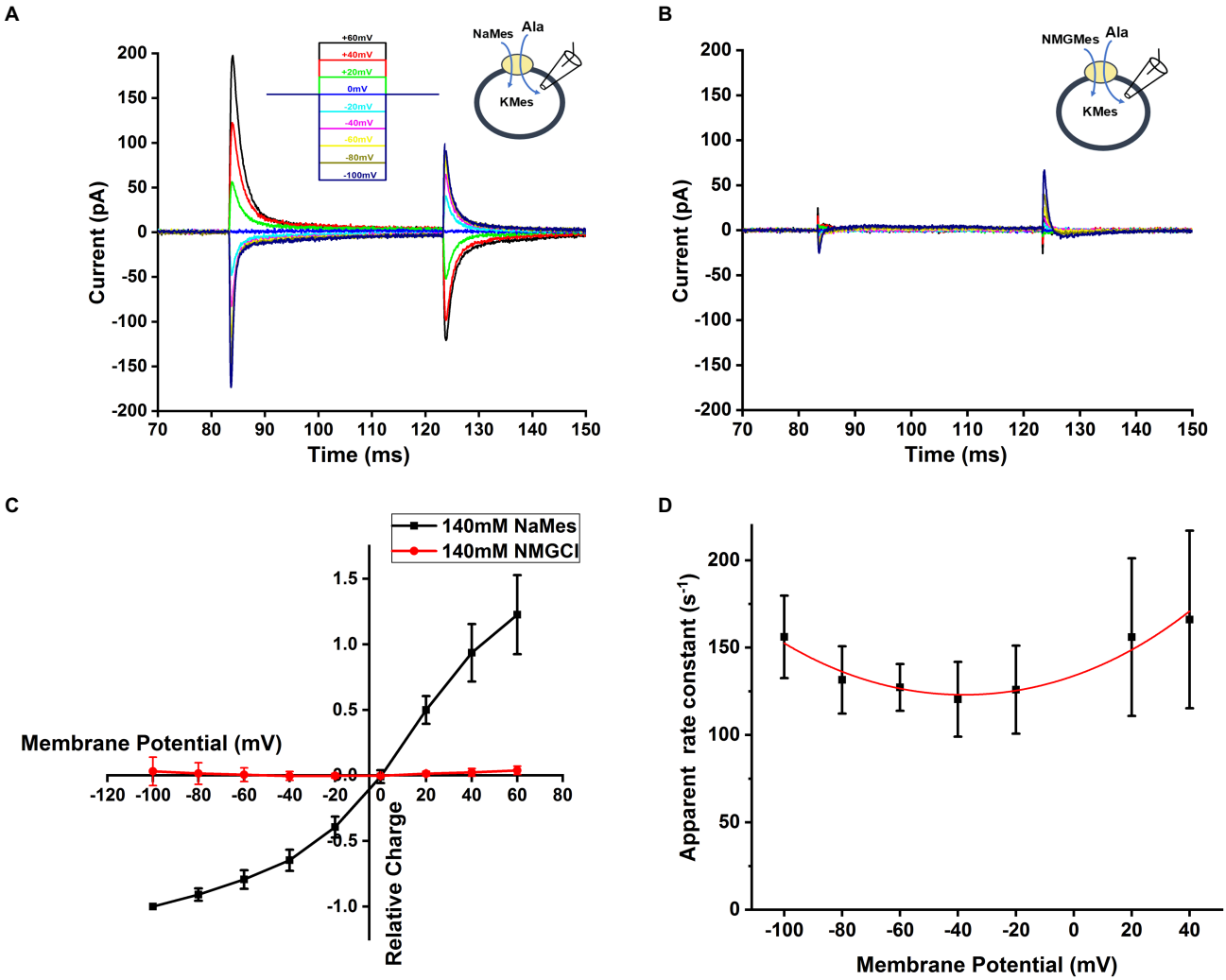

FIGURE 6 | Na^+-dependent transient currents in the absence of substrate. **(A)** Typical transient currents in response to voltage jumps from 0 mV to different membrane potential, ranging from −100 mV to +60 mV, in the presence of extracellular 140 mM NaMes and intracellular 130 mM KMes. The concentration of alanine was 1 mM. The voltage jump protocol is illustrated in the inset (top). **(B)** Similar experiment as in (A), but Na^+ was replaced by NMG^+. **(C)** The voltage dependence of the transient charge movement was analyzed by subtracting currents in response to a series of voltage jumps in the presence of α-Methyl-Tryptophan from corresponding currents in the absence of α-Methyl-Tryptophan, to eliminate any un-specific background currents. The charge-voltage relationship at 140 mM NaMes is shown in black, and at 140 mM NMGCl in red. Based on Boltzmann equation $Q(V_m) = Q_{min} + \frac{Q_{max}}{1+e^{\frac{Z_{\perp}(V_m - V_{\perp})\bullet F}{RT}}}$, where Q represents the charged moved, z is valence of charge moved, V is the membrane potential. The valence obtained from the fit was 0.9. **(D)** Voltage dependence of the relaxation rate constant of voltage jump-induced transient current decay fitted using equation is $k_{obs} = k^0_{for} e^{\frac{-zFV}{2RT}} + k^0_{rev} e^{\frac{zFV}{2RT}}$ with k^0_{for} as forward intrinsic binding rate, k^0_{rev} as reversed intrinsic dissociation rate and z as valence of the charge movement, $z = 0.56$.

This is probably an upper estimate of the real deactivation rate of the current.

Alanine Induced Current in Homo-Exchange Mode

Finally, we measured SLCA14 function under homo-exchange conditions. Here, the intracellular solution contained 130 mM NaCl and 10 mM alanine (likely saturating concentrations, although the intracellular affinities are not known). Initially, the extracellular solution only contained NaCl (140 mM), but no amino acid substrate. It is expected that the amino acid binding site is facing to the outside under these ionic conditions (the transporter can run in reverse under those conditions, but due to almost saturating concentrations of Na^+ and Cl^-, steady-state reverse transport current is expected to be small, due to *trans*-inhibition). Next, an alanine concentration jump is performed on the extracellular side, using photolysis of caged alanine, resulting in alanine binding and re-equilibration of the translocation equilibrium. Interestingly, transient inward current was observed under these conditions (**Figure 8A**), pointing to electrogenicity in the substrate translocation reaction

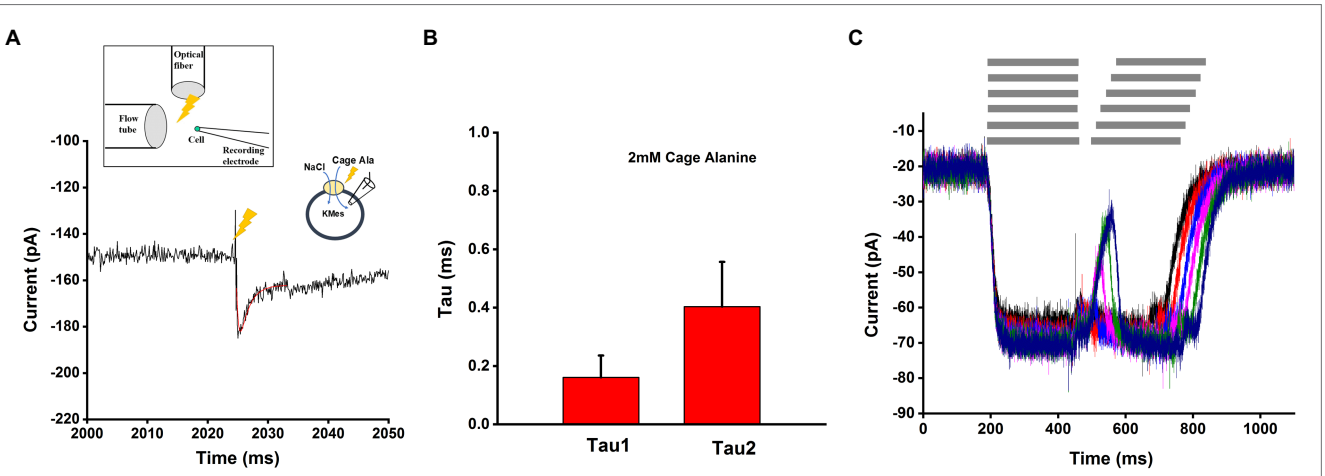

FIGURE 7 | Pre-steady state currents in response to alanine concentration jumps. **(A)** Application of the substrates with rapid solution exchange by photolysis of 2 mM caged alanine under forward transport conditions. The time of the laser flash is indicated by the arrow. Transient current was fitted with a sum of two-exponential functions, as shown by the red line. The time constants from fitted function were 0.17 ms (rising phase) and 0.43 ms (decay phase). The external buffer contained 140 mM NaCl and the internal buffer contained 130 mM KMes. **(B)** Average of the time constants obtained from the fit to responses from 15 cells of 0.16 ± 0.07 ms (rising phase) and 0.40 ± 0.15 ms (decaying phase). **(C)** Paired-pulse solution exchange experiments with a piezo-based solution switching system (10–20 ms time resolution) were performed under the same ionic conditions as **(A)** and **(B)**. Example of currents was recorded with 20 ms interval time. The gray bar on the top of **(C)** indicted the rapid solution exchange to substrate contained solution.

step(s). As expected, little steady state current was observed (**Figure 8A**), because the reaction is in equilibrium and no net transmembrane flow of charge occurs. We further tested the voltage dependence of the transient currents induced by caged alanine photolysis with membrane potentials ranging from −100 to +60 mV in exchange mode. The magnitude of inward currents generated increased with negative transmembrane potential as shown in **Figures 8B**,**C**. However, the time constants for the current rise and decay were largely independent of voltage (**Figure 8D**), indicating that the valence of the partial reaction causing this transient current is low.

DISCUSSION

Members of the SLC6 transporter family have been well studied, for example, the monoamine transporters, dopamine (DAT), norepinephrine (NET), serotonin (SERT) transporters, and glycine transporters (GlyTs), which are more closely related to SLC6A14. In previous studies (Sloan and Mager, 1999; Nakanishi et al., 2001; Ugawa et al., 2001; Umapathy et al., 2004; Karunakaran et al., 2008), the substrate selectivity of SLC6A14 has been reported. However, the electrophysiological properties and details of the transport mechanism have not been investigated as well as for other members of the SLC6 family. Here, we employed fast-solution exchange methods and rapid amino acid application through laser-photolysis to gain detailed insight into transporter function, mechanism and kinetics. With respect to amino acid selectivity, we found that amino acids with hydrophobic side chain, such as Trp, Leu, Met, Phe, and Ala generally interact with SLC6A14 with the highest apparent affinities, whereas glycine and positively charged amino acids generate the largest transport current at saturating substrate concentrations. These results on substrate selectivity are in agreement with previous reports (Sloan and Mager, 1999; Ugawa et al., 2001; Umapathy et al., 2004; Karunakaran et al., 2008) and highlight the broad recognition range of amino acid substrates for the SLC6A14 family member (Uchiyama et al., 2008).

Other members of the SLC6 family, including the GlyTs, are chloride dependent (Zafra and Gimenez, 1986; Aragon et al., 1987; Liu et al., 1993; Zafra et al., 1997; Lopez-Corcuera et al., 1998; Roux and Supplisson, 2000; Zhang et al., 2021). Consistently, SLC6A14 was also be found to be chloride dependent (Sloan and Mager, 1999; Nakanishi et al., 2001; Hatanaka et al., 2004; Umapathy et al., 2004; Karunakaran et al., 2008). In agreement with these previous results, our data suggest that the nature of the anion in the extracellular solution influences transport function. Here, the presence of external Cl^- largely increases transport currents. However, in contrast to previous reports, the amino acid substrate-induced current was not fully abolished in the absence of Cl^- (replacement by $Gluconate^-$ and Mes^-). Also, iodide was able to partially substitute for Cl^-. These results could be interpreted in several ways. First, it is possible that Gluconate- and Mes^- could substitute for chloride; however, their significantly larger size and inability to replace Cl^- in other transporters makes this possibility less likely. Second, the transporter may have some residual transport activity in the absence of bound Cl^-. Third, the residual current in the absence of Cl^- could be caused by an uncoupled conductance. We favor this last possibility, because in the closely-related glycine transporters, residual current in the absence of Cl^- was also observed, but glycine uptake strictly required Cl^- (Erdem et al., 2019).

Amino acid transport was previously reported to be Na^+ dependent, with a stoichiometry of two co-transported Na^+

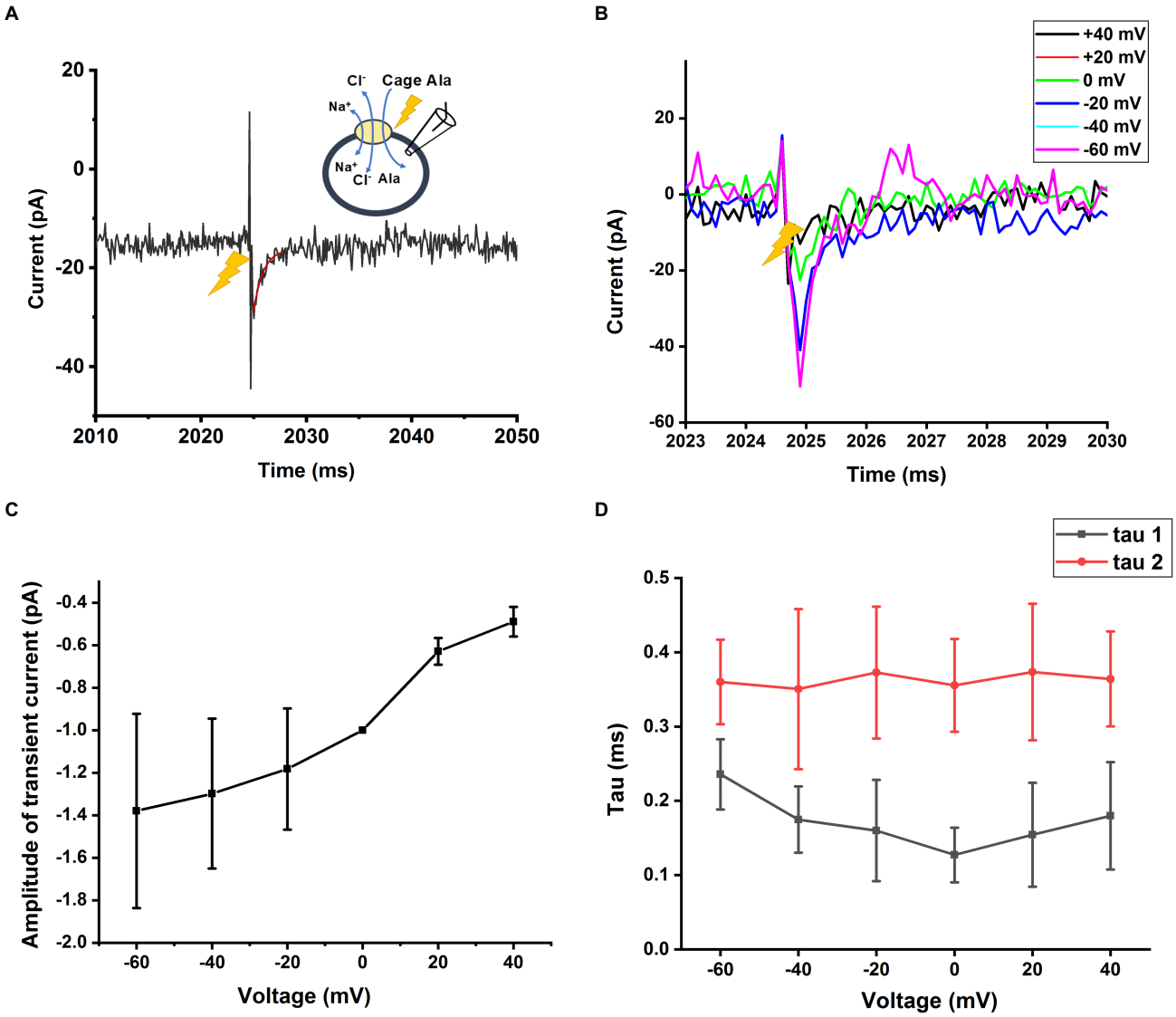

FIGURE 8 | Transient current is also present in homo-exchange mode. **(A)** Transient inward current upon caged alanine photolysis (2 mM) applied to the outside of the cell was also observed in the sodium/alanine exchange mode. The time of the laser flash is indicated by the arrow. The external solution contained 140 mM NaCl, the internal; solution 130 mM NaCl and 10 mM alanine. **(B)** Voltage dependence of the transient alanine-induced inward current in exchange mode. The voltage in **(A)** was 0 mV. **(C)** The amplitude of the transient current from **(B)** is plotted as a function of the transmembrane potential. **(D)** Time constants of the current rise and decay as a function of the membrane potential.

ions for each transported amino acid molecule (Nakanishi et al., 2001; Umapathy et al., 2004; Karunakaran et al., 2011). However, SLC6A14 shares the highest sequence identity with GlyT2 (SLC6A5, 53.38% identity), which was reported to have a stoichiometry of 3:1 for Na^+:substrate cotransport (Roux and Supplisson, 2000). Furthermore, the third Na^+ binding site residues appear to be conserved between the two transporters, raising the possibility of 3:1 stoichiometry for SLC6A14 also. This idea was confirmed in a recent preprint (Le Guellec et al., 2021). Our data confirm the Na^+ dependence of SLC6A14, with a Hill coefficient of 1.96, consistent with a Na^+ coupling stoichiometry of 2, or possibly 3. Experimental Hill coefficients >1, in general, point to a coupling stoichiometry larger than 1, but are a poor measure of the exact coupling ratio.

SLC6A14 also displayed Na^+ dependent transient currents in response to voltage jumps, similar to other SLC6 family members and amino acid transporters from other families (Mager et al., 1996; Mim et al., 2007; Zhang et al., 2007; Wang et al., 2018, 2020, 2021; Erdem et al., 2019; Zielewicz et al., 2019), including the GABA transporters (Bicho and Grewer, 2005) and GlyT2 (Erdem et al., 2019; Grewer et al., 2000b). These transient currents were present in the absence of substrate, indicating that they are related to Na^+ binding to the empty transporter, or conformational changes associated with it, for example, a potential redistribution of the

inward-outward-facing equilibrium of the empty transporter. The decay of the currents was biphasic, indicating the potential existence of two processes underlying these transient currents, potentially the binding of two Na^+ ions. The valence of the charge movement was 0.9, suggesting that the underlying process accounts for a substantial amount of the valence of the whole transport cycle. In contrast to the GABA transporter, in which the Na^+−dependent transient currents decayed on a 100 ms time scale, the SLC6A14 transient charge movement was much faster, with a decay time constant of 7.1 ± 1.0 ms at 0 mV (**Figure 6A**). This time constant is in line with GlyT2 results, showing 5 ms value (Erdem et al., 2019). In contrast, no Na^+-dependent transient currents were observed in GlyT1, again highlighting the seemingly close relationship between SLC6A14/GlyT2 sequence and function, with less similarities with GlyT1. As with other transporters, the Na^+-dependent charge movement allows an estimation of the number of transporters in the cell membrane. With a typical charge movement of 0.98 pC, and a valence of 0.9, the number of active transporters in the cell membrane can be calculated as 6.7×10^6. Together with a typical transport current of 150 pA, the turnover rate is in the range of 140 s^{-1}, depending on the number of charges transferred in one transport cycle (see section "Discussion" on Na^+ stoichiometry above). Turnover rate was also estimated from the decay of current after amino acid removal, a method that was previously applied to GlyTs (Erdem et al., 2019). From these data, the lower limit of the turnover rate is obtained, because of potential limitations by the rate of solution exchange. The turnover rate estimated from this method was >53 s^{-1}, close to the number from the transient current recordings. These results suggest that SLC6A14 is, to our knowledge, the transporter in the SLC6 family with the highest turnover rate, with other members ranging between 1 and 20 s^{-1} (Kristensen et al., 2011).

The results discussed in the previous paragraphs, while important for the details of SLC6A14 kinetics and function, are as expected from previous kinetic analysis of other SLC6 family members. On the other hand, information from pre-steady-state analysis of transport currents is less available, in particular for SLC6A14. Our results from rapid substrate application to the transporter indicate the existence of a rapidly-decaying pre-steady-state current signal before the steady state is reached. This transient current is extremely fast and was not observed with rapid solution exchange, even using piezo-based solution switching. With a time constant of 0.4 ms, the rate constant of the underlying transport reaction step(s) is 2,500 s^{-1}, much faster than the Na^+-dependent transient current and the turnover rate of the transporter. Therefore, the underlying reaction is not rate limiting for the overall amino acid transport rate. What are the transporter reaction step(s) responsible for this pre-steady-state current signal? Since the transient current is also present in exchange mode, in which the Na^+ and Cl^- concentrations on both sides of the membrane are high, and at least saturating for external ions (the internal binding site affinities are unknown), it stands to reason that states, in which the co-transported ions are dissociated cannot be visited. Therefore, the transient current most likely reflects on partial reactions in the translocation branch of the amino acid transporter cycle, which are likely very fast reaction steps. In addition, these steps contribute to the electrogenicity of the transporter, being responsible for at least a small part of the overall charge movement.

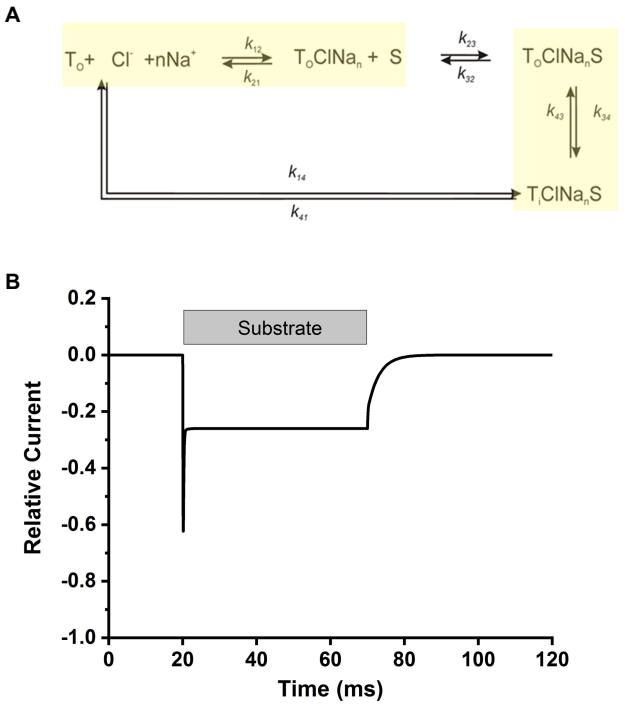

FIGURE 9 | Simplified transport cycle can explain the alanine-induced transient current. **(A)** Simplified kinetic model for substrate transport by SLC6A14. The sodium binding and substrate translocation steps, which were modeled to be voltage dependent, are highlighted in yellow. **(B)** Simulated transport current in response to rapid amino acid substrate application and removal, indicated by the grey bar. Simulations were performed with Berkeley Madonna software, using numerical integration of the differential rate equations pertaining to the kinetic scheme in **(A)**. Ionic conditions were 140 mM NaCl and 2 mM substrate (external). The kinetic parameters were: $k_{12} = 2\,M^{-1}ms^{-1}$, $k_{21} = 0.05\,ms^{-1}$ (zQ = 0.8), $k_{23} = 10{,}000\,M^{-1}ms^{-1}$, $k_{32} = 2\,ms^{-1}$, $k_{34} = 4\,ms^{-1}$, $k_{43} = 4\,ms^{-1}$ (zQ = 0.4), $k_{41} = 3\,ms^{-1}$, k_{14} was set to $0\,ms^{-1}$ for forward transport conditions. All simulations were performed at 0 mV. Voltage-dependent rate constants was calculated using the equations: $k_i(V) = k_i(0)\exp(-z_iFV/(2RT))$, where i denotes the respective reaction step. F, R and T have their usual meaning. The time-dependent transport current, I(t), was calculated using the following equation: $I(t) = T_0 e\left[\Sigma - z_i\left(k_i P_i - k_{-i} P_{i+1}\right)\right]$, where P denotes the fractional population of the respective state, i, as defined in **(A)**. T0 is the number of transporters under observation, e the elementary charge and k_i and k_{-i} are the rate constants for binding of the respective transition of valence z_i.

Overall, our data point to a kinetic model in analogy to other members of the SLC6 family, in particular the closely related glycine transporters (Erdem et al., 2019). Here, Na^+ and Cl^- bind from the extracellular side to the transporter before the amino acid substrate, with Na^+ binding being a voltage dependent step, contributing majorly to the electrogenicity of the transporter and being a relatively slow step in the transport cycle (**Figure 9A**). After binding of the ionic co-substrates, the amino acid substrate binds and results in a

transporter competent for translocation, a step that is fast and also slightly electrogenic. In this aspect, the mechanism of SLC6A14 appears to be somewhere in-between glycine transporter subtypes 1 and 2, with the former displaying the major electrogenicity in the substrate translocation step(s), whereas the latter shows voltage dependent Na^+ binding. This simple model can reproduce the major kinetic aspects of transporter behavior upon alanine concentrations jumps, as shown in **Figure 9B**, with electrogenic steps attributed to Na^+ binding (valence of 0.8) and, to a lesser extent, to substrate/sodium translocation (valence of 0.4).

Our results highlight the importance of using rapid kinetic techniques, together with kinetic modeling, to investigate partial reactions of secondary-active transporter cycles. While rapid solution exchange methods have been extensively used in the past, their time resolution is too slow to resolve rapid transporter reactions that occur in the low millisecond to sub-millisecond time scale. An excellent example is the SLC6A14 transient, alanine-induced current in forward transport and exchange mode. While the laser photolysis method with caged alanine allows one to temporally resolve the kinetics of this current component, even currents recorded using the very fast piezo-based solution exchange method do not show the transient current. Therefore, based on rapid solution exchange, the false conclusion could be reached that this rapid current component does not exist.

The disadvantage of the laser photolysis method is that caged compounds have to be synthesized first, if they are not commercially available. Generally, neurotransmitters and other biologically important compounds, such as ATP (Mccray et al., 1980), are available in caged form, but this is not the case for amino acids that are substrates for neutral amino acid transporters, such as SLC6A14. Here, we utilized the α-carboxy-nitrobenzyl (CNB) group as a photolabile protecting group for alanine. This group was previously shown to efficiently release amino acids when protected in the α-carboxy position (Grewer, 1999; Grewer et al., 2000a). CNB-caged amino acids are also water soluble and show other desirable properties, such as rapid release of the carboxylate upon photolysis. For example, the analogous CNB-caged glycine displayed release kinetics with time constants in the 5–100 µs range, and quantum yields of 0.38 (Grewer et al., 2001). While we did not test the detailed photophysical parameters of CNB-caged alanine, other than the reaction spectrum, we expect these properties to be very similar to CNB-caged glycine. Overall, these results highlight the ease of synthesis of CNB-caged amino acids and their applicability to study neutral amino acid transporter kinetics.

In conclusion, we have characterized the steady-state and pre-steady state kinetics of the neutral/basic amino acid transporter SLC6A14 in detail, providing novel information on the rates of important partial reactions in the transport cycle, and their voltage dependence. In particular, the turnover rate was found to be faster than that of other, previously characterized members of the SLC6 family, including the closely related glycine transporters. In addition, substrate translocation appears to be extremely fast, with a time constant in the sub-millisecond range. Na^+ binding to the empty transporter is electrogenic, and slower than other partial reaction, potentially contributing to the rate limitation of the transport cycle. In analogy to GlyT1, substrate translocation was also found to be electrogenic. Together, these mechanistic insights contribute to our understanding of SLC6A14 function, and how it plays a part in amino acid homeostasis.

DATA AVAILABILITY STATEMENT

The raw data supporting the conclusions of this article will be made available by the authors, without undue reservation.

AUTHOR CONTRIBUTIONS

YS acquired experimental data, performed data analysis and interpretation, performed kinetic simulations, synthesized caged alanine, and co-wrote the manuscript. JW acquired experimental data, performed data analysis and interpretation, performed kinetic simulations, and co-wrote the manuscript. EN synthesized compounds and planned synthetic strategies. CG conceptualized and directed the project, analyzed and interpreted data, acquired funding, and co-wrote the manuscript. All authors contributed to the article and approved the submitted version.

FUNDING

This study was supported by a grant from the National Institutes of Health (R01GM108911) to Avner Schlessinger and CG, and the R15 GM135843-01 awarded to CG.

SUPPLEMENTARY MATERIAL

The Supplementary Material for this article can be found online at: https://www.frontiersin.org/articles/10.3389/fphys.2021.777050/full#supplementary-material

REFERENCES

Aragon, M. C., Gimenez, C., and Mayor, F. (1987). Stoichiometry of sodium- and chloride-coupled glycine transport in synaptic plasma membrane vesicles derived from rat brain. *FEBS Lett.* 212, 87–90. doi: 10.1016/0014-5793(87)81562-4

Babu, E., Bhutia, Y. D., Ramachandran, S., Gnanaprakasam, J. P., Prasad, P. D., Thangaraju, M., et al. (2015). Deletion of the amino acid transporter Slc6a14 suppresses tumour growth in spontaneous mouse models of breast cancer. *Biochem. J.* 469, 17–23. doi: 10.1042/BJ20150437

Bhutia, Y. D., Babu, E., Ramachandran, S., and Ganapathy, V. (2015). Amino acid transporters in cancer and their relevance to "glutamine addiction": novel targets for the design of a new class of anticancer drugs. *Cancer Res.* 75, 1782–1788. doi: 10.1158/0008-5472.CAN-14-3745

Bicho, A., and Grewer, C. (2005). Rapid substrate-induced charge movements of the GABA transporter GAT1. *Biophys. J.* 89, 211–231. doi: 10.1529/biophysj.105.061002

Broer, S., and Gether, U. (2012). The solute carrier 6 family of transporters. *Br. J. Pharmacol.* 167, 256–278. doi: 10.1111/j.1476-5381.2012.01975.x

Coothankandaswamy, V., Cao, S., Xu, Y., Prasad, P. D., Singh, P. K., Reynolds, C. P., et al. (2016). Amino acid transporter SLC6A14 is a novel and effective drug target for pancreatic cancer. *Br. J. Pharmacol.* 173, 3292–3306. doi: 10.1111/bph.13616

Erdem, F. A., Ilic, M., Koppensteiner, P., Golacki, J., Lubec, G., Freissmuth, M., et al. (2019). A comparison of the transport kinetics of glycine transporter 1 and glycine transporter 2. *J. Gen. Physiol.* 151, 1035–1050. doi: 10.1085/jgp.201912318

Fairweather, S. J., Okada, S., Gauthier-Coles, G., Javed, K., Broer, A., and Broer, S. (2021). A GC-MS/single-cell method to evaluate membrane transporter substrate specificity and signaling. *Front. Mol. Biosci.* 8:646574. doi: 10.3389/fmolb.2021.646574

Grewer, C. (1999). Investigation of the alpha(1)-glycine receptor channel-opening kinetics in the submillisecond time domain. *Biophys. J.* 77, 727–738. doi: 10.1016/S0006-3495(99)76927-4

Grewer, C., Jager, J., Carpenter, B. K., and Hess, G. P. (2000a). A new photolabile precursor of glycine with improved properties: A tool for chemical kinetic investigations of the glycine receptor. *Biochemistry* 39, 2063–2070. doi: 10.1021/bi9919652

Grewer, C., Madani Mobarekeh, S. A., Watzke, N., Rauen, T., and Schaper, K. (2001). Substrate translocation kinetics of excitatory amino acid carrier 1 probed with laser-pulse photolysis of a new photolabile precursor of D-aspartic acid. *Biochemistry* 40, 232–240. doi: 10.1021/bi0015919

Grewer, C., Watzke, N., Wiessner, M., and Rauen, T. (2000b). Glutamate translocation of the neuronal glutamate transporter EAAC1 occurs within milliseconds. *Proc. Natl. Acad. Sci. U. S. A.* 97, 9706–9711. doi: 10.1073/pnas.160170397

Grewer, C., Zhang, Z., Mwaura, J., Albers, T., Schwartz, A., and Gameiro, A. (2012). Charge compensation mechanism of a Na^+—coupled, secondary active glutamate transporter. *J. Biol. Chem.* 287, 26921–26931. doi: 10.1074/jbc.M112.364059

Gupta, N., Miyauchi, S., Martindale, R. G., Herdman, A. V., Podolsky, R., Miyake, K., et al. (2005). Upregulation of the amino acid transporter $ATB^{0,+}$ (SLC6A14) in colorectal cancer and metastasis in humans. *Biochim. Biophys. Acta* 1741, 215–223. doi: 10.1016/j.bbadis.2005.04.002

Gupta, N., Prasad, P. D., Ghamande, S., Moore-Martin, P., Herdman, A. V., Martindale, R. G., et al. (2006). Up-regulation of the amino acid transporter ATB(0,+) (SLC6A14) in carcinoma of the cervix. *Gynecol. Oncol.* 100, 8–13. doi: 10.1016/j.ygyno.2005.08.016

Hatanaka, T., Haramura, M., Fei, Y. J., Miyauchi, S., Bridges, C. C., Ganapathy, P. S., et al. (2004). Transport of amino acid-based prodrugs by the Na^+— and cl(−) -coupled amino acid transporter $ATB^{0,+}$ and expression of the transporter in tissues amenable for drug delivery. *J. Pharmacol. Exp. Ther.* 308, 1138–1147. doi: 10.1124/jpet.103.057109

Hilgemann, D. W., and Lu, C. C. (1999). GAT1 (GABA:Na^+:Cl^-) cotransport function. Database reconstruction with an alternating access model. *J. Gen. Physiol.* 114, 459–475. doi: 10.1085/jgp.114.3.459

Jiang, G., Zhuang, L., Miyauchi, S., Miyake, K., Fei, Y. J., and Ganapathy, V. (2005). A Na^+/Cl^- -coupled GABA transporter, GAT-1, from Caenorhabditis elegans: structural and functional features, specific expression in GABA-ergic neurons, and involvement in muscle function. *J. Biol. Chem.* 280, 2065–2077. doi: 10.1074/jbc.M408470200

Jumper, J., Evans, R., Pritzel, A., Green, T., Figurnov, M., Ronneberger, O., et al. (2021). Highly accurate protein structure prediction with AlphaFold. *Nature* 596, 583–589. doi: 10.1038/s41586-021-03819-2

Karunakaran, S., Ramachandran, S., Coothankandaswamy, V., Elangovan, S., Babu, E., Periyasamy-Thandavan, S., et al. (2011). SLC6A14 ($ATB^{0,+}$) protein, a highly concentrative and broad specific amino acid transporter, is a novel and effective drug target for treatment of estrogen receptor-positive breast cancer. *J. Biol. Chem.* 286, 31830–31838. doi: 10.1074/jbc.M111.229518

Karunakaran, S., Umapathy, N. S., Thangaraju, M., Hatanaka, T., Itagaki, S., Munn, D. H., et al. (2008). Interaction of tryptophan derivatives with SLC6A14 ($ATB^{0,+}$) reveals the potential of the transporter as a drug target for cancer chemotherapy. *Biochem. J.* 414, 343–355. doi: 10.1042/BJ20080622

Kristensen, A. S., Andersen, J., Jorgensen, T. N., Sorensen, L., Eriksen, J., Loland, C. J., et al. (2011). SLC6 neurotransmitter transporters: structure, function, and regulation. *Pharmacol. Rev.* 63, 585–640. doi: 10.1124/pr.108.000869

Le Guellec, B., Rousseau, F., Bied, M., and Supplisson, S. (2021). A three-sodium-to-glycine stoichiometry shapes the structural relationships of $ATB^{0,+}$ with GLYT2 and Glyt1 in the SLC6 FAMILY. [Preprint]. doi:10.1101/2021.06.01.446649.

Liu, Q. R., Lopez-Corcuera, B., Mandiyan, S., Nelson, H., and Nelson, N. (1993). Cloning and expression of a spinal cord- and brain-specific glycine transporter with novel structural features. *J. Biol. Chem.* 268, 22802–22808. doi: 10.1016/S0021-9258(18)41598-0

Lopez-Corcuera, B., Martinez-Maza, R., Nunez, E., Roux, M., Supplisson, S., and Aragon, C. (1998). Differential properties of two stably expressed brain-specific glycine transporters. *J. Neurochem.* 71, 2211–2219. doi: 10.1046/j.1471-4159.1998.71052211.x

Mager, S., Kleinberger-Doron, N., Keshet, G. I., Davidson, N., Kanner, B. I., and Lester, H. A. (1996). Ion binding and permeation at the GABA transporter GAT1. *J. Neurosci.* 16, 5405–5414. doi: 10.1523/JNEUROSCI.16-17-05405.1996

Mccray, J. A., Herbette, L., Kihara, T., and Trentham, D. R. (1980). A new approach to time-resolved studies of ATP-requiring biological systems; laser flash photolysis of caged ATP. *Proc. Natl. Acad. Sci. U. S. A.* 77, 7237–7241. doi: 10.1073/pnas.77.12.7237

Mennerick, S., Shen, W., Xu, W., Benz, A., Tanaka, K., Shimamoto, K., et al. (1999). Substrate turnover by transporters curtails synaptic glutamate transients. *J. Neurosci.* 19, 9242–9251. doi: 10.1523/JNEUROSCI.19-21-09242.1999

Mim, C., Tao, Z., and Grewer, C. (2007). Two conformational changes are associated with glutamate translocation by the glutamate transporter EAAC1. *Biochemistry* 46, 9007–9018. doi: 10.1021/bi7005465

Nakanishi, T., Hatanaka, T., Huang, W., Prasad, P. D., Leibach, F. H., Ganapathy, M. E., et al. (2001). Na^+— and Cl^--coupled active transport of carnitine by the amino acid transporter ATB(0,+) from mouse colon expressed in HRPE cells and *Xenopus* oocytes. *J. Physiol.* 532, 297–304. doi: 10.1111/j.1469-7793.2001.0297f.x

Niu, L., Wieboldt, R., Ramesh, D., Carpenter, B. K., and Hess, G. P. (1996). Synthesis and characterization of a caged receptor ligand suitable for chemical kinetic investigations of the glycine receptor in the 3-microseconds time domain. *Biochemistry* 35, 8136–8142. doi: 10.1021/bi952364n

Notredame, C., Higgins, D. G., and Heringa, J. (2000). T-coffee: A novel method for fast and accurate multiple sequence alignment. *J. Mol. Biol.* 302, 205–217. doi: 10.1006/jmbi.2000.4042

Page, R. D. (1996). TreeView: an application to display phylogenetic trees on personal computers. *Comput. Appl. Biosci.* 12, 357–358. doi: 10.1093/bioinformatics/12.4.357

Palazzolo, L., Paravicini, C., Laurenzi, T., Adobati, S., Saporiti, S., Guerrini, U., et al. (2019). SLC6A14, a pivotal actor on cancer stage: when function meets structure. *SLAS Discov* 24, 928–938. doi: 10.1177/2472555219867317

Penheiter, A. R., Erdogan, S., Murphy, S. J., Hart, S. N., Felipe Lima, J., Rakhshan Rohakhtar, F., et al. (2015). Transcriptomic and Immunohistochemical profiling of SLC6A14 in pancreatic ductal adenocarcinoma. *Biomed. Res. Int.* 2015:593572. doi: 10.1155/2015/593572

Penmatsa, A., Wang, K. H., and Gouaux, E. (2013). X-ray structure of dopamine transporter elucidates antidepressant mechanism. *Nature* 503, 85–90. doi: 10.1038/nature12533

Pramod, A. B., Foster, J., Carvelli, L., and Henry, L. K. (2013). SLC6 transporters: structure, function, regulation, disease association and therapeutics. *Mol. Asp. Med.* 34, 197–219. doi: 10.1016/j.mam.2012.07.002

Reyes, N., Ginter, C., and Boudker, O. (2009). Transport mechanism of a bacterial homologue of glutamate transporters. *Nature* 462, 880–885. doi: 10.1038/nature08616

Roux, M. J., and Supplisson, S. (2000). Neuronal and glial glycine transporters have different stoichiometries. *Neuron* 25, 373–383. doi: 10.1016/S0896-6273(00)80901-0

Rudnick, G., Kramer, R., Blakely, R. D., Murphy, D. L., and Verrey, F. (2014). The SLC6 transporters: perspectives on structure, functions, regulation, and models for transporter dysfunction. *Pflugers Arch.* 466, 25–42. doi: 10.1007/s00424-013-1410-1

Schaller, L., and Lauschke, V. M. (2019). The genetic landscape of the human solute carrier (SLC) transporter superfamily. *Hum. Genet.* 138, 1359–1377. doi: 10.1007/s00439-019-02081-x

Sloan, J. L., and Mager, S. (1999). Cloning and functional expression of a human Na(+) and cl(−)-dependent neutral and cationic amino acid transporter B(0+). *J. Biol. Chem.* 274, 23740–23745. doi: 10.1074/jbc.274.34.23740

Tao, Z., Zhang, Z., and Grewer, C. (2006). Neutralization of the aspartic acid residue Asp-367, but not Asp-454, inhibits binding of Na^+ to the glutamate-free form and cycling of the glutamate transporter EAAC1. *J. Biol. Chem.* 281, 10263–10272. doi: 10.1074/jbc.M510739200

Uchiyama, T., Fujita, T., Gukasyan, H. J., Kim, K. J., Borok, Z., Crandall, E. D., et al. (2008). Functional characterization and cloning of amino acid transporter B(0,+) (ATB(0,+)) in primary cultured rat pneumocytes. *J. Cell. Physiol.* 214, 645–654. doi: 10.1002/jcp.21254

Ugawa, S., Sunouchi, Y., Ueda, T., Takahashi, E., Saishin, Y., and Shimada, S. (2001). Characterization of a mouse colonic system B(0+) amino acid transporter related to amino acid absorption in colon. *Am. J. Physiol. Gastrointest. Liver Physiol.* 281, G365–G370. doi: 10.1152/ajpgi.2001.281.2.G365

Umapathy, N. S., Ganapathy, V., and Ganapathy, M. E. (2004). Transport of amino acid esters and the amino-acid-based prodrug valganciclovir by the amino acid transporter ATB(0,+). *Pharm. Res.* 21, 1303–1310. doi: 10.1023/B:PHAM.0000033019.49737.28

Wang, J., Albers, T., and Grewer, C. (2018). Energy landscape of the substrate translocation equilibrium of plasma-membrane glutamate transporters. *J. Phys. Chem. B* 122, 28–39. doi: 10.1021/acs.jpcb.7b09059

Wang, J., Zhang, K., Goyal, P., and Grewer, C. (2020). Mechanism and potential sites of potassium interaction with glutamate transporters. *J. Gen. Physiol.* 152:e202012577. doi: 10.1085/jgp.202012577

Wang, J., Zielewicz, L., Dong, Y., and Grewer, C. (2021). Pre-steady-state kinetics and reverse transport in rat glutamate transporter EAAC1 with an immobilized transport domain. *Neurochem. Res.* 6, 1–5. doi: 10.1007/s11064-021-03462-3

Wang, J., Zielewicz, L., and Grewer, C. (2019). A K^+/Na^+ co-binding state: simultaneous versus competitive binding of K^+ and Na^+ to glutamate transporters. *J. Biol. Chem.* 294, 12180–12190. doi: 10.1074/jbc.RA119.009421

Watzke, N., Bamberg, E., and Grewer, C. (2001). Early intermediates in the transport cycle of the neuronal excitatory amino acid carrier EAAC1. *J. Gen. Physiol.* 117, 547–562. doi: 10.1085/jgp.117.6.547

Yamashita, A., Singh, S. K., Kawate, T., Jin, Y., and Gouaux, E. (2005). Crystal structure of a bacterial homologue of Na^+/Cl^--dependent neurotransmitter transporters. *Nature* 437, 215–223. doi: 10.1038/nature03978

Zafra, F., Aragon, C., and Gimenez, C. (1997). Molecular biology of glycinergic neurotransmission. *Mol. Neurobiol.* 14, 117–142. doi: 10.1007/BF02740653

Zafra, F., and Gimenez, C. (1986). Characterization of glycine uptake in plasma membrane vesicles isolated from cultured glioblastoma cells. *Brain Res.* 397, 108–116. doi: 10.1016/0006-8993(86)91374-0

Zhang, Z., Tao, Z., Gameiro, A., Barcelona, S., Braams, S., Rauen, T., et al. (2007). Transport direction determines the kinetics of substrate transport by the glutamate transporter EAAC1. *Proc. Natl. Acad. Sci. U. S. A.* 104, 18025–18030. doi: 10.1073/pnas.0704570104

Zhang, Y. W., Uchendu, S., Leone, V., Bradshaw, R. T., Sangwa, N., Forrest, L. R., et al. (2021). Chloride-dependent conformational changes in the GlyT1 glycine transporter. *Proc. Natl. Acad. Sci. U. S. A.* 118:118, e2020941118. doi: 10.1073/pnas.2020941118

Zielewicz, L., Wang, J., Ndaru, E., and Grewer, C. T. (2019). Transient kinetics reveal mechanism and voltage dependence of inhibitor and substrate binding to glutamate transporters. *ACS Chem. Biol.* 14, 1002–1010. doi: 10.1021/acschembio.9b00194

Conflict of Interest: The authors declare that the research was conducted in the absence of any commercial or financial relationships that could be construed as a potential conflict of interest.

Publisher's Note: All claims expressed in this article are solely those of the authors and do not necessarily represent those of their affiliated organizations, or those of the publisher, the editors and the reviewers. Any product that may be evaluated in this article, or claim that may be made by its manufacturer, is not guaranteed or endorsed by the publisher.

frontiers in Physiology

MINI REVIEW
published: 07 December 2021
doi: 10.3389/fphys.2021.792958

Structural Plasticity of the Selectivity Filter in Cation Channels

*Kitty Hendriks[1], Carl Öster[1] and Adam Lange[1,2]**

[1] Department of Molecular Biophysics, Leibniz-Forschungsinstitut für Molekulare Pharmakologie, Berlin, Germany, [2] Institut für Biologie, Humboldt-Universität zu Berlin, Berlin, Germany

Ion channels allow for the passage of ions across biological membranes, which is essential for the functioning of a cell. In pore loop channels the selectivity filter (SF) is a conserved sequence that forms a constriction with multiple ion binding sites. It is becoming increasingly clear that there are several conformations and dynamic states of the SF in cation channels. Here we outline specific modes of structural plasticity observed in the SFs of various pore loop channels: disorder, asymmetry, and collapse. We summarize the multiple atomic structures with varying SF conformations as well as asymmetric and more dynamic states that were discovered recently using structural biology, spectroscopic, and computational methods. Overall, we discuss here that structural plasticity within the SF is a key molecular determinant of ion channel gating behavior.

Keywords: protein dynamics, asymmetry, ion channel, channel gating, ion conduction

OPEN ACCESS

Edited by:
Christoph Fahlke, Helmholtz Association of German Research Centres (HZ), Germany

Reviewed by:
Carlos Alberto Villalba-Galea, The University of the Pacific, United States

***Correspondence:**
Adam Lange
alange@fmp-berlin.de

Specialty section:
This article was submitted to Membrane Physiology and Membrane Biophysics, a section of the journal Frontiers in Physiology

Received: *11 October 2021*
Accepted: *17 November 2021*
Published: *07 December 2021*

Citation:
Hendriks K, Öster C and Lange A (2021) Structural Plasticity of the Selectivity Filter in Cation Channels. Front. Physiol. 12:792958. doi: 10.3389/fphys.2021.792958

INTRODUCTION

The ability of ion channels to permit ion flux across biological membranes is essential for the functioning of a cell. There are a wide array of diseases associated with ion channel dysfunction that are collectively termed channelopathies including epilepsy, cardiac arrhythmia, deafness, asthma, and cancer (Kim, 2014). Pore loop channels are a family of tetrameric ion channels including potassium-, calcium-, and sodium-selective channels that all share a pore domain architecture. The pore domain consists of two transmembrane helices connected via a reentrant loop that forms the selectivity filter (SF) and a stabilizing pore helix (MacKinnon, 1995). For potassium-selective channels the SF is made from the conserved sequence TVGYG (Heginbotham et al., 1994). The backbone carbonyl oxygens plus the hydroxyl group of the threonine form four ion binding sites, called S1 to S4 from the extracellular side (see **Figure 1A**), and they perfectly mimic the hydration shell of potassium ions (Liu et al., 2012). There is an additional S0 site above the SF sequence with less precise ion coordination. The non-selective channel NaK has a similar SF sequence of TVGDG but forms only two ion binding sites that are equivalent to S3 and S4 (Shi et al., 2006). It is a model system for other non-selective pore loop channels, such as the hyper-polarization cyclic nucleotide-gated (HCN) channel (Lee and MacKinnon, 2017) and cyclic nucleotide-gated (CNG) channels (Li et al., 2017; Xue et al., 2021). Within the pore loop family there are several channels with a non-traditional SF sequence, such as calcium or sodium channels (Payandeh et al., 2011; Naylor et al., 2016). Here we will focus only on the potassium-selective and non-selective cation channels with traditional SF sequences.

The SF can act as a gate and modulate the electrophysiological behavior of the ion channel. One regulatory mechanism is C-type inactivation that was first discovered in voltage-gated potassium channels, where prolonged activation of the channel by an external stimulus leads to a non-conductive conformation of the SF. In the model potassium channel KcsA high external potassium concentrations are able to slow C-type inactivation, which highlights the link between the SF and C-type inactivation (Cuello et al., 2010).

In recent years there has been a strong increase in research demonstrating the dynamic nature of the SF in various channels. Commonly used structural biology techniques, such as X-ray crystallography or cryogenic electron microscopy (cryo-EM), lead to static snapshots of biological processes where the dynamics can easily be overlooked. Molecular dynamics (MD) simulations complement experimental approaches by obtaining information on the dynamics of previously determined structures (Li et al., 2018; Kopec et al., 2019; Saponaro et al., 2021). However, MD simulations are still limited in terms of the timescale that can be sampled and sometimes suffer from the inaccuracy of force field parameters. Solid-state nuclear magnetic resonance (ssNMR) spectroscopy is a technique that is able to detect and quantify the dynamics of membrane proteins, all while maintaining native-like conditions of a lipid bilayer environment at physiological conditions and temperatures (Wylie et al., 2014; Van Der Cruijsen et al., 2017; Mandala et al., 2018; Jekhmane et al., 2019). Combining various types of experimental data with MD simulations allows for a more complete investigation of biological systems, including the dynamics.

We will discuss several modes of structural plasticity for the SF region of potassium-selective and non-selective cation channels; specifically collapse, asymmetry and disorder. These discoveries highlight recent developments in the field and indicate the importance of SF plasticity in pore loop channel function.

SELECTIVITY FILTER COLLAPSE

The first glimpse of structural plasticity of the SF came from crystal structures of the conductive and collapsed conformations of KcsA with high and low potassium concentrations, respectively (Doyle et al., 1998; Zhou et al., 2001). The conformations described only concern the SF, as the activation gate of KcsA is in a closed state for both structures. The conductive SF conformation has the canonical four ion binding sites, whereas the collapsed conformation is constricted with only the S1 and S4 binding sites remaining (see **Figure 1B**). The constriction at the S2 site is caused by a reorientation of the glycine residue in the middle of the SF and this is stabilized through interactions with three water molecules behind the SF (Zhou et al., 2001). The SF conformational change is correlated to the potassium concentration as was also shown using NMR titration experiments (Chill et al., 2006; Bhate et al., 2010). The pore helix region surrounding the SF influences the transition between the conductive and collapsed SF state as demonstrated through a combination of point mutation experiments and MD simulations (Cordero-Morales et al., 2007). Solid-state NMR studies on KcsA showed allosteric regulation of the SF conformation by the activation gate, a pH sensor at the C-terminal end of the protein (Wylie et al., 2014; Xu et al., 2019). This allosteric control of the collapsed SF conformation was also observed in recent microsecond-scale MD simulations (Li et al., 2018), which clearly revealed that the SF of KcsA acts as another gate and plays an important role for ion channel functioning.

Mutations of E71 in the pore helix of KcsA change the equilibrium between the conductive and collapsed SF conformations. The E71A mutant was crystallized in two distinct conformations, one similar to wild-type KcsA and one with several flipped residues (Cordero-Morales et al., 2006). The flipped conformation shows W67 in the pore helix and D80 as well as V76 in the SF with a reoriented sidechain or carbonyl group (see **Figure 1C**). This flipped conformation was found again when the E71A mutant was crystallized under sodium conditions (Cheng et al., 2011). The flipped conformation was suggested to be responsible for the increased sodium conduction observed in the E71A mutant and therefore gives some insight into the principles behind selective ion conduction.

A recent study using MD simulations of a homology model of the Shaker channel also displayed a stable constricted SF conformation that was allosterically regulated (Li et al., 2021b). This conformation was stabilized by only one water molecule behind the SF and a hydrogen bond ring of donor-acceptor pairs at the bottom of the SF is in the opposite direction compared to KcsA, because the SF valine residue is in a flipped orientation. MD simulations of the KcsA mutant E71V revealed the same constricted conformation as for the Shaker channel, which has a valine residue at the position equivalent to E71 in KcsA (Li et al., 2021b).

SELECTIVITY FILTER ASYMMETRY

All SF conformations described so far assume fourfold symmetry across the tetramer assembly, but this is not necessarily the case. A functional example of an asymmetric SF conformation was found in the non-selective channel NaK with the unique SF sequence TVGDGN. Using ssNMR we discovered that the channel adopts two distinct SF conformations, stabilized by either potassium or sodium ions (Shi et al., 2018). This directly contradicted the previously reported identical structures of NaK that had been crystallized in the presence of potassium or sodium ions (see **Figure 1D**; Shi et al., 2006). One of the discovered SF conformations corresponds to the crystal structure of NaK, whereas the other conformation consists of a backbone carbonyl flipped conformation that distorts the SF. This flipped conformation was shown in MD simulations to be essential in creating an asymmetric pore, which has a mixture of subunits in the crystal and flipped conformation, and allows for efficient sodium permeation (Shi et al., 2018). The predicted sodium permeation pathway contained a novel side-entry ion binding site, which is the result of the sidechain reorientation of the SF residue D66. A recent crystal structure

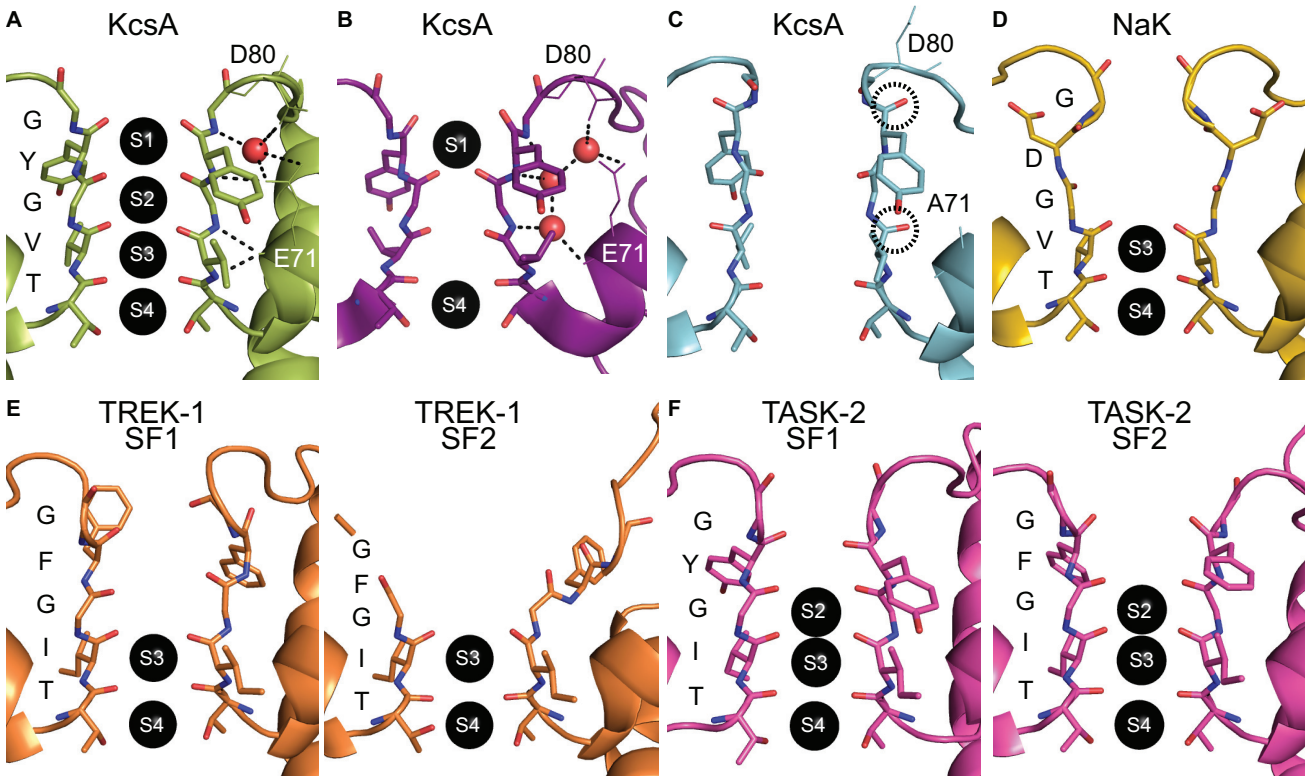

FIGURE 1 | Atomic structures of selectivity filter conformations. **(A)** The conductive conformation of the SF of KcsA (PDB ID: 1K4C) with two opposing subunits depicted and with the sequence and ion binding sites indicated. **(B)** The collapsed SF conformation of KcsA under low potassium conditions (PDB ID: 1K4D). **(C)** The flipped SF conformation of the E71A KcsA mutant (PDB ID: 2ATK) with the reoriented backbone carbonyl groups of the SF circled. Residues D80 and E71 are indicated and depicted as lines. The hydrogen bond network is symbolized with black dashed lines and water molecules are depicted as red spheres in one of the two opposing subunits. **(D)** The crystal conformation of the SF of NaK (PDB ID: 3E86). **(E)** The asymmetric SF conformations of TREK-1 under low potassium conditions (PDB ID: 6W7C) with the opposing subunit pairs of SF1 and SF2 shown. **(F)** The asymmetric SF conformations of TASK-2 at pH 6.5 (PDB ID: 6WLV) with the opposing subunit pairs of SF1 and SF2 shown.

of NaK revealed dual conformations of two residues in the SF, among them D66, and confirmed this side-entry ion binding site (Roy et al., 2021). In contrast, for potassium permeation the symmetric pore with all subunits in the crystal conformation is required in NaK (Shi et al., 2018). A recent study characterized the structural plasticity of NaK on multiple timescales using solution NMR (Lewis et al., 2021). The results from this study confirmed the ion dependence of the SF, which was even shown to continue along an allosteric pathway that couples the SF conformation to the lower region of the channel.

Since then, SF asymmetry has been observed in other pore loop channels. A subset of pore loop channels that lend themselves especially well for asymmetric SF configurations are K_{2P} channels. These channels consist of two dimers that form a pseudo-tetramer that can have different SF sequences, often with a tyrosine to phenylalanine substitution [T(V/I)GFG] in one or both of the SF sequences. The primary gating of K_{2P} channels occurs at the SF (Schewe et al., 2016). In a series of recent cryo-EM structures, the SF of the K_{2P} channel TREK-1 undergoes changes at low potassium concentrations (Lolicato et al., 2020). The SF1 of opposing subunits showed a pinching movement whereas the other SF2 pair of opposing subunits showed a dilation, disrupting the S1 and S2 ion binding sites (see **Figure 1E**). These changes highlight the dynamic nature of the inactivated state of the channel and were suppressed by the addition of a small molecule activator (Lolicato et al., 2020). Similarly, a recent cryo-EM structure of another K_{2P} channel, TASK-2, revealed that the closed channel is asymmetric instead of the open pseudo-fourfold symmetric channel (Li et al., 2020). There is an asymmetric expansion at the S1 site and strikingly the S0 site has a constriction for the opposing SF1 subunits, but an expansion for the SF2 subunit pair (see **Figure 1F**). Overall, this deformation of the SF in TASK-2 is not as pronounced as that observed for TREK-1. However, it is likely that other K_{2P} channels have similar asymmetric conformations of the SF as closed states of the channel that disrupt ion binding sites.

Recent work on an inactivated mutant of the potassium-selective Shaker channel showed a similar SF conformation to the closed TASK-2 channel (Li et al., 2021b). MD simulations revealed the SF conformation of the W434F mutant (equivalent to W67 in KcsA) where the aspartate residue above the SF has flipped outward and the SF is stabilized by the sidechain of the neighboring residue in an asymmetric constriction of the

S0 site. The constriction at the top of the SF does not seem to be allosterically linked to the activation gate, in contrast to the constriction at the S2 ion binding site seen in KcsA. The similarity between the asymmetric conformations of different pore loop channels, K2P and Shaker, points toward a potentially conserved mechanism.

The human ether-a-go-go related gene (hERG) channel is a pore loop channel that functions as a fast-inactivating potassium-selective channel, which has a phenylalanine instead of a tyrosine in its SF sequence (SVGFG). The cryo-EM structure of the open state of the channel revealed that the sidechain of the phenylalanine was slightly shifted compared to other potassium-selective channels, and this was proposed to be linked to the fast inactivation of the hERG channel (Wang and MacKinnon, 2017). A recent study of the hERG channel using MD simulations resulted in asymmetric SF constrictions for which no ion conduction was observed (Li et al., 2021a). The phenylalanine sidechains of two opposing subunits reorient and form stabilizing hydrogen bonds behind the other subunit. This reorientation constricts the conduction pathway at the S2 site, which is not constricted in the other pair of opposing subunits. Multiple mutants were analyzed and a correlation was found between the level of inactivation and the stabilization of the asymmetric SF conformation.

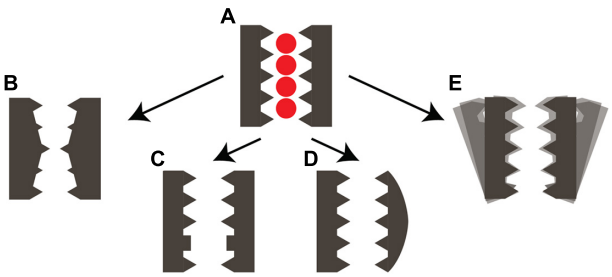

FIGURE 2 | Structural plasticity of the selectivity filter of cation channels. **(A)** Schematic representation of the conductive SF conformation with four ion binding sites. Arrows indicate the conversion into **(B)** a stable collapsed conformation as observed in KcsA (Zhou et al., 2001) or Shaker (Li et al., 2021b). **(C)** A carbonyl flipped conformation as observed in KcsA E71A (Cordero-Morales et al., 2006; Cheng et al., 2011) or NaK (Roy et al., 2021). **(D)** an asymmetric conformation as observed in NaK (Shi et al., 2018) or TREK-1 (Lolicato et al., 2020) or TASK-1 (Li et al., 2020). **(E)** An unstable disordered SF conformation as observed in hERG (Miranda et al., 2020) or the potassium-selective mutants of NaK in the presence of sodium (Hendriks et al., 2021).

SELECTIVITY FILTER DISORDER

The previously discussed non-selective channel NaK can be made potassium-selective by two point mutations in the SF sequence from TVGDGN to TVGYGD or TVGFGD (Alam and Jiang, 2009; Sauer et al., 2011). We have shown using ssNMR that these potassium-selective mutants lose their SF stability under sodium conditions and become disordered without stabilizing potassium ions (Öster et al., 2019; Hendriks et al., 2021). The loss of SF stability strongly influences the hydrogen bonding network behind the SF and through this network impacts the pore helix (Hendriks et al., 2021). Reintroduction of potassium ions allowed for the stabilization of the SF into the canonical four ion binding sites conformation. This finding shows the intrinsic instability of the potassium-selective SF and highlights the interplay between the SF and the permeant ions. It also highlights that a stable closed SF conformation, as found for the collapsed conformation in KcsA, is not available to all pore loop channels.

Another example of SF disorder comes from recent work using FRET (Förster resonance energy transfer) in the potassium-selective channel KirBac1.1. A decrease in the concentration of potassium ions changes the SF from a rigid high-FRET state to a more dilated and dynamic state with medium and low-FRET signals (Wang et al., 2019). This increase in disorder again shows that interactions with the permeant ion are essential for maintaining the integrity of the SF conductive conformation.

KcsA displays three different gating modes within the wild-type channel which can be mimicked by a set of three mutants for E71 (Chakrapani et al., 2011). Solid-state NMR investigations of these mutants pointed toward the water molecules behind the SF stabilizing different conformational landscapes (Jekhmane et al., 2019). The dynamics of the SF clearly have a great effect on the electrophysiological behavior of the channel.

Microsecond-timescale MD simulations of the hERG channel show SF instability (Miranda et al., 2020). This is in contrast to the stable asymmetric conformation of hERG discussed previously (Li et al., 2021a). Two distinct metastable states were found for hERG with transitions between the two states on a low-microsecond timescale, indicating the overall instability of the SF (Miranda et al., 2020). Both states were defined as non-conducting and are characterized by asymmetric SF conformations, where the distances between SF residues of opposing subunit pairs differ significantly. The most populated state shows a constricted pore for one SF pair, whilst the other pair remains structurally similar to the original cryo-EM structure. Importantly, the sidechain of the phenylalanine residue also displays large fluctuations in this state. The less populated metastable SF state is distinctive in the fact that the sidechain of the phenylalanine of one subunit blocks the conduction pathway of the channel. This study describes a SF that is both asymmetric as well as disordered, more research is needed to determine if this is linked to the fast inactivation of the channel.

DISCUSSION

It has become increasingly clear in recent years that structural data alone does not give enough information to describe ion channel functioning. Recent research has shown that a lack of dynamic information has limited the mechanistic understanding of ion channels. We have summarized all examples of structural plasticity of the SF in the pore loop channel family, focusing on the potassium- and non-selective cation channels. The SF

structures include various constricted, stable conformations as well as asymmetric or even disordered states (see **Figure 2**). Recently, the TRPV1 and the HCN4 pore loop channels were discovered to have more subtle structural plasticity of the SF in their ability to adapt to different ion types (Saponaro et al., 2021; Zhang et al., 2021).

It was already known that the SF is one of the structural elements responsible for gating in many pore loop channels. The balance between conductive, asymmetric, collapsed or disordered SF states is very important for the specific electrophysiological profile of a channel. The various constricted states of the SF, both collapsed and asymmetric, with a narrowed ion pore all show stabilization by either water molecules or a residue sidechain behind the SF. Interestingly, it seems that the constriction of the conduction pathway can be found at either the S2 or S0 ion binding site of the SF, where the constriction at the S0 site appears to be linked to an asymmetric state of the channel. It is unclear if all these different modes lead to the same behavior of C-type inactivation.

It is particularly challenging to obtain high-resolution structural information on the SF of ion channels by methods such as X-ray crystallography or cryo-EM when this is a dynamic region. MD simulations and NMR can provide additional information taking structural plasticity into account which aids the further understanding of ion channel functioning. An emerging theory links ion selectivity of the channel and SF disorder. It was first shown by us that multiple SF conformations are essential for non-selective ion conduction in NaK, with a symmetric state responsible for potassium and an asymmetric state responsible for sodium conduction (Shi et al., 2018). The disordered states of the SF, which might further influence the electrophysiology of the ion channel, could also play an important role in this. We expect that ssNMR in combination with MD simulations will continue to allow characterization of these dynamic SF states. More research is certainly needed to fully clarify the functional role of SF structural plasticity in pore loop channels.

AUTHOR CONTRIBUTIONS

KH wrote the original draft and prepared the figures. All authors contributed to the writing of the manuscript.

FUNDING

This work was funded by the Leibniz-Forschungsinstitut für Molekulare Pharmakologie (FMP) and Deutsche Forschungsgemeinschaft (DFG, German Research Foundation) under Germany's Excellence Strategy – EXC 2008 – 390540038 – UniSysCat. CÖ acknowledges support from the Human Frontier Science Program LT000303/2019-L.

ACKNOWLEDGMENTS

We thank Prof. Han Sun and Dr. Henry Sawczyc for helpful comments and discussion.

REFERENCES

Alam, A., and Jiang, Y. (2009). High-resolution structure of the open NaK channel. *Nat. Struct. Mol. Biol.* 16, 30–34. doi: 10.1038/nsmb.1531

Bhate, M. P., Wylie, B. J., Tian, L., and Mcdermott, A. E. (2010). Conformational dynamics in the selectivity filter of KcsA in response to potassium ion concentration. *J. Mol. Biol.* 401, 155–166. doi: 10.1016/j.jmb.2010.06.031

Chakrapani, S., Cordero-Morales, J. F., Jogini, V., Pan, A. C., Cortes, D. M., Roux, B., et al. (2011). On the structural basis of modal gating behavior in K+ channels. *Nat. Struct. Mol. Biol.* 18:67. doi: 10.1038/nsmb.1968

Cheng, W. W., Mccoy, J. G., Thompson, A. N., Nichols, C. G., and Nimigean, C. M. (2011). Mechanism for selectivity-inactivation coupling in KcsA potassium channels. *Proc. Natl. Acad. Sci. U. S. A.* 108, 5272–5277. doi: 10.1073/pnas.1014186108

Chill, J. H., Louis, J. M., Miller, C., and Bax, A. (2006). NMR study of the tetrameric KcsA potassium channel in detergent micelles. *Protein Sci.* 15, 684–698. doi: 10.1110/ps.051954706

Cordero-Morales, J. F., Cuello, L. G., Zhao, Y., Jogini, V., Cortes, D. M., Roux, B., et al. (2006). Molecular determinants of gating at the potassium-channel selectivity filter. *Nat. Struct. Mol. Biol.* 13, 311–318. doi: 10.1038/nsmb1069

Cordero-Morales, J. F., Jogini, V., Lewis, A., Vasquez, V., Cortes, D. M., Roux, B., et al. (2007). Molecular driving forces determining potassium channel slow inactivation. *Nat. Struct. Mol. Biol.* 14, 1062–1069. doi: 10.1038/nsmb1309

Cuello, L. G., Jogini, V., Cortes, D. M., Pan, A. C., Gagnon, D. G., Dalmas, O., et al. (2010). Structural basis for the coupling between activation and inactivation gates in K(+) channels. *Nature* 466, 272–275. doi: 10.1038/nature09136

Doyle, D. A., Morais Cabral, J., Pfuetzner, R. A., Kuo, A., Gulbis, J. M., Cohen, S. L., et al. (1998). The structure of the potassium channel: molecular basis of K+ conduction and selectivity. *Science* 280, 69–77. doi: 10.1126/science.280.5360.69

Heginbotham, L., Lu, Z., Abramson, T., and Mackinnon, R. (1994). Mutations in the K+ channel signature sequence. *Biophys. J.* 66, 1061–1067. doi: 10.1016/S0006-3495(94)80887-2

Hendriks, K., Oster, C., Shi, C., Sun, H., and Lange, A. (2021). Sodium ions do not stabilize the selectivity filter of a potassium channel. *J. Mol. Biol.* 433:167091. doi: 10.1016/j.jmb.2021.167091

Jekhmane, S., Medeiros-Silva, J., Li, J., Kummerer, F., Muller-Hermes, C., Baldus, M., et al. (2019). Shifts in the selectivity filter dynamics cause modal gating in K(+) channels. *Nat. Commun.* 10:123. doi: 10.1038/s41467-018-07973-6

Kim, J. B. (2014). Channelopathies. *Korean J. Pediatr.* 57, 1–18. doi: 10.3345/kjp.2014.57.1.1

Kopec, W., Rothberg, B. S., and De Groot, B. L. (2019). Molecular mechanism of a potassium channel gating through activation gate-selectivity filter coupling. *Nat. Commun.* 10:5366. doi: 10.1038/s41467-019-13227-w

Lee, C. H., and MacKinnon, R. (2017). Structures of the Human HCN1 Hyperpolarization-Activated Channel. *Cell* 168:e111. doi: 10.1016/j.cell.2016.12.023

Lewis, A., Kurauskas, V., Tonelli, M., and Henzler-Wildman, K. (2021). Ion-dependent structure, dynamics, and allosteric coupling in a non-selective cation channel. *Nat. Commun.* 12:6225. doi: 10.1038/s41467-021-26538-8

Li, B., Rietmeijer, R. A., and Brohawn, S. G. (2020). Structural basis for pH gating of the two-pore domain K(+) channel TASK2. *Nature* 586, 457–462. doi: 10.1038/s41586-020-2770-2

Li, J., Ostmeyer, J., Cuello, L. G., Perozo, E., and Roux, B. (2018). Rapid constriction of the selectivity filter underlies C-type inactivation in the KcsA potassium channel. *J. Gen. Physiol.* 150, 1408–1420. doi: 10.1085/jgp.201812082

Li, J., Shen, R., Reddy, B., Perozo, E., and Roux, B. (2021a). Mechanism of C-type inactivation in the hERG potassium channel. *Sci. Adv.* 7:eabd6203. doi: 10.1126/sciadv.abd6203

Li, J., Shen, R., Rohaim, A., Mendoza Uriarte, R., Fajer, M., Perozo, E., et al. (2021b). Computational study of non-conductive selectivity filter conformations and

C-type inactivation in a voltage-dependent potassium channel. *J. Gen. Physiol.* 153:e20211287. doi: 10.1085/jgp.202112875

Li, M., Zhou, X., Wang, S., Michailidis, I., Gong, Y., Su, D., et al. (2017). Structure of a eukaryotic cyclic-nucleotide-gated channel. *Nature* 542, 60–65. doi: 10.1038/nature20819

Liu, S., Bian, X., and Lockless, S. W. (2012). Preferential binding of K+ ions in the selectivity filter at equilibrium explains high selectivity of K+ channels. *J. Gen. Physiol.* 140, 671–679. doi: 10.1085/jgp.201210855

Lolicato, M., Natale, A. M., Abderemane-Ali, F., Crottes, D., Capponi, S., Duman, R., et al. (2020). K2P channel C-type gating involves asymmetric selectivity filter order-disorder transitions. *Sci. Adv.* 6:eabc9174. doi: 10.1126/sciadv.abc9174

MacKinnon, R. (1995). Pore loops: an emerging theme in ion channel structure. *Neuron* 14, 889–892. doi: 10.1016/0896-6273(95)90327-5

Mandala, V. S., Williams, J. K., and Hong, M. (2018). Structure and Dynamics of Membrane Proteins from Solid-State NMR. *Annu. Rev. Biophys.* 47, 201–222. doi: 10.1146/annurev-biophys-070816-033712

Miranda, W. E., Demarco, K. R., Guo, J., Duff, H. J., Vorobyov, I., Clancy, C. E., et al. (2020). Selectivity filter modalities and rapid inactivation of the hERG1 channel. *Proc. Natl. Acad. Sci. U. S. A.* 117, 2795–2804. doi: 10.1073/pnas.1909196117

Naylor, C. E., Bagneris, C., Decaen, P. G., Sula, A., Scaglione, A., Clapham, D. E., et al. (2016). Molecular basis of ion permeability in a voltage-gated sodium channel. *EMBO J.* 35, 820–830. doi: 10.15252/embj.201593285

Öster, C., Hendriks, K., Kopec, W., Chevelkov, V., Shi, C., Michl, D., et al. (2019). The conduction pathway of potassium channels is water free under physiological conditions. *Sci. Adv.* 5:eaaw6756. doi: 10.1126/sciadv.aaw6756

Payandeh, J., Scheuer, T., Zheng, N., and Catterall, W. A. (2011). The crystal structure of a voltage-gated sodium channel. *Nature* 475, 353–358. doi: 10.1038/nature10238

Roy, R. N., Hendriks, K., Kopec, W., Abdolvand, S., Weiss, K. L., De Groot, B. L., et al. (2021). Structural plasticity of the selectivity filter in a nonselective ion channel. *IUCrJ* 8, 421–430. doi: 10.1107/S205225252100213X

Saponaro, A., Bauer, D., Giese, M. H., Swuec, P., Porro, A., Gasparri, F., et al. (2021). Gating movements and ion permeation in HCN4 pacemaker channels. *Mol. Cell.* 81, 2929–2943.e6. doi: 10.1016/j.molcel.2021.05.033

Sauer, D. B., Zeng, W., Raghunathan, S., and Jiang, Y. (2011). Protein interactions central to stabilizing the K+ channel selectivity filter in a four-sited configuration for selective K+ permeation. *Proc. Natl. Acad. Sci. U. S. A.* 108, 16634–16639. doi: 10.1073/pnas.1111688108

Schewe, M., Nematian-Ardestani, E., Sun, H., Musinszki, M., Cordeiro, S., Bucci, G., et al. (2016). A Non-canonical Voltage-Sensing Mechanism Controls Gating in K2P K(+) Channels. *Cell* 164, 937–949. doi: 10.1016/j.cell.2016.02.002

Shi, C., He, Y., Hendriks, K., De Groot, B. L., Cai, X., Tian, C., et al. (2018). A single NaK channel conformation is not enough for non-selective ion conduction. *Nat. Commun.* 9:717. doi: 10.1038/s41467-018-03179-y

Shi, N., Ye, S., Alam, A., Chen, L., and Jiang, Y. (2006). Atomic structure of a Na+- and K+-conducting channel. *Nature* 440, 570–574. doi: 10.1038/s41467-018-03179-y

Van Der Cruijsen, E. A., Prokofyev, A. V., Pongs, O., and Baldus, M. (2017). Probing Conformational Changes during the Gating Cycle of a Potassium Channel in Lipid Bilayers. *Biophys. J.* 112, 99–108. doi: 10.1016/j.bpj.2016.12.001

Wang, S., Lee, S. J., Maksaev, G., Fang, X., Zuo, C., and Nichols, C. G. (2019). Potassium channel selectivity filter dynamics revealed by single-molecule FRET. *Nat. Chem. Biol.* 15, 377–383. doi: 10.1038/s41589-019-0240-7

Wang, W., and MacKinnon, R. (2017). Cryo-EM Structure of the Open Human Ether-a-go-go-Related K(+) Channel hERG. *Cell* 169, 422–430.e10. doi: 10.1016/j.cell.2017.03.048

Wylie, B. J., Bhate, M. P., and Mcdermott, A. E. (2014). Transmembrane allosteric coupling of the gates in a potassium channel. *Proc. Natl. Acad. Sci. U. S. A.* 111, 185–190. doi: 10.1073/pnas.1319577110

Xu, Y., Zhang, D., Rogawski, R., Nimigean, C. M., and Mcdermott, A. E. (2019). Identifying coupled clusters of allostery participants through chemical shift perturbations. *Proc. Natl. Acad. Sci. U. S. A.* 116, 2078–2085. doi: 10.1073/pnas.1811168116

Xue, J., Han, Y., Zeng, W., Wang, Y., and Jiang, Y. (2021). Structural mechanisms of gating and selectivity of human rod CNGA1 channel. *Neuron* 109, 1302–1313.e04. doi: 10.1016/j.neuron.2021.02.007

Zhang, K., Julius, D., and Cheng, Y. (2021). Structural snapshots of TRPV1 reveal mechanism of polymodal functionality. *Cell* 185, 5138–5150.e12. doi: 10.1016/j.cell.2021.08.012

Zhou, Y., Morais-Cabral, J. H., Kaufman, A., and Mackinnon, R. (2001). Chemistry of ion coordination and hydration revealed by a K+ channel-Fab complex at 2.0 A resolution. *Nature* 414, 43–48. doi: 10.1038/35102009

Conflict of Interest: The authors declare that the research was conducted in the absence of any commercial or financial relationships that could be construed as a potential conflict of interest.

Publisher's Note: All claims expressed in this article are solely those of the authors and do not necessarily represent those of their affiliated organizations, or those of the publisher, the editors and the reviewers. Any product that may be evaluated in this article, or claim that may be made by its manufacturer, is not guaranteed or endorsed by the publisher.

frontiers in Physiology

ORIGINAL RESEARCH
published: 03 February 2022
doi: 10.3389/fphys.2022.817886

Optimizing the Substrate Uptake Rate of Solute Carriers

*Klaus Schicker, Clemens V. Farr, Danila Boytsov, Michael Freissmuth and Walter Sandtner**

Center of Physiology and Pharmacology, Medical University of Vienna, Vienna, Austria

The diversity in solute carriers arose from evolutionary pressure. Here, we surmised that the adaptive search for optimizing the rate of substrate translocation was also shaped by the ambient extracellular and intracellular concentrations of substrate and co-substrate(s). We explored possible solutions by employing kinetic models, which were based on analytical expressions of the substrate uptake rate, that is, as a function of the microscopic rate constants used to parameterize the transport cycle. We obtained the defining terms for five reaction schemes with identical transport stoichiometry (i.e., Na^+: substrate = 2:1). We then utilized an optimization algorithm to find the set of numeric values for the microscopic rate constants, which provided the largest value for the substrate uptake rate: The same optimized rate was achieved by different sets of numerical values for the microscopic rate constants. An in-depth analysis of these sets provided the following insights: (i) In the presence of a low extracellular substrate concentration, a transporter can only cycle at a high rate, if it has low values for both, the Michaelis–Menten constant (K_M) for substrate and the maximal substrate uptake rate (V_{max}). (ii) The opposite is true for a transporter operating at high extracellular substrate concentrations. (iii) Random order of substrate and co-substrate binding is superior to sequential order, if a transporter is to maintain a high rate of substrate uptake in the presence of accumulating intracellular substrate. Our kinetic models provide a framework to understand how and why the transport cycles of closely related transporters differ.

Keywords: solute carriers, kinetic model, optimization, evolution, secondary active transporters, substrate uptake

OPEN ACCESS

Edited by:
Christof Grewer,
Binghamton University, United States

Reviewed by:
Reinhart Reithmeier,
University of Toronto, Canada
Stefan Broer,
Australian National University, Australia

***Correspondence:**
Walter Sandtner
walter.sandtner@meduniwien.ac.at

Specialty section:
This article was submitted to Membrane Physiology and Membrane Biophysics, a section of the journal Frontiers in Physiology

Received: *18 November 2021*
Accepted: *10 January 2022*
Published: *03 February 2022*

Citation:
Schicker K, Farr CV, Boytsov D, Freissmuth M and Sandtner W (2022) Optimizing the Substrate Uptake Rate of Solute Carriers. Front. Physiol. 13:817886. doi: 10.3389/fphys.2022.817886

INTRODUCTION

Cellular membranes are diffusion barriers for polar solutes. Uptake of these solutes into a cell or a subcellular compartment is, therefore, contingent on solute carriers (SLC). For this reason, SLCs are vital for many physiological functions. The latter include cellular uptake of nutrients and extrusion of toxic compounds from the interior of a cell (Hediger et al., 2004; Omote et al., 2006; Sano et al., 2020). In addition, SLCs are involved in higher order functions, such as neurotransmission (e.g., reuptake of neurotransmitters subsequent to their vesicular release; Rudnick and Sandtner, 2019; Bhat et al., 2021). Many of the SLCs can harvest the energy contained in the transmembrane ion gradients to drive uphill transport of their substrate against an opposing substrate gradient (Mitchell, 1979). These are termed concentrative or secondary active transporters, which either work as symporters or antiporters (Jennigs, 2018). Another class of SLCs only facilitates passive diffusion of a polar solute by providing an

aqueous pathway, *via* which the solute can enter or leave the cell. The latter are termed facilitating or equilibrative transporters. Both, the concentrative and the equilibrative SLC operate by the alternate access mechanism (Jardetzky, 1966) which entails the following sequence of events: Extracellular substrate first binds to the transporter in its outward-facing conformation. On substrate binding the transporter rearranges to adopt the inward-facing conformation. From there the substrate is released into the cytosol. Subsequent to this, the carrier rearranges again to return to the substrate-free outward-facing conformation. From this point on, this series of reactions can repeat all over. Substrate uptake by a solute carrier is, therefore, a process, which encompasses several partial reactions. These include conformational change and binding/unbinding reactions of substrate and (co)-substrates to and from the transporter. These partial reactions form a closed loop, which is also referred to as the transport cycle.

We have recently described an approach to kinetic modeling of a solute carrier, which allows for deriving analytical expressions for its functional descriptors (Schicker et al., 2021). These include the K_M and the V_{max} for substrate uptake, the rate of basal substrate release from the interior of the cell, etc. The corresponding terms express these descriptors as a function of the microscopic rate constants used to parameterize the kinetic model. In the present study, we derived the defining terms for the substrate uptake rate of a sodium symporter for five different reactions scheme, which all adhere to the same transporter stoichiometry (Na^+:substrate = 2:1). The rationale for obtaining these analytical terms was as follows: The substrate uptake rate is the only functional descriptor of a transporter, for which compelling arguments can be made that it has been optimized (i.e., maximized) by evolution. These are: the magnitude of solute flux through SLCs into a cell or a cell organelle is determined by the number of transporter units expressed on the cell or organelle surface and the substrate uptake rate (i.e., turnover rate) of the individual transporters. Accordingly, to maintain a substrate flux, which is commensurate with the physiological needs, the cell can either increase the number of transporters or the rate of substrate turnover. The former is associated with two problems: (i) Protein synthesis is energetically costly (Millward and Garlick, 1976; Waterlow et al., 1978; Siems et al., 1984) and (ii) additional transporters occupy space in the membrane. Membranes cannot be infinitely crowded by transmembrane proteins (Bar-Even et al., 2011). Having to have fewer transporters, thus, increases the energy efficiency of a cell/organism. This is expected to improve fitness at conditions in which nutrients are scarce. Accordingly, the substrate uptake rate of a solute carrier fulfills all criteria of a trait subject to evolutionary selection.

We emulated the evolutionary pressure on the substrate uptake rate by relying on an optimization algorithm. This searched for the set of microscopic rate constants, which returned the largest value for the substrate uptake rate at given intra- and extracellular concentrations of Na^+ and substrate. The resulting sets of values provided by the optimization algorithm were subjected to an in-depth analysis. This analysis showed how a solute carrier must adjust its operation to cycle at a high rate at the various conditions/challenges, which it may encounter.

MATERIALS AND METHODS

Numerical Simulations

Time-dependent changes in state occupancies of the model in **Figure 1A** were evaluated by numerical integration of the resulting system of differential equations using the Systems Biology Toolbox (Schmidt and Jirstrand, 2006) and MATLAB 2018a (MathWorks, Natick, MA, United States).

Optimization of the Substrate Uptake Rate

Explicit expressions for the substrate uptake rate were derived as described previously (Burtscher et al., 2019; Schicker et al., 2021). Numerical sets of values for the microscopic rate constants maximizing these expressions were generated by a simulated annealing algorithm (Metropolis et al., 1953; Tsallis and Stariolo, 1996). In brief, in an initial step, a set of values for the microscopic rate constants was randomly drawn from independent normal distributions, centered at chosen start values with SDs of the same size. The substrate uptake rate for the drawn set was then calculated and compared with the substrate uptake rate calculated from the original set (i.e., the start values). The probability of accepting the new set was: prob. = exp.[−(−current Value + best Value)/T(iter)], with T being a temperature parameter, which was chosen to decrease exponentially with the number of iterations. If accepted, the new set was used for the next iteration, if not, the old set was retained. This procedure was repeated for 5,000 iterations. We safeguarded against trapping in a local maximum by reinitiating the algorithm with the maximum T value increased by 10% using the best parameter set found in the first round of iterations. If this yielded a better overall value for the substrate uptake rate, the next run was reinitiated with the original T. Otherwise T was increased by additional 10%. This procedure was repeated until reheating was unsuccessful in obtaining a better set of values for 10 times. On completion, the algorithm reported the best parameter set (i.e., the set of values which gave the largest substrate uptake rate).

In the optimization of the sequential binding order schemes, we kept the detailed balance constraint, by allowing the algorithm to vary all microscopic rate constants except one. This rate constant was then calculated from the other rate constants such that detailed balance was maintained. In the case of the random order binding scheme, it was necessary to calculate three rate constants because of the larger number of loops. Each set of microscopic rate constants was also evaluated for adherence to the other imposed constraints (e.g., diffusion limit for the association rates of substrate and co-substrate). Only if a set of values complied with the imposed constraints it was passed on to the annealing algorithm.

RESULTS

Kinetic Models of SLC Can Predict Substrate Turnover Rates

Figure 1A shows the reaction scheme of a hypothetical symporter: In each cycle, the transporter translocates one substrate molecule through the membrane together with two Na^+ ions. We selected

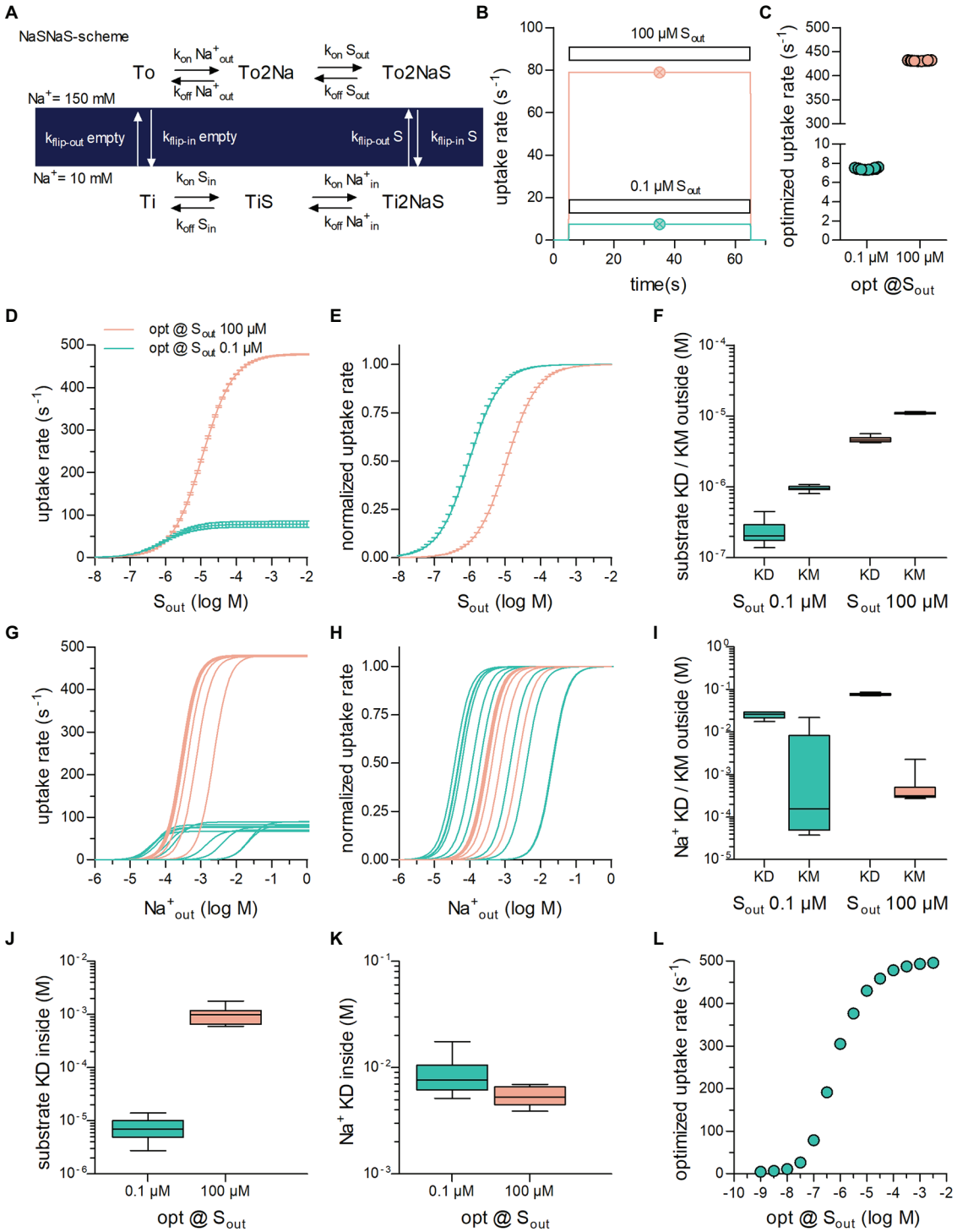

FIGURE 1 | Optimization of secondary active transporters operating in a sequential binding mode for translocation of substrate at a low and high concentration. **(A)** Reaction scheme of a Na^+ symporter in the sequential binding mode ("first in, first out") referred to as NaSNaS: The apo-outward-facing transporter (To) first binds two Na^+ ions (To2Na). On substrate binding, (To2NaS) the transporter rearranges to adopt the inward-facing conformation (Ti2NaS). Subsequent to the release of its cargo into the cytosol (TiNa2S → TiS → Ti) the substrate-free inward-facing transporter (Ti) undergoes a conformational change upon which the transporter returns to To. **(B)** Simulated substrate uptake rate of the symporter operating according to the scheme outlined in **(A)** after application of .1 µM (green trace) and 100 µM (magenta trace) of substrate (S_{out}). For this simulation the microscopic rate constants (i.e., $k_{on}Na^+_{out}$ and $k_{flip\text{-}in}S$) were parameterized with the values for the optimized transporter T1 shown in **Table 1**. The symbols in green and in magenta show the substrate uptake rates computed for T1 with the analytical expression (see supplement) for .1 µM and 100 µM S_{out}, respectively. The uptake rates obtained with the two different approaches were identical. **(C)** Substrate uptake rates of

(Continued)

FIGURE 1 | transporters optimized for .1 μM S_{out} (green open circles) and for 100 μM S_{out} (magenta open circles). The data points in the graph show the substrate uptake rates obtained from 10 optimization runs. The corresponding sets of numeric values for the microscopic rate constants are listed in **Table 1**. **(D)** The curves represent the substrate uptake rate as a function of S_{out} of transporters optimized for .1 μM S_{out} (in green) and 100 μM S_{out} (in magenta). The data are means from the 10 independently optimized transporters (T_1–T_{10} and T_{11}–T_{20}), error bars indicate S.D. **(E)** The data in panel **(D)** were plotted as normalized values ($V_{max} = 1$). **(F)** Plotted are the K_D values for binding of the substrate to the outward-facing conformation of the transporter and the corresponding K_M values of transporters optimized for .1 μM and 100 μM S_{out}, respectively. The coefficients of variation for the K_Ds were: .43 and .094 and for the K_Ms: .094 and .03 at .1 μM and 100 μM S_{out}, respectively. **(G)** Substrate uptake rate as a function of Na^+_{out} of transporters optimized for .1 μM S_{out} (in green) and for 100 μM S_{out} (in magenta). The concentration dependence for Na^+_{out} differed considerably between transporters optimized for the same S_{out}. **(H)** The same data as in **(G)** but normalized **(I)** Plotted are the K_D values for Na^+ binding to the outward-facing conformation of the transporter and the corresponding K_M values of transporters optimized for .1 μM S_{out} and for 100 μM S_{out}. The variation in the K_D values was much less than the variation in the K_M values. The coefficients of variation for the K_Ds were: .17 and .06 and for the K_Ms: 1.81 and 1.12 at .1 μM and 100 μM S_{out}, respectively. **(J)** Shown are the K_D values of substrate binding to the inward-facing conformation of transporters optimized for .1 μM and 100 μM S_{out}, respectively (coefficients of variation: .47 and .36). **(K)** Plotted are the K_D values of Na^+ binding to the inward-facing conformation of transporters optimized for .1 μM S_{out} and for 100 μM S_{out} (coefficients of variation: .43 and .2). **(L)** Plotted are the optimized substrate uptake rates as a function of the S_{out}, for which they were optimized. Each data point is the means ± SD of the substrate uptake rate obtained from 10 optimization runs. The optimized rate rose upon increase of S_{out}. It leveled out at 500 s^{-1} because of the constraints imposed in the optimization.

this stoichiometry, because it is frequently observed: For instance, sodium-dependent glucose (SGLT1/SLC5A1 and SGLT2/SLC5A2; Wright et al., 2011) and phosphate transporters (PiT-1/SLC20A1 and PiT-2/SLC20A2; Forster et al., 2013) operate with this stoichiometry. For the sake of simplicity, we assumed binding of the two sodium ions to occur in a single reaction. In **Figure 1B**, we used this model to predict the rate of substrate uptake through the transporter by assuming that two different concentrations of extracellular substrate (S_{out}) were applied, that is, .1 μM (magenta line in **Figure 1B**) and 100 μM (blue line in **Figure 1B**). As seen, on exposure of the cell to the substrate, the substrate uptake rate rose. The rise was large on application of 100 μM S_{out} and small on application of .1 μM S_{out}. In the simulation, the substrate was removed after 60 s upon which the substrate uptake rate dropped to zero.

The data in **Figure 1B** were obtained by numerically solving the system of differential equations underlying the kinetic model. An alternative approach to compute the substrate uptake rate relies on deriving its defining analytical term. For the sake of space, we show the term in the supplement. **Figure 1B** also displays the substrate uptake rates obtained by this second approach in the presence of .1 μM (open circle in magenta) and 100 μM S_{out} (open circle in blue). It is evident that the substrate uptake rates predicted by the two methods were identical.

Maximizing the Substrate Turnover Rate

The extracellular concentration of a substrate (S_{out}) is a given quantity, that is, it is typically not subject to control by a single cell. Accordingly, SLC, which are tasked with transporting a substrate into the interior of a cell, must adjust their operation to the substrate concentration they encounter. The substrate concentration surrounding a cell can therefore, be assumed to exert evolutionary pressure. To emulate optimization of the substrate uptake rate by evolution, we maximized this rate, utilizing its defining function. For this purpose, we employed an optimization algorithm, which can approximate global minima/maxima of a function (i.e., simulated annealing—for details see the method section). The optimization algorithm can find the set of numeric values for the microscopic rate constants, which returns the largest value for the substrate uptake rate at given intra- and extracellular concentrations of Na^+ and substrate.

We note that microscopic rate constants are *a priori* not mathematically constrained: They can assume values between zero and infinity. If they are permitted to vary across the entire mathematically possible range, the optimized substrate uptake rate will also adopt values between zero and infinity. It is a futile and meaningless exercise to maximize a function, for which it is known that no maximum exists. Fortunately, however, there are limits to the values of the microscopic rate constants. For instance, the association rates of co-substrates and substrate cannot be larger than the diffusion limit, which therefore imposes an upper limit on these rates. Likewise, the dissociation rates of substrate and co-substrate must also have an upper limit, because raising the dissociation rate constant results in affinity loss, which, when substantial, prevents the co-substrate and the substrate from interacting with the transporter in their physiological concentration ranges. It is also clear that a conformational change cannot occur with infinite velocity. We selected 1,000 s^{-1} as the upper limit for conformational transition rates. The choice of this value was based on information obtained from the literature (Zhang et al., 2007; Schicker et al., 2011; Hasenhuetl et al., 2018; Erdem et al., 2019). Another necessary constraint was to ensure that every set of optimized values complied with the rule of microscopic reversibility: The product of the rates in the forward direction in a loop must equal the product of the rates in the opposite direction. The combined constraints reshape the parameter space of the function, such that it harbors critical points, which do not exist in the unconstrained parameter space.

We performed ten optimization runs in which we assumed that S_{out} was .1 μM and 100 μM (**Figure 1C**). In all runs, we set the extra- and intracellular Na^+ concentration to 150 mM and 10 mM and the intracellular substrate concentration (S_{in}) to zero. The data points show the substrate uptake rates, to which the optimization algorithm converged when S_{out} was set to .1 μM (left column) and 100 μM (right column). The rates were low at .1 μM S_{out} (7.44 s^{-1} ± .08 s^{-1}) and high at 100 μM S_{out} (431.40 s^{-1} ± .66 s^{-1}). We emphasize that each point in **Figure 1C** represents a unique set of numeric values for the microscopic rate constants. In **Table 1**, we show the ten sets, which we obtained from the optimization runs where S_{out} was set to .1 μM and 100 μM. Although the values of the microscopic rate constants differed between sets, they all gave essentially

the same substrate uptake rate when optimized for the same substrate concentration. We therefore conclude that the optimized rate can be realized by different sets of numeric values for the microscopic rate constants. Because of the large differences in these values, each set can be viewed to define a transporter with an individual phenotype. For this reason, we will from here on treat the term "transporter" and "a set of optimized values" as a synonymous description.

Analysis of Optimized Transporters

The observations summarized in **Table 1** warranted further scrutiny. They suggest that not all reactions, which a transporter undergoes, require the same extent of fine-tuning to support a high substrate uptake rate. We analyzed the transporters in **Table 1** to understand, which reactions in the transport cycle do and do not require precise adjustment. Accordingly, we examined for each individual transporter, the values for a collection of descriptors of transporter function: (i) These included descriptors, which can be computed with the kinetic model but also obtained experimentally (i.e., V_{max} and the K_M for substrate/co-substrate) and (ii) descriptors, which can only be extracted from the kinetic model (i.e., K_Ds for substrate and co-substrate to the outward- and inward-facing conformation of the transporter). The rationale was as follows: If the values of a descriptor are all similar for transporters optimized for the same substrate concentration, we can conclude that fine-tuning of the reactions, which affect this descriptor, is essential for the realization of the optimized rate. Conversely, this is not the case, if the values are vastly different.

In **Figure 1D**, we plotted the substrate uptake rate as a function of S_{out} for the transporters in **Table 1**: The V_{max} values were low and high for the group of transporters, which were optimized for .1 μM and 100 μM S_{out}, respectively. Within the two groups of transporters, the V_{max} values varied, but the magnitude of this variation was small: V_{max} of transporter optimized for .1 μM S_{out} and 100 μM S_{out}, were $78.40 \pm 6.61\ s^{-1}$ and $478.38 \pm 1.58\ s^{-1}$, respectively. In **Figure 1E**, the data were normalized to maximum velocity, because differences in the apparent affinity of the optimized transporters for the substrate can be more readily appreciated in this representation. It is evident that the transporters, which were optimized for .1 μM S_{out} displayed a higher apparent affinity for the substrate than those optimized for 100 μM S_{out}. The K_M values within groups fell into narrow ranges, that is, $.95 \pm .08$ μM and $11.1 \pm .31$ μM for transporters optimized for .1 μM and 100 μM S_{out}, respectively. Our analysis therefore indicates that transporters, must have low K_M and low V_{max} values to support a high substrate uptake rate when S_{out} is low, but a high K_M and a high V_{max} value when S_{out} is high.

We computed the K_D values for substrate binding to the outward-facing conformation of the individual transporters (**Figure 1F**): It is evident that the K_D values for the substrate

TABLE 1 | Microscopic rate constants of optimized transporters.

S_{out} .1 μM	T_1	T_2	T_3	T_4	T_5	T_6	T_7	T_8	T_9	T_{10}
$k_{on}Na_{out}$ ($M^{-1}*s^{-1}$)	843.9	882.2	467824.2	172900	5103575	2668168	102801	11301.1	1305776	4117.5
$k_{off}Na_{out}$ (s^{-1})	18.4	23.1	13819.5	5033.6	89713.5	74711.5	2623.4	261	26895.4	121.7
$k_{on}Na_{in}$ ($M^{-1}*s^{-1}$)	144780.2	71436.7	3573458	63795.9	1053480	7485548	85572.9	242224.4	3001183	135554.6
$k_{off}Na_{in}$ (s^{-1})	1033.6	655.8	30079.9	757.1	5402.4	47223	516	1848.1	52802.7	562.9
$k_{on}S_{out}$ ($M^{-1}*s^{-1}$)	99756087	99321467	99900325	99781085	99971424	99749741	99780659	99786322	99766393	99715096
$k_{off}S_{out}$ (s^{-1})	23.9	19.1	13.8	17.6	41.4	17.4	25.2	21	44.7	19.6
$k_{on}S_{in}$ ($M^{-1}*s^{-1}$)	98320556	98934133	94504880	98557663	98674263	98891788	88619319	99302604	90444017	99325744
$k_{off}S_{in}$ (s^{-1})	578	688.3	661.2	299.1	966	859.6	1239.5	549	249.1	1091
$k_{flipin}S$ (s^{-1})	963	439.4	336	953.4	929	788.1	944.1	805	823	587.1
$k_{flipout}S$ (s^{-1})	887.5	623.2	630	910.1	368	816.3	924.2	910	802	263
k_{flipin}empty (s^{-1})	942.8	966.1	877.3	818	689	649	635.4	549.2	877	951
$k_{flipout}$empty (s^{-1})	332	307.5	399	272.4	136	266	201	217	190.5	384.3
S_{out} 100 μM	**T_{11}**	**T_{12}**	**T_{13}**	**T_{14}**	**T_{15}**	**T_{16}**	**T_{17}**	**T_{18}**	**T_{19}**	**T_{20}**
$k_{on}Na_{out}$ ($M^{-1}*s^{-1}$)	459612.4	464014.7	2147180	45080.1	13688.3	1819462	248255	112618	219098	1204854
$k_{off}Na_{out}$ (s^{-1})	34935.3	38332.5	154576.7	3414.9	1009.6	130362	19485.7	9815.8	16359.4	96032.4
$k_{on}Na_{in}$ ($M^{-1}*s^{-1}$)	4919690	3993649	12486840	6671406	20491995	16362423	6624730	12778355	30517371	11015465
$k_{off}Na_{in}$ (s^{-1})	25766.5	27738.4	59325	45413.9	79597.4	72486.4	35015.5	83510.1	137526	62251.8
$k_{on}S_{out}$ ($M^{-1}*s^{-1}$)	98615927	99737574	99830122	99892657	99369863	98985701	99041917	99525439	99582606	99961376
$k_{off}S_{out}$ (s^{-1})	518.2	484.7	517.8	505.8	523.3	485.6	415.6	378.9	486.2	463.8
$k_{on}S_{in}$ ($M^{-1}*s^{-1}$)	99322953	97562087	97649294	99729392	98979302	99787925	98616945	97467311	99781580	99521878
$k_{off}S_{in}$ (s^{-1})	107653.9	62043.6	114665.9	59904	177645	121233	87749	64743	118169.7	83413.3
$k_{flipin}S$ (s^{-1})	999.9	999.6	999.6	998.6	998.3	999.4	998.9	999.8	999.6	999
$k_{flipout}S$ (s^{-1})	994.9	942.8	984.3	993.2	977.2	990.2	998.5	992.2	917.3	965.9
k_{flipin}empty (s^{-1})	982.7	980.8	999.8	962.7	964.8	954.5	961.3	987.6	962.8	938.2
$k_{flipout}$empty (s^{-1})	998.5	999.9	998.4	999.6	999.2	998.9	999.4	999.2	999.9	998.9

The table shows ten sets of values for the microscopic rate constants optimized for .1 μM S_{out} (upper half) and ten sets optimized for 100 μM S_{out} (lower half). The depicted rate constants were obtained for the NaSNaS scheme. In these optimization runs, Na_{out}, Na_{in}, and S_{in} were set to 150 mM, 10 mM, and 0 μM, respectively. Values were rounded to one digit after the comma. The optimized substrate uptake rate was approximately the same within the two groups (i.e., 7.44 s^{-1} ± .08 s^{-1} and 431.40 s^{-1} ± .66 s^{-1} for .1 μM and 100 μM S_{out}, respectively). This is in contrast to the values for the microscopic rate constants, which differed substantially even in the same group. Each set can be viewed to represent a transporter with an individual phenotype (T_1–T_{20}).

were low and high for transporters, which were optimized for .1 μM and 100 μM S_{out}, respectively (.1 μM S_{out}: .24 μM ± .03 μM; 100 μM S_{out}: 4.72 μM ± .42 μM). It also evident that the K_D values were smaller and that they covered a larger range than the corresponding K_M values (**Figure 1F**).

Inspection of **Table 1** shows that the rate constants, which govern Na^+ binding to the outward-facing state, are subject to large variations in transporters 1–10; in contrast, these rate constants differed substantially less in transporters 11–20, which were optimized to cope with 100 μM S_{out}. We illustrated the resulting difference in apparent affinity for Na^+ by plotting the absolute (**Figure 1G**) and normalized substrate uptake rate (**Figure 1H**) of the optimized transporters as function of the Na^+ concentration: for those transporters, which were optimized for .1 μM S_{out} the apparent affinity for Na^+ varied over five orders of magnitude (blue curves in **Figures 1G,H**). In contrast, for transporters optimized for 100 μM S_{out}, the apparent affinity for Na^+ fell into a narrow range (magenta curve in **Figures 1G,H**). Thus, if the extracellular substrate concentration is low, the Na^+ binding reaction does not need to be fine-tuned to obtain optimal rates. However, at a higher substrate concentration, the Na^+ binding reaction is subject to stringent constraints. This observation can be rationalized by taking into account that, in the optimization, Na^+ was assumed to be present at a high concentration (i.e., 150 mM). At this concentration Na^+ binding is unlikely to become rate limiting for substrate transport if S_{out} is low. At a higher substrate concentration, the apparent association rate of the substrate (k_{app}) is expected to increase. In this scenario, Na^+ binding becomes rate limiting, if it occurs at too low a rate.

We compared the K_D values for Na^+ binding to the outward-facing conformation of the transporter *t* the corresponding K_M values (**Figure 1I**): Within each group, the variation in the K_D values was small, that is, K_D = 25.10 ± 3.91 mM and 79.21 ± 3.30 mM for transporters optimized for S_{out} .1 μM and S_{out} 100 μM, respectively. This contrasted with the large variation in the corresponding K_M values for Na^+ seen for transporters optimized for .1 μM S_{out}. This discrepancy can be explained as follows: The K_D values are determined by the ratio of the dissociation and association rates for Na^+ but not by the absolute values of these rates. Conversely, given that the K_D values and the K_M values for Na^+ were found to differ, it is safe to conclude that K_M values are highly dependent on the absolute values of these rates. These observations therefore imply that the affinity for Na^+—rather than the velocity of Na^+ binding to the transporter is subject to precise adjustment for supporting optimal uptake rates at low substrate concentrations.

Figures 1J,K summarize the K_D values for binding of substrate and of Na^+ to the inward-facing conformation of the transporter, respectively. The coefficients of variation in K_D values of the inward-facing state were larger by a factor of 2 to 4 than the corresponding K_D values of the outward-facing state: K_DS_{in} was 7.46 μM ± 3.4 μM and 701 μM ± 155 μM for transporters optimized for .1 μM S_{out} and for 100 μM S_{out}, respectively. Likewise, the $K_DNa^+_{in}$ was 8.81 mM ± 3.63 mM and 6.46 mM ± .70 mM for transporters optimized for .1 μM and 100 μM S_{out}, respectively. The high K_DS_{in} at 100 μM S_{out} was dictated by the low substrate affinity for the outward-facing state of transporters, which had been optimized for this condition, and the requirement to maintain microscopic reversibility. However, the larger variation in K_DS_{in} and $K_DNa^+_{in}$ indicates that the reactions, which define the substrate and co-substrate affinities for the inward-facing conformation, do not require as stringent an adjustment as those, which define the corresponding affinities to the outward-facing conformation. Finally, we surveyed transporter optimization over a large range of extracellular substrate concentration (1 nM to 10 mM; **Figure 1L**): The resulting optimized substrate uptake rate of the transporters increased as a function of S_{out} but leveled off at an uptake rate of about 500 s^{-1}. This upper limit reflect the constraint imposed by the boundary conditions of the optimization (i.e., a diffusion-limited k_{on} and an upper limit of 1,000 s^{-1} for the rate of conformational transitions, see above). It was 249.4, 499.4, and 997.8 s^{-1} when the upper limit of the rate of conformational transitions was set to 500, 1,000, and 2,000 s^{-1}, respectively.

Testing Different Modes of Transport

The reaction scheme in **Figure 1A** describes a hypothetical symporter, which binds co-substrate and substrate in a sequential order: The two Na^+ ions are the first to bind when the transporter adopts the outward-facing conformation and the first to dissociate upon conversion of the transporter to the inward-facing conformation. In the subsequent description, we will refer to this reaction scheme as the NaSNaS scheme. This notation lists from left to right the order of the binding/unbinding events starting at the outward-facing apo-state (To) in clockwise direction. In **Figures 2A–C**, we show the reaction schemes for the three (sequential) alternatives. According to our notation, we refer to these as NaSSNa, SNaNaS and SNaSNa schemes. In addition, we also examined the reaction scheme of a transporter, in which the two Na^+ ions and the substrate are allowed to bind in random order (**Figure 2D**).

We explored the impact of these five reaction schemes (**Figures 1A, 2A–D**) on the optimized substrate uptake rates by raising S_{out} from .1 (**Figure 2E**) to 30 (**Figure 2F**) and 100 μM (**Figure 2G**) and by conducting 10 optimization runs for each reaction scheme. As evident from **Figure 2E**, the substrate uptake rate was roughly the same for all schemes, when S_{out} was low (i.e., .1 μM). However, when optimized for a higher S_{out}, the schemes differed in the magnitude of the optimized substrate uptake rates, which they were able to support. The rank order was as follows: NaSSNa < SNaSNa < SNaSNa < SNaNaS = random. The rank order was the same for transporters optimized for 30 μM and 100 μM S_{out}, (*cf.* **Figures 2F,G**). Thus, random order of substrate and co-substrate binding and SNaNaS are best suited to support a large substrate uptake rate.

Raising the Intracellular Substrate Concentration

Due to the way SLC operate, the intracellular concentration of the substrate and the substrate uptake rate are inversely correlated. This can be explained as follows: The substrate must be released into the cytosol to complete a full cycle.

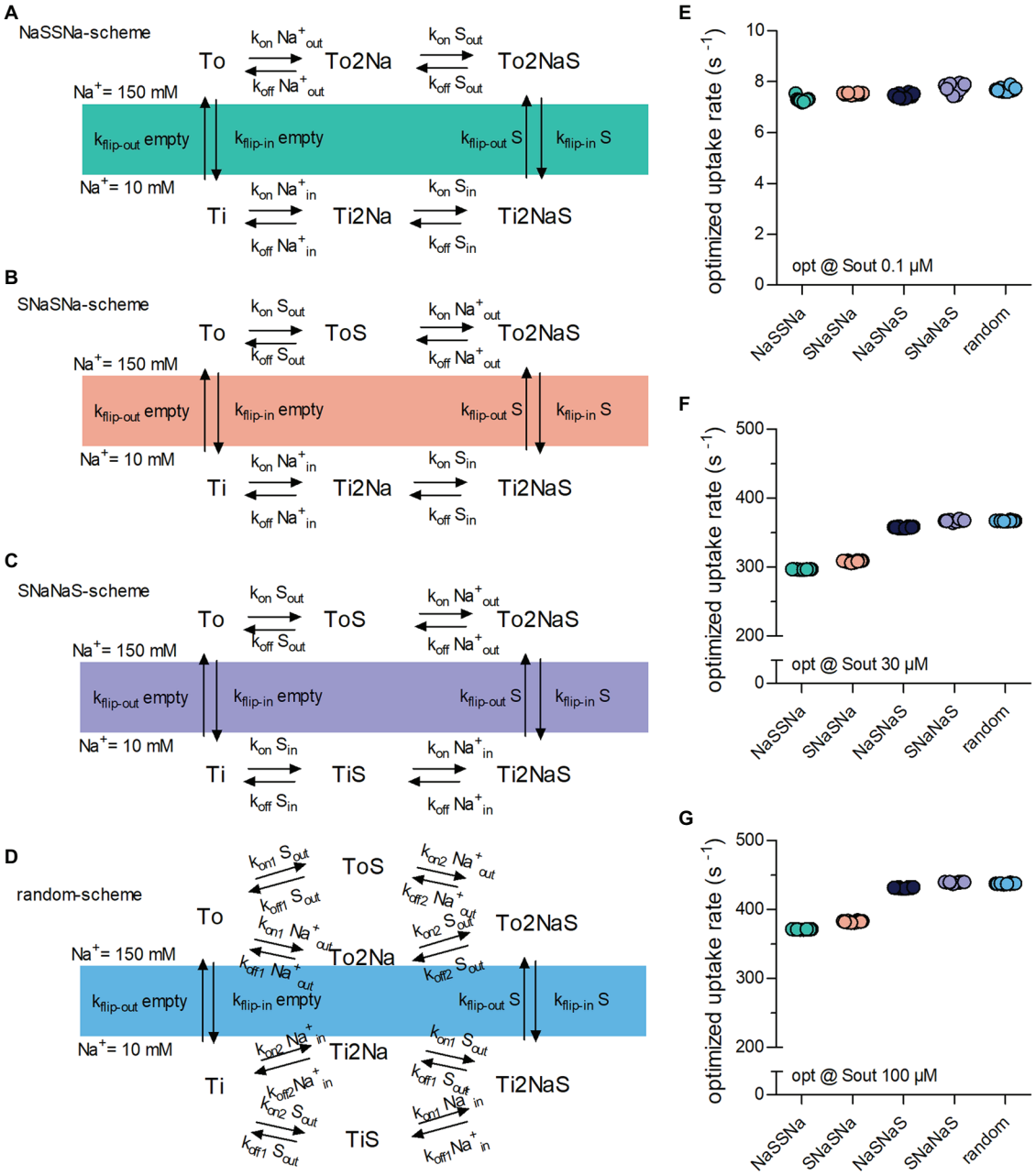

FIGURE 2 | Binding order of co-substrate and substrate affects the optimized substrate uptake rate. **(A)** NaSSNa scheme (sequential). Na^+ is the first to bind when the transporter adopts the outward-facing conformation and the last to dissociate from the inward-facing conformation. **(B)** SNaSNa scheme (sequential). Substrate is the first to bind to the outward-facing conformation and the first to dissociate from the inward-facing conformation. **(C)** SNaNaS scheme (sequential). Substrate is the first to bind to the outward-facing conformation and the last to dissociate from the inward-facing conformation **(D)**. Random binding order scheme. Na^+ and substrate bind in random order. **(E)** Plotted is the optimized substrate uptake rate for all schemes of transporter optimized for .1 µM S_{out}. At this low substrate concentration the optimized rate is approximately the same for all schemes. **(F)** Shown is the optimized substrate uptake rate for the different schemes optimized for 30 µM S_{out}. The height of the optimized rate differed between schemes **(G)** the same as in **(F)** but of transporter optimized for 100 µM S_{out}. The rank order of the optimized rates among schemes was the same as in **(F)**.

As the intracellular substrate concentration (S_{in}) increases progressively during uptake, rebinding of the substrate to the inward-facing conformation occurs at a more frequent rate. This hampers progression through the transport cycle and thus reduces the substrate uptake rate.

Here we propose that—similar to the extracellular substrate concentration (S_{out})—S_{in} can also exert an evolutionary pressure on the operation of a solute carrier. Depending on the physiological context, transporters may encounter intracellular concentrations of their cognate substrate, which range from low to high levels.

This can be illustrated by two examples in the SLC6 family: The cytosolic concentrations of the monoamines dopamine, norepinephrine, and dopamine are expected to be low. This is because of the presence of vesicular monoamine transporters (vMAT1/SLC18A1 & vMAT2/SLC18A2), which shuffle cytosolic monoamines into vesicles (Yaffe et al., 2018). Accordingly, under physiological conditions, monoamine transporters for dopamine (DAT/SLC6A3), norepinephrine (NET/SLC6A2) and (SERT/SLC6A4) are unlikely to encounter high intracellular concentrations of their substrate. Conversely, the creatine transporter-1 (SLC6A8) must maintain substrate influx in the presence of millimolar intracellular creatine (Snow and Murphy, 2001). It is clear that a solute carrier, which must support a high substrate uptake rate against high S_{in}, must adjust its operation differently than a transporter, which does not need to overcome the hurdle imposed by frequent rebinding of the substrate to the inward-facing conformation.

We first optimized the substrate uptake rate of a transporter operating according to the NaSNaS scheme (illustrated in **Figure 1A**) by performing 20 optimization runs each, where S_{out} was 30 µM and S_{in} was set at 0, .1, 1, and 5 mM. It is evident from **Figure 3A** that the optimized substrate uptake rate decreased by raising S_{in}. This is in line with the inverse correlation of S_{in} and the substrate uptake rate discussed above. **Figure 3B** illustrates the range of K_D values for substrate binding to the inward-facing conformation of the transporters, which had been optimized to cope with different concentrations of S_{in}: K_D values of substrate for the inward-facing conformation increased as S_{in} was raised. This was to be expected, because lowering the intracellular affinity for substrate reduces the extent by which S_{in} can rebind, and it thus allows for a higher substrate uptake rate in the presence of S_{in}.

We then compared the uptake rate of transporters optimized for 30 µM S_{out} and 0 mM or 1 mM S_{in} over a large range of extracellular substrate concentration. As can be seen from **Figure 3C**, it was inevitable that transporters optimized in the presence of 1 mM S_{in} had negative uptake rates at low extracellular substrate concentrations, that is, the transporters cycled in the backward rather than the forward mode and hence mediated substrate efflux from the cell. It is also clear that the presence of 1 mM S_{in} reduced the maximum achievable uptake rate V_{max} in the forward transport mode and shifted the K_M. Because K_M and K_D differ (*cf.* **Figure 1F**), we examined the range of K_D values for substrate binding to the outward-facing conformation of transporters optimized for 0 and 1 mM S_{in}; these are illustrated together with the corresponding K_M values in **Figure 3D**: Both the K_D values and the K_M values for substrate increased, if the transporter had to cope with a high intracellular substrate concentration. The variation in these parameters was low (coefficient of variations = .070 and .025 for K_D and K_M, respectively, of transporters optimized in the presence of 30 µM S_{out} and 1 mM S_{in}). We conclude that the decrease in the apparent (K_M) and the true affinity (K_D) for the substrate, is required to allow for rapid cycling of the transporters in the presence of high S_{in}.

Finally, we examined how the selective pressure exerted by high intracellular substrate affected the affinity of the transporters to the co-substrate ion. As can be seen from **Figure 3E**, many

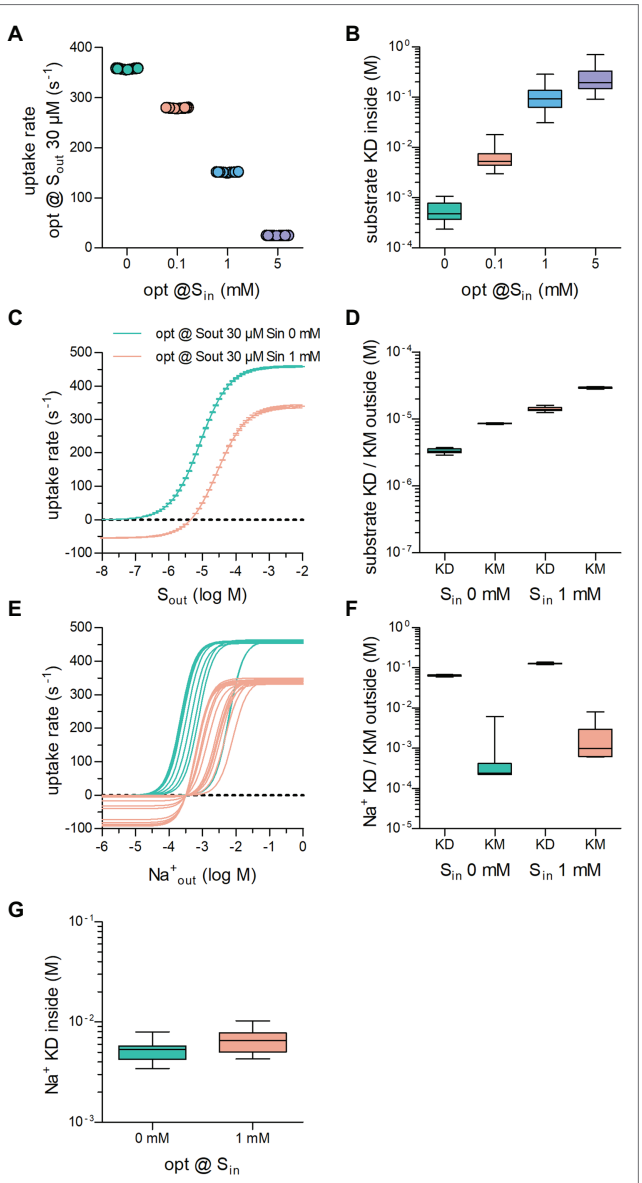

FIGURE 3 | The optimized substrate uptake rate depends on the intracellular substrate concentration (S_{in}). **(A)** Plotted are the optimized substrate uptake rates for transporters operating according to the NaSNaS scheme. S_{out} was set to 30 µM in all optimization runs. The data show the substrate uptake rate of transporters optimized for 0 mM, .1 mM, 1 mM, and 5 mM S_{in}, respectively. The rate decreased with rising S_{in}. Twenty optimization runs were carried out for each condition. **(B)** Shown is the K_D of substrate binding to the inward-facing conformation of transporters in **(A)**. The K_D decreased as S_{in} increased. **(C)** The curves show the substrate uptake rate as a function of S_{out} of transporters optimized for 0 mM (green) and 1 mM S_{in} (magenta). In the presence of S_{in}, the substrate uptake rate assumed negative values when S_{out} was low. In this range of S_{out}, the transporters cycled in the reverse direction. In the presence of 1 mM S_{in}, V_{max} was reduced. **(D)** Plotted are the K_D values for substrate binding to the outward-facing conformation of the transporter and the corresponding K_M values of transporters optimized for 0 mM S_{in} and for 1 mM S_{in}. At high S_{in} both the K_M and the K_D values rose. The coefficients of variation for the K_Ds were .080 and .070 and for the K_Ms .020 and .026 at .1 µM and 100 µM S_{out}, respectively. **(E)** Shown is the concentration dependence of the substrate uptake rate for Na^+_{out} of

(Continued)

FIGURE 3 | transporters optimized for 0 mM S_{in} and 1 mM S_{in}. The dependence on the Na^+ concentration was highly variable between transporters optimized for the same S_{in}. **(F)** Plotted are the K_D values for Na^+ binding to the outward-facing conformation of the transporter and the corresponding K_M values of transporters optimized for 0 mM S_{in} and for 1 mM S_{in}. The variation in the K_M values was larger than the variation in the K_D values. The coefficients of variation for the K_Ds were .041 and .033 and for the K_Ms 2.03 and .97 at .1 μM and 100 μM S_{out}, respectively. At high S_{in} both the K_M and the K_D values for Na^+ increased. **(G)** KDs for Na^+ for the inward facing conformation of the transporters optimized for 0 mM and 1 mM S_{in}, respectively.

different solutions emerged: On average, transporters optimized to cope with 1 mM S_{in} (magenta lines in **Figure 3E**) required higher extracellular Na^+ concentrations to support substrate uptake than those optimized in the absence of intracellular substrate (green lines in **Figure 3E**). However, in both groups, the optimized transporters displayed highly variable responses to Na^+_{out}. This is reflected in the large range of the K_M values for Na^+ (**Figure 3F**). In contrast, the K_D of Na^+ for binding the outward-facing conformation did not vary to any substantial extent. This observation is consistent with our conclusion from **Figure 1I**, namely, that the constraint is imposed by the true affinity for Na^+ rather than by its association rate (see above). We also computed K_Ds for Na^+ binding to the inward-facing conformation of the transporters optimized for 0 mM and 1 mM S_{in}: There was an overlap in the range of K_D values for Na^+_{in} (**Figure 3G**). In addition, their variation was larger than that of K_D values for Na^+_{iout} (*cf.* **Figures 3F,G**). Hence, we conclude that Na^+ binding to the inward-facing conformation need not be stringently adjusted to allow for high substrate uptake rates.

Binding Order Affects the Magnitude of the Optimized Substrate Uptake Rate Also in the Presence of S_{in}

We next addressed the question, if the binding order of substrate and co-substrate determined the cycle rate of a transporter challenged with high concentrations of intracellular substrate. Optimization runs were carried out with $S_{out} = 30$ μM and $S_{in} = 1$ mM for all five schemes (*cf.* **Figures 1A, 2A**). It is evident from **Figure 4A** that these schemes differed in the magnitude of the optimized substrate uptake rates, which they were able to support. The rank order was NaSSNa < NaSNaS < SNaSNa < SNaNaS = random. This rank order differed from that observed in the absence of S_{in} (*cf.* **Figure 2F**). At constant $S_{out} = 30$ μM, we also varied the internal substrate concentration by lowering to S_{in} 100 μM and raising it to the point, where net uptake rat was zero (**Figure 4B**). For all schemes we found an optimized substrate uptake rate of zero when S_{in} was 6.75 mM. This was to be expected because at the chosen concentrations of Na^+ (i.e., 150 mM Na^+_{out} and 10 mM Na^+_{in}) the concentrative power (S_{in}/S_{out}) of the transporter is 225. This numerical value is identical for all schemes, because they are governed by the same transport stoichiometry. Accordingly, the transporters cannot further cycle productively in a forward direction, when S_{in} becomes 225 times larger than S_{out} (30 μM * 225 = 6.75 mM). For all schemes, we extracted the K_D of substrate binding to the inward-facing conformation of the transporters optimized at varying S_{in} (**Figure 4C**). In all instances, this K_D increased with increasing S_{in}. However, the magnitude of the drop in affinity depended on the reaction scheme.

For several secondary active transporters, binding of substrate and co-substrate was shown to occur in a cooperative manner: The apparent substrate affinity for the transporter depended on the concentration of the co-substrate (Meinild and Forster, 2012; Perez et al., 2014; Hasenhuetl et al., 2018; Erdem et al., 2019). It was low and high when the concentration of the co-substrate was low and high, respectively. Thus, the substrate can bind with higher affinity to transporters, when they are bound to the co-substrate (e.g., Na^+). In this way, the concentration of the co-substrate determines the abundance of high and low affinity states for the substrate. Under physiological conditions, the co-substrate concentration is lower on the intracellular than on the extracellular side. Accordingly, cooperative binding is predicted to promote the forward cycling mode by reducing the substrate affinity to the inward-facing conformation. In fact, the drop in intracellular affinity resulting from cooperative binding is a requirement for maintaining a large substrate uptake rate at high S_{in} (Erdem et al., 2019). Notably, cooperative binding is contingent on a random binding order for substrate and co-substrate. For this reason cooperative binding can only be assessed in the random binding order scheme. Based on this consideration, a rise in S_{in} is predicted to increase the extent of cooperativity. We verified this prediction in optimization runs and extracted the cooperativity for transporters optimized at 30 μM S_{out} and 0 mM S_{in} or 1 mM S_{in} by calculating the ratio K_DS_{in} in the absence of bound Na^+/K_DSi_n in the presence of bound Na^+. It is evident from **Figure 4D** that there is a large range of optimized solutions, but on average cooperativity was more pronounced at higher S_{in}.

Substrate Selectivity Increases the Substrate Uptake Rate

Evolution also optimized SLCs for substrate specificity. Selective transporters presumably arose from unselective ancestors. As a starting point, we posited that an unselective SLC must display low affinity for the various substrates: It is difficult to envisage a substrate binding site, which can provide strong bonding interactions to accommodate many distinct molecular scaffolds. We also assumed that, in the evolutionary trajectory from an unselective to a specific transporter, an increase in substrate specificity ought to translate in higher uptake rates for the substrate. Accordingly, in the optimization, we modeled an unselective solute carrier as a transporter, which had a low (true) affinity (i.e., a high K_D) for substrate by implementing a constraint, which prevented the substrate K_D from dropping below a user-defined arbitrary value (e.g., 10 mM). With this constraint in place, the optimization algorithm only returned sets of values for the microscopic rate constants, which defined transporters with a high K_D for substrate. In the subsequent description, we refer to such sets as unselective transporters. In contrast, sets generated in optimization runs, in which the K_D for substrate was not constrained, are referred to as selective transporters. For the optimizations summarized in **Figure 5**, we employed the random binding order scheme, we assumed zero-trans conditions and the presence of 1 μM S_{out}. **Figure 5A** shows the

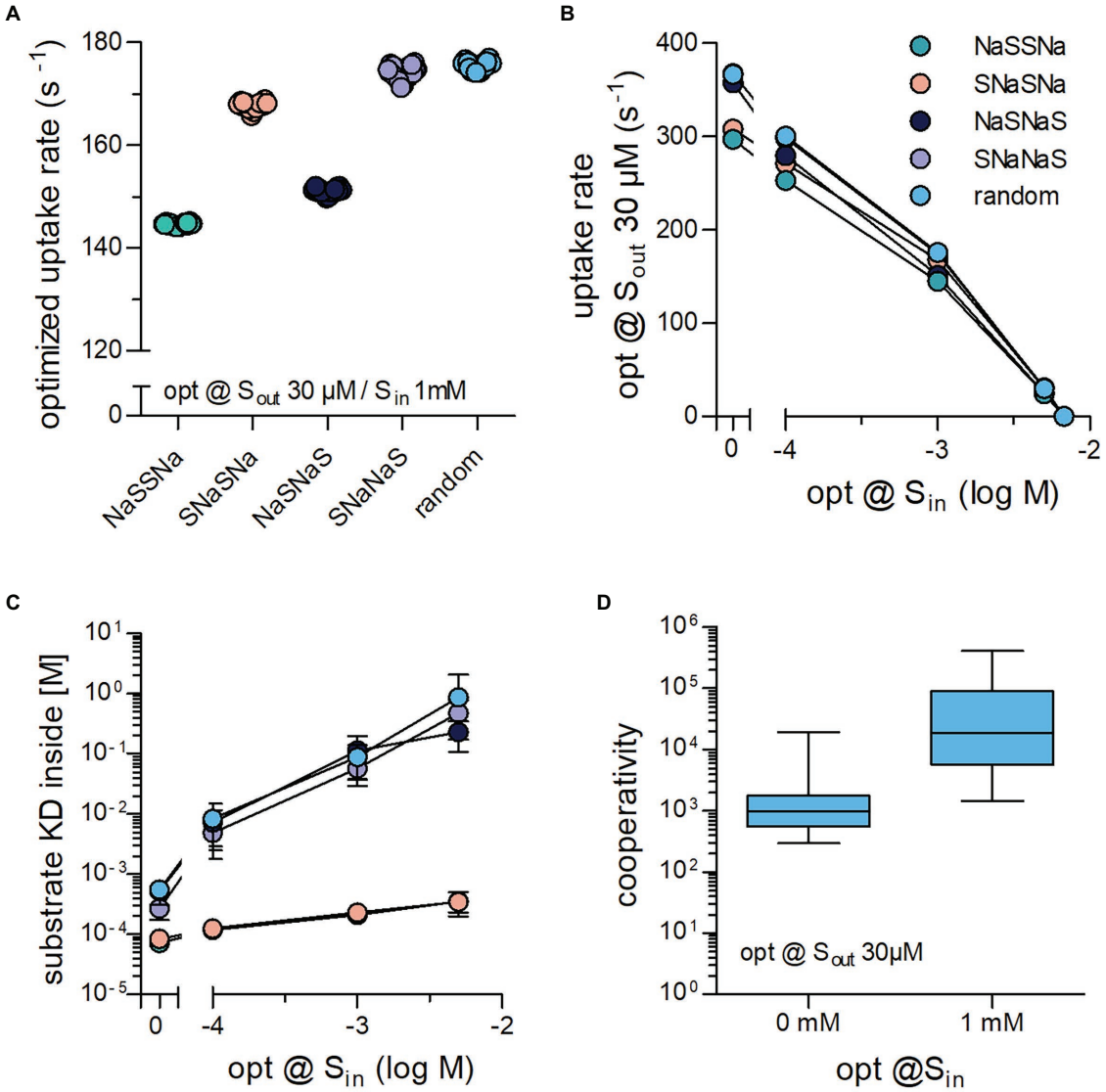

FIGURE 4 | Binding order of co-substrate and substrate affects the optimized substrate uptake rate, when S_{in} is high. **(A)** Shown are the substrate uptake rates for transporters, which operate according to the reaction schemes illustrated in **Figures 1A, 2A–D** and which were optimized for 30 µM S_{out} and 1 mM S_{in}. The optimized substrate uptake rate differed between reaction schemes. The data are the rates obtained from 20 optimization runs. **(B)** Plotted are the substrate uptake rates for all reaction schemes optimized for 0 mM, .1 mM, 1 mM, 5 mM, and 6.75 mM S_{in}, respectively. The data are means ± SD of the substrate uptake rates obtained from 20 optimization runs. At 6.75 mM S_{in}, the substrate uptake rate was zero for all reaction schemes. This is due to the fact that the concentrative power is defined by the transport stoichiometry (Na^+: substrate = 2:1) and the Na^+ gradient rather than the reaction scheme: With a gradient of 150 mM external to 10 mM internal Na^+, the concentrative power of the transporters is 225, which yields 6.75 mM S_i at 30 µM S_{out} **(C)** Shown are K_D values for the substrate binding to the inward-facing conformation for all reaction schemes of transporters optimized to 0 mM, .1 mM, 1 mM, and 5 mM S_{in}, respectively. While the absolute values of this K_D differed between schemes, they all rose with increasing S_{in}. **(D)** The random binding order scheme, allows for Na^+ and substrate to bind in a cooperative manner: The affinity for substrate is high when Na^+ is bound and low in its absence. Cooperativity was defined as the ratio of the K_D of substrate binding to the inward-facing conformation in the absence and presence of Na^+. Transporters optimized for 1 mM S_{in} displayed larger cooperativity values than those optimized for 0 mM S_{in} ($p < .0001$; Wilcoxon signed rank test).

result for 20 selective and unselective transporters ($K_D \geq 10$ mM): It is evident that the optimized substrate uptake rat of the unselective transporters (magenta symbols, **Figure 5A**) was lower by about three orders of magnitude than that of the selective SLCs (green symbols, **Figure 5A**). In **Figure 5B**, we examined the Michaelis–Menten kinetics of the substrate uptake rate of these optimized transporters. **Figure 5C** shows the same data normalized to V_{max} to illustrate the distribution of K_M. The V_{max} values of the unselective transporters were lower than those of the selective SLCs but they varied over about orders of magnitude (**Figure 5D**). Similarly, the K_M values of the unselective transporters, which were consistently higher than those of the selective SLCs, were again highly variable. In **Figure 5E**, we show optimized rates as a function of the concentration of substrate, for which the rates were optimized. Displayed in this plot are the data for selective transporters (unconstrained substrate K_D) and unselective

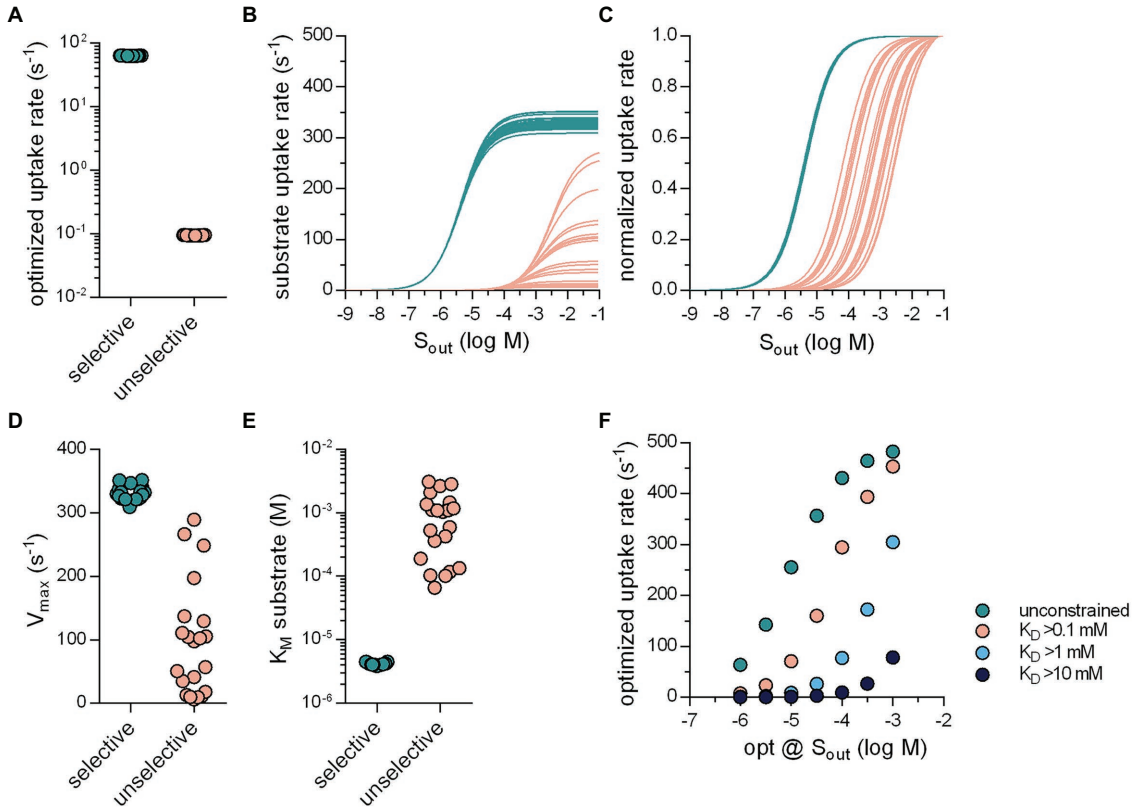

FIGURE 5 | Selective transporters can support larger substrate uptake rates. **(A)** Optimized substrate uptake rates for selective (green circles; 63.79 ± .19 s^{-1}; $n = 20$) and unselective transporters (pink circles; .095 ± .0006 s^{-1}; $n = 20$). The transporters were optimized for 1 μM S_{out}. The substrate K_D of the unselective transporters was not allowed to drop below 10 mM. For the optimizations we used the random binding order scheme. **(B)** Substrate uptake rate as a function of S_{out} for the selective (green lines) and the unselective transporters (pink lines). **(C)** The same data as in **(B)** but normalized **(D)** V_{max} values of selective and unselective transporters. The coefficient of variation of the V_{max} values was .034 and .91 for selective and unselective transporters, respectively **(E)** K_M values of selective and unselective transporters. The coefficient of variation of the K_M values was .042 and .90 for the selective and unselective transporters, respectively. **(F)** The substrate uptake rate as a function of the concentrations of S_{out} for which these rates were optimized. The green circles are the optimized rates of the selective transporters. The circles in pink, light blue, and dark blue are the optimized rates of unselective transporters, for which the substrate K_D was not allowed to drop below .1 mM, 1 mM, and 10 mM, respectively ($n = 10$ for each S_{out}). The optimized rates of the unselective transporters were lower than that of the selective ones.

transporters (constrained at $K_D > .1$ mM, 1 mM, and 10 mM). It is evident that at the various [S_{out}] tested the selective transporters had larger substrate uptake rates than the unselective ones.

These results confirm that SLCs can raise their transport capacity by becoming more specific for their cognate substrates. We, therefore, consider it plausible that specific SLCs arose from ancestors, which were unselective and that this transformation was driven by the need to support high substrate uptake rates. Conversely, there are transporters, which are under evolutionary pressure to remain unselective, because they support the disposition of xenobiotics. This is exemplified by members of the SLC22 family, which recognize diverse substrates to mediate disposition of drugs and xenobiotics: Both organic cation (OCT1-3/SLC22A1-3) and anion transporters (OAT1-3/SLC22A6-8) translocate most of their substrates with K_M values in the high μM range (VanWert et al., 2010; Motohashi and Inui, 2013). This is despite the fact that, in most instances, they are faced with substrate concentrations in the low micromolar range. However, we find this in good agreement with our results, which showed that the unselective transporters that we optimized for 1 μM S_{out}, displayed K_{Ms} in the submillimolar range (see **Figure 5E**). It is worth noting that the SLC22 family also encompasses members, which have a narrow substrate specificity; these have K_M value in the low micromolar range.

DISCUSSION

Solute carriers have a long evolutionary history: More than 50% of SLC subfamilies, which are present in the human genome, are also found in prokaryotes (Hoglund et al., 2011). Eukaryotic transporters have longer N- and C-termini than bacterial transporters. This presumably reflects evolutionary adaptation to the increase in complexity: The N- and C-termini harbor site for posttranslational modifications (e.g., phosphorylation by protein kinases) and docking sites for the protein machinery required for trafficking between cellular compartments (Chiba et al., 2014). The evolutionary history also suggests that individual SLC subfamilies expanded and contracted during phylogenesis (Caveney et al., 2006;

Denecke et al., 2020). Expansion was not only driven by the adaptation to new substrates but also by the requirements to optimize concentrative power and uptake rate: Phosphate transporters of the SLC34 subfamily differ in their concentrative power and in their electrogenicity (Forster et al., 2013). Similarly, the three closely related monoamine transporters provide different solution to the trade-off between harvesting the membrane potential and maintaining constant uptake at variable voltage (Bhat et al., 2021). Here, we explored how the concentration of substrate, which a solute carrier encounters on both, the extra- and intracellular side can exert evolutionary pressure on the operating mode of a transporter. Our approach relied on analytical expressions for descriptors of transporter function (i.e., K_M and V_{max} of substrate transport) as a function of the microscopic rate constants, which parameterize the kinetic models of SLC. Arguably, the outcome of evolutionary adaptation must maximize substrate uptake rate at the prevailing conditions. Accordingly, our optimization algorithm searched for the microscopic rate constants, which yielded the largest possible value for the substrate uptake rate. The pertinent insights can be summarized as follows: (i) low extracellular substrate concentrations select for transporters, which have low K_M and V_{max}. Only this combination allows for a high rate in the transport cycle, but there is a surprisingly broad range of microscopic rate constants, which support this solution. (ii) In contrast, a transporter operating at high extracellular substrate concentrations has a substantially more restricted parameter space and maintains a high uptake rate only if it has a high K_M and a high V_{max} for substrate. (iii) Random order of substrate and co-substrate binding is superior to all possible sequential orders, if a transporter is to maintain a high rate of substrate uptake in the presence of accumulating intracellular substrate, because it allows for cooperative binding.

Solute carriers have long been known to fall into two categories, that is, high-affinity–low-capacity transporters and low affinity–high capacity transporters. It is important to note, however, that there is not any relation between the K_M value and the V_{max} value, which *a priori* dictates that these two parameters must move in the same direction. We examined the relation between turnover rates and K_M in the SLC6 family, because turnover rates have been determined with high precision by electrophysiological recordings (Bicho and Grewer, 2005; Erdem et al., 2019; Bhat et al., 2021; Shi et al., 2021) and the individual steps of the transport cycle have been analyzed in detail. In addition, the K_M values for cognate substrate span more than two orders of magnitude. It is evident from **Figure 6A** that there is a good correlation ($r^2 = .915$) between turnover rate and K_M. Similarly, the monoamine transporter of the earthworm *Lumbricus terrestris* can translocate several substrates albeit with substantial differences in V_{max} and K_M: The K_M for norepinephrine is 20-fold higher than for tyramine (Caveney et al., 2006). Again, there is a remarkable correlation ($r^2 = .981$) between uptake velocity and K_M (**Figure 6B**). It is, therefore, safe to conclude that the existing dichotomy—in the real world and in our data sets—is a consequence of the optimization of the substrate uptake rates.

Similarly, our optimization algorithm required boundary conditions to identify realistic maxima. **Table 2** provides a compilation of substrate turnover rates reported for a collection of SLC. The list includes carriers, which cycle at a rate of $3\,s^{-1}$ as well as such that cycle at a rate of about $700\,s^{-1}$. These rates are reasonably close to those, which the optimization algorithm returned, that is, about $500\,s^{-1}$ and $4\,s^{-1}$ for S_{out} 100 µM and .1 µM, respectively. This confirms that the constraints, which we imposed in the optimization, were realistic. Importantly, our analysis establishes a relation between the turnover rate

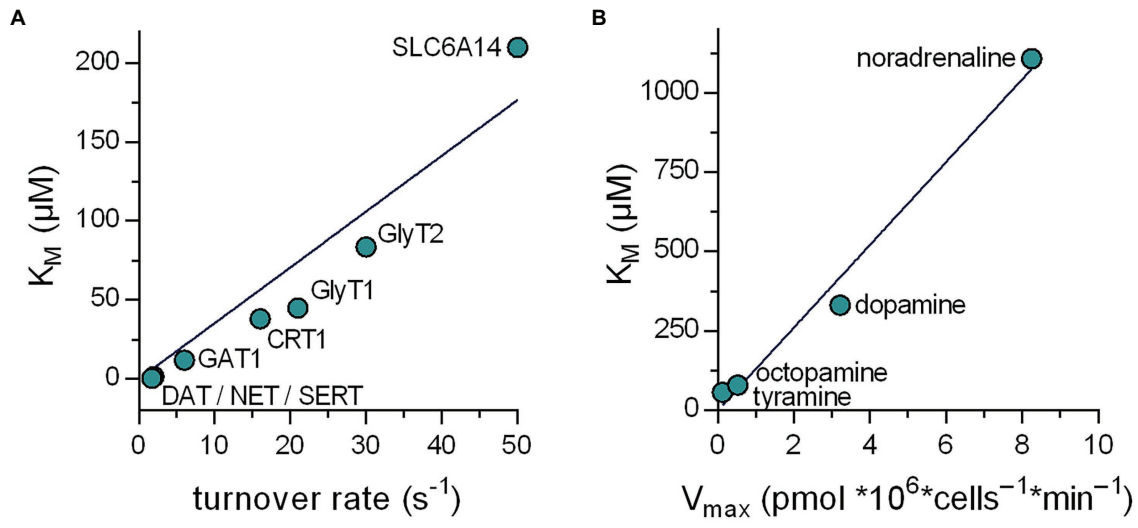

FIGURE 6 | Relation between the K_M and the substrate turnover rate of transporters in the SLC6 family. **(A)** Plotted are data obtained from literature of eight members of the SLC6 family. The line in the graph is a linear fit to the data points ($r^2 = .915$). It is evident that in the real world a positive correlation exists between the K_M and the turnover rate. **(B)** Relation between K_M and V_{max} for the various substrates of the *Lumbricus terrestris* monoamine transporter. The data were taken from Caveney et al. (2006). The line in the graph is a linear fit to the data points ($r^2 = .981$).

TABLE 2 | Substrate turnover rates of transporters from various species.

Transporter	Species	Turnover (s^{-1})	Reference	BNID
Lactose permease (LacY)	*Escherichia coli*	40–60	Wright and Overath, 1984	103159
		21	Smirnova et al., 2011	112482
High-affinity glucose transporter 2 HXT2	*Saccharomyces cerevisiae*	53	Kruckeberg et al., 1999	101739
High-affinity hexose transporter 7 HXT7	*Saccharomyces cerevisiae*	197	Ye et al., 2001	101737
Histidine permease	*Salmonella typhimurium*	2	Nikaido et al., 1997	109030
Na(+)/H(+) exchanger 1 (NHE1)	Chinese hamster	80.3 (22°C)	Cavet et al., 1999	105479
		742 (37°C)		
Na(+)/H(+) exchanger 2 (NHE2)	Chinese hamster	92.1 (22°C)	Cavet et al., 1999	105479
		459 (37°C)		
Na(+)/H(+) exchanger 3 (NHE3)	Chinese hamster	99.2 (22°C)	Cavet et al., 1999	105479
		609 (37°C)		

Values were obtained by searching the BioNumbers database (Milo et al., 2010). The respective entries can be accessed via the given BioNumbers ID (BNID).

of the transporter and the substrate concentration for which it was optimized. Thus, the substrate turnover rate allows for inferring the concentration range, in which a candidate solute carrier operates under physiological conditions.

We subjected transporters to a selection by optimization at low substrate concentration but at high concentrations of Na^+ co-substrate Nevertheless, some of the solutions produced hypothetical transporters, which were optimized to operate at very low Na^+ concentrations (*cf.* **Figures 1G,H**). While these are obviously of little benefit to a multicellular organism with homeostatic control of extracellular ion composition, these transporters are optimally adapted to support nutrient uptake of a unicellular organism invading ecological niches with low ambient salt concentrations. Bacterial transport is thought to rely mainly on the proton motive force. However, there are several examples of bacterial Na^+-dependent symporters (Wilson and Ding, 2001). In addition, our analysis showed that K_M values for substrate and co-substrate differed substantially from the K_D values for their binding to the outward-facing conformation (*cf.* **Figures 1F,I**). This highlights the fact that experimentally determined K_M values for substrate and co-substrate are not necessarily adequate measures of true affinity (i.e., k_{off}/k_{on}). Transporters are forced to adjust ratios of binding and unbinding reactions, which keep the optimum K_D values in a narrow range at both, low and high substrate concentrations. In contrast, the initiation of the transport cycle is limited by the apparent on rates of substrate and the co-substrate ion(s). It is worth noting that all solutions resulted in transporters, which bound substrate at a rate close to the diffusion-imposed limit (*cf.* **Table 1**). As a consequence, this allows for the emergence of high-affinity/low-capacity SLC, which translocate substrate effectively at very low co-substrate concentrations, because large variations in k_{on} for Na^+ are tolerated.

Substrate accumulation on the intracellular side also exerts a selective pressure. It is low, if the transporter operates in a relay with another transporter, which sequesters the substrate, or with an enzyme, which modifies the substrate: The monoamine transporters for dopamine (DAT/SLC6A3), norepinephrine (NET/SLC6A2), and (SERT/SLC6A4) need not cope with rising intracellular level of their cognate substrate because of the action of vesicular monoamine transporters (vMAT1/SLC18A1 & vMAT2/SLC18A2) which shuffle cytosolic monoamines into vesicles (Hou and Matherly, 2014; Sitte and Freissmuth, 2015). Similarly, the reduced folate carrier (RFC/SLC19A1) and the proton-coupled folate transporter (PCFT/SLC46A4) are unlikely to face inhibition by accumulation of intracellular folate, because it is converted to polyglutamylated folate by folylpolyglutamate synthase (Raz et al., 2016). In fact, it has been argued that, in several instances, transporters and metabolizing enzymes are spatially organized to promote sustained influx of substrate: Direct or indirect tethering of enzymes to SLCs creates membrane transport metabolons, which effectively lower $[S_{in}]$ to preclude inhibition on the intracellular side (Moraes and Reithmeier, 2012). In contrast, the creatine transporter-1 (CrT-1/SLC6A8) must maintain the forward transporter mode, although intracellular concentrations are in the range of 5–7 mM (Wyss and Kaddurah-Daouk, 2000). Our analysis allows for understanding how the adaptation to high intracellular substrate is achieved. It is obvious that the transporter can only progress in the forward cycle mode, if the inward-facing conformation of the transporter has a low affinity for the substrate, because a low affinity precludes rebinding of the substrate. However, to afford a lower substrate affinity to the inward-facing conformation, the K_M for substrate must increase and, as a corollary, the true affinities of the substrate and the Na^+ ions for the outward-facing must decrease. In this context, it is worth mentioning that the three monoamine transporter (NET/SLC6A2, DAT/SLC6A3, and SERT/SLC6A4) display high K_M for substrate and Na^+, that is, in the low micromolar and millimolar range, respectively, (Bulling et al., 2012; Li et al., 2017; Bhat et al., 2021). In contrast, the glycine transporter-1 (GlyT1/SLC6A9) and CrT1/SLC6A8 feature about 3–20-fold lower apparent affinities for their cognate substrate and co-substrate Na^+ (Boehm et al., 2003; Erdem et al., 2019). This is consistent with the fact that these transporters support influx of their cognate substrates in the presence of millimolar concentrations of S_{in}, while the monoamine transporters do not. Thus, the solutions, which were explored by our optimization algorithm, reflect parameter space visited during the evolutionary adaptation of transporters.

Our study has several limitations: (i) We restricted our analysis to sodium symporters with a 2 Na^+ and 1 substrate stoichiometry. It is evident, however, that the approach can be extended to any other stoichiometry of symport. Our approach is also applicable to antiporters although incorporating the k_{on} and k_{off} of the counter-transported solute substantially increases the parameter space and thus the computational effort. (ii) We did not examine the impact of allosteric regulation, which is a major computational challenge. It is clear, however, that evolution also selected for transporters for allostery: DAT/SLC6A3, for instance, harbors an allosteric Zn^{2+} binding site, while its next

relatives NET/SLC6A2 and SERT/SLC6A4 do not (Li et al., 2017). (iii) While modeling the evolutionary trajectory to substrate specificity, we assumed that an ancestral unselective transporter gave rise to a specific transporter. This need not be the case. In fact, two rounds of genome duplication events are thought to have occurred after the split of vertebrates from cephalochordates (Wolfe, 2001; Simakov et al., 2020). Duplicated transporters have two possible evolutionary fates: They can be subject to inactivating mutations and lost. Alternatively, they can accumulate mutations, which initially relax their substrate specificity and eventually evolve by further mutations into transporters with novel substrate specificity. We also did not explore the structural basis for evolution in substrate affinity. It is worth noting that solute carries can achieve the substrate translocation step by three different mechanisms, that is, based on a rocker switch, a rocking bundle and a sliding elevator (Diallinas, 2021). In transporters, which operate *via* a sliding elevator mechanism, the substrate binding site must reside in the elevator, which moves along the scaffold domain in a direction perpendicular to the membrane plane and thus translocates the substrate. Surprisingly, in the uric acid-xanthine permease *UapA* of *Aspergillus nidulans,* which operates *via* a sliding elevator mechanism, selectivity can be relaxed by several mutations, which are in the scaffold domain and thus outside of the binding site proper (Diallinas, 2021). Two non-mutually exclusive interpretations have been provided for the effect of the mutations: They may eliminate a selectivity filter, which restricts access to the binding site (Vlanti et al., 2006), and/or they may relax a brake and thus facilitate triggering of the elevator movement (Diallinas, 2021). In transporters, which operate by a rocker switch or a rocking bundle mechanism, the binding site is more deeply buried in the hydrophobic core of the protein than in those operating as sliding elevators. Accordingly, it is readily conceivable that restrictions can be imposed on access to the binding site. In fact, the selective binding to the closely related DAT/SLC6A3 and SERT/SLC6A4 is determined by the association rate constant rather than the dissociation rate constant (Hasenhuetl et al., 2015); access to the binding site is limited—at least in part—by the extracellular loops (Esendir et al., 2021). Exchanging the N-terminus of DAT/SLC6A3 with that of SERT/SLC6A4 reduces the K_M of the resulting chimaera for dopamine (Sweeney et al., 2017). Taken together, these observations suggest that changes in transporter selectivity and uptake rates can be brought about by mutations of many residues, which are not necessarily confined to the substrate binding site. During evolution the sequential impact of mutations is likely to change microscopic rate constants along trajectories as diverse as explored by our computational optimization. A long-term challenge is to delineate such an evolutionary path through the landscape of possible microscopic rate constants by sequential mutagenesis. This should be gratifying, because it is expected shed light on the evolutionary history underlying transporter diversity.

DATA AVAILABILITY STATEMENT

The original contributions presented in the study are included in the article/**Supplementary Material**, further inquiries can be directed to the corresponding author.

AUTHOR CONTRIBUTIONS

KS, MF, and WS conceptualized and wrote the manuscript. KS scripted the optimization algorithm. CF, DB, KS, and WS analyzed the data. All authors contributed to the article and approved the submitted version.

FUNDING

This work was funded by a grant from the Austrian Science Fund/FWF (P31813 to WS) and the Vienna Science and Technology Fund/WWTF (LSC17-026 to MF).

SUPPLEMENTARY MATERIAL

The Supplementary Material for this article can be found online at: https://www.frontiersin.org/articles/10.3389/fphys.2022.817886/full#supplementary-material

REFERENCES

Bar-Even, A., Noor, E., Savir, Y., Liebermeister, W., Davidi, D., Tawfik, D. S., et al. (2011). The moderately efficient enzyme: evolutionary and physicochemical trends shaping enzyme parameters. *Biochemistry* 50, 4402–4410. doi: 10.1021/bi2002289

Bhat, S., El-Kasaby, A., Freissmuth, M., and Sucic, S. (2021). Functional and biochemical consequences of disease variants in neurotransmitter transporters: a special emphasis on folding and trafficking deficits. *Pharmacol. Ther.* 222:107785. doi: 10.1016/j.pharmthera.2020.107785

Bicho, A., and Grewer, C. (2005). Rapid substrate-induced charge movements of the GABA transporter GAT1. *Biophys. J.* 89, 211–231. doi: 10.1529/biophysj.105.061002

Boehm, E., Chan, S., Monfared, M., Wallimann, T., Clarke, K., and Neubauer, S. (2003). Creatine transporter activity and content in the rat heart supplemented by and depleted of creatine. *Am. J. Physiol. Endocrinol. Metab.* 284, E399–E406. doi: 10.1152/ajpendo.00259.2002

Bulling, S., Schicker, K., Zhang, Y.-W., Steinkellner, T., Stockner, T., Gruber, C., et al. (2012). The mechanistic basis for non-competitive ibogaine inhibition of serotonin and dopamine transporters. *J. Biol. Chem.* 87, 18524–18534. doi: 10.1074/jbc.M112.343681

Burtscher, V., Schicker, K., Freissmuth, M., and Sandtner, W. (2019). Kinetic models of secondary active transporters. *Int. J. Mol. Sci.* 20:5365. doi: 10.3390/ijms20215365

Caveney, S., Cladman, W., Verellen, L., and Donly, C. (2006). Ancestry of neuronal monoamine transporters in the Metazoa. *J. Exp. Biol.* 209, 4858–4868. doi: 10.1242/jeb.02607

Cavet, M. E., Akhter, S., de Medina, F. S., Donowitz, M., and Tse, C. M. (1999). Na(+)/H(+) exchangers (NHE1-3) have similar turnover numbers but different percentages on the cell surface. *Am. J. Physiol.* 277, C1111–21. doi: 10.1152/ajpcell.1999.277.6.C1111

Chiba, P., Freissmuth, M., and Stockner, T. (2014). Defining the blanks – pharmacochaperoning of SLC6 transporters and ABC transporters. *Pharmacol. Res.* 83, 63–73. doi: 10.1016/j.phrs.2013.11.009

Denecke, S. M., Driva, O., Luong, H. N. B., Ioannidis, P., Linka, M., Nauen, R., et al. (2020). The identification and evolutionary trends of the solute carrier superfamily in arthropods. *Genome Biol. Evol.* 12, 1429–1439. doi: 10.1093/gbe/evaa153

Diallinas, G. (2021). Transporter specificity: a tale of loosened elevator-sliding. *Trends Biochem. Sci.* 46, 708–717. doi: 10.1016/j.tibs.2021.03.007

Erdem, F. A., Ilic, M., Koppensteiner, P., Gołacki, J., Lubec, G., Freissmuth, M., et al. (2019). A comparison of the transport kinetics of glycine transporter 1 and glycine transporter 2. *J. Gen. Physiol.* 151, 1035–1050. doi: 10.1085/jgp.201912318

Esendir, E., Burtscher, V., Coleman, J. A., Zhu, R., Gouaux, E., Freissmuth, M., et al. (2021). Extracellular loops of the serotonin transporter act as a selectivity filter for drug binding. *J. Biol. Chem.* 297:100863. doi: 10.1016/j.jbc.2021.100863

Forster, I. C., Hernando, N., Biber, J., and Murer, H. (2013). Phosphate transporters of the SLC20 and SLC34 families. *Mol. Asp. Med.* 34, 386–395. doi: 10.1016/j.mam.2012.07.007

Hasenhuetl, P. S., Bhat, S., Mayer, F. P., Sitte, H. H., Freissmuth, M., and Sandtner, W. (2018). A kinetic account for amphetamine-induced monoamine release. *J. Gen. Physiol.* 150, 431–451. doi: 10.1085/jgp.201711915

Hasenhuetl, P. S., Schicker, K., Koenig, X., Li, Y., Sarker, S., Stockner, T., et al. (2015). Ligand selectivity among the dopamine and serotonin transporters specified by the forward binding reaction. *Mol. Pharmacol.* 88, 12–18. doi: 10.1124/mol.115.099036

Hediger, M. A., Romero, M. F., Peng, J.-B., Rolfs, A., Takanaga, H., and Bruford, E. A. (2004). The ABCs of solute carriers: physiological, pathological and therapeutic implications of human membrane transport proteins. *Pflugers Arch. Eur. J. Physiol.* 447, 465–468. doi: 10.1007/s00424-003-1192-y

Hoglund, P. J., Nordstrom, K. J. V., Schioth, H. B., and Fredriksson, R. (2011). The solute carrier families have a remarkably long evolutionary history with the majority of the human families present before divergence of Bilaterian species. *Mol. Biol. Evol.* 28, 1531–1541. doi: 10.1093/molbev/msq350

Hou, Z., and Matherly, L. H. (2014). Biology of the major facilitative folate transporters SLC19A1 and SLC46A1. *Curr. Top. Membr.* 73, 175–204. doi: 10.1016/B978-0-12-800223-0.00004-9

Jardetzky, O. (1966). Simple allosteric model for membrane pumps. *Nature* 211, 969–970. doi: 10.1038/211969a0

Jennigs, M. L. (2018). Carriers, exchangers, and cotransporters in the first 100 years of the journal of general physiology. *J. Gen. Physiol.* 150, 1063–1080. doi: 10.1085/jgp.201812078

Kruckeberg, A. L., Ye, L., Berden, J. A., and van Dam, K. (1999). Functional expression, quantification and cellular localization of the Hxt2 hexose transporter of Saccharomyces cerevisiae tagged with the green fluorescent protein. *Biochem. J.* 339, 299–307.

Li, Y., Mayer, F. P., Hasenhuetl, P. S., Burtscher, V., Schicker, K., Sitte, H. H., et al. (2017). Occupancy of the zinc-binding site by transition metals decreases the substrate affinity of the human dopamine transporter by an allosteric mechanism. *J. Biol. Chem.* 292, 4235–4243. doi: 10.1074/jbc.M116.760140

Meinild, A.-K., and Forster, I. C. (2012). Using lithium to probe sequential cation interactions with GAT1. *Am. J. Physiol. Cell Physiol.* 302, C1661–C1675. doi: 10.1152/ajpcell.00446.2011

Metropolis, N., Rosenbluth, A. W., Rosenbluth, M. N., Teller, A. H., and Teller, E. (1953). Equation of state calculations by fast computing machines. *J. Chem. Phys.* 21, 1087–1092. doi: 10.1063/1.1699114

Millward, D. J., and Garlick, P. J. (1976). The energy cost of growth. *Proc. Nutr. Soc.* 35, 339–349. doi: 10.1079/PNS19760054

Milo, R., Jorgensen, P., Moran, U., Weber, G., and Springer, M. (2010). BioNumbers--the database of key numbers in molecular and cell biology. *Nucleic Acids Res.* 38, D750–3. doi: 10.1093/nar/gkp889

Mitchell, P. (1979). Compartmentation and communication in living systems. Ligand conduction: a general catalytic principle in chemical, osmotic and chemiosmotic reaction systems. *Eur. J. Biochem.* 95, 1–20. doi: 10.1111/j.1432-1033.1979.tb12934.x

Moraes, T. F., and Reithmeier, R. A. (2012). Membrane transport metabolons. *Biochim. Biophys. Acta* 1818, 2687–2706. doi: 10.1016/j.bbamem.2012.06.007

Motohashi, H., and Inui, K. (2013). Organic cation transporter OCTs (SLC22) and MATEs (SLC47) in the human kidney. *AAPS J.* 15, 581–588. doi: 10.1208/s12248-013-9465-7

Nikaido, K., Liu, P. Q., and Ames, G. F. (1997). Purification and characterization of HisP, the ATP-binding subunit of a traffic ATPase (ABC transporter), the histidine permease of *Salmonella typhimurium*. Solubility, dimerization, and ATPase activity. *J. Biol. Chem.* 272, 27745–52. doi: 10.1074/jbc.272.44.27745

Omote, H., Hiasa, M., Matsumoto, T., Otsuka, M., and Moriyama, Y. (2006). The MATE proteins as fundamental transporters of metabolic and xenobiotic organic cations. *Trends Pharmacol. Sci.* 27, 587–593. doi: 10.1016/j.tips.2006.09.001

Perez, C., Faust, B., Mehdipour, A. R., Francesconi, K. A., Forrest, L. R., and Ziegler, C. (2014). Substrate-bound outward-open state of the betaine transporter BetP provides insights into Na^+ coupling. *Nat. Commun.* 5:4231. doi: 10.1038/ncomms5231

Raz, S., Stark, M., and Assaraf, Y. G. (2016). Folylpoly-γ-glutamate synthetase: a key determinant of folate homeostasisand antifolate resistance in cancer. *Drug Resist. Updat.* 28, 43–64. doi: 10.1016/j.drup.2016.06.004

Rudnick, G., and Sandtner, W. (2019). Serotonin transport in the 21st century. *J. Gen. Physiol.* 151, 1248–1264. doi: 10.1085/jgp.201812066

Sano, R., Shinozaki, Y., and Ohta, T. (2020). Sodium–glucose cotransporters: functional properties and pharmaceutical potential. *J. Diabetes Investig.* 11, 770–782. doi: 10.1111/jdi.13255

Schicker, K., Bhat, S., Farr, C., Burtscher, V., Horner, A., Freissmuth, M., et al. (2021). Descriptors of secondary active transporter function and how they relate to partial reactions in the transport cycle. *Membranes* 11:178. doi: 10.3390/membranes11030178

Schicker, K., Uzelac, Z., Gesmonde, J., Bulling, S., Stockner, T., Freissmuth, M., et al. (2011). A unifying concept of serotonin transporter associated currents. *J. Biol. Chem.* 287, 438–445. doi: 10.1074/jbc.M111.304261

Schmidt, H., and Jirstrand, M. (2006). Systems biology toolbox for MATLAB: a computational platform for research in systems biology. *Bioinformatics* 22, 514–515. doi: 10.1093/bioinformatics/bti799

Shi, Y., Wang, J., Ndaru, E., and Grewer, C. (2021). Pre-steady-state kinetic analysis of amino acid transporter SLC6A14 reveals rapid turnover rate and substrate translocation. *Front. Physiol.* 12:777050. doi: 10.3389/fphys.2021.777050

Siems, W., Dubiel, W., Dumdey, R., Müller, M., and Rapoport, S. M. (1984). Accounting for the ATP-consuming processes in rabbit reticulocytes. *Eur. J. Biochem.* 139, 101–107. doi: 10.1111/j.1432-1033.1984.tb07982.x

Simakov, O., Marlétaz, F., Yue, J. X., O'Connell, B., Jenkins, J., Brandt, A., et al. (2020). Deeply conserved synteny resolves early events in vertebrate evolution. *Nat. Ecol. Evol.* 4, 820–830. doi: 10.1038/s41559-020-1156-z

Sitte, H. H., and Freissmuth, M. (2015). Amphetamines, new psychoactive drugs and the monoamine transporter cycle. *Trends Pharmacol. Sci.* 36, 41–50. doi: 10.1016/j.tips.2014.11.006

Smirnova, I., Kasho, V., Sugihara, J., and Kaback, H. R. (2011). Opening the periplasmic cavity in lactose permease is the limiting step for sugar binding. *Natl. Acad. Sci. U. S. A.* 108, 15147–51. doi: 10.1073/pnas.1112157108

Snow, R. J., and Murphy, R. M. (2001). Creatine and the creatine transporter: a review. *Mol. Cell. Biochem.* 224, 169–181. doi: 10.1023/A:1011908606819

Sweeney, C. G., Tremblay, B. P., Stockner, T., Sitte, H. H., and Melikian, H. E. (2017). Dopamine transporter amino and carboxyl termini synergistically contribute to substrate and inhibitor affinities. *J. Biol. Chem.* 292, 1302–1309. doi: 10.1074/jbc.M116.762872

Tsallis, C., and Stariolo, D. A. (1996). Generalized simulated annealing. *Phys. Stat. Mech. Appl.* 233, 395–406. doi: 10.1016/S0378-4371(96)00271-3

VanWert, A. L., Gionfriddo, M. R., and Sweet, D. H. (2010). Organic anion transporters: discovery, pharmacology, regulation and roles in pathophysiology. *Biopharm. Drug Dispos.* 31, 1–71. doi: 10.1002/bdd.693

Vlanti, A., Amillis, S., Koukaki, M., and Diallinas, G. (2006). A novel-type substrate-selectivity filter and ER-exit determinantsin the UapA purine transporter. *J. Mol. Biol.* 357, 808–819. doi: 10.1016/j.jmb.2005.12.070

Waterlow, J. C., Golden, M. H., and Garlick, P. J. (1978). Protein turnover in man measured with 15N: comparison of end products and dose regimes. *Am. J. Phys.* 235, E165–E174. doi: 10.1152/ajpendo.1978.235.2.E165

Wilson, T. H., and Ding, P. Z. (2001). Sodium-substrate cotransport in bacteria. *Biochim. Biophys. Acta* 1505, 121–130. doi: 10.1016/s0005-2728(00)00282-6

Wolfe, K. H. (2001). Yesterday's polyploids and the mystery of diploidization. *Nat. Rev. Genet.* 2, 333–341. doi: 10.1038/35072009

Wright, E. M., Loo, D. D. F. L., and Hirayama, B. A. (2011). Biology of human sodium glucose transporters. *Physiol. Rev.* 91, 733–794. doi: 10.1152/physrev.00055.2009

Wright, J. K., and Overath, P. (1984). Purification of the lactose:H^+ carrier of *Escherichia coli* and characterization of galactoside binding and transport. *Eur. J. Biochem.* 138, 497–508. doi: 10.1111/j.1432-1033.1984.tb07944.x

Wyss, M., and Kaddurah-Daouk, R. (2000). Creatine and creatinine metabolism. *Physiol. Rev.* 80, 1107–1213. doi: 10.1152/physrev.2000.80.3.1107

Yaffe, D., Forrest, L. R., and Schuldiner, S. (2018). The ins and outs of vesicular monoamine transporters. *J. Gen. Physiol.* 150, 671–682. doi: 10.1085/jgp.201711980

Ye, L., Berden, J. A., van Dam, K., and Kruckeberg, A. L. (2001). Expression and activity of the Hxt7 high-affinity hexose transporter of *Saccharomyces cerevisiae*. *Yeast* 18, 1257–67. doi: 10.1002/yea.771

Zhang, Z., Tao, Z., Gameiro, A., Barcelona, S., Braams, S., Rauen, T., et al. (2007). Transport direction determines the kinetics of substrate transport by the glutamate transporter EAAC1. *Proc. Natl. Acad. Sci. U. S. A.* 104, 18025–18030. doi: 10.1073/pnas.0704570104

Conflict of Interest: The authors declare that the research was conducted in the absence of any commercial or financial relationships that could be construed as a potential conflict of interest.

Publisher's Note: All claims expressed in this article are solely those of the authors and do not necessarily represent those of their affiliated organizations, or those of the publisher, the editors and the reviewers. Any product that may be evaluated in this article, or claim that may be made by its manufacturer, is not guaranteed or endorsed by the publisher.

frontiers | Frontiers in Physiology

ORIGINAL RESEARCH
published: 15 June 2022
doi: 10.3389/fphys.2022.874472

Modeling of SGLT1 in Reconstituted Systems Reveals Apparent Ion-Dependencies of Glucose Uptake and Strengthens the Notion of Water-Permeable Apo States

*Thomas Barta[1], Walter Sandtner[2], Johann Wachlmayr[1], Christof Hannesschlaeger[1], Andrea Ebert[3], Armin Speletz[1] and Andreas Horner[1]**

[1]Department of Molecular Biophysics and Membrane Biophysics, Institute of Biophysics, Johannes Kepler University Linz, Linz, Austria, [2]Center of Physiology and Pharmacology, Institute of Pharmacology and the Gaston H. Glock Research Laboratories for Exploratory Drug Development, Medical University of Vienna, Vienna, Austria, [3]Department of Analytical Environmental Chemistry, Helmholtz Centre for Environmental Research—UFZ, Leipzig, Germany

OPEN ACCESS

Edited by:
Christof Grewer,
Binghamton University, United States

Reviewed by:
Richard J. Naftalin,
King's College London,
United Kingdom
Alessio Accardi,
Cornell University, United States

***Correspondence:**
Andreas Horner
andreas.horner@jku.at

Specialty section:
This article was submitted to Membrane Physiology and Membrane Biophysics, a section of the journal Frontiers in Physiology

Received: 12 February 2022
Accepted: 10 May 2022
Published: 15 June 2022

Citation:
Barta T, Sandtner W, Wachlmayr J, Hannesschlaeger C, Ebert A, Speletz A and Horner A (2022) Modeling of SGLT1 in Reconstituted Systems Reveals Apparent Ion-Dependencies of Glucose Uptake and Strengthens the Notion of Water-Permeable Apo States. Front. Physiol. 13:874472. doi: 10.3389/fphys.2022.874472

The reconstitution of secondary active transporters into liposomes shed light on their molecular transport mechanism. The latter are either symporters, antiporters or exchangers, which use the energy contained in the electrochemical gradient of ions to fuel concentrative uptake of their cognate substrate. In liposomal preparations, these gradients can be set by the experimenter. However, due to passive diffusion of the ions and solutes through the membrane, the gradients are not stable and little is known on the time course by which they dissipate and how the presence of a transporter affects this process. Gradient dissipation can also generate a transmembrane potential (V_M). Because it is the effective ion gradient, which together with V_M fuels concentrative uptake, knowledge on how these parameters change within the time frame of the conducted experiment is key to understanding experimental outcomes. Here, we addressed this problem by resorting to a modelling approach. To this end, we mathematically modeled the liposome in the assumed presence and absence of the sodium glucose transporter 1 (SGLT1). We show that 1) the model can prevent us from reaching erroneous conclusions on the driving forces of substrate uptake and we 2) demonstrate utility of the model in the assignment of the states of SGLT1, which harbor a water channel.

Keywords: human sodium glucose co-transporter, water-permeable apo states, solute carrier, glucose uptake, lipid vesicles, mathematical modeling, passive membrane permeabilities

1 INTRODUCTION

Solute carriers (SLCs) serve as gatekeepers for vital physiological functions, including cellular uptake of minerals, vitamins, and nutrients as well as removal of metabolites from the interior of cells (Hediger et al., 2004; Omote et al., 2006; Sano et al., 2020). Mutations in the genes encoding SLC proteins are linked to a plethora of diseases, such as amyotrophic lateral sclerosis [prevalence in the United States in 2016; 0.52% (Mehta et al., 2021)], Alzheimer's disease [prevalence in Europe; 5.05% (Niu et al., 2017)], and schizophrenia [prevalence in 46 countries worldwide; 0.46% (Saha et al., 2005)]. Extrapolated to the world population of 2021, these three conditions alone amount to as

many as 470 million annual patients. In addition, SLC's like the sodium glucose transporter 1 (SGLT1) play a pivotal role in metabolism, i.e., glucose uptake. Although SLCs have been studied for many years using biophysical and biochemical approaches as for example electrophysiology and radio-ligand uptake experiments, nevertheless, there is a great deal that we still don't know about their true conformations whilst working against concentration gradients. Hence, there is an urgent need to employ novel approaches so as to gain insight into how SLCs operate.

SLCs undergo long range conformational changes between inward- and outward-open states. As a consequence, the substrate can either bind to the extra- or the intracellular side of the protein but not to both sides simultaneously. For this reason, all SLCs operate within the conceptual framework of the alternating access model (Jardetzky, 1966). Many of them can harvest the energy contained in ion gradients to drive uphill transport of their substrate against an opposing gradient. Others work as exchangers or facilitate passive diffusion of polar solutes. In addition to the ion and substrate gradients, the membrane potential (V_M) also impinges on transporter function. As intimated above, solute carrier function is classically explored by monitoring uptake of radiolabeled substrate into a cell in which the transporter is expressed. However, substrate accumulation can also be measured in an artificial vesicle system relying on radioactivity (Billesbolle et al., 2016) or fluorescence (Erokhova et al., 2016). Whereas the V_M across cellular membranes is largely stable, it is a dynamic variable in artificial vesicle systems. This is because in cells, the ion gradients are maintained by pumps so that they do not dissipate on passive diffusion and transport by SLCs, which is not the case in proteoliposomes. Hence, disregarding V_M in *in vitro* experiments may lead to erroneous conclusion on the driving forces of substrate uptake by SLCs.

Of the SLC group of proteins, SGLT1 is one of the best studied representatives. This transporter is expressed at high levels on the microvilli of the brush border membrane of enterocytes within the alimentary canal (Hwang et al., 1991). In addition to nutrients, the small intestine also absorbs approximately 8 L of fluid daily. Because aquaporines are absent in enterocytes, it was speculated that SGLT1 acts as conduit for water. Primary experimental evidence for the existence of a water channel passing through the transporter came from *in vitro* experiments utilizing reconstituted human SGLT1 and from experiments conducted on this protein while expressed in cell monolayers. Per second, the number of transported water molecules (10^9) exceeded by far the glucose turnover number of SGLT1, which was only in the order of a few hundred molecules (Erokhova et al., 2016). These results led to the postulation that perhaps additional SLCs (Erokhova et al., 2016; Zeuthen et al., 2016) might also be important in the regulation of transcellular water flux. Molecular dynamics (MD) simulations confirmed the passive water transport capability of SGLT1 in its inward-facing state (Li et al., 2013; Adelman et al., 2014). Moreover, a continuous water channel passing within the sugar-binding site was identified in the bacterial homologue vSGLT (Li et al., 2013; Adelman et al., 2014). Extensive simulations carried out on a variety of transporters superfamilies concluded that water-conducting states likely represent a universal phenomenon in membrane transporters, including those belonging to the solute sodium symporter; solute carrier 1; major facilitator superfamily; nucleobase-cationsymport-1; and ATP binding cassette families. It was speculated that this phenomenon is a consequence of transporter reliance on large-scale motions (Li et al., 2013). Experimental results using human SGLT1 (Erokhova et al., 2016; Zeuthen et al., 2016) indicated a shared pathway of water with glucose but not with Na^+. However, it is still unknown which states in the transport cycle are permeable for water and which are not.

In the present study, we built a mathematical model of SGLT1 incorporated into an artificial membrane (i.e., unilamellar vesicles). To model the flux of substrate and co-substrate through the transporter, we utilized a previously published kinetic model of human SGLT1 (Wright et al., 2011). Importantly, our approach also accounted for passive diffusion of ions and solutes through the vesicular membrane. We provided predictions regarding the intraluminal concentrations of the ions and solutes, vesicle volume (through osmotic effects), and the transmembrane potential change on (experimental) perturbation (e.g., challenge with the substrate or osmolytes). Another output of the computation were the state occupancies of SGLT1, which depended on the above-mentioned parameters (e.g., V_M and ion concentrations). We emulated two types of experiments: 1) radio-ligand uptake experiments and 2) stopped flow experiments of the kind that allow for measuring water flux. With these two approaches we demonstrated the utility of our equations in the interpretation of experimental outcomes.

2 RESULTS

2.1 Parameterizing a Virtual Model for a Unilamellar Vesicle

Displayed in **Figure 1** is a schematic representation of our model system (i.e., unilamellar vesicle). This system is comprised of a lipid bilayer, which separates the intra-vesicular space from the surrounding bath solution. In the model, the initial concentrations of the ions and the sugars (i.e., glucose and sucrose) on the opposing sides of the membrane can be set to user-defined values. On start of the simulation, the system equilibrates. Depending on the chosen initial concentrations of the ions and the sugars the following changes can ensue: 1) changes in vesicular volume, if the osmotic concentrations of the intra-and extra-vesicular solutions differ, 2) changes in the concentrations of the intra-vesicular ions and sugars due to passive diffusion of these molecules through the membrane and 3) changes in membrane potential, caused by positive/negative net-charge leaving or entering the vesicle. Indicated in the diagram are the passive fluxes of the ions [i.e., Na^+, K^+, H^+, Cl^-, and $NMDG^+$ (N-Methyl-D-glucamin)], water, and glucose/sucrose. In the model, we parameterized these fluxes, with membrane permeabilities (P_M values) obtained from the literature. In the case of $NMDG^+$ we determined this value

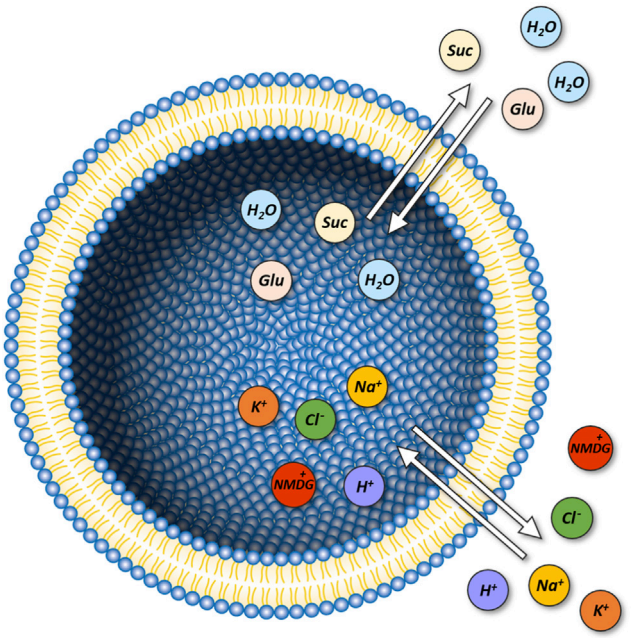

FIGURE 1 | Model of a unilamellar vesicle. Initial *NaCl*, *KCl*, buffer and proton concentrations inside and outside the vesicle can be set to user-defined values. An osmotic solute (e.g., sucrose) can be applied to the extra-vesicular side to simulate water flux experiments utilizing a stopped-flow device. The lipids comprising the membrane are shown with their headgroups in blue and their acyl chains in yellow. The arrows indicate passive permeation of H^+, Na^+, $NMDG^+$, Cl^-, and K^+. In the model we also accounted for passive flux of water (light blue circles), glucose, sucrose and $NMDG_0$ (beige circles).

experimentally (see **Section 4**). For simplicity, we assumed that the extra-vesicular concentrations of all ions and sugars remain constant. This was justified by the fact that in the experiments, which we simulated, the extra-vesicular volume exceeded the combined volume within the vesicles by more than two orders of magnitude. For this reason, depletion of the solutes in the bath solution was considered negligible. A comprehensive description of the model can be found in **Section 4**.

2.2 Passive Ion Permeation Through the Vesicular Membrane can Generate a Membrane Potential (V_M)

Ions differ in their ability to passively permeate through membranes (Hannesschlaeger et al., 2019a). For instance, anions like Cl^- can cross membranes more readily than cations such as Na^+. This is because of the dipole potential, which exists within the membrane and which repels positive charges. If the magnitudes of the passive fluxes of cations and anions differ and if for these ions a transmembrane gradient exists, a net flux of charge through the membrane ensues. The same is true, if the different species of cations and anions, present in the assay, permeate through the membrane with differing velocities due to differences in their ionic radii (e.g., Na^+ versus K^+ or Na^+ versus $NMDG^+$). The resulting net flux of charge gives rise to a change in the membrane potential (V_M). In turn, the electrical field generated by V_M impinges on the flux of the charged particles.

We used our model of the vesicle to better understand how passive ion fluxes through the membrane affect V_M and the intra-vesicular ion concentrations. In the example depicted in **Figure 2** we assumed that the Na^+ and Cl^- concentrations were the same on both sides of the membrane (i.e., 100 mM NaCl). We further assumed the additional presence of 10 mM K^+Cl^- and 10 mM $NMDG^+Cl^-$ on the extra- and intraluminal side, respectively. We stress that in the chosen example, the osmotic concentrations of the inner and outer solution were kept equal. In a first equilibration step we only allowed for passive diffusion of K^+ (grey shaded area in **Figure 2**). In the upper panel of **Figure 2** we show V_M as a function of time for two different reported P_M values of K^+. On equilibration, about 220 K^+ ions entered the lumen of the vesicle, upon which V_M adopted a value of approximately 80 mV. At this V_M the electric force equaled the force exerted by the chemical potential of K^+, which is why the K^+ flux seized. After equilibrium was reached (i.e., 150 h) we let all other ion-species permeate. As seen, this gave rise to anew change in V_M and the intracellular ion concentrations (lower panel of **Figure 2**). However, in contrast

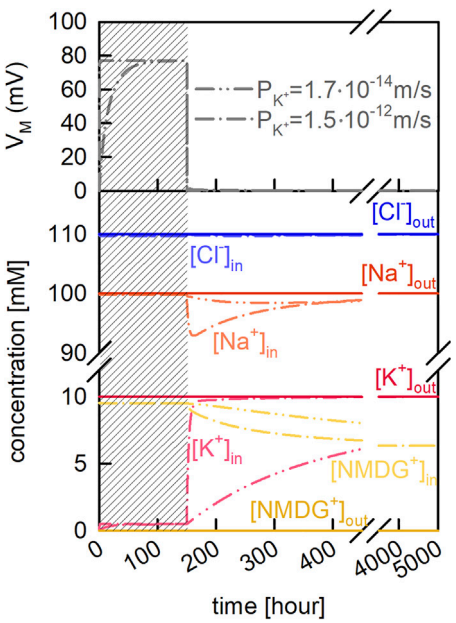

FIGURE 2 | Passive ion permeation through the vesicular membrane. Vesicle assay kinetics simulated with two different P_M values for potassium (taken from **Table 2** of Paula et al. [Paula et al., 1996)]. Dash-dot-dotted lines and dash-dotted lines show simulations in which P_{K^+} was set to $1.7 \cdot 10^{-14} m/s$, and $1.5 \cdot 10^{-12} m/s$, respectively. The initial extraluminal concentrations were 100 mM NaCl, 20 mM HEPES, and 10 mM KCl. The initial intraluminal concentrations were 100 mM NaCl, 20 mM HEPES, and 10 mM $NMDG^+Cl^-$. The pH on both sides of the membrane was 7.5. Upper panel. Time course of the change in membrane potential (V_M). On start of the simulations, K^+ was the only permeable solute (grey shaded area). After 150 h, all other ions (H^+, Na^+, $NMDG^+$, and Cl^-) were allowed to permeate. Lower panel. Evolution of all intra- (bright colors) and extraluminal (dark color) ion concentrations (except for H^+) over time.

to the changes which had ensued when K^+ was the only permeating ion, the changes on permeation of all ions were transient. This was because with all ions permeating their gradients eventually dissipated. This is evident on inspection of **Figure 2**, where we show that the final intra-vesicular ion concentrations matched exactly the concentrations on the extra-vesicular side. In the absence of ion gradients, V_M was zero and no osmotic force was exerted onto the membrane. The transient changes in V_M and the intracellular ion concentrations occurred before the system had reached equilibrium. However, the extent and time course of these changes depended on the velocities by which the different ion species traveled through the membrane. This is evident from the two plotted curves in **Figure 2**, which show that the changes in vesicle parameters were highly dependent on which of the two reported membrane permeabilities for K^+ were used in the simulation.

2.3 The Membrane Potential Across Vesicular Membranes Depends on the Initial Ion Concentrations at the Intra-and Extra-Vesicular Side

Secondary active transporters use the energy contained in the electrochemical gradient of ions to fuel concentrative uptake of their cognate substrate (Burtscher et al., 2019). Hence, assessment of their function relies on experimental systems, which allow for adjustment of the transmembrane ion gradients. In vesicles these gradients can be set by the experimenter. However, as shown before, in the vesicle these gradients and the membrane potential are expected to change in a time dependent manner, due to passive diffusion of ions through the membrane. This can complicate the interpretation of experimental outcomes. We demonstrate this with an example.

Let's assume we believe that a candidate Na^+ symporter antiports K^+ in the return step from the substrate-free inward- to the substrate-free outward-facing conformation and that it can thereby tap the energy contained in the electrochemical gradient of K^+. This, for instance, was shown to be the case for the serotonin transporter (SERT-SLC6A4) and for transporters in the SLC1 family (glutamate transporters) (Rudnick and Sandtner, 2019; Wang, et al., 2020). We could test this by preparing vesicles, which contain K^+ or the inert cation $NMDG^+$ instead. Let's further assume that we find the concentrative power of the secondary active transporter, which we reconstituted into these vesicles, higher in the presence than in the absence of intra-vesicular K^+. Is it now safe to conclude that this transporter antiports K^+?

The issue, here, is that the concentrative power of a secondary active transporter can also depend on V_M, if the transporter under scrutiny is electrogenic (i.e., one or more net charges are transported through the membrane in each transport cycle). The question, therefore, is whether the two tested experimental conditions can give rise to differing V_Ms. In **Figure 3** (left panel) we show the time course of the V_M change on equilibration for the two different conditions. The chosen P_M values for Na^+, Cl^-, and K^+ are indicated in the figure (black bar). We simulated the evolution of V_M for 1,000 s. As seen, on start of the simulation V_M rapidly diverged from zero. More importantly, the V_M values for the two conditions differed by about 10 mV after a few minutes. Given this result we can no longer be sure that the increase in concentrative power, which we observed in the experiment, is supportive of K^+ antiport. Arguably, this increase could also have been caused by the difference in V_M. Admittedly, the divergence in the V_M values in the shown simulations was conditioned on the chosen P_M values for the ions. We obtained the values for Na^+, Cl^- and K^+ from the literature. Yet, the spread in the reported values for these ions is considerable (see **Table 1**). For $NMDG^+$ no experimentally determined P_M value was available. Because of its large size this cation was considered impermeable (Dhoke et al., 2005; Elustondo et al., 2013; Reuss, 1979). However, what has been frequently overlooked is that NMDG can exist in an uncharged form ($NMDG_0$; pKa = 8.8). The latter is expected to diffuse through the membrane at a larger rate. For this reason, we determined the P_M value for $NMDG_0$ experimentally (see **Section 4**). In **Figure 3** (right panel) we show the predicted difference (ΔV_M) between the two experimental conditions when using different combinations of reported P_M values. Each bar shows the result of a simulation in which we did or did not account for diffusion of $NMDG_0$. It is evident that only for two of the chosen combinations this made a small difference (white bars indicate results obtained when $NMDG_0$ was assumed to permeate). In summary we conclude from the data depicted in **Figure 3**, that 1) the magnitude of ΔV_M depends on the chosen combination of P_M values, 2) that V_M is always more negative in the presence than in the absence of an outwardly directed K^+ gradient and 3) that the influence of the uncharged form of NMDG on V_M is negligible.

2.4 Model of a Unilamellar Vesicle Harboring SGLT1

To predict substrate uptake by the transporter into the vesicle, we incorporated SGLT1 into our model system. To this end, we used a previously published kinetic model of SGLT1 (see **Figure 8** in **Section 4**). The established stoichiometry of SGLT1 is that two Na^+ ions and one glucose molecule are transported through the membrane in each transport cycle. Reconstituted proteins are usually randomly oriented. We accounted for this in the model by assuming that one half of the SGLT1 units was oriented in the inside-out and the other half in the inside-in configuration.

It is possible with the kinetic model to calculate the flux of glucose and Na^+ through SGLT1. However, the magnitudes of these fluxes depend on the intra-and extraluminal Na^+ and glucose concentrations and on V_M. In the bare vesicle, the extents and time courses by which these vesicle parameters changed were conditioned on the rates by which the different ion species passively permeated. With SGLT1 incorporated into the vesicle, the situation is different. For instance, in the presence of SGLT1, a set Na^+ gradient is expected to dissipate faster because of the additional Na^+ ions, which can enter the vesicle via the transporter. Accordingly, with SGLT1 present, the evolution of the vesicle parameters over time ought to be different from that in its absence.

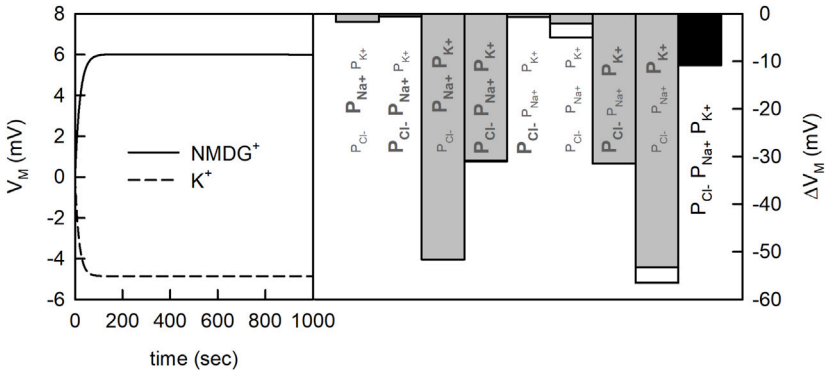

FIGURE 3 | Membrane potential generated by the net flux of charged particles. Vesicle assay kinetics simulated for two different experimental conditions. At both conditions, 200 mM NaCl was present outside the vesicle. Inside the vesicle there was either 200 mM KCl or 200 mM $NMDG^+Cl^-$. In the simulation 20 mM HEPES, was present inside and outside the vesicle and the pH was set to 7.5. Left panel Time course of the change in membrane potential (V_M) for a set of passive membrane permeabilities (i.e., $P_{Cl^-} = 5 \cdot 10^{-13}$ *m/s*, $P_{K^+} = 3 \cdot 10^{-13}$ *m/s*, $P_{Na^+} = 1.5 \cdot 10^{-13}$ *m/s*). Right panel Differences in transmembrane potentials between the two different experimental conditions for permutations of maximal and minimal P_M values of Cl^-, Na^+ and K^+ reported in the literature (grey bars) (bold values in **Table 1**) as well as our exemplary set (black bar). Minimal P_M values are indicated using smaller font size, maximal P_M values using bold letters. The effect of $P_{NMDG_0} = 1 \cdot 10^{-11}$ *m/s* is shown with empty white bars. ΔV_M was defined as the maximal difference between $V_{M,K^+} - V_{M,NMDG^+}$.

TABLE 1 | Literature values for passive membrane permeabilities of Cl^-, K^+, and Na^+. Indicated are the lipid composition and temperature for which the value was estimated and the method employed for the measurement. Bold values indicate for each ion the values for P_{max} and P_{min} chosen in the simulations.

Type of Ion	Value [10^{-13} m/s]	Lipid composition	Method	T [°C]	References
Cl^-	1,000	POPC	pH sensitive fluorophore in vesicles	25	Megens et al. (2014)
	0.1–100	egg lecithin	—	—	Kanehisa & Tsong, (2002)
	40	Egg yolk phosphotidylcholine	pH sensitive vesicle experiments	23	Nozaki & Tanford, (1981)
	1.5–11.3	egg phosphatidylcholine	radioactive labelling	3.2–20	Toyoshima & Thompson, (1975)
	7.6	Hen egg lecithin	radioactive labelling	24	Mimms, Zampighi, Nozaki, Tanford, & Reynolds, (1981)
	5.5	egg lecithin	radioactive labelling	4	Hauser, Phillips, & Stubbs, (1972)
	0.65	PS	radioactive labelling	36	Papahadjopoulos, Nir, & Oki, (1972)
	0.37	PS-Chol	radioactive labelling	36	Papahadjopoulos et al. (1972)
K^+	**0.17**–**15**	phosphatidylcholines with monounsaturated fatty acids composed of 14–24 carbon atoms	Electrodes	30	Paula et al. (1996)
	0.091	PS	radioactive labelling	36	Papahadjopoulos et al. (1972)
	0.033	4% phosphatidic acid-phosphatidyl choline	radioactive labelling	37	Johnson & Bangham, (1969)
	0.01	POPC	pH sensitive measurement	22	Shen et al. (2020)
	0.0047	PS-Chol	radioactive labelling	36	Papahadjopoulos et al. (1972)
Na^+	1,000	POPC	pH sensitive fluorophore in vesicles	25	Megens et al. (2014)
	3–**27**	egg phosphatidylcholine in decane	electrical conductance and pH electrode techniques	24	John Gutknecht & Anne Walter, (1981a)
	0.15	PG	radioactive labelling	36	Papahadjopoulos et al. (1972)
	0.15	Egg yolk phosphotidylcholine	pH sensitive vesicle experiments	23	Nozaki & Tanford, (1981)
	0.1	egg lecithin	—	—	Kanehisa & Tsong, (2002)
	0.095	Hen egg lecithin	radioactive labelling	24	Mimms et al. (1981)
	0.05	Egg yolk phosphotidylcholine	pH sensitive vesicle experiments	23	Nozaki & Tanford, (1981)
	0.021	egg lecithin	radioactive labelling	25	Brunner et al. (1980)
	0.02	PG-Chol	radioactive labelling	36	Papahadjopoulos et al. (1972)
	0.016	PS	radioactive labelling	36	Papahadjopoulos et al. (1972)
	0.011	PA-PC	radioactive labelling	36	Papahadjopoulos et al. (1972)
	0.01	PA-PC-Chol	radioactive labelling	36	Papahadjopoulos et al. (1972)
	0.005	PS-Chol	radioactive labelling	36	Papahadjopoulos et al. (1972)
	0.0012	egg lecithin	radioactive labelling	4	Hauser et al. (1972)

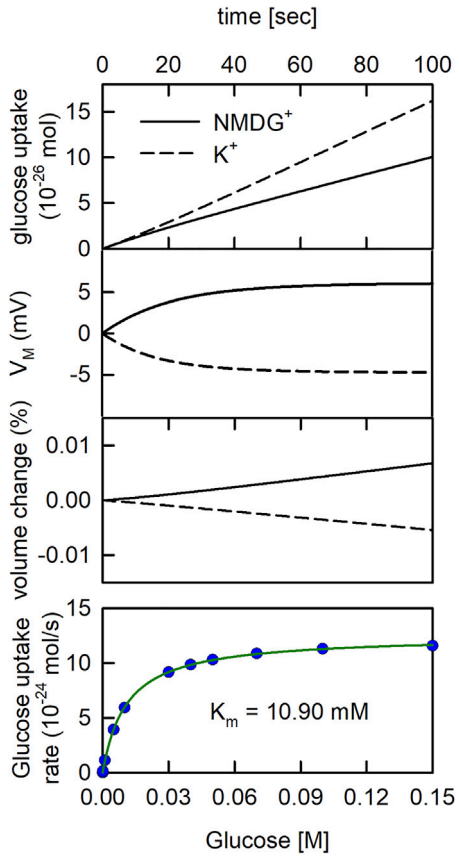

FIGURE 4 | The glucose uptake rate of SGLT1 is larger in the presence than in the absence of a K^+ gradient. Upper. Glucose uptake by SGLT1. In the simulation 1 μM glucose was applied to the extraluminal side of the vesicle. In the *in-silico* experiment, we assumed that on average 4.3 monomers were inserted into the vesicle with half of them oriented outside-in (Erokhova et al., 2016). The extraluminal concentration of 200 mM NaCl was osmotically balanced with either 200 mM KCl or 200 mM $NMDG^+Cl^-$ in the vesicle lumen. The rate of glucose uptake was higher in the presence of a K^+ gradient (dashed line) than in its absence (solid line). Upper middle panel Time course of V_M change. V_M was more negative in the presence of the K^+ gradient (dashed line) than in its absence (solid line). Lower middle panel Time course of vesicle volume change. The volume of the vesicle slightly increased and decreased when 200 mM $NMDG^+$(solid line) and 200 mM K^+ (dashed line) were initially contained in the vesicle, respectively. Lower panel Simulated glucose uptake as a function of glucose concentration (blue dots). The synthetic data were fit to the Michaelis Menten equation (green curve):
$Glucose\ uptake\ rate = (V_{max} \cdot [S])/(K_m + [S])$. The K_{m-} and the V_{max} value estimated by the fit were 10.90 mM and V_{max} of $1.22 \pm 0.006 \cdot 10^{-23}$ mol/s (simulation conditions: 150 mM NaCl, 20 mM MOPS, and pH 7.5 with 4.3 hSGLT1's per vesicle), respectively.

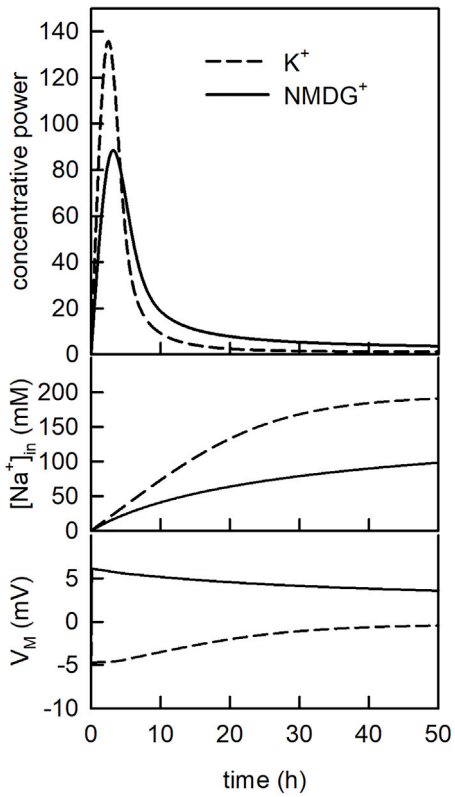

FIGURE 5 | The concentrative power of SGLT1 changes over time. Upper panel Evolution of the concentrative power of SGLT1 over time. In the simulation 1 μM glucose was applied for 50 h. The dashed line and the solid line show the concentrative power ($[Glu]_{in}/[Glu]_{out}$) in the presence and in the absence of the K^+ gradient, respectively. Middle panel Time course of the intraluminal sodium concentration $[Na^+]_{in}$ for the two conditions. Lower panel Time course of the membrane voltage (V_M) for the two conditions.

In **Figure 4** we revisited the question, which we posed above. That is: is it safe to conclude that a solute carrier antiports K^+ if we find its concentrative power increased in the presence of a transmembrane K^+ gradient? To tackle this question, we conducted simulations in the assumed presence and absence of a K^+ gradient, respectively. However, in contrast to the simulation shown above (**Figure 3**) we now assumed that SGLT1 was inserted into the vesicular membrane. The reaction scheme of SGLT1 does not specify K^+ binding to the transporter. Accordingly, if in the simulations the presence of a K^+ gradient gives rise to elevated glucose uptake by SGLT1 we know that this cannot be due to K^+ antiport. In **Figure 4** (upper panel), we simulated glucose uptake into the vesicle for a period of 100 s on addition of 1 μM glucose to the extra-vesicular solution. We note that 1 μM is within the range of concentrations, which are typically employed in radioligand uptake assays. As seen, in the presence of the K^+ gradient, uptake of glucose into the vesicle was increased. In **Figure 4** (upper middle panel) we plotted the evolution of V_M over time for the two experimental conditions. The plot confirmed that the observed increase in glucose uptake in the presence of the K^+ gradient had been a corollary of the more negative V_M, which had built up at this condition. In the lower middle panel of **Figure 4** we show the time dependent change in vesicular volume in percent. We also simulated glucose uptake as a function of the extra-vesicular glucose concentration (lower panel of **Figure 4**). These data were fit to the Michaelis Menten equation. The K_m and the V_{max} values for glucose uptake estimated by the fit were 10.90 mM and $1.22 \pm 0.006\ 10^{-23}$ mol/s, respectively.

In **Figure 5** (upper panel) we plotted the concentrative power of SGLT1 (i.e., $[Glu]_{in}/[Glu]_{out}$) as a function of time in the assumed presence (dashed line) and absence (solid line) of a K^+ gradient. In the simulation we applied 1 μM glucose to the

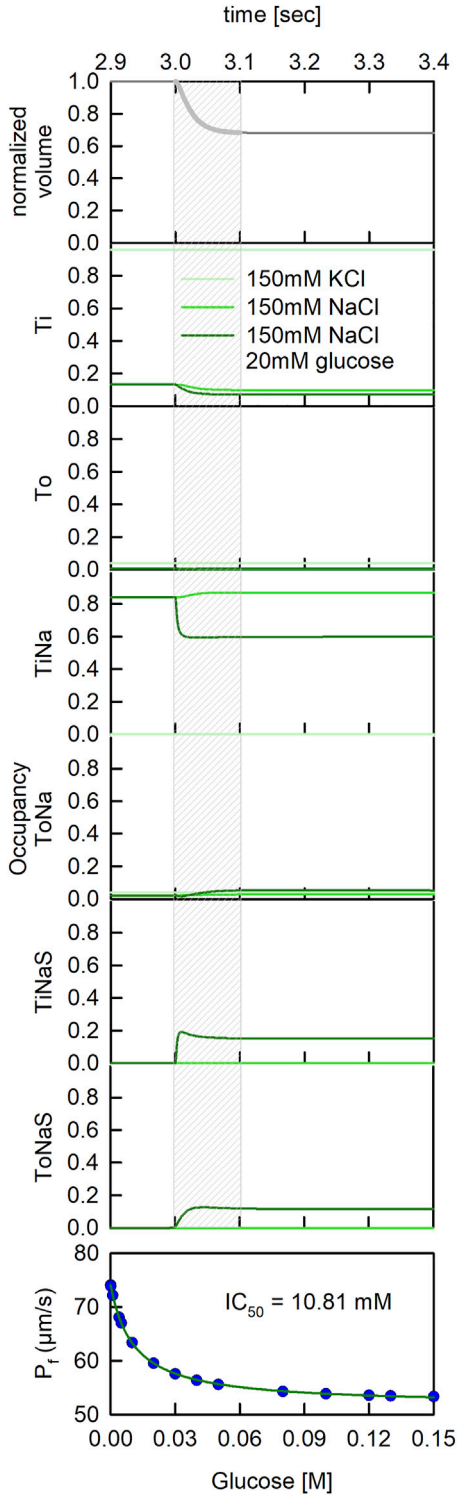

FIGURE 6 | Dynamic changes of state occupancies in a stopped flow experiment. State occupancies of SGLT1 before and after application of a hyperosmotic gradient (at time t = 3 s). We simulated three different experimental conditions: (light green line) PLs reconstituted in 150 mM KCl buffer and subjected to a 150 mOsm sucrose gradient, (green line) PLs reconstituted in 150 mM NaCl buffer and subjected to a 150 mOsm sucrose gradient and (dark green line) PLs reconstituted in 150 mM NaCl buffer and subjected to a hyperosmotic gradient of 150 mM sucrose and 20 mM glucose. The grey shaded area indicates the time period during which the vesicles shrunk (see uppermost panel). It was during this period that the scattered light intensities changed and that we obtained information on water flux through SGLT1.

extraluminal side of the vesicle for 50 h. As seen, at both conditions, the concentrative power first increased and then decreased. The decrease occurred on dissipation of the Na^+ gradient (**Figure 5**-middle panel). This transient change in concentrative power is a frequently observed phenomenon if radio-ligand uptake is monitored over an extended period of time (i.e., overshoot phenomenon) (Heinz and Weinstein, 1984). Most notably, however, we found the concentrative power of SGLT1 increased when the K^+ gradient was present. Since SGLT1 did not interact with K^+, this was also a consequence of the differing V_Ms between the two different experimental conditions (**Figure 5**-lower panel).

2.5 State Occupancies Depend on the Intra- and Extra Luminal Buffer Conditions

Our model system can also be used to address more sophisticated questions. We demonstrate this with an example. We recently showed that SGLT1 is highly permeable for water (Erokhova et al., 2016). We also found that the conductivity of SGLT1 for water was not contingent on the presence of the co-substrate (i.e., Na^+), because when K^+ was used as the substituting ion, the water flux remained essentially unchanged. Addition of 20 mM glucose, on the other hand, decreased water transport through SGLT1 by approx. 17%. However, it remained unclear, which conformation visited during glucose transport had or had not been water permeable. Here, we tackled this question with our model.

In the actual measurement of water flux through SGLT1, vesicles which contained this transporter (proteoliposomes) were subjected to a hyperosmotic buffer in a stopped-flow device. Application of the hyperosmotic buffer led to shrinkage of the vesicles, which was monitored by measuring the scattered light intensities at 90° (Hoomann et al., 2013; Hannesschlager et al., 2018). These data allowed for calculating the unitary water permeability through SGLT1 (Horner et al., 2015). To emulate stopped-flow experiments with our mathematical model we first let the proteoliposomes (PL) equilibrate. We then applied a step change of sucrose/glucose with the characteristic time constant of the dead time of our stopped-flow device (τ = 2 ms). To gain a deeper understanding of our published data on water flux through SGTL1 (Erokhova et al., 2016) we simulated three experimentally tested conditions: 1) PLs reconstituted in 150 mM KCl buffer and subjected to a 150 mOsm sucrose gradient, 2) PLs reconstituted in 150 mM NaCl buffer and subjected to a 150 mOsm sucrose gradient and 3) PLs reconstituted in 150 mM NaCl buffer and subjected to a hyperosmotic gradient of 150 mM sucrose and 20 mM glucose.

In our model, application of the hyperosmotic buffer led to a spontaneous decrease of vesicle volume (**Figure 6**-upper panel). The volume settled at about two-thirds of its original value, 100 ms after application of the osmolyte. The decrease in volume was accompanied by concentration changes of the solutes in the vesicle (data not shown). An additional output of our model are the state occupancies of SGLT1, which because they depended on the vesicle parameters, also changed on application of the osmolyte. In **Figure 6** we plotted the state occupancies of all states specified in the reaction scheme of SGLT1. The equilibrated proteoliposomes were challenged with 150 mM sucrose 3 seconds after start of the simulation. The three curves in each panel are the state occupancies for the three experimentally tested conditions. In the lower panel of **Figure 6** we also plotted the inhibitory effect of glucose on water flux as a function of the applied glucose concentration. These data were fit to an inhibition curve. The fit yielded an IC_{50} value of 10.81 mM. This value agreed well with the K_m for glucose uptake (cf. **Figure 4** -lower panel and **Figure 6** -lower panel).

Displayed in **Figure 7** are the state occupancies averaged over the period during which the proteoliposomes shrunk (i.e., the first 100 ms following the application of sucrose). This is the period during which we had obtained information on the water flux through SGLT1. As seen, in the presence of 150 mM KCl the transporter mostly dwelled in the apo-inward facing conformation (Ti—96% occupancy) (see **Figure 7**). In contrast, in the presence of 150 mM NaCl, SGLT1 adopted the sodium bound inward facing conformation (TiNa—87% occupancy) and the Ti state (10% occupancy). In the additional presence of 20 mM glucose, the transporter also visited substrate bound states (i.e., TiNaS—12% occupancy and ToNaS—15% occupancy).

We note that the summed fraction of glucose bound states amounted to 27% when 20 mM glucose was present. Because water flux through SGLT1 was reduced by approximately 17% at the same condition, it is tempting to speculate that it were the substrate-free states which conducted water and the substrate bound states which were water impermeable. The blue bar in **Figure 7** shows the summed fraction of the substrate-free states (in light blue) and the summed fraction of the substrate bound states (in dark blue) in the presence of 20 mM glucose. The bar in purple summarizes our recent experimental findings (i.e., water flux in the presence of glucose normalized to the water flux measured in its absence). The occupancies of the substrate bound states and the loss in water flux were in reasonable agreement.

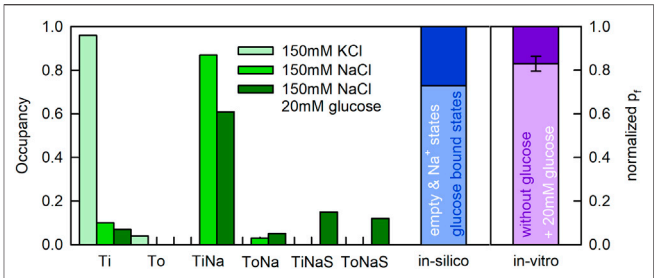

FIGURE 7 | State occupancies of SGLT1 during water flux though the transporter. Upper panel To and Ti represent the outward and inward facing apo-conformations, respectively (**Figure 8**). ToNa, TiNa, ToNaS, and TiNaS denote the sodium and the sodium/glucose bound states. State occupancies were averaged over the first 100 ms after application of the osmolyte (**Figure 6**). We used the same color code as in **Figure 6** to indicate the different experimental conditions. The bar in blue shows the summed fraction of the substrate bound states (dark blue) and, the summed fraction of the substrate free states (light blue). The difference between the light purple and dark purple bar shows the decreased unitary water permeability measured in the presence of 20 mM glucose. Lower panel Simulated water permeability of SGLT1 (assuming water impermeable glucose states) as a function of the glucose concentration (blue dots). The green curve denotes the fit of an inhibition curve to the data: $P_f = b + (a - (a \cdot [S]))/([S] + IC_{50})$ The extracted IC_{50} value was 10.81 mM (simulation conditions: 150 mM NaCl, 20 mM MOPS, and pH 7.5 with 4.3 hSGLT1's per vesicle +150 mM sucrose outside the vesicle).

3 DISCUSSION

Here, we present an *in-silico* model, which allows to predict the time courses of solute concentration changes within the confinement of a unilamellar vesicle, both in the absence and presence of a glucose transporter (SGLT1). The model accounts for passive diffusion of ions, sucrose, glucose, and water through the vesicular membrane and for solute flux through the transporter (i.e., Na^+ and glucose). In addition, we also incorporated state-dependent water flux through SGLT1. In the model, the solutes and solvent, which entered or left the vesicle gave rise to changes in the intra-vesicular solute concentrations, vesicle volume and transmembrane potential (V_M). These parameters in turn impinged on the operation of the embedded transporter. The model can emulate a wide range of experiments and it can therefore be used to predict and interpret experimental outcomes. In addition, it can help find optimal experimental conditions. That is: it can 1) assist in ruling out initial conditions, which would lead to vesicle rupture due to excessive volume increase and/or large membrane potential, and 2) provide estimates for the expected signal change to help chose the measurement strategy, which has the highest chance of success. In the present study, we simulated radioligand uptake and stopped-flow experiments, of the kind used to measure water flux through proteoliposomes.

We previously showed by utilizing proteoliposomes that SGLT1 is an efficient facilitator of passive water transport (Erokhova et al., 2016). The measured unitary permeability for water amounted to $3.3 \pm 0.4 \times 10^{-13}$ cm^3/s at 5°C. These rates were comparable to those reported for aquaporins (Erokhova et al., 2016). Water flux through SGLT1 did not depend on the presence of the co-substrate Na^+, because it remained the same when Na^+ was substituted with K^+. Less water flew through SGLT1 when 20 mM glucose, a saturating concentration, was present in the bath solution. However, the reduction in the conductivity for water was small (i.e., 17%). This suggested that during transport, SGLT1 dwelled longer in states, which conducted water than in states, which were water-impermeable. Our model predicted that at the condition at which the water flux was found reduced, SGLT1 dwelled 27 percent of the time in glucose-bound states. This tempted us to speculate that the water-

impermeable states were those, which were bound to glucose. This view is in line with results obtained from MD simulations of the bacterial homolog vSGLT in the inward-facing state. These showed that residues located close to the glucose binding site gated water flux (Li et al., 2013) and that the permeability for water was modulated albeit not tightly coupled to substrate release (Adelman et al., 2014). However, a shortcoming of our modeling approach is that for technical reasons water flux through SGLT1 had to be measured at 5°C, while the employed six state model (see **Figure 8**) was parametrized using data obtained at room-temperature. Arguably, the conformational equilibrium of SGLT1 at 5°C can differ from that at room temperature. However, the low activation energy for water transport through SGLT1, reported by others (i.e., in the range of 4.2–5 kcal/mol) (Meinild et al., 1998; Zeuthen et al., 2016), suggests that temperature dependent changes of the conformational equilibrium of the transporter are likely modest. The explanation for this could be as follows: the two reactions in the transport cycle, which ought to be most affected by temperature are the conformational rearrangements (i.e., 1) the transition, which carries substrate and co-substrate through the membrane and 2) the return of the empty transporter to the outward facing conformation). Because, the reaction paths of these two transitions are similar, there is no reason to believe that their temperature dependencies are vastly different. If true, the rates of these two reactions are expected to change with temperature by a similar factor. As a consequence of this, the conformational equilibrium (but not the glucose uptake rate), remains the same at different temperatures.

Our vesicle model is unique in that it incorporates a solute carrier. Yet, other vesicle models exist, which account for passive diffusion of water (Wachlmayr et al., 2022), weak acids (Hannesschlaeger et al., 2019a; Gabba and Poolman, 2020), and ions (Megens et al., 2014; Shen et al., 2020) through the vesicular membrane. However, due to their different scopes, none of them simultaneously modeled 1) membrane potential (Gabba and Poolman, 2020), 2) partial volume effects (Hannesschlaeger et al., 2019b; Gabba and Poolman, 2020; Shen et al., 2020), 3) de/protonation of the buffer (Gabba and Poolman, 2020; Shen et al., 2020), and 4) self-dissociation of water (Gabba and Poolman, 2020). While we modeled all of the above, we disregarded the size distribution of the vesicle ensemble as was included in models, which dealt with water (Wachlmayr et al., 2022) and weak acid permeation (Gabba and Poolman, 2020).

It is important to point out, however, that the predictive power of any given model hinges on its accurate parameterization. For example, we showed that the time course and extent by which V_M changed, depended 1) on the initial intra- and extra-vesicular ion concentrations and 2) on the P_M values used in the simulation. The rates of passive ion fluxes can be measured in experiments. However, we found for the same ion vastly different values in the literature (**Table 1**). The variabilities in the reported P_M values for the same ion likely reflect differences in the experimental conditions at which this parameter was determined (e.g., the lipid composition of the membranes), and inaccuracies of the methods used to estimate it. We, therefore, surmise that accurate parametrization of the model may necessitate measuring these

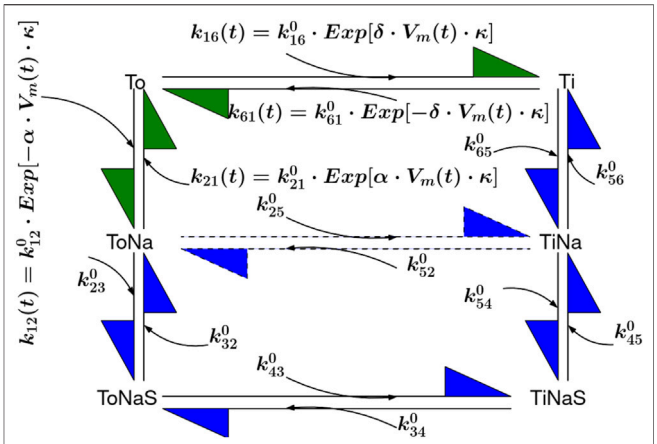

FIGURE 8 | Six State Model of SGLT1. The transitions To to Ti and To to ToNa are voltage dependent and indicated with green arrows. The reactions denoted by blue arrows are voltage independent and described with constant rates k^0_{xy} were xy describes the reaction number in the figure. δ and α are phenomenological constants with 0.7 and 0.3 and $\kappa = F/RT$, describe the fraction of the electrical field sensed by the reaction (Parent et al., 1992; Wright et al., 2011). The rate constants are listed in **Table 3**.

rates for membranes of exactly the same lipid composition as used in the experiment. For lack of such a coherent set of values we selected for most simulations, literature values, which adhered to the generally accepted rank order of permeability: $P_{H^+} > P_{Cl^-} > P_{K^+} > P_{Na^+} > P_{NMDG^+}$. In this context, it is worth mentioning that the main determinants of ion permeation are the Born penalty, the image energy, the dipole potential, and the surface potential. The Born penalty incurs on transfer of an ion from one dielectric medium ($\varepsilon_{water} \sim 80$) into another ($\varepsilon_{membrane} \sim 2$) (Born, 1920). It is independent of the sign of the charged molecule, decreases with increasing Born radius and is slightly lowered by a polarizing effect, which emanates from charged solutes in the vicinity of dielectric interfaces (image energy) (Parsegian, 1969). The Born-image energy decreases with decreasing membrane width. The dipole potential, on the other hand, is generated by oriented water molecules and the polar carbonyl groups of ester bonds (Gawrisch et al., 1992). Because the dipole potential is positive, it favours partitioning of anions over cations. Surface charges, selectively attract or repel anions and cations, which offsets their chemical potential (McLaughlin, 1989).

Proteoliposomes are well suited for studies of solute carrier function. This is because 1) the experimental outcomes are not confounded by the presence of other proteins, 2) the number of protein units reconstituted into a vesicle can be titrated and- if so wished- even down to a single molecule 3) the ion concentrations in and outside the vesicle can be set as desired and 4) the lipid composition of the vesicular membrane is in the hands of the experimenter. However, one major challenge when using proteoliposomes is that vesicle parameters such as membrane voltage and the intraluminal ion-concentrations are difficult to control. Here we tried to address this problem with our model. The idea was that if we cannot control these parameters, we can at the very least try to model how they change over time and on (experimental) perturbation. We demonstrated in an example that

TABLE 2 | Model parameters.

Parameter	Symbol	value	References
Vesicle radius $t = 0$	r_0	60 nm	Horner et al. (2015)
Specific membrane capacity	μ	1 $\mu F/cm^2$	Hannesschlaeger, Barta, et al. (2019b)
Bilayer thickness	h	3.75 nm	Paula et al. (1996)
Partial molar volume H_2O	v_w	0.018 1/*mol*	Hannesschlaeger, Barta, et al. (2019a)
Partial molar volume Na^+	v_{Na}	$-1.21 \cdot 10^{-6}$ m^3/mol	Millero, (2002)
Partial molar volume K^+	v_K	$9.02 \cdot 10^{-6}$ m^3/mol	Millero, (2002)
Partial molar volume Cl^-	v_{Cl}	$1.78 \cdot 10^{-5}$ m^3/mol	Millero, (2002)
Partial molar volume OH^-	v_{OH}	$-4.04 \cdot 10^{-6}$ m^3/mol	Millero, (2002)
Partial molar volume Glucose	v_{Glu}	$1.12 \cdot 10^{-4}$ m^3/mol	Fucaloro et al. (2007)
Partial molar volume H^+	v_H	$-5.5 \cdot 10^{-9}$ m^3/mol	Borsarelli & Braslavsky, (1998)
Water dissociation rate	k_w^+	$2.5 \cdot 10^{-5}$ s^{-1}	Stillinger, (1978)
passive H^+ permeability	P_{H^+}	$3.5 \cdot 10^{-7} m/s$	Hannesschlaeger, Barta, et al. (2019b)
passive OH^- permeability	P_{OH^-}	0 m/s[a]	
passive Na^+ permeability	P_{Na^+}	$1.5 \cdot 10^{-13}$ m/s	Brunner et al. (1980)
passive Glucose permeability	P_{Glu}	$3.1 \cdot 10^{-13}$ m/s	Brunner et al. (1980)
passive Sucrose permeability	P_{Suc}	$3.1 \cdot 10^{-14}$ m/s	Stefely et al. (2002)
passive K^+ permeability	P_{K^+}	$3. \cdot 10^{-13}$ m/s	Paula et al. (1996)
passive Na^+ permeability	P_{Cl^-}	$5. \cdot 10^{-13}$ m/s	Toyoshima & Thompson, (1975)
HEPES		0 m/s[b]	
$NMDG^+$	P_{NMDG} +	$1.6 \cdot 10^{-21}$ m/s	prediction
$NMDG_0$	P_{NMDG0}	$(1.6 \cdot 10^{-21} - 1. \cdot 10^{-11})$ m/s[c]	Experimental, prediction, (Reuss, 1979; Dhoke et al., 2005; Elustondo et al., 2013)

[a]*We set P_{OH^-} to zero as at pH 7.5 with equal concentrations of H^+ and OH^- P_{OH^-}, can be neglected. P_{H^+} exceeds P_{OH^-} by more than two orders of magnitude (Gutknecht and Walter, 1981b).*

[b]*The contribution of HEPES, is negligible due to its low concentration and low predicted membrane permeabilities. Moreover, exact treatment is challenging due to its zwitterionic states.*

[c]*In **Figure 3** we showed that the potential effect of a P_{NMDG0} permeability of $1.0 \cdot 10^{-11} \frac{m}{s}$ is minor. Therefore, and due to the lack of more accurate values we used $P_{NMDG^+} = P_{NMDG_0}$ elsewhere.*

the presence of a K^+ gradient accelerated the rate of glucose uptake and increased the concentrative power of SGLT1, although K^+ binding was not specified in the reaction scheme of this transporter. In the model this had occurred because SGLT1 is an electrogenic transporter, which reacted to the more negative V_M that arose in the presence of the K^+ gradient. In this context, it is worth mentioning that a study exists, in which it was proposed that LeuT (a bacterial homolog of neurotransmitter transporters) antiports K^+ (Billesbolle et al., 2016). The main argument was that the concentrative power of reconstituted LeuT was found increased in the presence of a K^+ gradient. While it may turn out that LeuT indeed antiports K^+, this conclusion can be challenged on the grounds that the vesicle parameters, in particular V_M were not monitored in this study. The same is true for a more recent study on the *drosophila* dopamine transporter, which was conducted by the same group (Loland et al., 2022).

Another challenge when using proteoliposomes, is the difficulty to influence the orientation of the transporter in the membrane during reconstitution. Whereas protein orientation in cellular membranes is mainly determined by the positive-inside rule (von Heijne, 1992), with basic residues being more abundant on the cytoplasmic side, *in-vitro* protein orientation is- in most instances- random (i.e., 50% in the proper orientation and 50% inserted upside down). We accounted for this in our model by implementing both orientations with the two fractions kept tunable. This allows for predicting the impact of random-, biased- or perfect-orientation of membrane transporters on experimental outcomes. Thereby, the model can help to direct efforts to tune the orientation of reconstituted membrane transporters.

The ultimate goal of our modelling exercise is to find a model, which can faithfully predict the time dependence of the vesicle parameters. However, it is unlikely that our model already fulfills this criterion. To improve the model, its predictions must be tested in experiments. A readily accessible parameter, for instance, is the time course of volume change *via* scattering or fluorescence self-quenching experiments (Wachlmayr et al., 2022). The latter is performed *via* intra luminal trapped fluorophores as volume readout. The time course and extent of the change in the concentration of the individual ion species and the magnitude of the transmembrane potential are accessible *via* ion-(Feroz et al., 2021) or voltage- (Cortes et al., 2018; Gest et al., 2021) sensitive fluorophores. These parameters can be measured for different intra and extraluminal ion concentrations in the presence and absence of SGLT1, with and without substrate. The results of these measurements can then be compared with the predictions of the model and discrepancies therein resolved by adapting the model. However, testing the feasibility of this approach is beyond the scope of the present study, but we intend to test utility in follow-up investigations.

4 MATERIALS AND METHODS

We simulated substrate uptake by SGLT1 embedded into a unilamellar vesicle. We accounted for solute flux through SGLT1 by employing a recently published kinetic model of this transporter (Parent et al., 1992; Adelman et al., 2016; Wright et al., 2011). Passive diffusion of solutes through the

TABLE 3 | The six different states after **Figure 8** and corresponding shortcuts used in the code implementation are listed in the first two columns. The overall rate gain and loss is always contributed to the corresponding state in the row. The right column refers to the initial rates given at $t = 0$ after Table S3 in Adelman et al. (2016). The remaining rates $k^{0^*}_{54}$ and $k^{0^*}_{52}$ were estimated according to Kirchhoff's mesh rule by multiplying all rates along the states To—ToNa—ToNaS—TiNaS—TiNa—Ti—To and subtracting them from the other direction by setting the difference to zero. For $k^{0^*}_{52}$ the mesh ToNa—ToNaS—TiNaS—TiNa—ToNa was used for evaluation. Values are given for 22°C.

State	Abbreviation	gain	Loss	Corresponding k^0 values [1]
apo outward facing state	To(t)	$k_{61}(t) + k_{21}(t)$	$k_{16}(t) + k_{12}(t)$	k^0_{61} = 25 1/*s*, k^0_{16} = 600 1/*s*, k^0_{12} = 50000 1/M^2*s*, k^0_{21} = 300 1/*s*
apo inward facing state	Ti(t)	$k_{16}(t) + k^0_{54}$	$k_{61}(t) + k^0_{45}$	k^0_{61} = 25 1/*s*, k^0_{16} = 600 1/*s*, $k^{0^*}_{54} \simeq$ 44444 1/*M*, k^0_{45} = 800 1/*s*
sodium bound outward facing state	ToNa(t)	$k_{12}(t) + k^0_{52} + k^0_{32} + k^0_{72}$	$k_{21}(t) + k^0_{25} + k^0_{23} + k^0_{27}$	k^0_{12} = 50000 1/M^2*s*, $k^{0^*}_{52} \simeq$ 0.000246914 1/*s*, k^0_{25} = 0.01 1/*s*, k^0_{32} = 20 1/*s*, k^0_{23} = 45000 1/*Ms*, k^0_{72} = 0.01 1/*s*, k^0_{27} = 50000 1/*s*
sodium bound inward facing state	TiNa(t)	$k^0_{65} + k^0_{25} + k^0_{45}$	$k^0_{56} + k^0_{52} + k^0_{54}$	k^0_{65} = 4500 1/M^2*s*, k^0_{56} = 16 1/*s*, $k^{0^*}_{52} \simeq$ 0.000246914 1/*s*, k^0_{25} = 0.01 1/*s*, $k^{0^*}_{54} \simeq$ 44444 1/*Ms*, k^0_{45} = 800 1/*s*
sodium and glucose bound outward facing state	ToNaS(t)	$k^0_{23} + k^0_{34}$	$k^0_{32} + k^0_{43}$	k^0_{32} = 20 1/*s*, k^0_{23} = 45000 1/*Ms*, k^0_{34} = 50 1/*s*, k^0_{43} = 50 1/*s*,
sodium and glucose bound inward facing state	TiNaS(t)	$k^0_{43} + k^0_{54}$	$k^0_{34} + k^0_{45}$	k^0_{34} = 50 1/*s*, k^0_{43} = 50 1/*s*, $k^{0^*}_{54} \simeq$ 44444 1/*Ms*, k^0_{45} = 800 1/*s*

membrane was described using the Goldman-Hodgkin-Katz flux equation. If for a solute no experimentally determined P_M value was available, we calculated it from estimated hexadecane/water partition coefficients. The system of differential equations constituting the model, was solved numerically with Mathematica's NDSolve IDA package (V. 12) (RRID: SCR_014448).

4.1 Vesicle Model

The change in vesicle volume caused by the presence of an osmotic gradient δ_{OSm} was described by the following equation:

$$\frac{dV}{dt} = S \cdot P_f \cdot v_w \cdot \delta_{OSm} + \sum_{i=0}^{k} \frac{dn_{i+}}{dt} \cdot v_i \tag{1}$$

where S, P_f and v_w are the surface area of the vesicle, membrane permeability for water and the partial molar volume of water, respectively. δ_{Osm} is the difference in the osmotic concentration between the inner and outer solution. The first term in **Eq. 1** accounts for the volume change evoked by the osmotic gradient δ_{Osm}. The second term considers partial volume effects (Borsarelli and Braslavsky, 1998; Fucaloro et al., 2007; Millero, 2002). k is the number of solutes present in the assay. The change in the amount of each solute $\frac{dn_{i+}}{dt}$ was multiplied with its molar volume (v_i). The values for v_i are listed in **Table 2**.

δ_{OSm} was calculated as follows:

$$\delta_{Osm} = \left(\sum_{i=0}^{k} [X(t)]_i^{inside} + \sum_{i=0}^{n} [Y(t=0)]_i^{inside} \cdot \frac{V_0}{V(t)} \right) - \left(\sum_{i=0}^{m} [Z(t)]_i^{outside} \right) \tag{2}$$

where $[X(t)]^{inside}$ is the luminal concentration of the (k) permeable solutes and $[Y(t=0)]^{inside}$ the luminal concentration of the (n) impermeable solutes. $[Z(t)]^{outside}$ is the sum of all extra-vesicular solute concentrations (m). V_0 is the initial volume of the lipid vesicle (**Table 2**):

$$V_0 = \frac{4}{3}\pi \cdot (r_0 - h)^3 \tag{3}$$

where we corrected the outer radius r_0 with the membrane bilayer thickness h.

We used the Goldman-Hodgkin-Katz flux equation to describe passive diffusion of solutes through the membrane

$$j_{GHK}(t) = \frac{dn_q}{dt} = -\frac{z_q \cdot S \cdot V_M(t) \cdot P_{M,q} \cdot F}{R \cdot T} \cdot \frac{[q]_{in} - [q]_{out} \cdot Exp\left[-\frac{z_q \cdot V_M(t) \cdot F}{R \cdot T}\right]}{1 - Exp\left[-\frac{z_q \cdot V_M(t) \cdot F}{R \cdot T}\right]} \tag{4}$$

where $P_{M,q}$, z_q , F , R, $[q]_{in}$, and $[q]_{out}$ are the membrane permeability of species q, its valance, the Faraday constant, the Gas constant and the concentration of the charged species q inside and outside the vesicle, respectively. In the simulation, the charged species were Na^+, K^+, H^+, $NMDG^+$, and Cl^-. V_M is the membrane potential, which at time $t = 0$ was set to zero. $P_{M,q}$ values used in the simulations are listed in **Table 2**.

The membrane was modeled as a capacitor, which was charged by the charged molecules entering the vesicle. For membrane potentials below $V_M < 300$ mV (Benz et al., 1979) electrical breakdowns of the lipid bilayer can be neglected and the vesicle membrane can be described as a capacitor with charge difference Q: (Hannesschlaeger et al., 2019a; Montal and Mueller, 1972)

$$Q = \mu \cdot S \cdot V_M \tag{5}$$

where μ is the specific membrane capacity and S the surface area.

Q can be expressed as: $Q = n_q \cdot z_q \cdot F$. From this we can obtain V_M:

$$V_M = -\frac{\sum_{q=0}^{k} [n_q \cdot z_q] \cdot F}{S \cdot \mu} \tag{6}$$

where q indicates a charged species that can diffuse through the membrane with its corresponding amount n_q and valence z_q. The impermeable solutes do not contribute to V_M.

Since permeation of free ions like H^+ and OH^- also contributes to V_M we considered also self-dissociation of

water into protons and hydroxide ions according to (Hannesschlaeger et al., 2019b):

$$\frac{d[OH^-]}{dt} = \frac{d[H^+]}{dt} = k_w^+ \cdot [H_2O] - k_w^- \cdot [OH^-] \cdot [H^+] \quad (7)$$

where k_w^+ and $k_w^- = [H_2O] \cdot k_w^+ / K_w$ are the dissociation and the association rates of water with $[H_2O] = v_w^{-1}$ and K_w the water equilibrium constant. Additionally to the change in pH described in **Eq. 7**, the proton concentration $[H^+]$ depends on the protonation and deprotonation rates of the available buffer M, the concentration of the deprotonated $[M^-]$ and protonated buffer form $[MH]$ inside the vesicle can be calculated using the following relations between the protonated and deprotonated species of buffer M:

$$\frac{d[M^-]}{dt} = \frac{1}{V(t)} \cdot \frac{dn_{M^-}}{dt} = k_d \cdot [MH] - k_p \cdot [H^+] \cdot [M^-] \quad (8)$$

$$\frac{d[MH]}{dt} = \frac{1}{V(t)} \cdot \frac{dn_{MH}}{dt} = -k_d \cdot [MH] + k_p \cdot [H^+] \cdot [M^-] \quad (9)$$

For the formulation of **Eq. 8** and **Eq. 9** we used the following relation: $c = n/V(t)$, where c is the concentration, $V(t)$ the vesicle volume and n the amount of solute. The corresponding protonation rates k_p and deprotonation rates k_d can be estimated from a linear regression of **Figure 4** in (Gutman and Nachliel, 1990):

$$k_d = 1. \cdot 10^{-0.98+pK\cdot 10.98} \quad k_p = \frac{k_d}{K_A} \quad K_A = 1. \cdot 10^{-pK} \quad (10)$$

where pK is the pK value of the buffer M and K_A the corresponding equilibrium constant. To calculate the change in free protons dn_{H^+}/dt inside the vesicle according to **Eq. 4**, every reaction involving proton exchange as in **Eqs 7–9** was considered in the form of:

$$\frac{dn_{H^+}}{dt} = j_{GHK}^{H^+} + \left(k_w^+ \cdot [H_2O] - k_w^- \cdot [OH^-] \cdot [H^+] + \left(\frac{d[M^-]}{dt} \right) \right) \cdot V(t) \quad (11)$$

We predicted water flux through proteoliposome by emulating stopped flow experiments. For these it was necessary to change the osmotic concentration outside the vesicle by adding an osmolyte such as glucose or sucrose with a concentration $[S_{add}]$. Addition occurred at time t_s and was modeled as an exponential rise (**Eq. 12**) with a rate constant of $k_0 = 300 s^{-1}$ to account for the dead time of the stopped flow mixing process:

$$\frac{d[S_{tot}]}{dt} = \begin{cases} 0, t < t_s \\ k_0 \cdot [S_{add}] - k_0 \cdot [S_{tot}], t \geq t_s \end{cases} \quad (12)$$

The total concentration can be calculated as: $[S_{tot}](t) = [S](t) + [S_0]$, where $[S_0]$ is the concentration at the start of the application.

4.2 SGLT1 Model

SGLT1 was modeled utilizing a recently published *Six State Model* (see **Figure 8**) (Adelman et al., 2016; Parent et al., 1992; Wright et al., 2011). Voltage dependent transitions are indicated with green arrows, all other transitions with blue arrows. The published model accounts for Na^+ slippage (dotted arrow between $TiNa(t)$ and $ToNa(t)$). The transition rates used in the model were adapted from Table S3 in Adelman et al. (2016) and they are listed in **Table 3**. When we incorporated the kinetic model of SGLT1 into the vesicle we also accounted for: 1) transporter orientation (*IN* and *OUT*) after insertion into the vesicular membrane (see **Figure 9**) and 2) for passive water flux through the transporter. We implemented the two orientations of the transporter by switching in the equations, which constitute the kinetic model the concentration terms (i.e., $[Na]_{OUT}$ and $[glucose]_{OUT}$ became $[Na]_{IN}$ and $[glucose]_{IN}$ and vice versa) (Parent et al., 1992). The outward facing conformation of the fraction of the properly oriented transporters interacted with $[Na]_{OUT}$ and $[glucose]_{OUT}$. For the fraction which was inserted upside down it was opposite.

We introduced a passive water permeability for SGLT1 according to Erokhova et al. (2016) in our model. This enhanced the rate of volume shrinkage according to **Eq. 1**. As a first estimate we assumed that SGLT1 is only water permeable in its apo states but not in the glucose bound states. Therefore, we weighted the water permeability P_f of SGLT1 with the corresponding state occupancies:

$$P_f = P_{f,fast} \cdot (To_{OUT}(t) + Ti_{OUT}(t) + ToNa_{OUT}(t) + TiNa_{OUT}(t) + To_{IN}(t) + Ti_{IN}(t) + ToNa_{IN}(t) + TiNa_{IN}(t)) + P_{f,passive}, \quad (13)$$

The passive water permeability through the membrane is: $P_{f,passive} = 20 \mu m/s$ (Pohl et al., 2001). The fast water permeability $P_{f,fast}$ is the estimated single channel water permeability $p_f = 5 \cdot 10^{-19} m^3/s$ at $22^\circ C$ assuming an activation energy of ~ $4 kcal/mol$ (Erokhova et al., 2016):

$$P_{f,fast} = N \cdot \frac{p_f}{4\pi r_0^2} \quad (14)$$

where N is the number of SGLT1 transporters per vesicle.

We calculated the membrane potential $V_M(t)$ according to **Eq. 6**. Sodium uptake into the vesicle ($Na_{up}^+(t)$ in mol) by SGLT1 was computed for the different orientations as:

$$\frac{dNa_{up}^+}{dt} = 2 \cdot \left(-\left(To_{IN}(t) \cdot k_{12}(t) \cdot [Na_{in}^+]^2 - ToNa_{IN}(t) \cdot k_{21}(t) \right) \cdot \left(N \cdot \frac{p_{IN}}{N_A} \right) + \left(TiNa_{OUT}(t) \cdot k_{21}(t) - Ti_{OUT}(t) \cdot k_{12}(t) \cdot [Na_{in}^+]^2 \right) \cdot \left(N \cdot \frac{p_{OUT}}{N_A} \right) \right) \quad (15)$$

The factor two at the beginning of **Eq. 15** accounts for the fact that in each transport cycle two sodium ions are transported. N_A is *Avogadro's constant*, p_{in} and p_{out} are the fractions of the two possible orientations of SGLT1 after integration into the membrane ($0 \leq p_{OUT} + p_{IN} \leq 1$). The total sum of outward and inward configured occupancies is p_{OUT} and p_{IN}, respectively. The total contribution of sodium $dn_{Na^+}/dt\,[mol/s]$ to the estimated $V_m(t)$ is the sum of **Eq. 15** and **Eq. 4**:

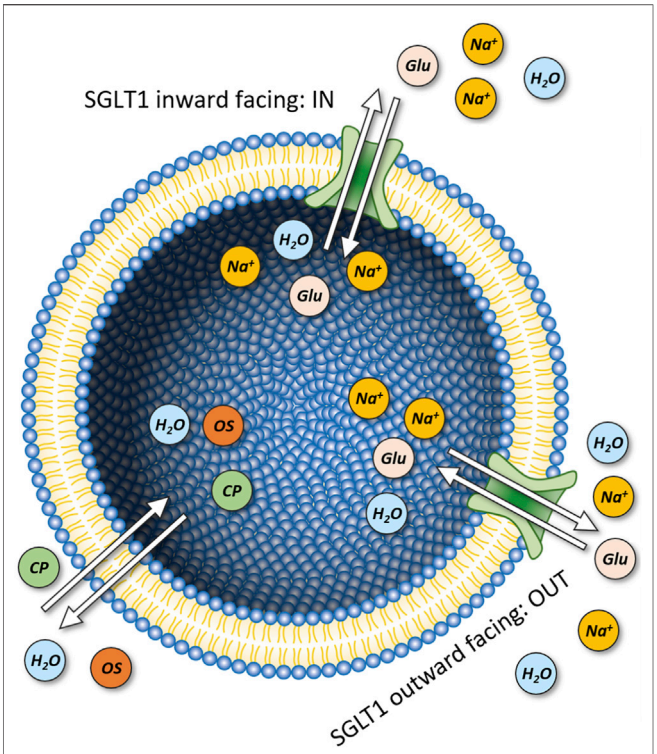

FIGURE 9 | Vesicles containing SGLT1. Model of a unilamellar vesicle with SGLT1 incorporated in two different orientations. The inward- and outward facing configurations oriented towards the intra and extra luminal side are denoted as IN and OUT, respectively. In each transport cycle SGLT1 transports 2 Na^+ ions and one glucose molecule. The model takes into account passive permeation of osmotically active solutes (OS) (i.e., sucrose, glucose, and $NMDG_0$) and charged particles (CP) (i.e., Na^+, K^+, $NMDG^+$, Cl^-, and protons) as well as passive flux of water.

$$\frac{dn_{Na^+}}{dt} = \frac{dNa^+_{up}}{dt} + j^{Na^+}_{GHK} = \frac{dNa^+_{up}}{dt} - \frac{z_{Na^+} \cdot S \cdot V_m(t) \cdot P_{Na^+} \cdot F}{R \cdot T} \cdot \frac{[Na^+]_{in} - [Na^+]_{out} \cdot Exp\left[-\frac{z_{Na^+} V_M(t) F}{R \cdot T}\right]}{1 - Exp\left[-\frac{z_{Na^+} V_M(t) F}{R \cdot T}\right]} \tag{16}$$

where S, $V(t)$, P_{Na^+}, z_{Na^+}, F, R, T, $[Na^+]_{in}$, $[Na^+]_{out}$ are the vesicle surface, the membrane potential, the passive Na^+ membrane permeability, its ion valence, the Faraday constant, the temperature, the Gas constant and the concentration of Na^+ inside and outside the vesicle, respectively.

Glucose uptake $S_{up}(t)$ [mol] through SGLT1 into the vesicle is:

$$\frac{dS_{up}}{dt} = \left(-\left(ToNa_{IN}(t) \cdot k^0_{23} \cdot [S]_{in}(t) - ToNaS_{IN}(t) \cdot k^0_{32}(t)\right) \cdot N \cdot \frac{p_{IN}}{N_A}\right) + \left(\left(TiNaS_{OUT}(t) \cdot k^0_{45} - TiNa_{OUT}(t) \cdot k^0_{54} \cdot [S]_{in}(t)\right) \cdot N \cdot \frac{p_{OUT}}{N_A}\right) \tag{17}$$

Since glucose is also an osmolyte but uncharged, the passive glucose flux $j_s(t)$ through the membrane was taken into account by using *Fick's first diffusion Law* (Wang et al., 2014):

$$j_s(t) = -(S \cdot P_{Glu} \cdot ([S]_{in}(t) - [S]_{out}(t))) \tag{18}$$

where $[S]_{out}(t)$ is the extra-vesicular glucose concentration. The total glucose uptake into the vesicle is the sum of **Eqs 17**, **18**.

4.3 Estimation of Passive Membrane Permeabilities

For solutes for which experimentally determined P_M-values were unavailable, we calculated them from the estimated hexadecane/water partition coefficients $K_{hex/w}$ in accordance with the solubility diffusion model, using semi-empirical correlations for neutral (Walter and Gutknecht, 1986), anionic (Ebert et al., 2018), and cationic (Ebert, 2020) molecules. Predicted values and the pertinent correlations are listed in **Table 4**. Partition coefficients were predicted using commercial software based on quantum chemical calculations and the COSMO-RS ("Conductor-like Screening Model for Realistic Solvation") theory. Thereby, Turbomole (TURBOMOLE V7.3 2018, a development of University of Karlsruhe and Forschungszentrum Karlsruhe GmbH, 1989–2007, TURBOMOLE GmbH, since 2007; available from http://www.turbomole.com) was used to generate so called COSMOfiles—surface charge densities of energetically optimized structures. Using COSMOconf (COSMOlogic GmbH & Co. KG; http://www.cosmologic.de: Leverkusen, Germany) we accounted for different possible conformers. COSMOtherm (Release 18 [2018] COSMOlogic GmbH & Co. KG) was used to calculate the partition coefficients. For more details see (Eckert and Klamt, 2002). All values were calculated at 22°C using the BP_TZVPD_FINE_parametrization.

4.4 Reliability of Predictions for Passive Membrane Permeabilities

A deviation of about 1 log unit between an experimentally determined and predicted *p*-value is normal when using COSMOtherm to calculate the membrane permeability of neutral solutes (Schwobel et al., 2020). For glucose the predicted value (listed in **Table 4**) and the experimentally determined value were in good agreement (P_{exp} = $3.0{\cdot}10^{-13}$ m/s (Brunner et al., 1980); P_{pred} = $2.5{\cdot}10^{-13}$ m/s). The deviation in the case of sucrose was higher (P_{exp} = $3.1{\cdot}10^{-14}$ m/s (Stefely et al., 2002); P_{exp} = $8{\cdot}10^{-16}$ m/s (Brunner et al., 1980); P_{pred} = $8{\cdot}10^{-18}$ m/s). NMDG can exist in a neutral and in a charged form (i.e., $NMDG_0$ and $NMDG^+$; pKa = 8.8). The predicted permeability of $NMDG_0$ was $2.5{\cdot}10^{-8}$ m/s. This value seemed high given that NMDG was thought to permeate slower through membranes than sodium or potassium ions (Dhoke et al., 2005; Elustondo et al., 2013; Reuss, 1979). To resolve this discrepancy, we determined the $NMDG_0$ permeability experimentally. These measurements allowed for calculating an upper limit of ~ 10^{-11} $\frac{m}{s}$ for $NMDG_0$ (**Figure 10**). The large deviation between predicted and measured value can be explained by conformer effects (22 relevant conformers were detected by COSMOconf, other important conformers might have been overlooked) and possible tautomeric effects. In addition, the complexity of the NMDG molecule (i.e., it harbors multiple functional groups) leads to larger prediction uncertainties (Ulrich et al., 2021). Due to the strongly decreased membrane permeability of cations as compared

TABLE 4 | Estimated values for passive $HEPES_0$, $HEPES^-$, glucose, sucrose, $NMDG_0$, and $NMDG^+$ membrane permeabilities, the corresponding hexadecane/water partition coefficients $K_{hex/w}$ (see Sections 4.3 and 4.4) and the pertinent correlations to calculate logP.

Compound	Log. Passive permeability log *P* [m/s]	Log $K_{hex/w}$	Used correlation	References
$NMDG^+$	−20.8	−21.2	$\log P = 0.6*\log K_{hex/w} - 8.1$	Ebert (2020)
$HEPES^-$	−17.4	−33.7	$\log P = 0.6*\log K_{hex/w} + 2.8$	Ebert et al. (2018)
HEPES	−20.1[a]		$\log P = 1.06*\log K_{hex/w} - 0.9$	(Walter and Gutknecht, 1986)
Zwitterion 1	−19.9	−17.9		
Zwitterion 2	−39.7	−35.1		
NMDG	−7.6	−6.3		
Glucose	−12.6	−11.0		
Sucrose	−17.1	−15.3		

[a]*Total zwitterionic HEPES permeability was calculated by multiplying the fraction of zwitterion 1 with the corresponding permeability. The HEPES zwitterion is present 59% of the time as zwitterion 1 (SMILES: OCCN1CC [NH+] (CC1)CCS([O-]) (=O) = O) and 41% as zwitterion 2 (SMILES: OCC [NH+] 1CCN (CC1) CCS ([O-]) (=O) = O) according to JChem for Office (Excel). This information was used for micro-pK_a calculation [JChem for Office 20.2.0.589, 2020, ChemAxon (http://www.chemaxon.com)].*

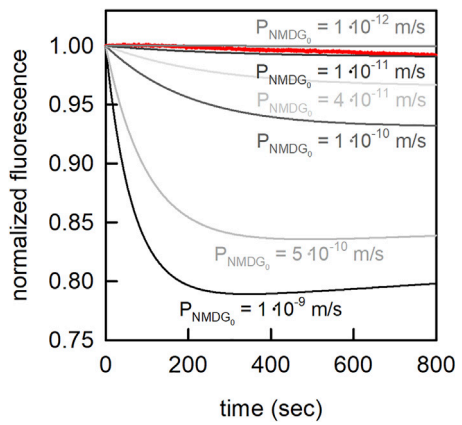

FIGURE 10 | Estimation of the passive membrane permeability of $NMDG_0$. In the presence of an outwardly directed NMDG gradient (10 mM inside to 3.33 mM outside) $NMDG_0$ diffused out of the vesicle, which led to a drop of the intraluminal pH. The extra- and intraluminal solutions contained 1 mM MES, and 100 mM NaCl. The pH on both sides of the membrane was 7.0. Shown in red is the measured change in carboxyfluorescein fluorescence on imposition of the NMDG gradient at time point zero. From these measurements we estimated an upper limit for the membrane permeability of $NMDG_0 \sim 10^{-11} m/s$

to their neutral counterparts, a significant $NMDG^+$ membrane permeability can be excluded.

4.5 Experimental Estimation of the Neutral NMDG Species Membrane Permeability

We measured $NMDG_0$ permeability with a pH sensitive vesicle assay (Hannesschlaeger et al., 2019a). In brief, *E. coli* polar lipids (PLE, Avanti Polar Lipids) were dried on a rotary evaporator. The thin lipid film was rehydrated in 100 mM NaCl, 1 mM MES, 0.5 mM Carboxyfluorescein, and 10 mM NMDG-Cl at pH 7.0 to obtain a final lipid concentration of 10 mg/ml. Subsequently, the solution was extruded through polycarbonate filters with 100-nm pore sizes using a mini-extruder from Avanti Polar Lipids. Free Carboxyfluorescein was removed using a PD10 column. Vesicle formation was confirmed by dynamic light scattering (DELSA Nano HC, Beckmann Coulter, data not shown). Finally, the 4x diluted vesicle suspension was mixed in a 1:2 ratio at room temperature with a solution void of NMDG-Cl in a stopped-flow apparatus (μ-SFM, Bio-Logic, Claix, France). At the final extra-vesicular ion concentrations (i.e., 100 mM NaCl, 1 mM MES, and 3.3 mM NMDG-Cl at pH 7.0) $NMDG_0$ effluxed out of the vesicles. The resulting drop in pH inside the vesicle was monitored using carboxyfluorescein at an excitation wavelength of 480 nm and a detector angle of 90°. At least three single shots were recorded and averaged per experiment. To correct for photo bleaching of carboxyfluorescein the same experiment was repeated using 10 mM NMDG-Cl outside, to eliminate efflux of NMDG. The experiment was repeated three times. To estimate an upper limit of $NMDG_0$ membrane permeability we simulated the kinetics using similar conditions but $NMDG_0$ flux rates varying between $10^{-9} - 10^{-12} m/s$.

DATA AVAILABILITY STATEMENT

The original contributions presented in the study are included in the article/Supplementary Material, further inquiries can be directed to the corresponding author.

AUTHOR CONTRIBUTIONS

AH and WS conceptualized the study. TB performed simulations. TB, WS, JW, CH, AE, AS, and AH contributed to the model and analyzed and discussed the *in-silico* data. JW is responsible for the art work. TB, WS, and AH wrote the manuscript. All authors approved the manuscript.

FUNDING

The financial support for this study is from the Austrian Science Fund (No. P31074) to AH and (No. P31813) to WS.

ACKNOWLEDGMENTS

We thank Aner Gurvitz for proofreading the manuscript.

REFERENCES

Adelman, J. L., Sheng, Y., Choe, S., Abramson, J., Wright, E. M., Rosenberg, J. M., et al. (2014). Structural Determinants of Water Permeation through the Sodium-Galactose Transporter vSGLT. *Biophysical J.* 106 (6), 1280–1289. doi:10.1016/j.bpj.2014.01.006

Adelman, J. L., Ghezzi, C., Bisignano, P., Loo, D. D. F., Choe, S., Abramson, J., et al. (2016). Stochastic Steps in Secondary Active Sugar Transport. *Proc. Natl. Acad. Sci. U.S.A.* 113 (27), E3960–E3966. doi:10.1073/pnas.1525378113

Benz, R., Beckers, F., and Zimmermann, U. (1979). Reversible Electrical Breakdown of Lipid Bilayer Membranes: a Charge-Pulse Relaxation Study. *J. Membrain Biol.* 48 (2), 181–204. doi:10.1007/BF01872858

Billesbølle, C. B., Mortensen, J. S., Sohail, A., Schmidt, S. G., Shi, L., Sitte, H. H., et al. (2016). Transition Metal Ion FRET Uncovers K+ Regulation of a Neurotransmitter/sodium Symporter. *Nat. Commun.* 7 (1), 12755. doi:10.1038/ncomms12755

Born, M. (1920). Volumen und Hydratationswärme der Ionen. *Z. Phys.* 1 (1), 45–48. doi:10.1007/bf01881023

Borsarelli, C. D., and Braslavsky, S. E. (1998). The Partial Molar Volume of the Proton in Water Determined by Laser-Induced Optoacoustic Studies. *J. Photochem. Photobiol. B Biol.* 43 (3), 222–228. doi:10.1016/s1011-1344(98)00112-2

Brunner, J., Graham, D. E., Hauser, H., and Semenza, G. (1980). Ion and Sugar Permeabilities of Lecithin Bilayers: Comparison of Curved and Planar Bilayers. *J. Membrain Biol.* 57 (2), 133–141. doi:10.1007/BF01868999

Burtscher, V., Schicker, K., Freissmuth, M., and Sandtner, W. (2019). Kinetic Models of Secondary Active Transporters. *Ijms* 20 (21), 5365. doi:10.3390/ijms20215365

Cortes, S., Barette, C., Beroud, R., De Waard, M., and Schaack, B. (2018). Functional Characterization of Cell-free Expressed Kv1.3 Channel Using a Voltage-Sensitive Fluorescent Dye. *Protein Expr. Purif.* 145, 94–99. doi:10.1016/j.pep.2018.01.006

Dhoke, M. A., Ladha, P. J., Boerio, F. J., Lessard, L. B., Malinowska, D. H., Cuppoletti, J., et al. (2005). Porous Membranes for Reconstitution of Ion Channels. *Biochimica Biophysica Acta (BBA) - Biomembr.* 1716 (2), 117–125. doi:10.1016/j.bbamem.2005.09.008

Ebert, A., Hannesschlaeger, C., Goss, K.-U., and Pohl, P. (2018). Passive Permeability of Planar Lipid Bilayers to Organic Anions. *Biophysical J.* 115 (10), 1931–1941. doi:10.1016/j.bpj.2018.09.025

Ebert, A. (2020) Permeability of Organic Ions through Biological Membranes, PhD Dissertation. Linz: Universität Linz

Eckert, F., and Klamt, A. (2002). Fast Solvent Screening via Quantum Chemistry: COSMO-RS Approach. *AIChE J.* 48 (2), 369–385. doi:10.1002/aic.690480220

Elustondo, P. A., Angelova, P. R., Kawalec, M., Michalak, M., Kurcok, P., Abramov, A. Y., et al. (2013). Polyhydroxybutyrate Targets Mammalian Mitochondria and Increases Permeability of Plasmalemmal and Mitochondrial Membranes. *PLoS One* 8 (9), e75812. doi:10.1371/journal.pone.0075812

Erokhova, L., Horner, A., Ollinger, N., Siligan, C., and Pohl, P. (2016). The Sodium Glucose Cotransporter SGLT1 Is an Extremely Efficient Facilitator of Passive Water Transport. *J. Biol. Chem.* 291 (18), 9712–9720. doi:10.1074/jbc.M115.706986

Feroz, H., Ferlez, B., Oh, H., Mohammadiarani, H., Ren, T., Baker, C. S., et al. (2021). Liposome-based Measurement of Light-Driven Chloride Transport Kinetics of Halorhodopsin. *Biochimica Biophysica Acta (BBA) - Biomembr.* 1863 (8), 183637. doi:10.1016/j.bbamem.2021.183637

Fucaloro, A. F., Pu, Y., Cha, K., Williams, A., and Conrad, K. (2007). Partial Molar Volumes and Refractions of Aqueous Solutions of Fructose, Glucose, Mannose, and Sucrose at 15.00, 20.00, and 25.00 °C. *J. Solut. Chem.* 36 (1), 61–80. doi:10.1007/s10953-006-9100-7

Gabba, M., and Poolman, B. (2020). Physiochemical Modeling of Vesicle Dynamics upon Osmotic Upshift. *Biophysical J.* 118 (2), 435–447. doi:10.1016/j.bpj.2019.11.3383

Gawrisch, K., Ruston, D., Zimmerberg, J., Parsegian, V. A., Rand, R. P., and Fuller, N. (1992). Membrane Dipole Potentials, Hydration Forces, and the Ordering of Water at Membrane Surfaces. *Biophysical J.* 61 (5), 1213–1223. doi:10.1016/s0006-3495(92)81931-8

Gest, A. M. M., Yaeger-Weiss, S. K., Lazzari-Dean, J. R., and Miller, E. W. (2021). VoltageFluor Dyes and Fluorescence Lifetime Imaging for Optical Measurement of Membrane Potential. *Methods Enzym.* 653, 267–293. doi:10.1016/bs.mie.2021.02.009

Gutknecht, J., and Walter, A. (1981a). Hydroxyl Ion Permeability of Lipid Bilayer Membranes. *Biochimica Biophysica Acta (BBA) - Biomembr.* 645 (1), 161–162. doi:10.1016/0005-2736(81)90525-3

Gutknecht, J., and Walter, A. (1981b). Transport of Protons and Hydrochloric Acid through Lipid Bilayer Membranes. *Biochimica Biophysica Acta (BBA) - Biomembr.* 641 (1), 183–188. doi:10.1016/0005-2736(81)90582-4

Gutman, M., and Nachliel, E. (1990). The Dynamic Aspects of Proton Transfer Processes. *Biochimica Biophysica Acta (BBA) - Bioenergetics* 1015 (3), 391–414. doi:10.1016/0005-2728(90)90073-d

Hannesschlaeger, C., Barta, T., Pechova, H., and Pohl, P. (2019a). The Effect of Buffers on Weak Acid Uptake by Vesicles. *Biomolecules* 9 (2), 63. doi:10.3390/biom9020063

Hannesschlaeger, C., Horner, A., and Pohl, P. (2019b). Intrinsic Membrane Permeability to Small Molecules. *Chem. Rev.* 119 (9), 5922–5953. doi:10.1021/acs.chemrev.8b00560

Hannesschläger, C., Barta, T., Siligan, C., and Horner, A. (2018). Quantification of Water Flux in Vesicular Systems. *Sci. Rep.* 8 (1), 8516. doi:10.1038/s41598-018-26946-9

Hauser, H., Phillips, M. C., and Stubbs, M. (1972). Ion Permeability of Phospholipid Bilayers. *Nature* 239 (5371), 342–344. doi:10.1038/239342a0

Hediger, M. A., Romero, M. F., Peng, J.-B., Rolfs, A., Takanaga, H., and Bruford, E. A. (2004). The ABCs of Solute Carriers: Physiological, Pathological and Therapeutic Implications of Human Membrane Transport Proteins. *Pflugers Archiv Eur. J. Physiology* 447 (5), 465–468. doi:10.1007/s00424-003-1192-y

Heinz, E., and Weinstein, A. M. (1984). The Overshoot Phenomenon in Cotransport. *Biochimica Biophysica Acta (BBA) - Biomembr.* 776 (1), 83–91. doi:10.1016/0005-2736(84)90253-0

Hoomann, T., Jahnke, N., Horner, A., Keller, S., and Pohl, P. (2013). Filter Gate Closure Inhibits Ion but Not Water Transport through Potassium Channels. *Proc. Natl. Acad. Sci. U.S.A.* 110 (26), 10842–10847. doi:10.1073/pnas.1304714110

Horner, A., Zocher, F., Preiner, J., Ollinger, N., Siligan, C., Akimov, S. A., et al. (2015). The Mobility of Single-File Water Molecules Is Governed by the Number of H-Bonds They May Form with Channel-Lining Residues. *Sci. Adv.* 1 (2), e1400083. doi:10.1126/sciadv.1400083

Hwang, E.-S., Hirayama, B. A., and Wright, E. M. (1991). Distribution of the SGLT1 Na+glucose Cotransporter and mRNA along the Crypt-Villus axis of Rabbit Small Intestine. *Biochem. Biophysical Res. Commun.* 181 (3), 1208–1217. doi:10.1016/0006-291x(91)92067-t

Jardetzky, O. (1966). Simple Allosteric Model for Membrane Pumps. *Nature* 211 (5052), 969–970. doi:10.1038/211969a0

Johnson, S. M., and Bangham, A. D. (1969). Potassium Permeability of Single Compartment Liposomes with and without Valinomycin. *Biochimica Biophysica Acta (BBA) - Biomembr.* 193 (1), 82–91. doi:10.1016/0005-2736(69)90061-3

Kanehisa, M. I., and Tsong, T. Y. (2002). Cluster Model of Lipid Phase Transitions with Application to Passive Permeation of Molecules and Structure Relaxations in Lipid Bilayers. *J. Am. Chem. Soc.* 100 (2), 424–432. doi:10.1021/ja00470a011

Li, J., Shaikh, S. A., Enkavi, G., Wen, P.-C., Huang, Z., and Tajkhorshid, E. (2013). Transient Formation of Water-Conducting States in Membrane Transporters. *Proc. Natl. Acad. Sci. U.S.A.* 110 (19), 7696–7701. doi:10.1073/pnas.1218986110

Loland, C., Schmidt, S., Malle, M., Nielsen, A., Bohr, S., Pugh, C., et al. (2022). The Dopamine Transporter Counter-transports Potassium to Increase the Uptake of Dopamine. *Nat. Commun.* 13, 1–7701. doi:10.1038/s41467-022-30154-5

McLaughlin, S. (1989). The Electrostatic Properties of Membranes. *Annu. Rev. Biophys. Biophys. Chem.* 18, 113–136. doi:10.1146/annurev.bb.18.060189.000553

Megens, M., Korman, C. E., Ajo-Franklin, C. M., and Horsley, D. A. (2014). Faster-Than-anticipated Na+/Cl− Diffusion across Lipid Bilayers in Vesicles. *Biochimica Biophysica Acta (BBA) - Biomembr.* 1838 (10), 2420–2424. doi:10.1016/j.bbamem.2014.05.010

Mehta, P., Raymond, J., Punjani, R., Larson, T., Bove, F., Kaye, W., et al. (2021). Prevalence of Amyotrophic Lateral Sclerosis (ALS), United States, 2016. *Amyotroph. Lateral Scler. Frontotemporal Degener.* 23, 220–225. doi:10.1080/21678421.2021.1949021

Meinild, A.-K., Klaerke, D. A., Loo, D. D. F., Wright, E. M., and Zeuthen, T. (1998). The Human Na+-Glucose Cotransporter Is a Molecular Water Pump. *J. Physiol.* 508 (Pt 1), 15–21. doi:10.1111/j.1469-7793.1998.015br.x

Millero, F. J. (2002). Molal Volumes of Electrolytes. *Chem. Rev.* 71 (2), 147–176. doi:10.1021/cr60270a001

Mimms, L. T., Zampighi, G., Nozaki, Y., Tanford, C., and Reynolds, J. A. (1981). Phospholipid Vesicle Formation and Transmembrane Protein Incorporation Using Octyl Glucoside. *Biochemistry* 20 (4), 833–840. doi:10.1021/bi00507a028

Montal, M., and Mueller, P. (1972). Formation of Bimolecular Membranes from Lipid Monolayers and a Study of Their Electrical Properties. *Proc. Natl. Acad. Sci. U.S.A.* 69 (12), 3561–3566. doi:10.1073/pnas.69.12.3561

Niu, H., Álvarez-Álvarez, I., Guillén-Grima, F., and Aguinaga-Ontoso, I. (2017). Prevalence and Incidence of Alzheimer's Disease in Europe: A Meta-Analysis. *Neurol. Engl. Ed.* 32 (8), 523–532. doi:10.1016/j.nrleng.2016.02.009

Nozaki, Y., and Tanford, C. (1981). Proton and Hydroxide Ion Permeability of Phospholipid Vesicles. *Proc. Natl. Acad. Sci. U.S.A.* 78 (7), 4324–4328. doi:10.1073/pnas.78.7.4324

Omote, H., Hiasa, M., Matsumoto, T., Otsuka, M., and Moriyama, Y. (2006). The MATE Proteins as Fundamental Transporters of Metabolic and Xenobiotic Organic Cations. *Trends Pharmacol. Sci.* 27 (11), 587–593. doi:10.1016/j.tips.2006.09.001

Papahadjopoulos, D., Nir, S., and Ohki, S. (1972). Permeability Properties of Phospholipid Membranes: Effect of Cholesterol and Temperature. *Biochimica Biophysica Acta (BBA) - Biomembr.* 266 (3), 561–583. doi:10.1016/0005-2736(72)90354-9

Parent, L., Supplisson, S. p., Loo, D. F., and Wright, E. (1992). Electrogenic Properties of the Cloned Na+/glucose Cotransporter: II. A Transport Model under Nonrapid Equilibrium Conditions. *J. Membarin Biol.* 125 (1), 63–79. doi:10.1007/BF00235798

Parsegian, A. (1969). Energy of an Ion Crossing a Low Dielectric Membrane: Solutions to Four Relevant Electrostatic Problems. *Nature* 221 (5183), 844–846. doi:10.1038/221844a0

Paula, S., Volkov, A. G., Van Hoek, A. N., Haines, T. H., and Deamer, D. W. (1996). Permeation of Protons, Potassium Ions, and Small Polar Molecules through Phospholipid Bilayers as a Function of Membrane Thickness. *Biophysical J.* 70 (1), 339–348. doi:10.1016/s0006-3495(96)79575-9

Pohl, P., Saparov, S. M., Borgnia, M. J., and Agre, P. (2001). Highly Selective Water Channel Activity Measured by Voltage Clamp: Analysis of Planar Lipid Bilayers Reconstituted with Purified AqpZ. *Proc. Natl. Acad. Sci. U.S.A.* 98 (17), 9624–9629. doi:10.1073/pnas.161299398

Reuss, L. (1979). Electrical Properties of the Cellular Transepithelial Pathway inNecturus Gallbladder: III. Ionic Permeability of the Basolateral Cell Membrane. *J. Membrain Biol.* 47 (3), 239–259. doi:10.1007/BF01869080

Rudnick, G., and Sandtner, W. (2019). Serotonin Transport in the 21st Century. *J. General Physiology* 151 (11), 1248–1264. doi:10.1085/jgp.201812066

Saha, S., Chant, D., Welham, J., and McGrath, J. (2005). A Systematic Review of the Prevalence of Schizophrenia. *PLoS Med.* 2 (5), e141. doi:10.1371/journal.pmed.0020141

Sano, R., Shinozaki, Y., and Ohta, T. (2020). Sodium-glucose Cotransporters: Functional Properties and Pharmaceutical Potential. *J. Diabetes Investig.* 11 (4), 770–782. doi:10.1111/jdi.13255

Schwöbel, J. A. H., Ebert, A., Bittermann, K., Huniar, U., Goss, K.-U., and Klamt, A. (2020). COSMOperm: Mechanistic Prediction of Passive Membrane Permeability for Neutral Compounds and Ions and its pH Dependence. *J. Phys. Chem. B* 124 (16), 3343–3354. doi:10.1021/acs.jpcb.9b11728

Shen, Y., Zhong, Y., Fei, F., Sun, J., Czajkowsky, D. M., Gong, B., et al. (2020). Ultrasensitive Liposome-Based Assay for the Quantification of Fundamental Ion Channel Properties. *Anal. Chim. Acta* 1112, 8–15. doi:10.1016/j.aca.2020.03.044

Stefely, J., Markowitz, M. A., and Regen, S. L. (2002). Permeability Characteristics of Lipid Bilayers from Lipoic Acid-Derived Phosphatidylcholines. Comparison of Monomeric, Crosslinked and Noncrosslinked Polymerized Membranes. *J. Am. Chem. Soc.* 110 (22), 7463–7469. doi:10.1021/ja00230a030

Stillinger, F. H. (1978). Proton Transfer Reactions and Kinetics in Water. *Theor. Chem. Adv. Perspect.* 3, 177–234. doi:10.1016/b978-0-12-681903-8.50011-4

Toyoshima, Y., and Thompson, T. E. (1975). Chloride Flux in Bilayer Membranes. Chloride Permeability in Aqueous Dispersions of Single-Walled, Bilayer Vesicles. *Biochemistry* 14 (7), 1525–1531. doi:10.1021/bi00678a028

Ulrich, N., Goss, K.-U., and Ebert, A. (2021). Exploring the Octanol-Water Partition Coefficient Dataset Using Deep Learning Techniques and Data Augmentation. *Commun. Chem.* 4 (1), 90. doi:10.1038/s42004-021-00528-9

von Heijne, G. (1992). Membrane Protein Structure Prediction. *J. Mol. Biol.* 225 (2), 487–494. doi:10.1016/0022-2836(92)90934-c

Wachlmayr, J., Hannesschlaeger, C., Speletz, A., Barta, T., Eckerstorfer, A., Siligan, C., et al. (2022). Scattering versus Fluorescence Self-Quenching: More Than a Question of Faith for the Quantification of Water Flux in Large Unilamellar Vesicles? *Nanoscale Adv.* 4 (1), 58–76. doi:10.1039/d1na00577d

Walter, A., and Gutknecht, J. (1986). Permeability of Small Nonelectrolytes through Lipid Bilayer Membranes. *J. Membrain Biol.* 90 (3), 207–217. doi:10.1007/BF01870127

Wang, J., Dlamini, D. S., Mishra, A. K., Pendergast, M. T. M., Wong, M. C. Y., Mamba, B. B., et al. (2014). A Critical Review of Transport through Osmotic Membranes. *J. Membr. Sci.* 454, 516–537. doi:10.1016/j.memsci.2013.12.034

Wang, J., Zhang, K., Goyal, P., and Grewer, C. (2020). Mechanism and Potential Sites of Potassium Interaction with Glutamate Transporters. *J. General Physiology* 152 (10). e202012577. doi:10.1085/jgp.202012577

Wright, E. M., Loo, D. D. F., and Hirayama, B. A. (2011). Biology of Human Sodium Glucose Transporters. *Physiol. Rev.* 91 (2), 733–794. doi:10.1152/physrev.00055.2009

Zeuthen, T., Gorraitz, E., Her, K., Wright, E. M., and Loo, D. D. F. (2016). Structural and Functional Significance of Water Permeation through Cotransporters. *Proc. Natl. Acad. Sci. U.S.A.* 113 (44), E6887–E6894. doi:10.1073/pnas.1613744113

Conflict of Interest: The authors declare that the research was conducted in the absence of any commercial or financial relationships that could be construed as a potential conflict of interest.

frontiers | Frontiers in Physiology

ORIGINAL RESEARCH
published: 25 August 2022
doi: 10.3389/fphys.2022.895324

Uncoupling of Voltage- and Ligand-Induced Activation in HCN2 Channels by Glycine Inserts

Sezin Yüksel[1†], Michele Bonus[2†], Tina Schwabe[1], Christopher Pfleger[2], Thomas Zimmer[1], Uta Enke[1], Inga Saß[1], Holger Gohlke[3,2†], Klaus Benndorf[1*†] and Jana Kusch[1*†]*

[1]Universitätsklinikum Jena, Institut für Physiologie II, Jena, Germany, [2]Institut für Pharmazeutische und Medizinische Chemie, Heinrich-Heine-Universität Düsseldorf, Düsseldorf, Germany, [3]John von Neumann Institute for Computing (NIC), Jülich Supercomputing Centre (JSC), Institute of Biological Information Processing (IBI-7: Structural Biochemistry) and Institute of Bio- and Geosciences (IBG-4: Bioinformatics), Forschungszentrum Jülich GmbH, Jülich, Germany

OPEN ACCESS

Edited by:
Han Sun,
Leibniz-Institut für Molekulare Pharmakologie (FMP), Germany

Reviewed by:
Gucan Dai,
Saint Louis University, United States
Eric Accili,
University of British Columbia, Canada

***Correspondence:**
Holger Gohlke
gohlke@uni-duesseldorf.de
Klaus Benndorf
Klaus.Benndorf@med.uni-jena.de
Jana Kusch
Jana.Kusch@med.uni-jena.de

[†]These authors have contributed equally to this work

Specialty section:
This article was submitted to Membrane Physiology and Membrane Biophysics, a section of the journal Frontiers in Physiology

Received: 13 March 2022
Accepted: 20 June 2022
Published: 25 August 2022

Citation:
Yüksel S, Bonus M, Schwabe T, Pfleger C, Zimmer T, Enke U, Saß I, Gohlke H, Benndorf K and Kusch J (2022) Uncoupling of Voltage- and Ligand-Induced Activation in HCN2 Channels by Glycine Inserts. Front. Physiol. 13:895324. doi: 10.3389/fphys.2022.895324

Hyperpolarization-activated cyclic nucleotide-modulated (HCN) channels are tetramers that generate electrical rhythmicity in special brain neurons and cardiomyocytes. The channels are activated by membrane hyperpolarization. The binding of cAMP to the four available cyclic nucleotide-binding domains (CNBD) enhances channel activation. We analyzed in the present study the mechanism of how the effect of cAMP binding is transmitted to the pore domain. Our strategy was to uncouple the C-linker (CL) from the channel core by inserting one to five glycine residues between the S6 gate and the A′-helix (constructs 1G to 5G). We quantified in full-length HCN2 channels the resulting functional effects of the inserted glycines by current activation as well as the structural dynamics and statics using molecular dynamics simulations and Constraint Network Analysis. We show functionally that already in 1G the cAMP effect on activation is lost and that with the exception of 3G and 5G the concentration-activation relationships are shifted to depolarized voltages with respect to HCN2. The strongest effect was found for 4G. Accordingly, the activation kinetics were accelerated by all constructs, again with the strongest effect in 4G. The simulations reveal that the average residue mobility of the CL and CNBD domains is increased in all constructs and that the junction between the S6 and A′-helix is turned into a flexible hinge, resulting in a destabilized gate in all constructs. Moreover, for 3G and 4G, there is a stronger downward displacement of the CL-CNBD than in HCN2 and the other constructs, resulting in an increased kink angle between S6 and A′-helix, which in turn loosens contacts between the S4-helix and the CL. This is suggested to promote a downward movement of the S4-helix, similar to the effect of hyperpolarization. In addition, exclusively in 4G, the selectivity filter in the upper pore region and parts of the S4-helix are destabilized. The results provide new insights into the intricate activation of HCN2 channels.

Keywords: HCN2 channels, voltage-dependent gating, cAMP-dependent gating, autoinhibition, patch-clamp technique, confocal patch-clamp fluorometry, molecular modeling, molecular dynamics simulations

1 INTRODUCTION

Hyperpolarization-activated cyclic nucleotide-modulated (HCN) channels are members of the superfamily of voltage-gated ion channels (Clapham, 1998). They are involved in a large variety of physiological and pathophysiological processes by playing a pivotal role in mediating electrical pacemaking activity of specialized cardiac and neuronal cells (Wahl-Schott and Biel, 2009). For mammalians, four isoforms have been described so far, HCN1-HCN4, all of them forming functional homo- or heterotetrameric channels (Biel et al., 2009).

Each of the four subunits consists of four domains: 1) a transmembranal voltage sensor domain (VSD) including the helices S1 to S4, 2) a pore domain (PD), 3) an intracellular domain formed by the C-linker (CL) disk and the binding site for cyclic nucleotides (CNBD), and 4) an HCN domain at the channel's periphery (HCND) (**Figure 1A**). The channel gate is formed by the intracellular ends of the S6-helices (Rothberg et al., 2002) that are arranged in a right-handed, tightly packed bundle at the inner entrance of the pore (Lee and MacKinnon, 2017). The four C-linkers form a gating-ring (Craven and Zagotta, 2004) between the transmembrane channel core and the ring-like structure built by the four CNBDs, as shown previously by resolving the crystal structure of isolated tetrameric CNBDs (Zagotta et al., 2003; Xu et al., 2010; Lolicato et al., 2011).

HCN channels are dually regulated by membrane hyperpolarization and cyclic nucleotide (cNMP) binding (Wang et al., 2001; Craven and Zagotta, 2006), with membrane voltage as the obligatory trigger and cNMP binding as a gating modulator. It has been proposed that the closed state of the channel is stabilized by a tight packing of the S4 to S6 helices and an unusually long S4-helix, protruding until the CL (Lee and MacKinnon, 2017). Membrane hyperpolarization would move the S4-helix into an intracellular direction, thereby disrupting the stabilizing effects of the mentioned components, presumably with a specific significance of only a few residues at the C-terminal part of S4 (Ramentol et al., 2020), leading to an opening of the gate. Additionally, previous work on HCN2 channels presented evidence for various interactions between the S4-S5 linker and the A′-helix of the CL during the gating process (Decher et al., 2004). It has been proposed that the gate opens by unwinding the S6-helix bundle as a consequence of an anti-clockwise rotation viewed from the extracellular side and an iris-like movement of the CL gating-ring (Craven and Zagotta, 2004; Shin et al., 2004; Lee and MacKinnon, 2017; Weissgraeber et al., 2017; Gross et al., 2018; Marchesi et al., 2018). In a recent study, Porro and co-workers assigned a regulatory role to the HCN-domain: it exerts an inhibitory effect on the voltage sensor via keeping it in a position unfavorable for channel opening (Porro et al., 2019). This supports the structural findings of Lee and MacKinnon, who suggested that the HCN domain stabilizes the closed state (Lee and MacKinnon, 2017).

According to the tetrameric structure of HCN channels, up to four cNMP molecules can bind to a channel. cNMP binding stabilizes a state that promotes the opening of the channels by relieving an autoinhibitory effect of the empty CNBD-CL portion on the gate (Wainger et al., 2001; Zhou and Siegelbaum, 2007; Craven et al., 2008). Consequently, both the rate and the extent of channel activation evoked by hyperpolarization are increased, and steady-state activation is shifted to less negative voltages (Robinson and Siegelbaum, 2003; Craven and Zagotta, 2006). Structural data showed that cNMP binding causes a similar rotation of the gating as VSD movement, but to a lesser degree and with a smaller resulting S6 displacement. Thus, cAMP supports activation by initiating the rotation of the gate-forming helices towards opening (Lee and MacKinnon, 2017).

In the present study, we focused on the mechanism of how cAMP binding controls the channel gate in the PD. Our strategy was to uncouple the CL from the S6 gate by inserting one to five glycine residues between the S6 and the A′-helix and to identify the resulting functional effects on both the activation gating and, reciprocally, on cAMP binding. We furthermore probed the effects of the additional amino acid sequences (AAASs) between channel gate and C-linker on the structural dynamics and statics of full-length HCN2 by molecular dynamics simulations and Constraint Network Analysis (CNA).

Here We show that the average residue mobility of the CL and CNBD domains is increased in 1G through 5G, which results in a destabilized S6 gate in all constructs. A stronger downward displacement was identified for 3G and 4G, which was not observed in HCN2 and the other constructs. This downward displacement loosens the contacts between the S4-helix and the CL, promoting a downward movement of the S4-helix similar to the effect of hyperpolarization. Exclusively in 4G, two additional effects distant from the CL-CNBD were observed: the selectivity filter in the upper pore region and parts of the S4-helix are destabilized. These computational interpretations can explain the lost cAMP effect by inserting only a single glycine, the observed shifts of steady-state activation to depolarized voltages, and the accelerated activation time courses by all constructs, as well as the exceedingly large effects observed for 4G. Our results help to improve our understanding of the activation mechanism in HCN2 channels.

2 MATERIALS AND METHODS

2.1 *Xenopus laevis* Oocytes as Heterologous Expression System

Oocytes were surgically removed from adult female South African claw frogs *Xenopus laevis* under anesthesia with 0.3% tricaine methanesulfonate (MS-222) (Pharmaq Ltd. Fordingbridge, United Kingdom). After removal, the oocytes were treated with collagenase A (3 mg/ml; Roche, Grenzach-Wyhlen, Germany) for 105 min in Ca^{2+}-free Barth's solution containing (in mM) 82.5 NaCl, 2 KCl, 1 $MgCl_2$, and 5 Hepes, pH 7.5. Oocytes of stages IV and V were manually dissected and injected with cRNA encoding either mHCN2 channels of Mus musculus or the mHCN2 mutants 1G, 2G, 3G, 4G, 5G, respectively. After injection with cRNA, the oocytes were incubated at 18°C for 2–6 days in Barth's solution containing (in mM) 84 NaCl, 1 KCl, 2.4 $NaHCO_3$, 0.82 $MgSO_4$, 0.41 $CaCl_2$, 0.33 $Ca(NO_3)_2$, 7.5 TRIS, pH 7.4. Oocytes harvested in our lab were complemented with

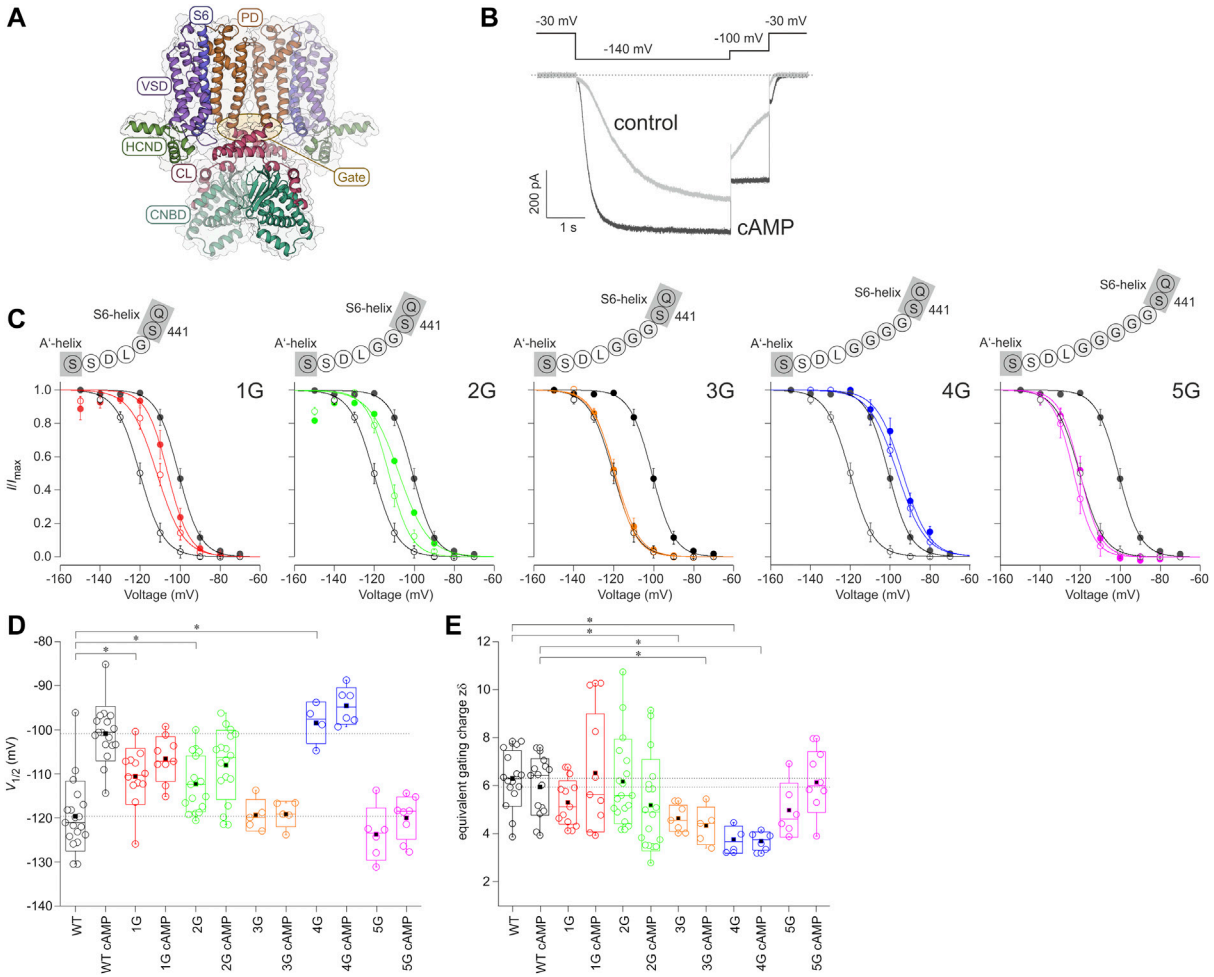

FIGURE 1 | Effect of inserting different numbers of glycines between S6 and A′-helix on channel gating. **(A)** Structural model of the homotetrameric HCN2 channel (residues L136 to D650) as a side view. The gray bars depict the approximate location of the membrane bilayer. The voltage sensor domain (VSD), pore domain (PD), C-Linker (CL), cyclic nucleotide-binding domain (CNBD), and HCN domain (HCND) are illustrated. The arrow indicates the site of glycine insertion. **(B)** Exemplary current traces for HCN2 activation under control conditions without cAMP (grey trace) and with a saturating concentration of 10 μM cAMP (black trace). The used voltage protocol is shown above. **(C)** Steady-state activation relationships for all five mutated constructs in comparison to HCN2. Open symbols represent control conditions without cAMP, filled symbols represent recordings at 10 μM cAMP (n = 4–18). In all panels, black lines and symbols represent HCN2. The modified sequences are illustrated for each construct. **(D)** Box plots resenting $V_{1/2}$ values without cAMP and with 10 μM cAMP with the following representations of the box features: center lines = medians, box limits = standard deviation, whiskers = minimum and maximum values, circles = individual recordings, squares = means. Horizontal black lines illustrate the wildtype values with and without cAMP for comparison. Significant differences are indicated by asterisks. **(E)** Box plot of $z\delta$ values. Box features are the same as in **(D)**. Significant differences are indicated by asterisks.

ready-to-use oocytes purchased from Ecocyte Bioscience (Dortmund, Germany). The surgery procedures were carried out in accordance with the German Animal Welfare Act with the approval of the Thuringian State Office for Consumer Protection on 30.08.2013 and 09.05.2018.

2.2 Molecular Biology

One to five additional glycines were introduced into the mouse HCN2 cDNA (UniProt ID O88703 including two modifications, G8E and E55G without functional relevance) between residues S441 and L442 in mouse pGEM-HCN2 (Kusch et al., 2010) using overlapping PCR. First, PCRs were set up using forward outside primer (5′-CCTGCTGGGATCCGAATTCCACCATGGATG CGCG-3′) and reverse primer introducing the glycine (1G: 5′-GTGACGAATCCAGGCCGGACTGGATGAGC-3’; 2G: 5′-GTGACGAATCCAGGCCGCCGGACTGGATGAGC-3’; 3G: 5′-GTGACGAATCCAGGCCTCCGCCGGACTGGATGAGC-3’; 4G: 5′-CGTGACGAATCCAGTCCGCCTCCGCCGGAC TGGATG-3′) as well as reverse outside primer (5′-CTCGTG AGCAAGCAGATCTCCCCGAAATAGGAGC-3′) and forward primer introducing the mutation (1G: 5′-CTCATCCAGTCC GGCCTGGATTCGTCAC-3’; 2G: 5′-GCTCATCCAGTCCGG CGGCCTGGATTCGTCAC-3’; 3G: 5′-GCTCATCCAGTC CGGCGGAGGCCTGGATTCGTCAC-3’; 4G: 5′-CTGCGC TCATCCAGTCCGGCGGAGGCGGACTGGATTC-3′). The PCR products were used as templates in a final PCR using the

two outer primers containing restriction sites for EcoRI and BglII, respectively. The resulting fragments were subcloned into the pGEM-HCN2. To construct 5G we used pGem-HCN2-4G as a template and the following internal primer pair: 5′-CCGGCG GAGGCGGGGGACTGGATTCGTCACGGCG-3′ and 5′-TGA CGAATCCAGTCCCCCGCCTCCGCCGGACTGGATGAG-3'. The flanking forward and reverse primers were: 5′-CTCCCTGCGGATGTTCGGCA-3′and 5′-ATTCCTCCAGCA CCTCGTTGA-3′, respectively. The recombinant PCR product was inserted as a PsyI/BglII fragment into the corresponding sites of pGEM-HCN2. A thermostable DNA polymerase with proofreading activity was used for the respective PCR reactions (Pfu DNA polymerase, Promega, Madison, United States). The accuracy of the sequences of the inserts was confirmed by restriction digests and sequencing (Microsynth, Balgach, Switzerland). cRNAs were prepared using the mMESSAGE mMACHINE T7 Kit (Ambion).

2.3 Electrophysiological Experiments

Macroscopic currents were recorded using the inside-out configuration of the patch-clamp technique. All measurements were started after a delay of 3.5 min to minimize run-down phenomena. Patch pipettes were pulled from quartz tubings with outer and inner diameters of 1.0 and 0.7 mm (VITROCOM, New Jersey, United States), respectively, using a laser puller (P-2000, Sutter Instrument, Novato, United States). The pipette resistance was 1.2–2.1 MOhm. The bath solution contained (in mM) 100 KCl, 10 EGTA, and 10 Hepes, pH 7.2, and the pipette solution contained (in mM) 120 KCl, 10 Hepes, and 1.0 CaCl2, pH 7.2. For parts of the experiments, a saturating concentration of 10 µM cAMP (BIOLOG LSI GmbH & Co. KG, Bremen, Germany) was applied with the bath solution. A HEKA EPC 10 USB amplifier (Harvard Apparatus, Holliston, United States) was used for current recording. Pulsing and data recording were controlled by the Patchmaster software (Harvard Apparatus, Holliston, United States). The sampling rate was 5 kHz. The holding potential was generally −30 mV. Maximally two membrane patches were excised from one individual oocyte. For steady-state activation curves, relative current values for each recording were fitted individually (see Quantification and statistical analysis).

2.4 Quantification and Statistical Analysis

Steady-state activation curves were analyzed by fitting the Boltzmann equation to each individual recording using the OriginPro 9.0G software (Northampton, United States):

$$\frac{I}{I_{max}} = \frac{\frac{I}{I_{max,satV}}}{1 + e^{\frac{z\delta F\left(V - V_{1/2}\right)}{RT}}} \quad (1)$$

$I/I_{\max}$ is the relative current, $I/I_{\max,\,satV}$ is the relative current at a saturating voltage and the actual cAMP concentration, $V_{1/2}$ is the voltage of half-maximum activation, and $z\delta$ the effective gating charge. F, R, and T are the Faraday constant, the molar gas constant, and the temperature in Kelvin, respectively. The time courses of current activation were fitted with a single exponential starting after an initial delay using the OriginPro 9.0G software (Northampton, United States):

$$I(t) = Ae^{\frac{-t}{\tau}} \quad (2)$$

A is the amplitude, t the time, and τ the time constant for activation.

Experimental data are given as mean ± standard error of the mean (SEM). Statistical analysis was performed by an unpaired Student's t-test. A value of $p < 0.05$ was accepted as statistically significant.

2.5 Confocal Patch-Clamp Fluorometry

The fluorescence intensity in the patch quantifying ligand binding was measured by patch-clamp fluorometry (Zheng and Zagotta, 2000; Zheng and Zagotta, 2003) combined with confocal microscopy (Biskup et al., 2007; Kusch et al., 2010). As fluorescent ligand, we used 8-AHT-Cy3B-cAMP (f1cAMP), a cAMP derivative in which the fluorescent dye Cy3B (GE Healthcare, Frankfurt, Germany) was linked via an aminohexylthio spacer to position 8 of the adenosine moiety (Otte et al., 2018; Otte et al., 2019). The recordings were performed with an LSM 710 confocal microscope (Carl Zeiss AG, Jena, Germany). They were triggered by the ISO3 software (MFK, Niedernhausen, Germany). To distinguish the fluorescence of the non-bound f1cAMP from that of the bound f1cAMP, a second, chemically related dye, DY647 (Dyomics GmbH, Jena, Germany), was added to the bath solution. The 543 and 633 nm lines of a He-Ne laser were used to excite f1cAMP and DY647, respectively. For quantifying the bound fcAMP, the fluorescence intensities of the red and the green channels were corrected for small offsets, and the fluorescence in the red channel was scaled to the fluorescence in the green channel in the bath. The difference between the measured green and the scaled red profile for each pixel of the confocal image represents the fraction of the fluorescence signal originating from the bound f1cAMP. Only the free patch membrane (patch dome) was used to quantify binding by setting a mask at a region of interest. The fluorescence, F, was averaged over all pixels inside this mask and normalized in each patch with respect to the fluorescence at saturating [f1cAMP] and full channel activation (−130 mV), $F_{\max}$. The recording rate of the confocal images was 10 Hz.

Concentration-binding relationships were analyzed by fitting the Hill equation to the mean data using the OriginPro 9.0G software (Northampton, United States):

$$\frac{F}{F_{max}} = \frac{1}{1 + \left(\frac{BC_{50}}{x}\right)^{H_b}} \quad (3)$$

with F being the actual fluorescence intensity, $F_{\max}$ the maximal current amplitude at a saturating f1cAMP concentration and −130 mV, BC_{50} the concentration of half-maximum binding, and H_b the Hill coefficient.

2.6 Computational Studies

To determine if changes in the structural dynamics of specific regions in the 1G-5G constructs can be related to the

electrophysiological results, we applied a combination of comparative modeling, molecular dynamics (MD) simulations, and rigidity analyses.

2.6.1 Comparative Structural Modeling of mHCN2 Wildtype and the mHCN2-1G, -3G, -4G, and -5G Constructs

We generated structural models of the murine HCN2 wildtype channel (mHCN2; UniProt ID: O88703) and the corresponding 1G, 3G, 4G, and 5G constructs (Ser441_Leu442ins$Gly_{1\text{-}5}$) using the RosettaCM method (Song et al., 2013) within the Rosetta macromolecular modeling, docking and design software (Koehler Leman et al., 2020). We did not generate a structure for 2G, given that the electrophysiological phenotype of 2G was similar to 1G with respect to $V_{1/2}$. We selected two HCN1 structures (PDB IDs: 5U6O (Lee and MacKinnon, 2017) and 6UQG (Lee and MacKinnon, 2019)) and one HCN4 structure (PDB ID: 6GYN (Shintre et al., 2019)) as template structures for the hybridization approach in RosettaCM (Song et al., 2013). Among the available template structures with the highest sequence identity to HCN2, these structures also showed the highest structural similarity to each other. By excluding template structures in other conformational states, we aimed to avoid hybridization artifacts that might result from erroneous recombination of template structures in different conformational states. To predict the secondary structure of the protein for 3mer- and 9mer-fragment picking, we used both the server implementation of PSIPRED (Buchan et al., 2013; Buchan and Jones, 2019) and the corresponding standalone version (Jones, 1999), as well as the RaptorX-Property server (Wang et al., 2016). We used the standalone version of PSIPRED with a position-specific scoring matrix obtained from a PSI-BLAST (Altschul et al., 1997) run against the NCBI NR database (as of 05/2020) executed with the same arguments as specified in the Rosetta internal utility make_fragments.pl. To identify residues in transmembrane regions for the RosettaMP framework (Alford et al., 2015), we submitted the threaded template structures to the PPM Web Server (Lomize et al., 2012) and considered the consensus transmembrane residues in all structures in the final span file. We determined the required centroid and full atom parameter sets for cAMP using the Rosetta tool molfile_to_params.py with the cAMP conformers in 6UQG and 6UQF (Lee and MacKinnon, 2019). Subsequently, using equal weights for all template structures, we generated 100 symmetric models for the wildtype channel and each glycine linker construct. Then, maintaining symmetry, we relaxed each lowest-energy model using eight repetitions of the FastRelax Mover in RosettaScripts (Fleishman et al., 2011) with the franklin2019 scoring function (Alford et al., 2020), again creating 100 models. We considered the relaxed structure with the lowest total energy as the final model for all subsequent steps.

2.6.2 MD Simulations

2.6.2.1 System Setup

The structures of wildtype mHCN2 and the mHCN2-1G, -3G, -4G, and -5G constructs were embedded in a membrane bilayer consisting of approximately 34% cholesterol, 36% 1-palmitoyl-2-oleoyl-*sn*-glycero-3-phosphocholine (POPC), 17% 1-palmitoyl-2-oleoyl-*sn*-glycero-3-phosphoethanolamine, and 13% 1-palmitoyl-2-oleoyl-*sn*-glycero-3-phospho-L-serine (composition adjusted from ref. (Casares et al., 2019) to the lipids available in the force field) using CHARMM-GUI (Jo et al., 2008; Wu et al., 2014) and solvated with the OPC water model (Izadi et al., 2014) such that the minimum thickness of the water slab on top of and below the protein/membrane system was 25 Å. KCl was added to the system such that the charges of protein and membrane were counterbalanced and that its total concentration was ~150 mM. Parameters for the protein and lipids were taken from the ff19SB force field (Tian et al., 2020) and the lipid17 force field (Gould et al., 2018), respectively; cAMP was described with parameters from the GAFF2 force field (Wang et al., 2004; Vassetti et al., 2019) and electrostatic point charges derived from a multiconformational RESP fit (Besler et al., 1990; Bayly et al., 1993; Wang et al., 2000).

2.6.2.2 Simulation Protocol

MD simulations were performed using the mixed-precision (SPFP) GPU implementation (Le Grand et al., 2013) in the Amber 20 package (Case et al., 2020). Unless specified otherwise, a time step of 4 fs was defined for integration using a topology file with repartitioned hydrogen masses. The Langevin thermostat (Pastor et al., 1988; Loncharich et al., 1992) with a collision frequency of $\gamma = 1.0\ ps^{-1}$ and a target temperature of $T = 300$ K was used for temperature control. Covalent bonds to hydrogen atoms were constrained using the SHAKE algorithm (Ryckaert et al., 1977) with a tolerance of 10^{-5} Å. The Particle Mesh Ewald method (Darden et al., 1993) was used to compute long-range electrostatic interactions; short-range electrostatic and van der Waals interactions were computed with a cutoff of 10 Å.

To mitigate unfavorable contacts of the water molecules and the lipid tails in the initial simulation systems, these structural elements were first minimized for 2,500 steps using the steepest descent algorithm, followed by 2,500 steps of minimization with the conjugate gradient algorithm. Harmonic positional restraints with force constants of 2.5–10.0 kcal mol^{-1} $Å^{-2}$ were applied to the remaining structural elements (**Table 1**). Retaining the restraints and starting at $T = 100$ K, the system was then thermalized for 50.0 ps in the NVT ensemble to reach the target temperature; this initial simulation step was performed with an integration time step of 1 fs to ensure a stable integration even at high system energies. The timestep was gradually increased to 4 fs in the next seven equilibration steps (total simulation time: 950 ps) performed in the NPT ensemble with semiisotropic pressure scaling. In parallel, the restraints were gradually removed (**Table 1**). The resulting system was used for five production runs of 1 μs length each, giving a total length of 30 μs for all production runs.

2.6.3 Rigidity Analysis

Rigidity analysis was performed with the CNA software package (Pfleger et al., 2013b). CNA efficiently decomposes a constraint network into rigid clusters and interconnecting flexible hinge regions by applying rigidity theory (Hermans et al., 2017).

TABLE 1 | Simulation scheme. Characteristics of the minimization, thermalization, equilibration, and production steps in the MD simulations of the HCN2 systems and the 1G-5G constructs.

Process	Number of Steps	Algorithm	Restrained Structures and Force Constant [kcal mol^{-1} Å^{-2}]					
			PBB[a]	*PSC*[b]	*ChO*[c]	*LiP*[d]	*Ion*[e]	*CMP*[f]
Minimization	2,500/2,500	Steepest descent/Conjugate gradient	10.0	5.0	2.5	2.5	10.0	2.5
Process	**Simulation Time [ps]**	**Ensemble/ Time Step [fs]**	**Restrained Structures and Force Constant [kcal mol^{-1} Å^{-2}]**					
			PBB[a]	*PSC*[b]	*ChO*[c]	*LiP*[d]	*Ion*[e]	*CMP*[f]
Thermalization	50.0	NVT/1.0	10.0	5.0	2.5	2.5	10.0	2.5
Equilibration 1	100.0	NPT/2.0	5.0	2.5	2.5	2.5		2.5
Equilibration 2	100.0	NPT/2.0	2.5	1.0	1.0	1.0		1.0
Equilibration 3	100.0	NPT/4.0	1.0	0.5	0.5	0.5		0.5
Equilibration 4	100.0	NPT/4.0	0.1	0.1	0.1	0.1		0.1
Equilibration 5	100.0	NPT/4.0	0.1	-	-	-	-	-
Equilibration 6	150.0	NPT/4.0	0.05	-	-	-	-	-
Equilibration 7	300.0	NPT/4.0	-	-	-	-	-	-
Production	10^6	NPT/4.0	-	-	-	-	-	-

[a]*protein backbone.*
[b]*protein side-chain heavy atoms.*
[c]*cholesterol oxygen atoms.*
[d]*lipid phosphorus atoms.*
[e]*ions.*
[f]*cAMP.*

Whether a region in a biomolecule is flexible or rigid may depend on remote structural details, which makes rigidity analysis an attractive tool for studying altered structural stability due to distant influences (Jacobs and Hendrickson, 1997; Moukarzel and Duxbury, 1999).

Networks of covalent and non-covalent interactions (hydrogen bonds including salt bridges and hydrophobic tethers) were constructed from conformational ensembles extracted from MD trajectories of HCN2 and the HCN2-1G-5G constructs using the FIRST software (v.6.2) (Jacobs et al., 2001), for which CNA is a front and back end. The strength of the hydrogen bonds (including salt bridges) was assigned via the energy term E_{HB} calculated by FIRST (Dahiyat et al., 1997). Hydrophobic interactions between carbon or sulfur atoms were taken into account if the distance between these atoms was less than the sum of their van der Waals radii (C: 1.7 Å; S: 1.8 Å) plus an offset of D_{cut} = 0.25 Å (Rader et al., 2002).

To elucidate the hierarchy of structural stability in a biomolecule, a trajectory of network states $\{\sigma\}$, generated by successively removing hydrogen bond constraints in the order of increasing strength (Hespenheide et al., 2002; Rader et al., 2002; Radestock and Gohlke, 2008; Rader, 2009), was analyzed. In this process, only those hydrogen bonds are retained in a network state σ that have an energy $E_{\mathrm{HB}} \leq E_{\mathrm{cut}}$. Altered biomolecular stability along a constraint dilution trajectory was quantified based on neighbor stability maps ($rc_{ij,\ \mathrm{neighbor}}$ with i, j being residue numbers) (Rathi et al., 2015).

$$rc_{ij} = \min\left\{E_{cut} | \exists c \in C^{E_{cut}} \colon R_i \wedge R_j \in c\right\}$$

Here, only short-range rigid contacts were considered that have ≥ 1 pair of heavy atoms of the residue pair $R_{\{i,j\}}$ separated by a distance ≤ 4.5 Å (Skolnick et al., 1997). A rigid contact rc_{ij} between pairs of residues ceases to exist when both residues stop sharing the same rigid cluster c of a set of rigid clusters $C^{E\mathrm{cut}}$. The double sum

$$E_{\mathrm{CNA}} = \sum_i^n \sum_{j>1}^n rc_{ij,\mathrm{neighbor}} \tag{4}$$

yields the chemical potential energy (E_{CNA}) due to non-covalent bonding, obtained from the coarse-grained, residue-wise network representation of the underlying biomolecular structure (Rathi et al., 2015; Pfleger et al., 2017). A per-residue decomposition of this equation yields the chemical potential energy of residue i because of the n short-range rigid contacts the residue is involved in:

$$E_{i,\mathrm{CNA}} = \frac{1}{2} \sum_{j \neq i}^n rc_{ij,\mathrm{neighbor}} \tag{5}$$

We extracted the conformational ensembles that served as input to CNA as 1,000 snapshots from the 200–300 ns time interval of the MD simulations described in section "2.6.2 MD simulations".

2.6.4 Postprocessing and Data Analysis

Postprocessing and analysis of the MD trajectories were performed with CPPTRAJ (Roe and Cheatham, 2013) as implemented in AmberTools20 (Case et al., 2020). Unless stated otherwise, averages for observables from the MD simulations are expressed as grand mean ± standard error (SEM), calculated from the time averages over the four

TABLE 2 | Half-maximum activation in the absence of cAMP and at 10 μM cAMP (mean ± SEM). Number of recordings, *n,* are given in brackets for each construct and condition.

Construct	$V_{1/2}$ (mV) w/o cAMP	$V_{1/2}$ (mV) at 10 μM cAMP
HCN2	−119.6 ± 1.8 (*n* = 19)	−100.6 ± 1.5 (*n* = 17)
1G	−110.6 ± 1.8 (*n* = 12)	−106.6 ± 1.7 (*n* = 9)
2G	−112.3 ± 1.5 (*n* = 17)	−108.0 ± 1.9 (*n* = 18)
3G	−119.4 ± 1.6 (*n* = 5)	−119.1 ± 1.3 (*n* = 5)
4G	−98.5 ± 2.4 (*n* = 4)	−94.7 ± 1.7 (*n* = 6)
5G	−123.7 ± 2.4 (*n* = 6)	−120.1 ± 1.7 (*n* = 8)

subunits, which were then averaged over the $n = 5$ trajectories. Error propagation was performed using the uncertainties python package (Lebigot, 2021).

3 RESULTS

3.1 Effects of Additional Amino Acid Sequences (AAASs) Between Channel Gate and C-Linker on Steady-State Activation

Figure 1A shows the comparative model of an HCN2 channel, based on the templates of hHCN1 and hHCN4 channels. HCN channels are primarily activated by hyperpolarizing voltages, while binding of cAMP enhances opening by accelerating activation, decelerating deactivation, and increasing the current amplitude (**Figure 1B**). Consequently, steady-state activation is shifted to less negative voltages (black curves in **Figure 1C**). To study how the effect of cAMP is transmitted from the cyclic nucleotide-binding site to the pore domain, we progressively uncoupled the C-linker from the S6-helix by adding one to five glycines between the last residue of the S6-helix, S441, and the first residue of the A′-helix of the C-linker, L442, resulting in the constructs 1G, 2G, 3G, 4G, and 5G (**Figure 1C**).

All five constructs formed functional channels in *Xenopus laevis* oocytes. Voltage families ranging from −70 to −150 mV with 10 mV increments were applied to analyze steady-state activation by fitting the Boltzman equation (Eq. Error! Digit expected.) to normalized current amplitudes (see Materials and Methods), yielding the voltage of half-maximum current, $V_{1/2}$ (**Table 2**), and the effective gating charge, $z\delta$ (**Figures 1C–E**).

The mean $V_{1/2}$ for HCN2 was −119.6 ± 1.8 mV, matching earlier results from our lab (Sunkara et al., 2018). For 1G and 2G, steady-state activation in the absence of cAMP was shifted to more depolarized voltages, resulting in $V_{1/2}$ = −110.6 ± 1.8 mV and −112.3 ± 1.5 mV, respectively. These values are significantly different from HCN2 but not from each other. As expected, adding a saturating concentration of 10 μM cAMP to HCN2 resulted in a shift of $V_{1/2}$ to more depolarized voltages ($V_{1/2}$ = −100.9 ± 1.5 mV). In contrast, adding 10 μM cAMP to 1G or 2G did not affect steady-state activation (**Figure 1D**). It is noteworthy that 2G showed an additional effect compared to HCN2: The currents regularly decayed after passing a maximum, resembling the inactivation process in spHCN channels in the absence of cAMP (**Supplementary Figure S1**) (Shin et al., 2004; Dai et al., 2021). Because the late current at the end of the pulse and, thus, the tail current used for forming the Boltzmann analysis were compromised, we corrected the currents for this decay in the analysis (**Figure 1**). A detailed description of the correction procedure is described in the **Supplementary Materials**. We are aware that the two processes of inactivation and activation cannot be fully separated using this approach. Consequently, the correction will not reveal a fully uncompromised activation. Therefore, we do not interpret the 2G results extensively herein.

For 3G and 5G, $V_{1/2}$ values in the absence of cAMP were similar to those from HCN2 with $V_{1/2}$ = −119.4 ± 1.6 mV for 3G and −123.7 ± 2.4 for 5G. As in 1G and 2G, 10 μM cAMP had no significant effect on $V_{1/2}$ (3G: $V_{1/2}$ = −119.1 ± 1.3 mV; 5G: $V_{1/2}$ = −120.1 ± 1.7 mV).

Notably, at zero cAMP, 4G showed the most pronounced difference to HCN2. With $V_{1/2}$ = −98.5 ± 2.4 mV, it resembled HCN2 in the presence of saturating cAMP (−100.9 ± 1.5 mV). As in the other insertion constructs, adding cAMP to 4G had no effect ($V_{1/2}$ = −94.7 ± 1.7 mV).

To analyze the effects of the glycine insertions on voltage sensitivity, we compared $z\delta$ values obtained from the Boltzmann fit, specifying the equivalent gating charges moving through the electric field across the membrane. The data variability for 1G with cAMP and 2G with and without cAMP was higher than for all other cases due to a considerable number of recordings giving exceptionally high $z\delta$ values. For 2G, we assume that the reason for this is the unusual gating behavior described above, resulting in erroneously steep Boltzmann relationships. Such a gating behavior also seems to appear in 1G with cAMP, but to a lesser extent, so that the current decay observed in 1G was not as visible as for 2G (**Figure 1**). Moreover, for 3G and 4G with and without cAMP, the $z\delta$ values were lower than the respective HCN2 values (**Figure 1**).

Together, these data suggest that the function of HCN2 is more disturbed in 4G than in the other four constructs, apparently by a stronger uncoupling of the effects of cAMP and voltage on activation.

3.2 Effects of AAASs Between Channel Gate and C-Linker on Structural Dynamics and Statics

To determine whether and how the glycine insertions between the S6 and A′-helices affect the structural dynamics of HCN2, we first studied the differences between the domain-wise mobility in the 1G to 5G variants and the wildtype channel. To this end, we determined the residue-wise root mean-square fluctuations (RMSF) after the structural superposition of all MD snapshots onto the pore domain, which is the structurally most invariant region in HCN2. The mobility of the CL and CNBD domains is increased in the 1G to 5G variants compared to wildtype channels, whereas the mobility of the HCND and VSD domains hardly differed from that of wildtype channels (**Figure 2**). Interestingly, the increase in mobility in CL and CNBD did not correlate with the number of inserted glycine

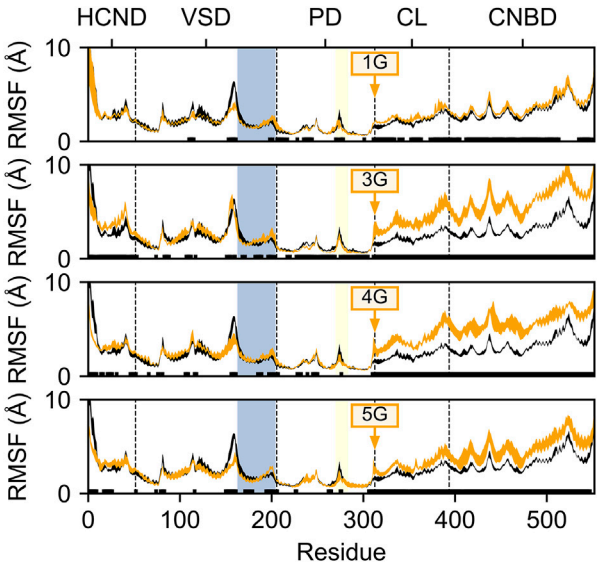

FIGURE 2 | Residue mobility in wildtype HCN2 and the 1G, 3G, 4G, and 5G constructs. Residue-wise root-mean-square fluctuation (RMSF) in MD simulations of HCN2 (black line) and 1G, 3G, 4G, and 5G (orange lines, from top to bottom). The thickness of the lines represents the standard error across all subunits (n = 4). Residues with significant differences (p < 0.05) between HCN2 and the respective construct are indicated with a black bar above the x-axis. Residue numbers are according to the AMBER numbering; domains are denoted above the plots; domain boundaries are indicated by a vertical dashed line. The S4-helix in the VSD is marked with a blue background, and the glycine insertion site is indicated with an orange arrow. For consistency, RMSF values for the glycine insertions were omitted from each subplot.

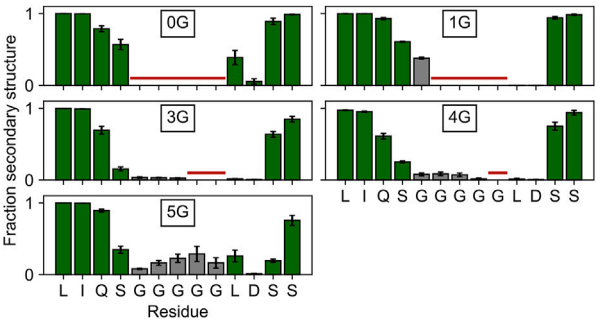

FIGURE 3 | Secondary structure content in and around the insertion site. The secondary structure content of the four residues adjacent to the insertion site is depicted with green bars, that of the glycine insertions with gray bars. Residues not present in the wildtype or a particular construct are marked with a horizontal red line. Any β-strand or helix–but no turns or bends–were counted as secondary structure elements.

residues. In 1G, the average residue-wise mobility in CL and CNBD increased by 0.42 ± 0.02 Å (**Figure 2A**). The most pronounced increases occurred in 3G (2.90 ± 0.03 Å, **Figure 2B**) and 4G (2.44 ± 0.03 Å, **Figure 2C**), but mobility decreased again in 5G (1.50 ± 0.03 Å, **Figure 2D**).

Since the lower mobility in 5G suggests secondary structure formation, we inspected the average secondary structure content within the region of the insertion. In 5G, the secondary structure content (18.5 ± 5.8%) is significantly (p < 0.05) increased within the glycine insertion when compared to the 3G (3.1 ± 0.8%) and 4G (6.3 ± 2.1%) constructs (**Figure 3**), but not when compared to the 1G construct (38.0 ± 2.7%). 3_{10} helices, β-sheets, and stable turns are the dominant secondary structure elements in the 5G insertion (**Supplementary Movie S1**). Note that a PG_{II} (polyglycine type II) secondary structure would form only in the presence of neighboring polyGly chains (Crick and Rich, 1955). Since no structure has been deposited in the PDB in which two α-helices are joined by five glycine residues, a comparison with other structures to substantiate this secondary structure formation is not possible.

The increased mobility of the CL-CNBD relative to the other structural elements suggests that the CL-CNBD motions may be uncoupled from motions of the other domains in the glycine variants. These data may explain why cAMP does not affect the activation of 1G to 5G in the electrophysiological experiments (**Figures 1C, D**). To substantiate this, we studied the conformational changes that accompany increased mobility. Upon visual inspection of the MD trajectories, we observed vertical movements of the CL-CNBD with respect to the pore domain. Particularly for 3G and 4G, this movement is reflected by an increase in the distance between the z-coordinates of the centers of mass of the four C-terminal residues of the S6 helices and the z-coordinates of the centers of mass of the C-linker of the counter-clockwise preceding subunit as viewed from the extracellular side, indicating a downward displacement of the CL-CNBD (**Figure 4A**). The downward displacement (**Figure 4B**) was typically concomitant with an increase in the kink angle between the S6 and A′-helix (**Figures 4A,C**). Therefore, this conformational change is likely a direct consequence of the high flexibility of the preceding glycine insertions, which turn the junction between the S6 and A′-helix into a flexible hinge within the subunit. While the average distance in the MD ensemble of the wildtype amounted to 14.45 ± 0.01 Å, it increased by 1.77 ± 0.01 Å, 2.30 ± 0.01 Å, and 2.61 ± 0.01 Å in the 1G, 3G, and 4G constructs, respectively.

Counterintuitively, but consistent with the observed secondary structure formation (**Figure 3**), the insertion of five glycine residues in 5G led to similar distances like in the wildtype channel (14.70 ± 0.01 Å). The peak values for the downward displacements observed in the simulation ensembles of the 1G-5G constructs with respect to the average distance in the wildtype channel were 5.08 Å for 1G, 9.52 Å for 3G, 10.46 Å for 4G, and 4.83 Å for 5G. These values highlight that the observed downward displacement cannot be a mere consequence of the elongation of the peptide chain. We speculate that the loss of contacts between S4 and CL (**Figure 5**) resulting from the downward displacement might foster a subsequent downward movement of S4 similar to the one induced by hyperpolarization but smaller in magnitude.

However, given that HCN channels take hundreds of milliseconds to open, we cannot expect to routinely observe such a conformational change of the S4-helix in our simulations, even if activation was accelerated by a factor of

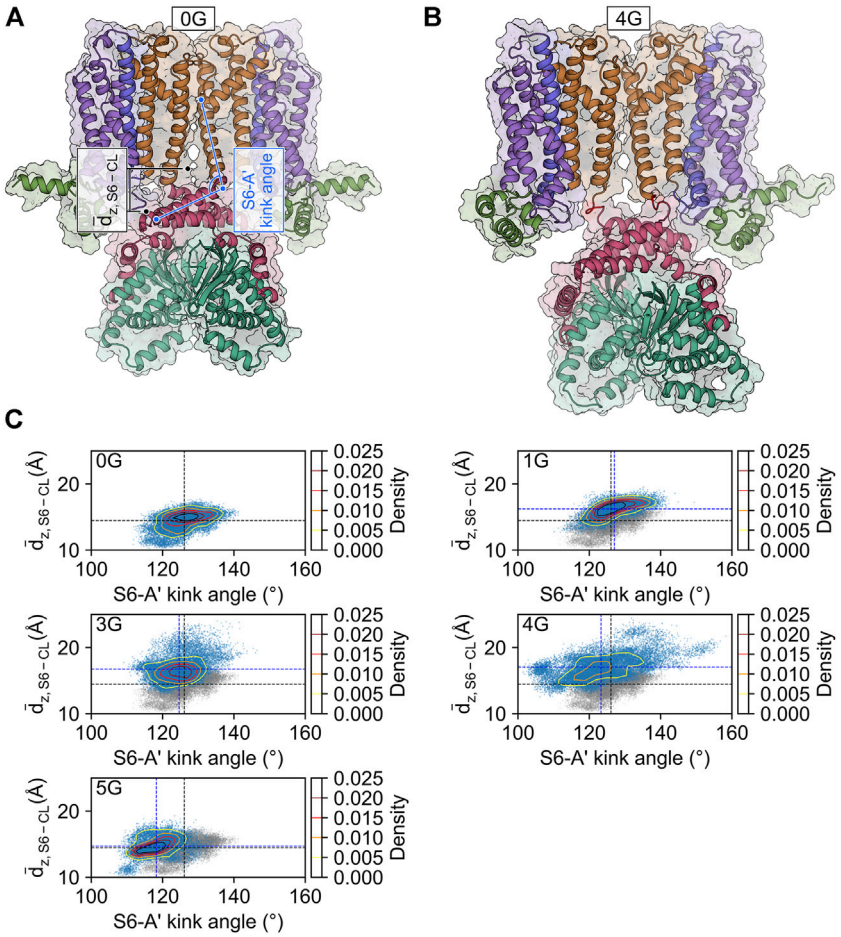

FIGURE 4 | CL-CNBD displacement in glycine linker-carrying constructs. **(A)** Starting structure for the MD simulation of the HCN2 wildtype channel (0G). The color scheme corresponds to the one in **Figure 1A**. The geometric parameters used to characterize the conformational changes are the vertical distance between the C-terminus of the S6-helix and the C-linker of the counter-clockwise preceding subunit as viewed from the extracellular side ($d_{z,\,S6-CL}$, black), and the S6-A′ kink angle (light blue). **(B)** Snapshot of the final state of the second simulation of 4G. The color scheme is identical to that in panel A, with the glycine linkers colored in red. Compared to the wild type, 4G displays a pronounced downward displacement of the CL-CNBD. **(C)** Scatter and contour plots of the two geometric parameters in the MD simulations of 0G, 1G, 3G, 4G, and 5G. Values of the average structure of HCN2 are indicated with dashed black lines and those of the constructs with dashed blue lines. In the plots for the glycine linker constructs, the scatter plot for HCN2 is shown in gray for comparison.

~25 at weakest hyperpolarization to ~4 at strongest hyperpolarization (see below and **Figure 7**). Observation of voltage sensor motion in unbiased MD simulations has so far only been achieved under strongly hyperpolarizing conditions (–550 mV) and simulation times of >20 µs (Kasimova et al., 2019). The reduced equivalent gating charges in 3G and 4G (**Figure 1E**) support this model in that fewer charges would cross the membrane upon activation if an S4 displacement towards intracellular had already occurred in the closed state.

Although the increase in mobility and the conformational changes of the CL-CNBD relative to the core are very similar in 3G and 4G, $V_{1/2}$ is increased only in 4G but is similar to HCN2 in 3G (**Figure 1D**). We suspected that structural stabilization of certain channel regions in 3G counterbalances the priming of S4 in this construct. Therefore, we sought to identify regions in the constructs that are structurally stabilized or destabilized compared to HCN2 using the rigidity theory-based CNA (Pfleger et al., 2013b). In CNA, biomolecules are represented as constraint networks and then decomposed into rigid clusters and flexible hinge regions according to rigidity theory (Jacobs and Thorpe, 1995; Hermans et al., 2017). Post-processing of constraint dilution simulations as implemented in CNA (Radestock and Gohlke, 2011; Rathi et al., 2015) provides information on the contributions of individual residues to local stability (Pfleger et al., 2013a). Comparing these contributions between wild-type and a construct can thus reveal which regions in the construct become more flexible or rigid. Note that these static analyses are time-independent (Rathi et al., 2015) and, hence, may detect structural (de)stabilizations before these lead to conformational changes.

Expectedly, and consistent with the increased mobility of the domains following the insertion (**Figure 2**), the structural flexibility is markedly increased in the regions preceding and following the insertion sites (i.e., the C-terminal end of S6 and the

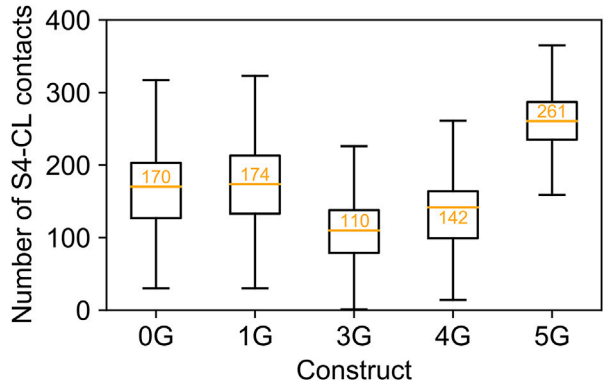

FIGURE 5 | Contacts between S4 and C-linker. Number of contacts between S4 and C-linker in MD simulations of each construct. The values are displayed as a standard boxplot, with the difference that the orange line indicates the mean (additionally depicted as orange number).

A′ and B' helices in the C-linker) in all constructs compared to the wildtype channel (**Figure 6A**). This supports our suggestion that the motions of the CL-CNBD and the other domains is decoupled in the constructs, thereby abolishing the cAMP effect. As a consequence, the gate is destabilized in all constructs (**Figure 6D**). Moreover, parts of the selectivity filter in 1G and the entire selectivity filter in 4G are destabilized, in contrast to 3G and 5G (**Figures 6C, D**). Additionally, parts of the S4 are destabilized in 4G, but stabilized in all other constructs (**Figure 6D**). Most notably, the stability of the upper pore region is increased in 3G and decreased in 4G (**Figures 6B, D**). Our data suggest that destabilization of the upper pore region is determined by the extent and strength of the destabilization of the S6 C-terminus. In 1G and 4G, destabilization spreads furthest towards the pore domain (**Figure 6B**), but is more pronounced in 4G and propagates to the selectivity filter. However, in 3G and 5G, the destabilization spreads less towards the pore domain (**Figure 6B**), which might not suffice to destabilize the selectivity filter similarly. Taken together, these data suggest that destabilization of the S6 C-terminus in 1G and 4G causes destabilization of the selectivity filter and, in 4G, additionally destabilizes other parts of the upper pore region. This could facilitate the passage of ions through the selectivity filter or pore and thus explain the increased $V_{1/2}$ values in these constructs.

3.3 Increased Flexibility Causes Fast Activation Kinetics

The observed higher flexibility of the CL-CNBD domains and of the gate structure (here defined by amino acids Y428, I432, T436, and Q440) led us to hypothesize that these changes cause an accelerated activation when skipping to hyperpolarizing voltage. The additionally destabilized S4 domain and selectivity filter in 4G should further accelerate activation compared to the other insertion constructs. To test this hypothesis, we used the patch-clamp technique to analyze time courses of activation for all five constructs at different voltages and compared the results with those from HCN2 wildtype in the absence and presence of cAMP.

The speed of activation was quantified by fitting a single exponential (Eq. Error! Digit expected.) to current time courses, yielding the activation time constant τ (**Figure 7A**). For HCN2 in the absence of cAMP, τ shows the characteristically steep decrease towards hyperpolarizing voltages (**Figure 7B**). 10 μM cAMP caused the typical decrease of τ at all voltages. For all mutant constructs, this accelerating effect of cAMP has vanished in parallel with the lost effect on steady-state activation. For 1G, 2G, 3G, and 5G, the time constants of all constructs were almost always between those of HCN2 without and with cAMP, but with less pronounced voltage dependencies. The data for 2G are largely consistent with the data series for the other constructs, but the exponential fits might be compromised due to the correction procedure. In contrast, 4G showed exceptionally fast activation kinetics, even faster than HCN2 at saturated cAMP. Moreover, in 4G, the voltage dependence of activation has completely vanished (**Figure 7B**). Hence, these experimental data match the predictions of the MD simulations above.

Previous data from our group showed that there is reciprocity between ligand binding and channel activation in HCN2: By measuring ligand binding and channel activation in parallel, using confocal patch-clamp fluorometry (cPCF) with a fluorescent cAMP derivative, we experimentally verified this context by showing an activation-induced increase of the binding affinity (Kusch et al., 2010).

In line with this, we expected that channel constructs that are not reactive to ligand binding do not show an activation-induced affinity increase. For 1G and 4G, we tested this by recording ligand binding in parallel with channel activation using cPCF. Similar to previous measurements, ligand binding was quantified by the fluorescence intensity of a fluorescent cAMP derivative binding to the channels in the excised patch membrane (Biskup et al., 2007; Kusch et al., 2010). As cAMP derivative, 8-AHT-Cy3B-cAMP (f1cAMP) was used (Otte et al., 2019; Pfleger et al., 2021), which contains a different dye moiety and a longer linker compared to the originally used cAMP derivative 8-AET-Dy547-cAMP (fcAMP) (Kusch et al., 2010) (see also Materials and Methods).

In line with our previous results, in HCN2, the fluorescence increased when activating the channels by stepping from −30 to −130 mV (**Figure 8**). The channels transit from a low-affinity state to a high-affinity state. Neither for 1G nor 4G did we observe such an increase in cAMP binding upon activation. **Figure 8A** shows representative fluorescence traces obtained at 0.25 μM f1cAMP.

To understand at which affinity level the insertion constructs are stabilized, we measured concentration-binding relationships for 1G and 4G and compared them with HCN2 (**Figure 8B**). To this end, the fluorescence intensity F, measured at different f1cAMP concentrations at either −30 mV or −130 mV, was related to the maximum fluorescence intensity, F_{max}, measured at a saturating concentration of 2.5 μM f1cAMP and −130 mV. F/F_{max} values are averages from 3 to 9 recordings. Fitting the Hill equation for ligand binding (Eq. Error! Digit expected.) to the averaged data yielded the concentration of half-maximum binding, BC_{50}, and the Hill coefficient of binding, H_b (**Figure 8B**).

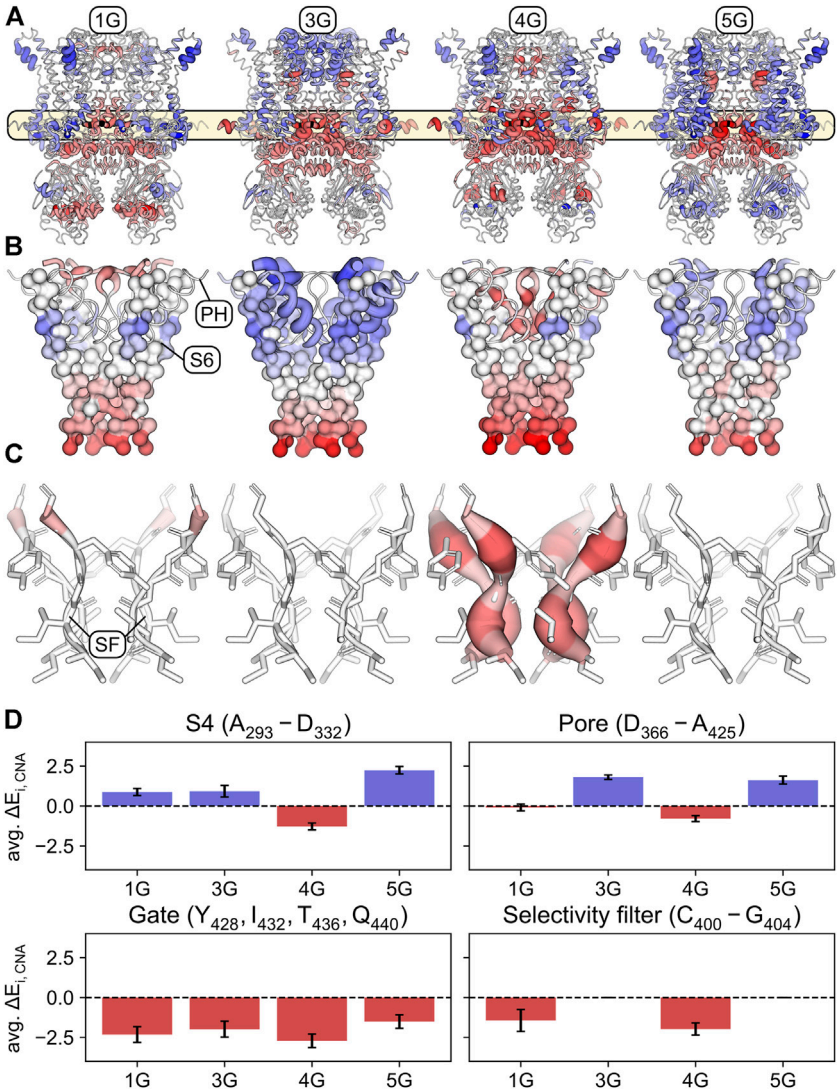

FIGURE 6 | Stabilized and destabilized regions of the glycine-linker constructs according to rigidity analyses. **(A)** Mapping of the differences $\Delta E_{i,CNA} = E_{i,CNA(0G)} - E_{i,CNA(nG)}$ – averaged across simulations and subunits – onto the structure of the wildtype channel (0G). Regions that are significantly stabilized in the respective construct compared to 0G (positive $\Delta E_{i,CNA}$ values) are shown in shades of blue. Regions that are significantly destabilized compared to 0G (negative $\Delta E_{i,CNA}$ values) are shown in shades of red. Shading is defined by a divergent color map with $\Delta E_{i,CNA} \leq$ -5.5 kcal mol^{-1}: red, $\Delta E_{i,CNA} = 0$ kcal mol^{-1}: white, and $\Delta E_{i,CNA} \geq 5.5$ kcal mol^{-1}: blue. The thickness of the cartoon representation is scaled using the absolute value $|\Delta E_{i,CNA}|$. Residues for which the differences were not significant ($p \geq 0.05$) were assigned $\Delta E_{i,CNA} = 0$ kcal mol^{-1}. **(B)** Similar representation as in panel A with a focus on S6, the pore helix, and the selectivity filter. S6 is depicted in a surface representation of its C-alpha trace. **(C)** Same representation as in panel A with a focus on the selectivity filter. **(D)** Average $\Delta E_{i,CNA}$ over the S4 (top left), the upper part of the pore (top right), the S6 gate (bottom left), and the selectivity filter (bottom right). Error bars indicate standard deviations.

The binding affinity BC_{50} of HCN2 not activated by voltage was 0.51 μM. Notably, the binding affinity of both 1G (BC_{50} = 0.24 μM) and 4G (BC_{50} = 0.32 μM) not activated by voltage approximates the binding affinity of HCN2 activated by voltage (BC_{50} = 0.28 μM). These data suggest that both insertion constructs exist already in the high-affinity state when not being activated by voltage, a state that HCN2 can adopt only at activation by voltage. Therefore, in both 1G and 4G, a further increase of binding affinity is absent. The Hill coefficient was similar for all constructs under all conditions (HCN2 at −30 mV: H_b = 1.4; HCN2 at −130 mV: H_b = 1.5; 1G: H_b = 1.3; 4G: H_b = 1.4).

4 DISCUSSION

The aim of this study was to further analyze the processes underlying cAMP modulation of HCN channels. We manipulated the interaction between the CL-CNBD and membrane portion by inserting one through five glycines directly after the activation gate formed by the S6-helix bundle, yielding the constructs 1G-5G. We then studied the effects of these insertions on structure and function using molecular simulation approaches and electrophysiological techniques.

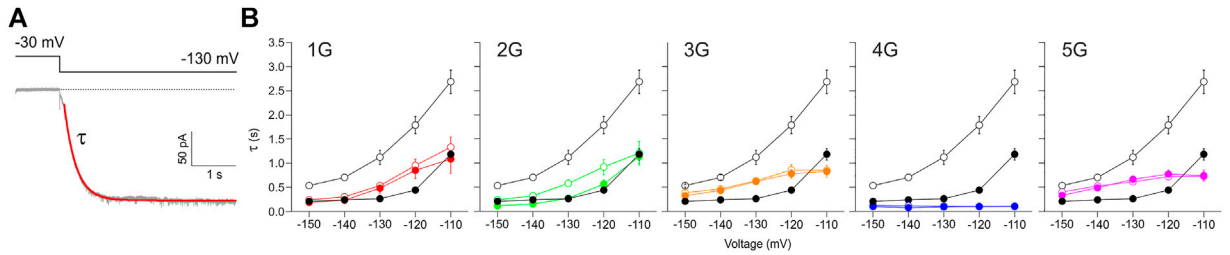

FIGURE 7 | Effect of inserted glycines on activation kinetics. **(A)** Example trace for 1G illustrating a fitted exponential curve (red) to obtain the time constant of activation, τ, by using Eq. Error! Digit expected **(B)** Plots of activation time constants versus voltage for all five mutant constructs in comparison to HCN2 (black lines and symbols in all five panels). Empty symbols represent cAMP-free condition, filled symbols represent recordings at 10 μM cAMP. Glycine-induced uncoupling interrupts the reciprocal feedback from VSD to CNBD.

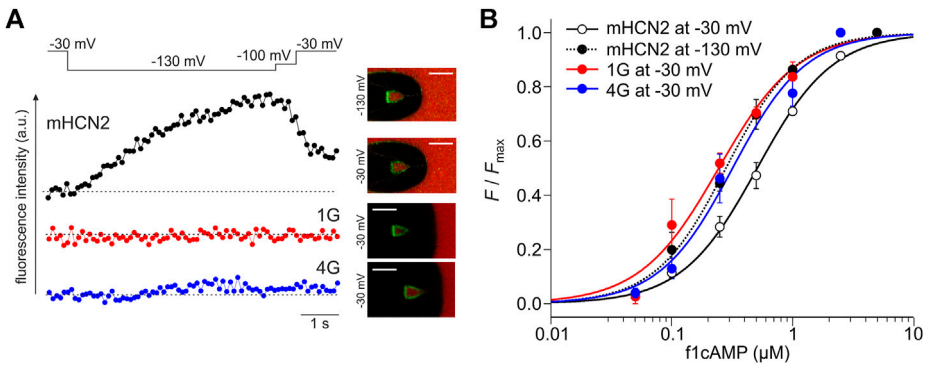

FIGURE 8 | Reciprocity between binding and gating in glycine constructs. **(A)** Examples of fluorescence traces for HCN2, 1G, and 4G at 0.25 μM f1cAMP. The confocal fluorescence images in the insets show pipette tips holding membrane patches with the given constructs expressed. Green fluorescence arises from f1cAMP binding to the channel. **(B)** Concentration-binding curves for HCN2 at −30 and −130 mV, 1G at −30 mV, and 4G at −30 mV. Color coded lines were obtained by fitting the Hill equation (Eq. Error! Digit expected.) to the data points (dotted line for mHCN2 at −130 mV, solid lines for 1G, 4G and mHCN at −30 mV). Single data points are averages of recordings from 3 to 20 different patches (except mHCN2 at 1 μM: n = 1).

All five insertion constructs led to channels that could be activated by hyperpolarizing voltage. Voltage-dependent activation at steady-state and in the absence of cAMP in 1G and 2G was shifted moderately towards depolarizing voltages (**Figure 1**). Thus, in these constructs, channel opening was favored moderately compared to HCN2. Regarding that in HCN2 the empty CNBD exerts an autoinhibitory effect on channel gating (Wainger et al., 2001), the observed $V_{1/2}$ shift can be interpreted as a reduction of such an effect. In empty 4G channels, activation was shifted more to depolarizing voltages, resembling $V_{1/2}$ values of cAMP-saturated HCN2. By contrast, in 3G and 5G, steady-state activation was not affected (**Figure 1**). These data indicate that the extent of the functional effects of AAA insertion is not simply a function of the length of such a sequence but that each AAA sequence exerts specific effects. Steady-state activation also showed that in all five constructs the characteristic cAMP-induced shift of $V_{1/2}$ to more depolarized voltages was completely abolished (**Figure 1**), indicating that insertion of only one glycine already suffices to uncouple the CL-CNBD portion from the membrane portion.

To gain deeper insight into the structural and functional changes of the AAAs insertion, we performed different computational approaches. First, we studied the domain-wise mobility in all five constructs and compared it to the mobility in HCN2 (**Figure 2**). For all insertions, the mobility is increased in the CL-CNBD domain, but hardly in the HCN domain and VSD. Interestingly, the highest mobility was found for 3G and 4G. The reason why a chain of 5 glycines did not cause higher mobility than a chain of 4 glycines is presumably due to secondary structure formation in 5G (**Figure 3**). Nevertheless, independent of the degree of the mobility increase, these changes in the insertion constructs are suggested to be a consequence of a CL-CNBD uncoupled from the other channel domains. So far, these data show that the insertion of the additional amino acids is a suitable tool to uncouple two protein regions from each other to understand their interaction better.

What are the structural consequences for the channel conformation near the insertion site? The glycine residues were inserted directly after the S6 segment and the beginning of the A′-helix in the C-linker. The MD simulations revealed a

downward displacement of the CL-CNBD. This downward displacement is accompanied by an increase in the kink angle between S6 and A′-helix, which is most pronounced in 3G and 4G (**Figure 4**). Furthermore, the junction between S6 and A′-helix is turned into a flexible hinge. Both S6 and A′-helix play a relevant role in the opening process: The C-terminal ends of S6 form the channel gate, a right-handed helical bundle (Rothberg et al., 2002), which is held closed by the presence of the S4-helix at depolarized voltages (Lee and MacKinnon, 2017). The C-linkers of the four subunits tetramerize to form a disc-like gating ring. The characteristically long S4-helix allows the S4-S5 linker to directly contact the C-linker of the left neighboring subunit (viewed from extracellular). At hyperpolarized voltages, the displacement of S4 releases the constraints on the C-linker and on S6, which is followed by an unwinding of the gate due to a rotational movement of the gating ring (Lee and MacKinnon, 2017). Interestingly, this mechanism is still functional after AAA insertion between the S6 and A′-helix. All insertion constructs responded to hyperpolarizing voltages. For 1G, 4G, and eventually also for 2G, the opening was even favored compared to HCN2 wildtype. Based on the gating scenario described above, this could be a consequence of a downward displacement of the S4 helix, favored by a void between S4 and CL that would form upon downward displacement of the CL-CNBD (**Figure 5**). Disruption of such contacts in response to hyperpolarization has been proposed to energetically favor channel opening (Decher et al., 2004). This presumed downward displacement of the S4-helix is likely similar to the one induced by hyperpolarizing voltages (Männikkö et al., 2002; Bell et al., 2004; Vemana et al., 2004; Vemana et al., 2004; Bruening-Wright and Larsson, 2007; Dai et al., 2019) but to a lesser extent, reducing the energy needed for activation by voltage. The similarity between conformational changes induced by hyperpolarization and conformational changes induced by glycine insertion led us to speculate, that those changes might be responsible for the increased affinity in glycine constructs (see **Figure 8**).

But why did 3G behave so differently from 4G, despite showing similar downward displacements of the CL-CNBD? To answer this question, we performed a rigidity theory-based Constraint Network Analysis (CNA) (Pfleger et al., 2013b) to identify a structural stabilization of certain channel regions in 3G counterbalancing the priming of S4 in this construct (**Figure 6**). For all insertion constructs, also the CNA showed markedly increased structural flexibility in the regions preceding and following the inserted AAAs. This supports the conclusion drawn from the mobility analysis that the CL-CNBD is decoupled in the insertion constructs. As a consequence, the gate is destabilized in all constructs. However, a destabilization of the whole selectivity filter and parts of the S4 domain were found exclusively for 4G. The most notable difference between 3G and 4G is the increased stability of the upper pore region (defined as amino acids D366-A425) in 3G and decreased stability of the same region in 4G.

How can we explain the missing cAMP-effect in the insertion constructs? Previous publications showed that the binding of cAMP to the CNBD induces an iris-like rotation of the gating ring, which is in the direction of pore opening (counter-clockwise viewed from the extracellular side). This unwraps the right-handed S6 bundle, but to a lesser extent than the unwrapping caused by hyperpolarization. Therefore, cAMP binding supports channel opening but is not able to induce it without hyperpolarization (Shin et al., 2004; Lee and MacKinnon, 2017; Weissgraeber et al., 2017; Gross et al., 2018; Marchesi et al., 2018). Herein, cAMP did not show an effect on the insertion constructs, indicating that the conformational changes needed for priming the CL-disk rotation or the transmission of this rotation to the gate are compromised. Our results from MD analysis support both options: 1) The higher flexibility seen in the CL-CNBD portions of all constructs might affect the binding-induced conformational changes in the CNBD and their upwards transmission along the C-linker; 2) The high flexibility of the hinge and the increased angle between A′-helix and S6 might hamper the transition of the CL rotation to the S6-helix bundle.

Based on the mentioned gating scenario, an accelerated channel activation is expected from the higher flexibility of the S4 domain and S6 gate region and a downward displacement of the CL-CNBD in the sense of priming. We tested this by measuring current responses to different hyperpolarizing voltage jumps and determining the activation time constant τ, both in the absence and presence of cAMP. As expected, for all insertion constructs, the activation speed in the absence of cAMP was faster compared to HCN2. The characteristic accelerating effect of cAMP vanished in all cases. One potential reason for such an acceleration of activation kinetics may be a depolarizing shift in the voltage dependence. However, if this was the only reason for the accelerations observed herein, the respective τ_{act}-voltage curves would show a similar slope as the wildtype curve, just covering a different voltage range. For all five glycine constructs, the slopes were clearly different from HCN2, indicating that the depolarizing shift in voltage dependence cannot account for the speed of activation alone. Interestingly, again, 4G showed an exceptional behavior: the activation was fastest among all insertion constructs and even faster as seen for cAMP-saturated HCN2. This matches the exceptionally high structural flexibility of the 4G S4 and the destabilization of the whole selectivity filter, which both may facilitate conformational changes, allowing for fast channel opening.

Regarding the impact of cAMP on the channel protein, the data obtained showed that both communication pathways, from the CNBD to the transmembrane part and, vice versa, from the transmembrane part to the CNBD, are corrupted by the AAAs insertion near the gate. In the most simple scenario, this is solely caused by the higher flexibility of S6, A′-helix, and the hinge between them, interrupting the transmission of conformational changes in both directions. However, Porro and co-workers suggested in a recent report a mechanism by which the two stimuli of activation, hyperpolarizing voltage and cAMP binding, are integrated by the HCN domain via forming a mechanical continuum between the voltage sensor and the CNBD (Porro et al., 2019). In this scenario, information between the CNBD and VSD is transmitted at the periphery of the channel, bypassing the

pore. Considering these findings, not only the higher flexibility close to the central axis of the channel but also regions and interactions further away are suggested to be significantly affected by the AAAs insertion (**Figure 6A**).

The combined electrophysiological and computational results provide new insights into the intricate activation of HCN2 channels.

DATA AVAILABILITY STATEMENT

The datasets presented in this study can be found in online repositories. The names of the repository/repositories and accession number(s) can be found in the article/**Supplementary Material**.

ETHICS STATEMENT

The animal study was reviewed and approved by Thuringian State Office for Consumer Protection.

AUTHOR CONTRIBUTIONS

SY carried out electrophysiological and cPCF experiments, analyzed data, and prepared figures. MB carried out the molecular simulation studies, analyzed data, prepared figures, and wrote the manuscript. TS and TZ engineered the mutants. UE carried out electrophysiological experiments and analyzed data. IS carried out electrophysiological and cPCF experiments and analyzed data. CP carried our rigidity analysis and analyzed data. HG designed molecular simulation studies, analyzed data, and wrote the manuscript. KB designed experiments and wrote the manuscript. JK carried out electrophysiological and cPCF experiments and analyzed data, prepared figures, and wrote the manuscript.

FUNDING

This work was supported by the grant Research Unit 2518 DynIon of the Deutsche Forschungsgemeinschaft (DFG) (projects P2 (KU 3092/2-1; BE1250/19-1) and P7 (GO 1367/2-1)). We are grateful for computational support and infrastructure provided by the "Zentrum für Informations-und Medientechnologie" (ZIM) at the Heinrich Heine University Düsseldorf and the computing time provided by the John von Neumann Institute for Computing (NIC) to HG on the supercomputer JUWELS at Jülich Supercomputing Centre (JSC) (user IDs: HKF7; VSK33; HDD17; HCN2COOP).

ACKNOWLEDGMENTS

We thank Sandra Bernhardt, Andrea Kolchmeier, Claudia Ranke, and Karin Schoknecht for excellent technical assistance.

SUPPLEMENTARY MATERIAL

The Supplementary Material for this article can be found online at: https://www.frontiersin.org/articles/10.3389/fphys.2022.895324/full#supplementary-material

REFERENCES

Alford, R. F., Koehler Leman, J., Weitzner, B. D., Duran, A. M., Tilley, D. C., Elazar, A., et al. (2015). An Integrated Framework Advancing Membrane Protein Modeling and Design. *PLoS Comput. Biol.* 11, e1004398. doi:10.1371/journal.pcbi.1004398

Alford, R. F., Fleming, P. J., Fleming, K. G., and Gray, J. J. (2020). Protein Structure Prediction and Design in a Biologically Realistic Implicit Membrane. *Biophysical J.* 118, 2042–2055. doi:10.1016/j.bpj.2020.03.006

Altschul, S., Madden, T. L., Schäffer, A. A., Zhang, J., Zhang, Z., Miller, W., et al. (1997). Gapped BLAST and PSI-BLAST: a New Generation of Protein Database Search Programs. *Nucleic Acids Res.* 25, 3389–3402. doi:10.1093/nar/25.17.3389

Bayly, C. I., Cieplak, P., Cornell, W., and Kollman, P. A. (1993). A Well-Behaved Electrostatic Potential Based Method Using Charge Restraints for Deriving Atomic Charges: The RESP Model. *J. Phys. Chem.* 97, 10269–10280. doi:10.1021/j100142a004

Bell, D. C., Yao, H., Saenger, R. C., Riley, J. H., and Siegelbaum, S. A. (2004). Changes in Local S4 Environment Provide a Voltage-Sensing Mechanism for Mammalian Hyperpolarization-Activated HCN Channels. *J. General Physiology* 123, 5–20. doi:10.1085/jgp.200308918

Besler, B. H., Merz, K. M., Jr., and Kollman, P. A. (1990). Atomic Charges Derived from Semiempirical Methods. *J. Comput. Chem.* 11, 431–439. doi:10.1002/jcc.540110404

Biel, M., Wahl-Schott, C., Michalakis, S., and Zong, X. (2009). Hyperpolarization-Activated Cation Channels: From Genes to Function. *Physiol. Rev.* 89, 847–885. doi:10.1152/physrev.00029.2008

Biskup, C., Kusch, J., Schulz, E., Nache, V., Schwede, F., Lehmann, F., et al. (2007). Relating Ligand Binding to Activation Gating in CNGA2 Channels. *Nature* 446, 440–443. doi:10.1038/nature05596

Bruening-Wright, A., and Larsson, H. P. (2007). Slow Conformational Changes of the Voltage Sensor during the Mode Shift in Hyperpolarization-Activated Cyclic-Nucleotide-Gated Channels. *J. Neurosci.* 27, 270–278. doi:10.1523/jneurosci.3801-06.2007

Buchan, D. W. A., and Jones, D. T. (2019). The PSIPRED Protein Analysis Workbench: 20 Years On. *Nucleic Acids Res.* 47, W402–W407. doi:10.1093/nar/gkz297

Buchan, D. W. A., Minneci, F., Nugent, T. C. O., Bryson, K., and Jones, D. T. (2013). Scalable Web Services for the PSIPRED Protein Analysis Workbench. *Nucleic Acids Res.* 41, W349–W357. doi:10.1093/nar/gkt381

Casares, D., Escribá, P. V., and Rosselló, C. A. (2019). Membrane Lipid Composition: Effect on Membrane and Organelle Structure, Function and Compartmentalization and Therapeutic Avenues. *Int. J. Mol. Sci.* 20, 2167. doi:10.3390/ijms20092167

Case, D. A., Belfon, K., Ben-Shalom, I. Y., Brozell, S. R., Cerutti, D. S., Cheatham, T. E., et al. (2020). *AMBER 2020*. University of California, San Francisco.

Clapham, D. E. (1998). Not so Funny Anymore: Pacing Channels Are Cloned. *Neuron* 21, 5–7. doi:10.1016/s0896-6273(00)80508-5

Craven, K. B., Olivier, N. B., and Zagotta, W. N. (2008). C-Terminal Movement During Gating in Cyclic Nucleotide-Modulated Channels. *J. Biol. Chem.* 283, 14728–14738. doi:10.1074/jbc.m710463200

Craven, K. B., and Zagotta, W. N. (2004). Salt Bridges and Gating in the COOH-Terminal Region of HCN2 and CNGA1 Channels. *J. General Physiology* 124, 663–677. doi:10.1085/jgp.200409178

Craven, K. B., and Zagotta, W. N. (2006). CNG and HCN Channels: Two Peas, One Pod. *Annu. Rev. Physiology* 68, 375–401. doi:10.1146/annurev.physiol.68.040104.134728

Crick, F. H. C., and Rich, A. (1955). Structure of Polyglycine II. *Nature* 176, 780–781. doi:10.1038/176780a0

Dahiyat, B. I., Gordon, D. B., and Mayo, S. L. (1997). Automated Design of the Surface Positions of Protein Helices. *Protein Sci.* 6, 1333–1337. doi:10.1002/pro.5560060622

Dai, G., Aman, T. K., DiMaio, F., and Zagotta, W. N. (2019). The HCN Channel Voltage Sensor Undergoes a Large Downward Motion during Hyperpolarization. *Nat. Struct. Mol. Biol.* 26, 686–694. doi:10.1038/s41594-019-0259-1

Dai, G., Aman, T. K., DiMaio, F., and Zagotta, W. N. (2021). Electromechanical Coupling Mechanism for Activation and Inactivation of an HCN Channel. *Nat. Commun.* 12 (1), 2802. doi:10.1038/s41467-021-23062-7

Darden, T. A., York, D. M., and Pedersen, L. (1993). Particle Mesh Ewald - An N·Log(N) Method for Ewald Sums in Large Systems. *J. Chem. Phys.* 98, 10089–10092. doi:10.1063/1.464397

Decher, N., Chen, J., and Sanguinetti, M. C. (2004). Voltage-Dependent Gating of Hyperpolarization-Activated, Cyclic Nucleotide-Gated Pacemaker Channels: Molecular Coupling Between the S4-S5 and C-Linkers. *J. Biol. Chem.* 279, 13859–13865. doi:10.1074/jbc.m313704200

Fleishman, S. J., Leaver-Fay, A., Corn, J. E., Strauch, E.-M., Khare, S. D., Koga, N., et al. (2011). RosettaScripts: A Scripting Language Interface to the Rosetta Macromolecular Modeling Suite. *PLOS ONE* 6, e20161. doi:10.1371/journal.pone.0020161

Gould, I. R., Skjevik, Å. A., Dickson, C. J., Madej, B. D., and Walker, R. C. (2018). *Lipid17: A Comprehensive AMBER Force Field for the Simulation of Zwitterionic and Anionic Lipids. Manuscript in preparation.*

Gross, C., Saponaro, A., Santoro, B., Moroni, A., Thiel, G., and Hamacher, K. (2018). Mechanical Transduction of Cytoplasmic-To-Transmembrane-Domain Movements in a Hyperpolarization-Activated Cyclic Nucleotide-Gated Cation Channel. *J. Biol. Chem.* 293, 12908–12918. doi:10.1074/jbc.ra118.002139

Hermans, S. M. A., Pfleger, C., Nutschel, C., Hanke, C. A., and Gohlke, H. (2017). Rigidity Theory for Biomolecules: Concepts, Software, and Applications. *Wiley Interdiscip. Rev. Comput. Mol. Sci.* 7, e1311. doi:10.1002/wcms.1311

Hespenheide, B. M., Rader, A. J., Thorpe, M. F., and Kuhn, L. A. (2002). Identifying Protein Folding Cores from the Evolution of Flexible Regions during Unfolding. *J. Mol. Graph. Model.* 21, 195–207. doi:10.1016/s1093-3263(02)00146-8

Izadi, S., Anandakrishnan, R., and Onufriev, A. V. (2014). Building Water Models: A Different Approach. *J. Phys. Chem. Lett.* 5, 3863–3871. doi:10.1021/jz501780a

Jacobs, D. J., and Hendrickson, B. (1997). An Algorithm for Two-Dimensional Rigidity Percolation: The Pebble Game. *J. Comput. Phys.* 137, 346–365. doi:10.1006/jcph.1997.5809

Jacobs, D. J., Rader, A. J., Kuhn, L. A., and Thorpe, M. F. (2001). Protein Flexibility Predictions Using Graph Theory. *Proteins* 44, 150–165. doi:10.1002/prot.1081

Jacobs, D. J., and Thorpe, M. F. (1995). Generic Rigidity Percolation: The Pebble Game. *Phys. Rev. Lett.* 75, 4051–4054. doi:10.1103/physrevlett.75.4051

Jo, S., Kim, T., Iyer, V. G., and Im, W. (2008). CHARMM-GUI: A Web-Based Graphical User Interface for CHARMM. *J. Comput. Chem.* 29, 1859–1865. doi:10.1002/jcc.20945

Jones, D. T. (1999). Protein Secondary Structure Prediction Based on Position-Specific Scoring Matrices. *J. Mol. Biol.* 292, 195–202. doi:10.1006/jmbi.1999.3091

Kasimova, M. A., Tewari, D., Cowgill, J. B., Ursuleaz, W. C., Lin, J. L., Delemotte, L., et al. (2019). Helix Breaking Transition in the S4 of HCN Channel Is Critical for Hyperpolarization-Dependent Gating. *Elife* 8, 53400. doi:10.7554/eLife.53400

Koehler Leman, J., Weitzner, B. D., Lewis, S. M., Adolf-Bryfogle, J., Alam, N., Alford, R. F., et al. (2020). Macromolecular Modeling and Design in Rosetta: Recent Methods and Frameworks. *Nat. Methods* 17, 665–680. doi:10.1038/s41592-020-0848-2

Kusch, J., Biskup, C., Thon, S., Schulz, E., Nache, V., Zimmer, T., et al. (2010). Interdependence of Receptor Activation and Ligand Binding in HCN2 Pacemaker Channels. *Neuron* 67, 75–85. doi:10.1016/j.neuron.2010.05.022

Le Grand, S., Götz, A. W., and Walker, R. C. (2013). SPFP: Speed Without Compromise-A Mixed Precision Model for GPU Accelerated Molecular Dynamics Simulations. *Comput. Phys. Commun.* 184, 374–380. doi:10.1016/j.cpc.2012.09.022

Lebigot, E. O. (2021). *Uncertainties: A Python Package for Calculations with Uncertainties*. 3.1.5 ed.

Lee, C.-H., and MacKinnon, R. (2017). Structures of the Human HCN1 Hyperpolarization-Activated Channel. *Cell.* 168, 111–120 e111. doi:10.1016/j.cell.2016.12.023

Lee, C.-H., and MacKinnon, R. (2019). Voltage Sensor Movements during Hyperpolarization in the HCN Channel. *Cell.* 179, 1582–1589. e1587. doi:10.1016/j.cell.2019.11.006

Lolicato, M., Nardini, M., Gazzarrini, S., Möller, S., Bertinetti, D., Herberg, F. W., et al. (2011). Tetramerization Dynamics of C-Terminal Domain Underlies Isoform-specific cAMP Gating in Hyperpolarization-Activated Cyclic Nucleotide-Gated Channels. *J. Biol. Chem.* 286, 44811–44820. doi:10.1074/jbc.m111.297606

Lomize, M. A., Pogozheva, I. D., Joo, H., Mosberg, H. I., and Lomize, A. L. (2012). OPM Database and PPM Web Server: Resources for Positioning of Proteins in Membranes. *Nucleic Acids Res.* 40, D370–D376. doi:10.1093/nar/gkr703

Loncharich, R. J., Brooks, B. R., and Pastor, R. W. (1992). Langevin Dynamics of Peptides - the Frictional Dependence of Isomerization Rates of N-Acetylalanyl-N'-Methylamide. *Biopolymers* 32, 523–535. doi:10.1002/bip.360320508

Männikkö, R., Elinder, F., and Larsson, H. P. (2002). Voltage-sensing Mechanism Is Conserved Among Ion Channels Gated by Opposite Voltages. *Nature* 419, 837–841. doi:10.1038/nature01038

Marchesi, A., Gao, X., Adaixo, R., Rheinberger, J., Stahlberg, H., Nimigean, C., et al. (2018). An Iris Diaphragm Mechanism to Gate a Cyclic Nucleotide-Gated Ion Channel. *Nat. Commun.* 9, 3978. doi:10.1038/s41467-018-06414-8

Moukarzel, C., and Duxbury, P. M. (1999). Comparison of Rigidity and Connectivity Percolation in Two Dimensions. *Phys. Rev. E* 59, 2614–2622. doi:10.1103/physreve.59.2614

Otte, M., Schweinitz, A., Bonus, M., Enke, U., Schumann, C., Gohlke, H., et al. (2018). Hydrophobic Alkyl Chains Substituted to the 8-Position of Cyclic Nucleotides Enhance Activation of CNG and HCN Channels by an Intricate Enthalpy - Entropy Compensation. *Sci. Rep.* 8, 14960. doi:10.1038/s41598-018-33050-5

Otte, M., Schweinitz, A., Lelle, M., Thon, S., Enke, U., Yüksel, S., et al. (2019). Novel Fluorescent Cyclic Nucleotide Derivatives to Study CNG and HCN Channel Function. *Biophysical J.* 116, 2411–2422. doi:10.1016/j.bpj.2019.05.006

Pastor, R. W., Brooks, B. R., and Szabo, A. (1988). An Analysis of the Accuracy of Langevin and Molecular-Dynamics Algorithms. *Mol. Phys.* 65, 1409–1419. doi:10.1080/00268978800101881

Pfleger, C., Radestock, S., Schmidt, E., and Gohlke, H. (2013a). Global and Local Indices for Characterizing Biomolecular Flexibility and Rigidity. *J. Comput. Chem.* 34, 220–233. doi:10.1002/jcc.23122

Pfleger, C., Rathi, P. C., Klein, D. L., Radestock, S., and Gohlke, H. (2013b). Constraint Network Analysis (CNA): A Python Software Package for Efficiently Linking Biomacromolecular Structure, Flexibility, (Thermo-)stability, and Function. *J. Chem. Inf. Model.* 53, 1007–1015. doi:10.1021/ci400044m

Pfleger, C., Minges, A., Boehm, M., Mcclendon, C. L., Torella, R., and Gohlke, H. (2017). Ensemble- and Rigidity Theory-Based Perturbation Approach to Analyze Dynamic Allostery. *J. Chem. Theory Comput.* 13, 6343–6357. doi:10.1021/acs.jctc.7b00529

Pfleger, C., Kusch, J., Kondapuram, M., Schwabe, T., Sattler, C., Benndorf, K., et al. (2021). Allosteric Signaling in C-Linker and Cyclic Nucleotide-Binding Domain of HCN2 Channels. *Biophysical J.* 120, 950–963. doi:10.1016/j.bpj.2021.01.017

Porro, A., Saponaro, A., Gasparri, F., Bauer, D., Gross, C., Pisoni, M., et al. (2019). The HCN Domain Couples Voltage Gating and cAMP Response in Hyperpolarization-Activated Cyclic Nucleotide-Gated Channels. *eLife* 8, 49672. doi:10.7554/eLife.49672

Rader, A. J., Hespenheide, B. M., Kuhn, L. A., and Thorpe, M. F. (2002). Protein Unfolding: Rigidity Lost. *Proc. Natl. Acad. Sci. U. S. A.* 99, 3540–3545. doi:10.1073/pnas.062492699

Rader, A. J. (2009). Thermostability in Rubredoxin and its Relationship to Mechanical Rigidity. *Phys. Biol.* 7, 16002. doi:10.1088/1478-3975/7/1/016002

Radestock, S., and Gohlke, H. (2008). Exploiting the Link between Protein Rigidity and Thermostability for Data-Driven Protein Engineering. *Eng. Life Sci.* 8, 507–522. doi:10.1002/elsc.200800043

Radestock, S., and Gohlke, H. (2011). Protein Rigidity and Thermophilic Adaptation. *Proteins* 79, 1089–1108. doi:10.1002/prot.22946

Ramentol, R., Perez, M. E., and Larsson, H. P. (2020). Gating Mechanism of Hyperpolarization-Activated HCN Pacemaker Channels. *Nat. Commun.* 11 (1), 1419. doi:10.1038/s41467-020-15233-9

Rathi, P. C., Jaeger, K.-E., and Gohlke, H. (2015). Structural Rigidity and Protein Thermostability in Variants of Lipase A from Bacillus Subtilis. *PLOS ONE* 10, e0130289. doi:10.1371/journal.pone.0130289

Robinson, R. B., and Siegelbaum, S. A. (2003). Hyperpolarization-activated Cation Currents: from Molecules to Physiological Function. *Annu. Rev. Physiology* 65, 453–480. doi:10.1146/annurev.physiol.65.092101.142734

Roe, D. R., and Cheatham, T. E., Iii (2013). PTRAJ and CPPTRAJ: Software for Processing and Analysis of Molecular Dynamics Trajectory Data. *J. Chem. Theory Comput.* 9, 3084–3095. doi:10.1021/ct400341p

Rothberg, B. S., Shin, K. S., Phale, P. S., and Yellen, G. (2002). Voltage-controlled Gating at the Intracellular Entrance to a Hyperpolarization-Activated Cation Channel. *J. Gen. Physiol.* 119, 83–91. doi:10.1085/jgp.119.1.83

Ryckaert, J.-P., Ciccotti, G., and Berendsen, H. J. C. (1977). Numerical Integration of the Cartesian Equations of Motion of a System with Constraints: Molecular Dynamics of N-Alkanes. *J. Comput. Phys.* 23, 327–341. doi:10.1016/0021-9991(77)90098-5

Shin, K. S., Maertens, C., Proenza, C., Rothberg, B. S., and Yellen, G. (2004). Inactivation in HCN Channels Results from Reclosure of the Activation Gate: Desensitization to Voltage. *Neuron* 41, 737–744. doi:10.1016/s0896-6273(04)00083-2

Shintre, C. A., Pike, A. C. W., Tessitore, A., Young, M., Bushell, S. R., Strain-Damerell, C., et al. (2019). *Structure of Human HCN4 Hyperpolarization-Activated Cyclic Nucleotide-Gated Ion Channel.* (Unpublished Work, PDB-ID: 6GYN)".).

Skolnick, J., Jaroszewski, L., Kolinski, A., and Godzik, A. (1997). Derivation and Testing of Pair Potentials for Protein Folding. When is the Quasichemical Approximation Correct? *Protein Sci.* 6, 676–688. doi:10.1002/pro.5560060317

Song, Y., Dimaio, F. P., Wang, R. Y.-R., Kim, D., Miles, C., Brunette, T., et al. (2013). High-Resolution Comparative Modeling with RosettaCM. *Structure* 21, 1735–1742. doi:10.1016/j.str.2013.08.005

Sunkara, M. R., Schwabe, T., Ehrlich, G., Kusch, J., and Benndorf, K. (2018). All Four Subunits of HCN2 Channels Contribute to the Activation Gating in an Additive but Intricate Manner. *J. Gen. Physiol.* 150, 1261–1271. doi:10.1085/jgp.201711935

Tian, C., Kasavajhala, K., Belfon, K. a. A., Raguette, L., Huang, H., Migues, A. N., et al. (2020). ff19SB: Amino-Acid-Specific Protein Backbone Parameters Trained Against Quantum Mechanics Energy Surfaces in Solution. *J. Chem. Theory Comput.* 16, 528–552. doi:10.1021/acs.jctc.9b00591

Vassetti, D., Pagliai, M., and Procacci, P. (2019). Assessment of GAFF2 and OPLS-AA General Force Fields in Combination with the Water Models TIP3P, SPCE, and OPC3 for the Solvation Free Energy of Druglike Organic Molecules. *J. Chem. Theory Comput.* 15, 1983–1995. doi:10.1021/acs.jctc.8b01039

Vemana, S., Pandey, S., and Larsson, H. P. (2004). S4 Movement in a Mammalian HCN Channel. *J. Gen. Physiol.* 123, 21–32. doi:10.1085/jgp.200308916

Wahl-Schott, C., and Biel, M. (2009). HCN Channels: Structure, Cellular Regulation and Physiological Function. *Cell. Mol. Life Sci.* 66, 470–494. doi:10.1007/s00018-008-8525-0

Wainger, B. J., Degennaro, M., Santoro, B., Siegelbaum, S. A., and Tibbs, G. R. (2001). Molecular Mechanism of cAMP Modulation of HCN Pacemaker Channels. *Nature* 411, 805–810. doi:10.1038/35081088

Wang, J., Cieplak, P., and Kollman, P. A. (2000). How Well Does a Restrained Electrostatic Potential (RESP) Model Perform in Calculating Conformational Energies of Organic and Biological Molecules? *J. Comput. Chem.* 21, 1049–1074. doi:10.1002/1096-987x(200009)21:12<1049::aid-jcc3>3.0.co;2-f

Wang, J., Chen, S., and Siegelbaum, S. A. (2001). Regulation of Hyperpolarization-Activated HCN Channel Gating and cAMP Modulation Due to Interactions of COOH Terminus and Core Transmembrane Regions. *J. General Physiology* 118, 237–250. doi:10.1085/jgp.118.3.237

Wang, J., Wolf, R. M., Caldwell, J. W., Kollman, P. A., and Case, D. A. (2004). Development and Testing of a General Amber Force Field. *J. Comput. Chem.* 25, 1157–1174. doi:10.1002/jcc.20035

Wang, S., Li, W., Liu, S., and Xu, J. (2016). RaptorX-Property: A Web Server for Protein Structure Property Prediction. *Nucleic Acids Res.* 44, W430–W435. doi:10.1093/nar/gkw306

Weissgraeber, S., Saponaro, A., Thiel, G., and Hamacher, K. (2017). A Reduced Mechanical Model for cAMP-Modulated Gating in HCN Channels. *Sci. Rep.* 7, 40168. doi:10.1038/srep40168

Wu, E. L., Cheng, X., Jo, S., Rui, H., Song, K. C., Dávila-Contreras, E. M., et al. (2014). CHARMM-GUI Membrane Builder Toward Realistic Biological Membrane Simulations. *J. Comput. Chem.* 35, 1997–2004. doi:10.1002/jcc.23702

Xu, X., Vysotskaya, Z. V., Liu, Q., and Zhou, L. (2010). Structural Basis for the cAMP-Dependent Gating in the Human HCN4 Channel. *J. Biol. Chem.* 285, 37082–37091. doi:10.1074/jbc.m110.152033

Zagotta, W. N., Olivier, N. B., Black, K. D., Young, E. C., Olson, R., and Gouaux, E. (2003). Structural Basis for Modulation and Agonist Specificity of HCN Pacemaker Channels. *Nature* 425, 200–205. doi:10.1038/nature01922

Zheng, J., and Zagotta, W. N. (2000). Gating Rearrangements in Cyclic Nucleotide-Gated Channels Revealed by Patch-Clamp Fluorometry. *Neuron* 28, 369–374. doi:10.1016/s0896-6273(00)00117-3

Zheng, J., and Zagotta, W. N. (2003). Patch-Clamp Fluorometry Recording of Conformational Rearrangements of Ion Channels. *Science's STKE* 2003, PL7. doi:10.1126/stke.2003.176.pl7

Zhou, L., and Siegelbaum, S. A. (2007). Gating of HCN Channels by Cyclic Nucleotides: Residue Contacts that Underlie Ligand Binding, Selectivity, and Efficacy. *Structure* 15, 655–670. doi:10.1016/j.str.2007.04.012

Conflict of Interest: The authors declare that the research was conducted in the absence of any commercial or financial relationships that could be construed as a potential conflict of interest.

Publisher's Note: All claims expressed in this article are solely those of the authors and do not necessarily represent those of their affiliated organizations, or those of the publisher, the editors and the reviewers. Any product that may be evaluated in this article, or claim that may be made by its manufacturer, is not guaranteed or endorsed by the publisher.

frontiers | Frontiers in Physiology

TYPE Original Research
PUBLISHED 05 May 2023
DOI 10.3389/fphys.2023.1166450

OPEN ACCESS

EDITED BY
Claus Loland,
University of Copenhagen, Denmark

REVIEWED BY
Aravind Penmatsa,
Indian Institute of Science (IISc), India
Stefan Gahbauer,
University of California, San Francisco, United States
Clara T. Schoeder,
Leipzig University, Germany

*CORRESPONDENCE
W. Sandtner,
walter.sandtner@meduniwien.ac.at

RECEIVED 15 February 2023
ACCEPTED 24 April 2023
PUBLISHED 05 May 2023

CITATION
Boytsov D, Schicker K, Hellsberg E, Freissmuth M and Sandtner W (2023), Allosteric modulators of solute carrier function: a theoretical framework. *Front. Physiol.* 14:1166450. doi: 10.3389/fphys.2023.1166450

Allosteric modulators of solute carrier function: a theoretical framework

D. Boytsov[1], K. Schicker[1], E. Hellsberg[2], M. Freissmuth[1] and W. Sandtner[1]*

[1]Center of Physiology and Pharmacology, Medical University of Vienna, Vienna, Austria, [2]Computational Structural Biology Unit, National Institute of Neurological Disorders and Stroke (NINDS), National Institutes of Health (NIH), Bethesda, MD, United States

Large-scale drug screening is currently the basis for the identification of new chemical entities. This is a rather laborious approach, because a large number of compounds must be tested to cover the chemical space in an unbiased fashion. However, the structures of targetable proteins have become increasingly available. Thus, a new era has arguably been ushered in with the advent of methods, which allow for structure-based docking campaigns (i.e., virtual screens). Solute carriers (SLCs) are among the most promising drug targets. This claim is substantiated by the fact that a large fraction of the 400 solute carrier genes is associated with human diseases. The ability to dock large ligand libraries into selected structures of solute carriers has set the stage for rational drug design. In the present study, we show that these structure-based approaches can be refined by taking into account how solute carriers operate. We specifically address the feasibility of targeting solute carriers with allosteric modulators, because their actions differ fundamentally from those of ligands, which bind to the substrate binding site. For the pertinent analysis we used transition state theory in conjunction with the linear free energy relationship (LFER). These provide the theoretical framework to understand how allosteric modulators affect solute carrier function.

KEYWORDS

transition-state theory, linear free energy relationship, allosteric modulator, drug design, solute carrier

Introduction

Biological membranes are diffusion barriers for polar solutes. The solute carrier (SLC) group of membrane proteins affords the permeation of polar solutes across plasma- and intracellular membranes (Colas et al., 2016). Accordingly, SLCs play a central role in maintaining cell homeostasis, in supporting metabolism and in extruding toxic compounds (Klaassen and Aleksunes, 2010; Kristensen et al., 2011; Zhang et al., 2019). Given their physiological importance, it is not surprising that many inherited diseases have been linked to mutations in SLC genes (Bhat et al., 2021): in fact, of 9,178 monogenic diseases listed in the OMIM database, 187 and 434 are linked to SLCs and transporters, respectively. More importantly, SLCs can be plausibly argued to be druggable targets, which are underrepresented when compared to other protein families (Wang et al., 2020). Progress in identifying new SLC ligands, however, is slow (Casiraghi et al., 2021). Therefore, there is an urgent need to develop new strategies in drug development.

Historically, the majority of therapeutically relevant drugs were found by serendipity. Some 30 years ago, large-scale drug screens (high-throughput screening) were introduced to probe the chemical space for ligands with suitable properties. High-throughput screening has several limitations, though, in particular false positives and false negatives, which can result in substantial costs (Mayr and Bojanic, 2009). The structures of candidate drug targets are being solved at an increasing pace. Accordingly, approaches based on bioinformatics have become an attractive alternative, because they can be used to conduct virtual screens. Structure-based docking of large chemical libraries has resulted in the discovery of novel ligands for e.g., several G protein-coupled receptors (Orry et al., 2006; Kolb et al., 2009; Kolb and Irwin, 2009; Katritch et al., 2011; Rognan, 2011; Gabrielsen et al., 2012; Kufareva et al., 2012; Gabrielsen et al., 2013; Ngo et al., 2016; Rognan, 2017; Roth et al., 2017; Scharf et al., 2019; Alon et al., 2021; Ballante et al., 2021; Bender et al., 2021); in addition, the σ2-receptor is another recent example (Alon et al., 2021). Transporters can also be targeted by this approach: Singh et al. (2022) provided a proof-of-concept by docking a large library against the inward-facing conformation of the serotonin transporter (SERT), which led to the identification of molecules of novel chemotypes and pharmacology.

The monoamine transporters—i.e., the transporters for norepinephrine (NET/SLC6A2), dopamine (DAT/SLC6A3) and serotonin (SERT/SLC6A4) stand out among the SLC family members: they have a rich pharmacology (Sitte and Freissmuth, 2015). Most drugs bind to the orthosteric binding site (i.e., the substrate binding site). However, some compounds were reported to bind to allosteric sites (e.g., vilazodone, ATM7) (Kortagere et al., 2013; Plenge et al., 2021). Allosteric modulators are of interest because they can exert actions, which orthosteric ligands do not: this includes a drug-induced acceleration of the transport cycle, increased/decreased substrate release and allosteric (i.e., non-competitive) inhibition of substrate uptake (Hasenhuetl et al., 2019; Niello et al., 2020). Arguably, any of these actions may prove to be useful from a therapeutic perspective. However, at the current state of affairs, there isn't any theoretical framework for the rational design of allosteric modulators. This framework must take into account how SLCs operate. Only then can we identify the key levers for modulating SLC function by small molecule modulators. Substrate uptake by solute carriers is contingent on their ability to undergo a series of partial reactions. These include binding/unbinding reactions of (co)-substrates and conformational rearrangements such as the isomerization from the outward-facing (OF) to the inward-facing (IF) state (Rudnick and Sandtner, 2019). The collective partial reactions form a closed loop, which is also referred to as the transport cycle. In the present study, we used transition state theory and the linear free energy relationship (LFER) to analyze and predict the effects of allosteric modulators on the reaction kinetics of solute carriers.

Methods

Figure 1 displays the reaction scheme of the model used to simulate the effect of positive (Figure 1A) and negative allosteric modulators (Figure 1B) on the transport cycle of a solute carrier. The schemes depicted in Figures 4A, 5A are simplified representations thereof. In Figure 1C we show the system of differential equations, which underlies the two reaction schemes. The shown reaction diagrams are comprised of one reaction loop in the front (indicated in black) and one in the rear (indicated in blue). The two loops, which represent the transport cycle of a hypothetical solute carrier in the absence and presence of the modulator, were biased in the forward direction (i.e., clockwise) by setting the concentration of Na^+ to 150 mM on the extracellular and to 0 mM on the intracellular side. In the absence of the modulator all transporters cycle in the front loop, while at saturating concentrations of the modulator all transporters cycle in the rear loop. At concentrations below saturation, the fraction of the transporter, which is free and occupied by the modulator, cycles in the front and rear loop, respectively. Positive allosteric modulation of substrate transport was modelled by assuming that the substrate-free outward-facing state (state **To** in the diagram) had a higher affinity for the modulator than all other states in the diagram. Negative allosteric modulation of substrate transport was modelled by assigning high affinity of the modulator to the (co)-substrate-bound outward-facing conformation (state **ToNaS** in the diagram). In the model, high affinity was conferred to an allosteric ligand by lowering its dissociation rate.

The following set of rate constants, which we used to parameterize the reaction scheme shown in Figure 1A (i.e., for a positive allosteric modulator), is listed here as an example: $k_{12} = 10^{16*}[Na_{out}]*[S_{out}]s^{-2}$, $k_{23} = 10^6\ s^{-1}$, $k_{34} = 10^{12}\ s^{-2}$; $k_{41} = 2\ s^{-1}$ (i.e., rate constants in the clockwise direction of the front loop); $k_{14} = 2\ s^{-1}$; $k_{43} = 10^{16*}[Na_{in}]*[S_{in}]\ s^{-2}$; $k_{32} = 10^6\ s^{-1}$; $k_{21} = 10^{12}\ s^{-2}$ (i.e., rate constants in the counter-clockwise direction of the front loop); $k_{56} = 10^{16*}[Na_{out}]*[S_{out}]s^{-2}$; $k_{67} = 10^6\ s^{-1}$; $k_{78} = 10^{12}\ s^{-2}$; $k_{85} = 20\ s^{-1}*\mathbf{X}$ (i.e., rate constants in the clockwise direction of the rear loop); $k_{58} = 2\ s^{-1}*\mathbf{X}$; $k_{87} = 10^{16*}[Na_{in}]*[S_{in}]s^{-2}$; $k_{76} = 10^6\ s^{-1}$; $k_{65} = 10^{13}\ s^{-2}$ (i.e., rate constants in the counter clockwise direction of the rear loop); $k_{26} = 10^{6*}[M]*s^{-1}$; $k_{62} = 10\ s^{-1}$; $k_{37} = 10^{6*}[M]*s^{-1}$; $k_{73} = 10\ s^{-1}$; $k_{48} = 10^{6*}[M]*s^{-1}$; $k_{84} = 10\ s^{-1}$ (i.e., rate constants, which define binding of the modulator to the low affinity states); and $k_{15} = 10^{6*}[M]s^{-1}$; $k_{51} = 1\ s^{-1}$ (i.e., rate constants, which define binding of the modulator to the high affinity state). $[Na_{out}]$ and $[S_{out}]$ are the extracellular Na^+ and substrate concentration, respectively, $[Na_{in}]$ and $[S_{in}]$ the corresponding intracellular concentrations, and [M] the concentration of the allosteric modulator. **X** is a factor that allows for adjusting the value of α (i.e., the position of the transition state on the reaction coordinate). **X** can assume values between zero and infinity. The loop was biased into the forward direction by setting $[Na_{out}]$, $[S_{out}]$, $[Na_{in}]$, and $[S_{in}]$ to 0.15 M, 10^{-3} M, 0 M and, 0 M, respectively. The chosen set of rate constants (i) keeps microscopic reversibility, (ii) sets the K_Ds of the modulator for the low and high affinity state of the hypothetical transporter to 10 and 1 μM, respectively and (iii) allows for the reaction from TiM to ToM to remain rate-limiting over a wide range of **X** values.

We used the Systems Biology Toolbox (Schmidt and Jirstrand, 2006) and MATLAB 2018a (MathWorks, Natick, MA, United States) to evaluate by numerical integration the time-dependent changes in state occupancies of the system of differential equations shown in Figure 1C. Substrate uptake was modelled as the sum of the flux through the front and the rear loop.

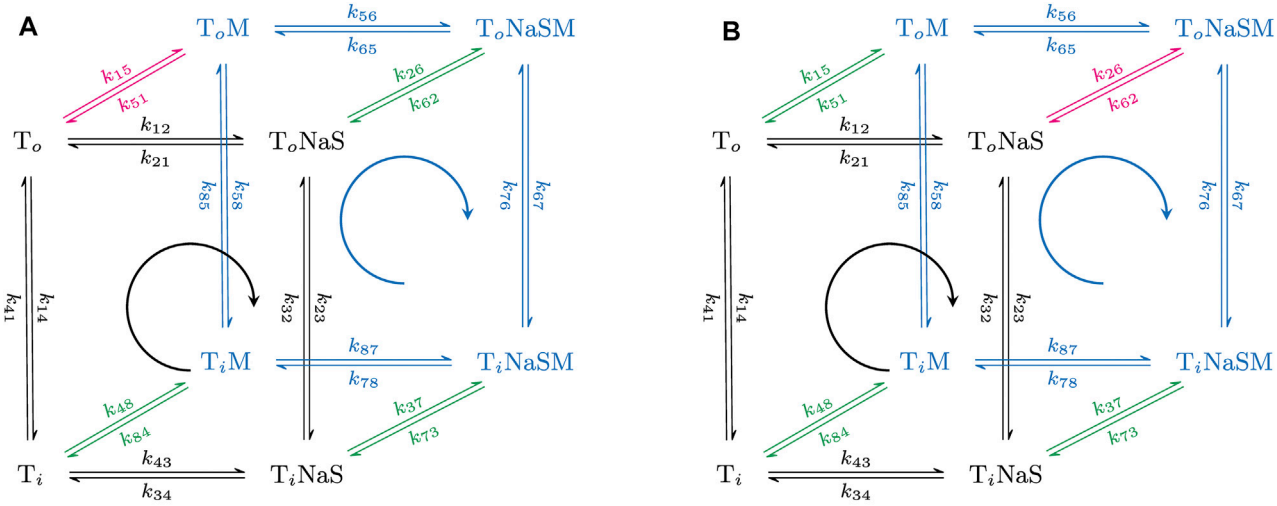

C

$$\frac{dT_o}{dt} = -T_o \cdot k_{12} - T_o \cdot k_{14} - T_o \cdot k_{15} + T_oNaS \cdot k_{21} + T_i \cdot k_{41} + T_oM \cdot k_{51}$$
$$\frac{dT_i}{dt} = -T_i \cdot k_{41} - T_i \cdot k_{43} - T_i \cdot k_{48} + T_o \cdot k_{14} + T_iNaS \cdot k_{34} + T_iM \cdot k_{84}$$
$$\frac{dT_oM}{dt} = -T_oM \cdot k_{51} - T_oM \cdot k_{56} - T_oM \cdot k_{58} + T_o \cdot k_{15} + T_oNaSM \cdot k_{65} + T_iM \cdot k_{85}$$
$$\frac{dT_iM}{dt} = -T_iM \cdot k_{84} - T_iM \cdot k_{85} - T_iM \cdot k_{87} + T_i \cdot k_{48} + T_oM \cdot k_{58} + T_iNaSM \cdot k_{78}$$
$$\frac{dT_oNaS}{dt} = -T_oNaS \cdot k_{21} - T_oNaS \cdot k_{23} - T_oNaS \cdot k_{26} + T_o \cdot k_{12} + T_iNaS \cdot k_{32} + T_oNaSM \cdot k_{62}$$
$$\frac{dT_iNaS}{dt} = -T_iNaS \cdot k_{32} - T_iNaS \cdot k_{34} - T_iNaS \cdot k_{37} + T_oNaS \cdot k_{23} + T_i \cdot k_{43} + T_iNaSM \cdot k_{73}$$
$$\frac{dT_oNaSM}{dt} = -T_oNaSM \cdot k_{62} - T_oNaSM \cdot k_{65} - T_oNaSM \cdot k_{67} + T_oNaS \cdot k_{26} + T_oM \cdot k_{56} + T_iNaSM \cdot k_{76}$$
$$\frac{dT_iNaSM}{dt} = -T_iNaSM \cdot k_{73} - T_iNaSM \cdot k_{76} - T_iNaSM \cdot k_{78} + T_iNaS \cdot k_{37} + T_oNaSM \cdot k_{67} + T_iM \cdot k_{87}$$

FIGURE 1
Simplified reaction schemes of the transport cycle of a solute carrier in the absence and presence of an allosteric modulator. **(A,B)** show the reaction diagrams of the kinetic models, which were used to emulate the action of a positive and a negative allosteric modulator, respectively. **To** and **Ti** are the substrate-free outward (OF)- and substrate-free inward-facing (IF) conformations. **ToNaS** is the (co)-substrate bound OF state and **TiNaS** the (co)-substrate bound IF state. **ToM**, **TiM**, **ToNaSM** and **TiNaSM** are the modulator-bound counterparts. The reaction diagrams are comprised of one reaction loop in the front (indicated in black) and one in the rear (indicated in blue). The two loops, which represent the transport cycle of a hypothetical solute carrier in the absence (front loop) and presence (rear loop) of the modulator (M), were biased in the forward direction (i.e., clockwise) by setting the concentration of Na^+ to 150 mM on the extracellular and to 0 mM on the intracellular side. The red and green arrows indicate the high and low affinity binding reaction(s) of the modulator, respectively. In **(A)**, the modulator was assumed to bind with higher affinity to the **To** state. In **(B)**, the modulator was assumed to bind with higher affinity to the **ToNaS** state. **(C)** System of differential equations, which underlies the reaction schemes in **(A,B)**. Each of the displayed equations defines the time-dependent change in state occupancy of one of the eight states specified in **(A,B)**.

We used the Eyring equation to relate the unidirectional rate constants of a reaction to the free energy of the corresponding transition state ($G^‡$).

$$k = \kappa^{\star}\frac{k_B}{h}{}^{\star}T^{\star}e^{\frac{-\Delta G^‡}{RT}}$$

where k is the unidirectional rate constant, k_B/h (Boltzmann constant/Plank constant) is the universal attempt frequency, T is the temperature and R is the gas constant. For the transmission coefficient κ we assumed a value of 1 (i.e., no reflection from the transition state back to the reactant state). We calculated the position of the transition state on the reaction coordinate (i.e., α) by converting the values of the unidirectional rate constants into the corresponding values of $G^‡$ and used these to construct the free energy landscape. The following equation allowed for extracting α: $\alpha = (\Delta\Delta G^‡ - \Delta\Delta G_R)/(\Delta\Delta G_P + \Delta\Delta G_R)$. The energy terms in this equation are illustrated in Figure 3.

For the molecular visualization in Figure 7 we used PyMOL (The PyMOL Molecular Graphics System, Version 2.5 Schrödinger, LLC) (Schrodinger, 2022).

Results

Allosteric modulators of SLC function

Allosteric modulators of solute carriers are molecules, which act by changing the rate(s) of one or more partial reactions in the transport cycle of the targeted transporter. For a molecule/ligand to alter the rate of a partial reaction, it must bind with higher affinity to the reactant than to the product state or *vice versa*. This point is illustrated in Figure 2, which shows the free energy landscapes of a reversible elementary reaction that is amenable to modulation by a ligand. The blue and red lines represent the free energy landscapes in the absence and presence of an allosteric modulator, respectively.

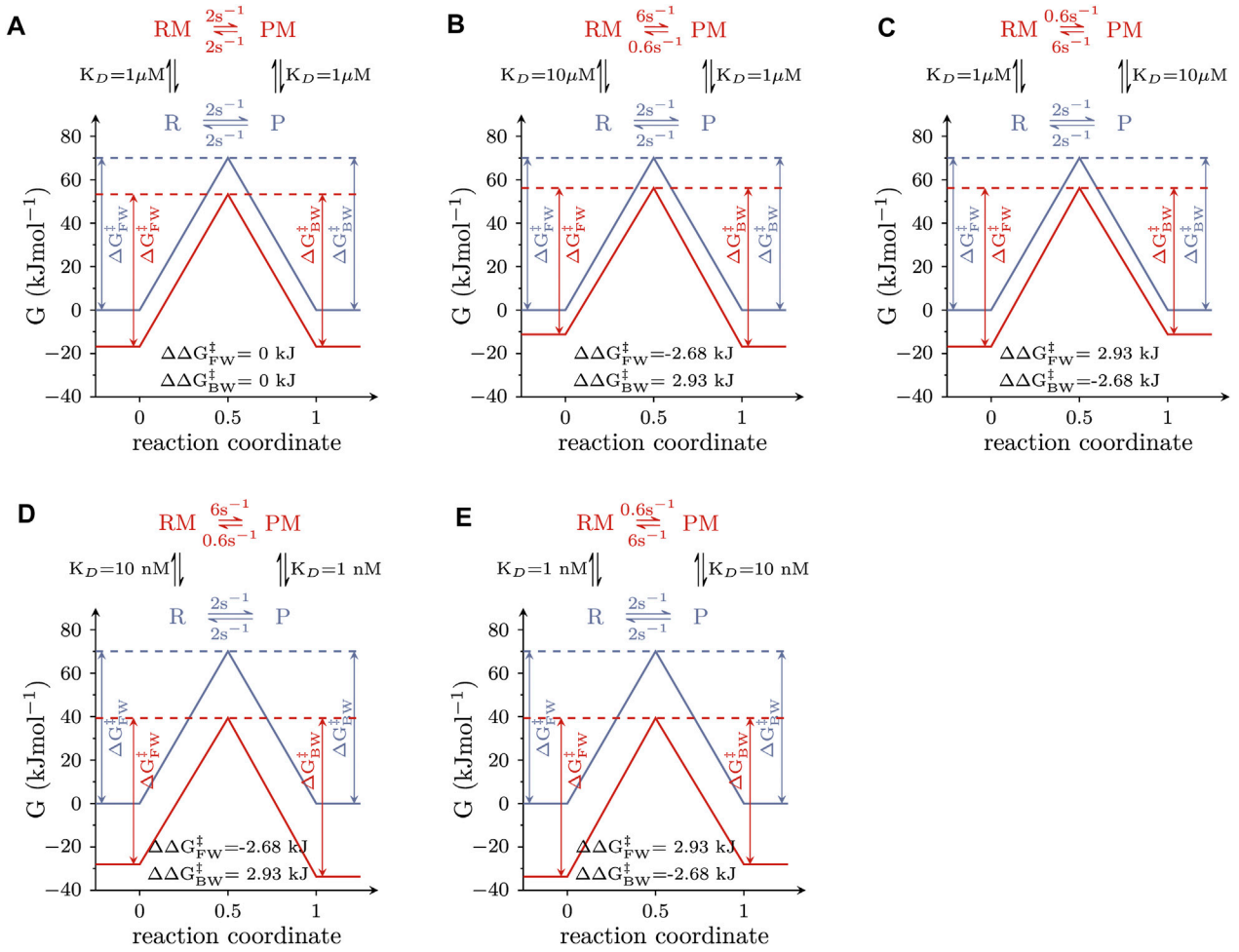

FIGURE 2
Free energy landscapes of elementary reactions that are responsive to modulation by a ligand. The blue and red lines show the landscape of the Gibbs energy (G) in the absence and presence of 1 mM modulator, respectively. The corresponding reaction scheme is displayed on the top of each panel, where R and P are the reactant and the product state, and RM and PM are the modulator-bound counterparts. **(A)** Free energy landscapes of a modulator that binds to both states with equal affinity (i.e., K_D = 1 μM). Stated in the figure are the values of $\Delta\Delta G^{\ddagger}_{FW}$ and $\Delta\Delta G^{\ddagger}_{FW}$. **(B)** The same as in **(A)** for an allosteric modulator that binds to the product state with higher affinity than the reactant state (i.e., K_D = 1 μM and 10 μM, respectively). **(C)** The same as in **(A)** for an allosteric modulator that binds the reactant state with higher affinity than the product state (i.e., K_D = 1 μM and 10 μM, respectively). The position of the transition state in **(A–C)** was assumed to be located halfway on the reaction coordinate. **(D,E)** Free energy landscapes of a hypothetical allosteric modulator, which binds to the reactant and product state with affinities in the nanomolar range. In **(D)** the K_Ds for the reactant and product state are 10 and 1 nM, respectively. In **(E)** the K_Ds for the reactant and product state are 1 and 10 nM. The affinity ratio (i.e., K_D reactant state/K_D product state) is 10 in **(B,D)** and 0.1 in **(C,E)**. As a consequence, the reaction rates in **(B)** are the same as in **(D)** and the reaction rates in **(C)** the same as in **(E)**.

The insets depict the corresponding reaction schemes, where the modulator-free reactant and product-state are indicated as R and P and the modulator-bound counterparts as RM and PM. In the absence of the allosteric modulator, the reaction rate in the forward direction was assumed to equal the rate in the backward direction. We considered three scenarios: (i) The allosteric modulator binds to the reactant and the product state with equal affinity (Figure 2A). A modulator with these properties reduces both, the free energy (G) of the reactant and the product state by the same amount. Thus, $\Delta G^{\ddagger}$ (the free energy difference between the ground- and the transition state) in the forward ($\Delta G^{\ddagger}_{FW}$) and the backward direction ($\Delta G^{\ddagger}_{BW}$) remains constant (compare the length of the red and blue arrows in Figure 2A). The Eyring equation (see Methods) allows for converting $\Delta G^{\ddagger}_{FW}$ and $\Delta G^{\ddagger}_{BW}$ into the unidirectional rate constants in the forward and backward direction, respectively. Because $\Delta G^{\ddagger}_{FW}$ and $\Delta G^{\ddagger}_{BW}$ are unchanged the rate constants of this reaction (values in blue) are not affected by the allosteric modulator. (ii) The allosteric modulator binds to the product state with a tenfold higher affinity than to the reactant state (Figure 2B). In this case, the modulator lowers the free energy of the product state more than that of the reactant state. As a result, $\Delta G^{\ddagger}_{FW}$ becomes smaller and $\Delta G^{\ddagger}_{BW}$ larger. This leads to an increase and decrease of the unidirectional rate constant in the forward and backward reaction, respectively (see reaction diagram Figure 2B). (iii) The allosteric modulator binds to the reactant state with higher affinity than to the product state (Figure 2C). In this instance, the rate constant in the forward direction decreases while the rate constant in the backward direction increases. Thus, depending on

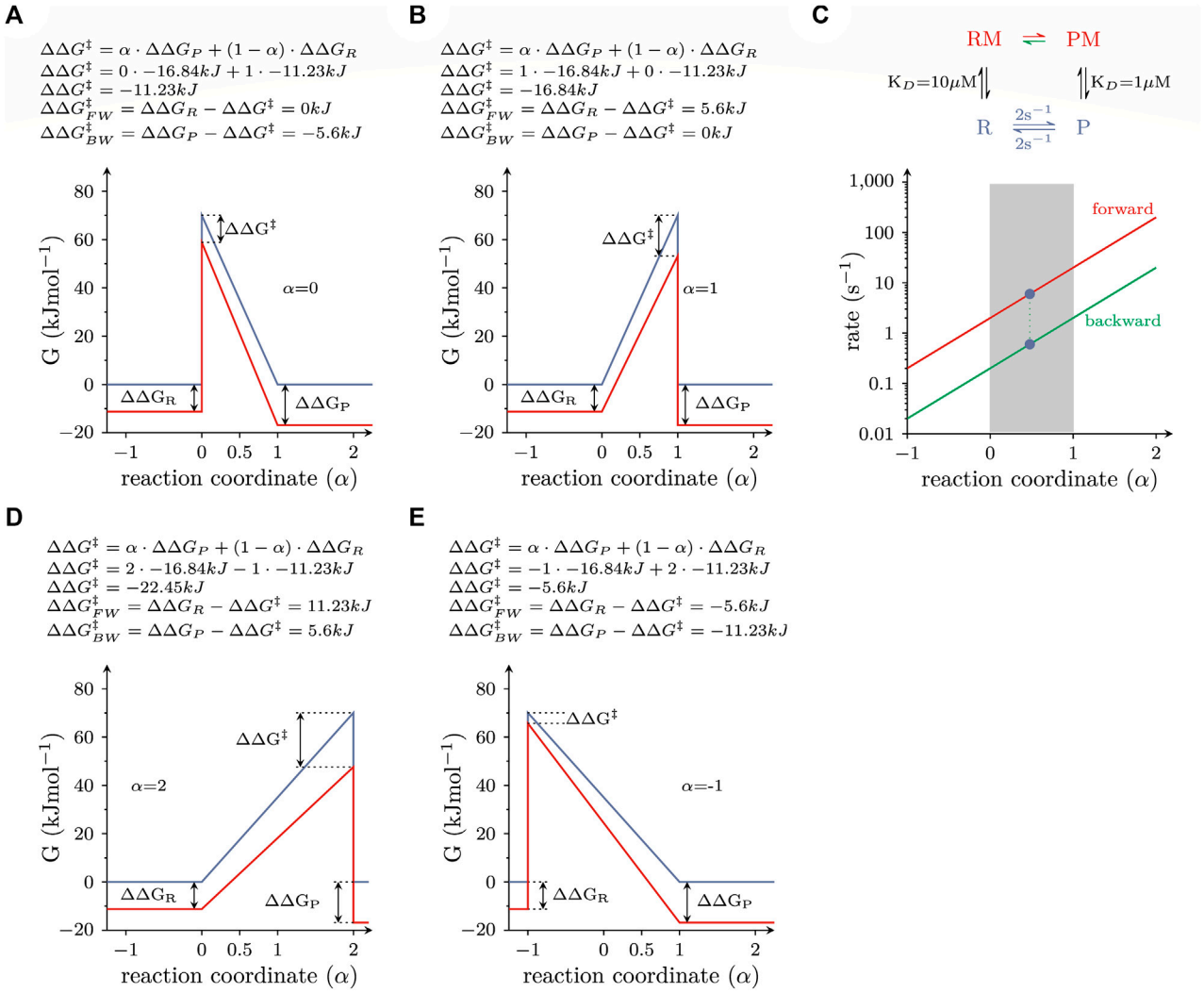

FIGURE 3
Energy landscapes of reactions, which do or do not comply with LFER **(A)** Free energy landscape of a reversible elementary reaction, which is responsive to modulation by a ligand. The blue and red lines are the landscapes in the absence and presence of 1 mM ligand, respectively. The equation on top of the panel provides a mathematical description of the LFER principle. For the calculation, α was assumed to equal zero (i.e., the properties of the transition state resemble those of the reactant state). **(B)** Same as in **(A)**, but with the assumption that α equals 1 (i.e., the properties of the transition state resemble those of the product state). **(C)** Plotted are the rate constants connecting the RM and PM states, which fulfill the detailed balance constraint as a function of α. The rate constants are plotted on a logarithmic axis. The red and green lines show the forward and backward rate constants, respectively. Each pair of rate constants on a vertical line defines a unique free energy landscape. Pairs that fall into the shaded range comply with LFER. All other pairs do not. **(D,E)** show the free energy landscapes of two pairs of rate constants, which defy LFER. In D and E, α is 2 and −1, respectively.

which state the allosteric modulator favors, a reaction proceeding in the forward direction can either be slowed or accelerated. In Figures 2A–C we assumed that the allosteric modulator bound to the reactant and the product state with affinities in the micromolar range. In Figures 2D, E we show the free energy landscapes, in the presence and absence of a modulator with K_Ds in the low nanomolar range. In Figure 2D the K_D is 10 and 1 nM for the reactant and product state, respectively, and the reverse in Figure 2E. The low and high affinity modulators affect the rates of the reaction to the same extent (cf., 2B and 2D; cf., 2C and 2E), provided that the affinity ratios for reactant and product state (K_D reactant state/K_D product state) are equivalent. This demonstrates that it is not the absolute but the relative affinity of the modulator for the two ground states, which determines the extent of the change in the reaction rate.

The reaction schemes in Figure 2 comprise a loop. The rules of thermodynamics dictate that the numeric values of the rate constants used to parameterize a reaction loop must fulfill the detailed balance constraint (the product of the rates in the forward direction of the loop must equal the product of the rates in the backward direction). This constraint explains why in the reaction schemes in Figures 2B–E the rate constants in the forward and the backward direction, connecting the RM and PM state differ by a factor of 10: it results from the tenfold difference in the K_Ds of the allosteric modulator for R and P (and from the requirement for maintaining microscopic reversibility). However, it is evident that other pairs of rate constants exist, which also fulfill the detailed balance constraint (e.g., 8 and 0.8 s^{-1}). In the following, we show that the specific values

stated in the reaction schemes in Figures 2B–E are dictated by the linear free energy relation.

Linear free energy relationship

LFER links the change in ΔG of the reactant and product state (i.e., $\Delta\Delta G_R$; $\Delta\Delta G_P$) to the corresponding change of $\Delta G^{\ddagger}$ (i.e., $\Delta\Delta G^{\ddagger}$). When LFER applies, these parameters are related as follows:

$$\Delta\Delta G^{\ddagger} = \alpha^{*}\Delta\Delta G_P + (1-\alpha)^{*}\Delta\Delta G_R$$

The energy terms of the equation are illustrated in Figure 3. The above equation implies that the transition state of a reaction must have properties, which lie between those of the reactant and the product state (i.e., the ground states). For instance, if a chemical reaction is accompanied by a volume change, the transition state is posited to adopt a volume, which lies between that of the reactant and the product. Similarly, the possible positions of the transition state within the energy landscape are constraint: in LFER the transition state is defined by boundaries imposed by the ground states, where the value of $\Delta\Delta G^{\ddagger}$ lies between that of $\Delta\Delta G_P$ and $\Delta\Delta G_R$. This applies, if the variable α in the equation is only allowed to adopt values between 0 and 1. The latter is a key assumption of LFER, where α is thought to account for the position of the transition state along the reaction coordinate: α equals zero, if the transition state resembles the reactant state. Conversely, α equals 1, if the transition state resembles the product state.

The energy landscapes shown in Figure 2 were calculated assuming that the transition state was located halfway on the reaction coordinate of the reaction (i.e., symmetric barrier assumption): accordingly, the properties of the transition state resemble those of both ground states to the same extent. This, however, need not be the case, as the transition state can either resemble more the reactant or the product state.

In the examples depicted in Figure 3, we considered the same scenario as in Figure 2B, i.e., the allosteric modulator bound with 10-fold higher affinity to the product than to the reactant state (K_D = 1 vs. 10 μM) and was present at a saturating concentration (1 mM). In Figure 3A, the transition state was assumed to resemble the reactant state (α = 0). The change in $\Delta\ G^{\ddagger}_{FW}$ (i.e., $\Delta\Delta\ G^{\ddagger}_{FW}$) can be calculated by subtracting $\Delta\Delta\ G^{\ddagger}$ from $\Delta\Delta G_R$. Similarly, the change in $\Delta\ G^{\ddagger}_{BW}$ (i.e., $\Delta\Delta\ G^{\ddagger}_{BW}$) can be computed by subtracting $\Delta\Delta\ G^{\ddagger}$ from $\Delta\Delta G_P$. Under the assumption that α is zero the calculated values for $\Delta\Delta\ G^{\ddagger}_{FW}$ and $\Delta\Delta\ G^{\ddagger}_{BW}$ are 0 and −5.6 kJ/mol, respectively. Thus, $\Delta\ G^{\ddagger}_{FW}$ remains unchanged, while $\Delta\ G^{\ddagger}_{BW}$ is increased by 5.6 kJ/mol. As a consequence, the unidirectional rate constant in the forward direction (as calculated by the Eyring equation) is not affected, but the unidirectional rate constant in the backward direction decreases from 2 to 0.2 s^{-1}. Figure 3B demonstrates the other extreme, where the transition state resembles the product state (α = 1). In this instance, ligand binding lowers $\Delta G^{\ddagger}_{FW}$ by about 5.6 kJ/mol but $\Delta\ G^{\ddagger}_{BW}$ is unchanged. As a corollary, the rate in the forward direction increases tenfold, while the rate in the backward reaction remains unchanged. Figure 3C illustrates, how the position of the transition state on the reaction coordinate (α) affects the forward and backward rates (red and green line, respectively): we specifically highlight the pair of values (green dots in Figure 3C), which was used to calculate the free energy landscape displayed in Figure 2B (α = 0.5), and stress that, in this plot, each pair of rate constants on a vertical line fulfills the detailed balance constraint. We further emphasize that only those pairs of rate constants, which fall into the shaded range, comply with LFER: all other pairs outside of this range also fulfill the detailed balance constraint, but they violate LFER, because α adopts values, which are either smaller than zero or larger than 1. Figures 3D, E exemplify these free energy landscapes, which defy LFER. If α is assumed to be 2 (Figure 3D), $\Delta\Delta\ G^{\ddagger}$ is larger than $\Delta\Delta G_P$ and $\Delta\Delta G_R$. Thus, the transition state is more sensitive to the ligand-induced change in ΔG than either of the ground states. The opposite (i.e. $\Delta\Delta\ G^{\ddagger} < \Delta\Delta G_P$; $\Delta\Delta\ G^{\ddagger} < \Delta\Delta G_R$) is true with α = −1 (Figure 3E).

Positive allosteric modulators

Allosteric modulators of SLC function are of interest because they can exert actions other than those elicited by orthosteric ligands (i.e., compounds trapped in the substrate binding site): drug-induced acceleration of the transport cycle is of particular interest, because it leads to increased substrate uptake. For a molecule to increase substrate uptake, it must accelerate the velocity of one or more partial reactions in the transport cycle of the targeted solute carrier. However, a substantial increase in the substrate uptake rate of a transporter, can only be achieved by augmenting the velocity of reactions, which are slow and thus rate-limiting in the transport cycle. For many solute carriers, including the monoamine transporters, the slowest reaction in the transport cycle is the return step from the substrate-free inward-facing (IF) to the substrate-free outward-facing (OF) conformation. This reaction is depicted in the schematic representation in Figure 4A. We simulated cellular substrate uptake through an SLC by focusing on this reaction in the transport cycle, which was biased into the forward direction by an inwardly-directed Na^+ gradient. All other reactions were lumped together and represented by the curved arrow. It was further assumed that the allosteric ligand was present at a saturating concentration (i.e., 1 mM). Because the cycle is biased in the forward direction, the OF state is the product state. As discussed above, a ligand, which accelerates a reaction, must bind to the product state with higher affinity than the reactant state. Therefore, by analogy with Figures 2B, 3, the ligand affinity for the OF state was assumed to be ten times higher than that of the IF state. LFER predicts that the reaction rate (red arrow in Figure 4A) is approximately 3 times larger in the presence than in the absence of the allosteric modulator, if the transition state is located halfway on the reaction coordinate (α = 0.5).

To investigate the impact of α on the substrate uptake rate, we systematically varied the location of the transition state on the reaction coordinate. Figure 4B depicts the ligand-induced fold change (gain) of the substrate uptake velocity at different ligand concentrations as a function of α. As is evident from the plot, a ligand with the properties described in Figure 4A can accelerate the rate of substrate uptake by a maximum factor of 10. However, the magnitude of the gain depends on the value of α (i.e., the position of the transition state on the reaction coordinate) and the ambient ligand concentration. Notably, if α = 0, the modulator is unable to accelerate the reaction (i.e., gain = 1). In this context, it is important to emphasize that the position of the transition state on the reaction

10.3389/fphys.2023.1166450

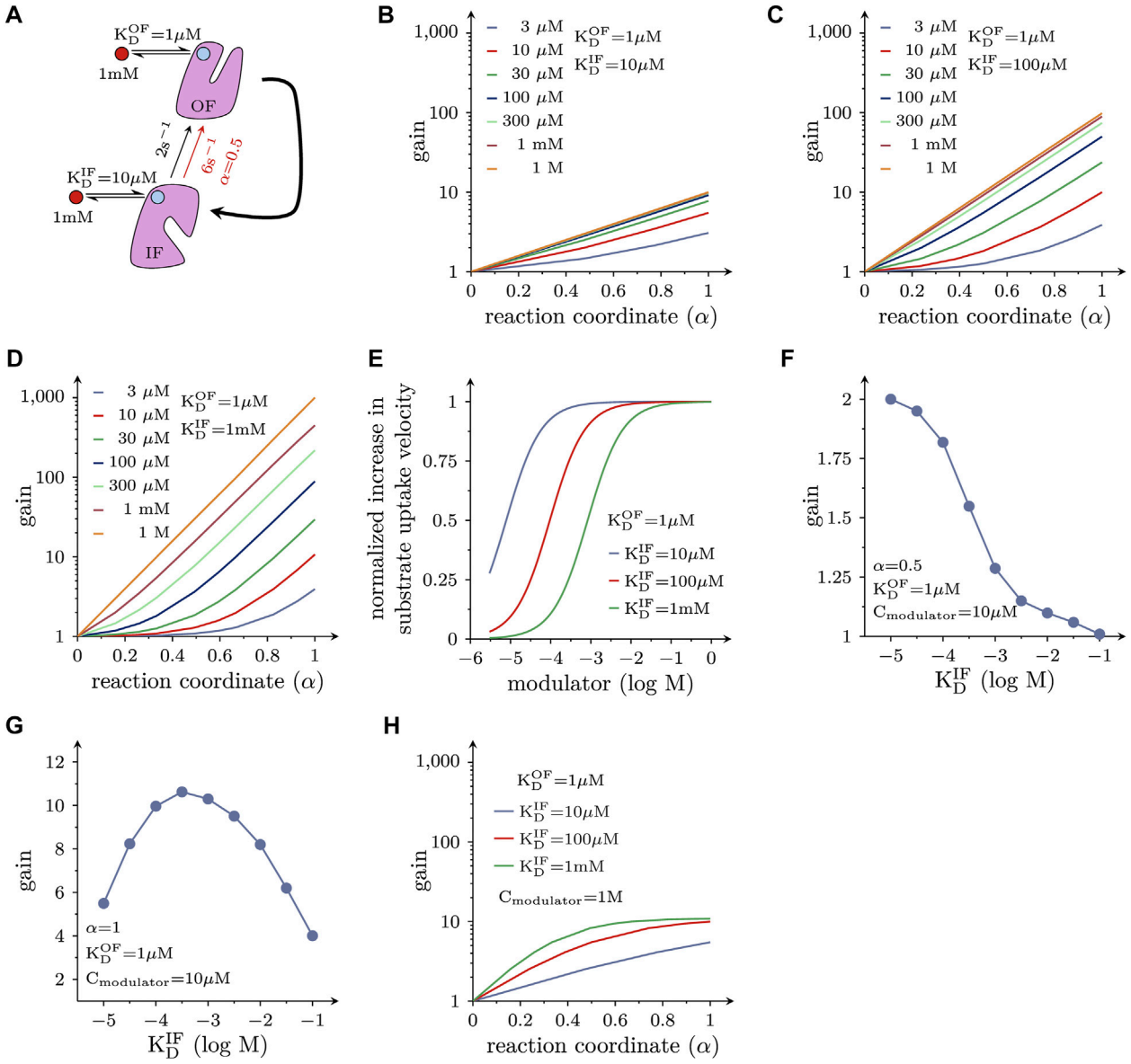

FIGURE 4
Positive allosteric modulation of solute carrier function. **(A)** Reaction diagram. Displayed is the return step from the substrate-free IF to the substrate-free OF state. This is the rate-limiting reaction in the transport cycle of many, if not most, solute carriers. This reaction was assumed to be a partial reaction in a forwardly biased reaction loop (i.e., in the transport cycle). All other reactions in the loop were lumped together and are represented by the bold curved arrow. The red circle indicates the hypothetical allosteric modulator. The light blue circles indicate the corresponding binding site on the OF state and IF state of the transporter, respectively. In the assumed presence of the modulator the rate of the reaction increased threefold when α = 0.5 (i.e., from 2 s^{-1} - black arrow - to 6 s^{-1}- red arrow) **(B)** Plotted is the fold increase (gain) in substrate uptake velocity, which is induced by the hypothetical allosteric modulator, as a function of α. The modulator was assumed to bind with a tenfold higher affinity to the OF state than to the IF state. The colored lines show the gain at the indicated concentrations of the hypothetical allosteric modulator. If α = 0, the modulator is ineffective. **(C,D)** The same type of plots as in **(B)** for a hypothetical allosteric modulator, which is 100-fold and 1000-fold more selective for the OF state, respectively. **(E)** Shown is the normalized increase in the substrate uptake rate as a function of the modulator concentration for three hypothetical modulators with variable selectivity. As seen, the EC_{50} value for the allosteric effect shifts to the right as the modulator becomes more selective for the OF state. **(F)** Gain induced by hypothetical allosteric modulators with variable selectivity for the OF over the IF state (ranging from 10- to 10,000 fold) for α = 0.5. At 10 μM of the modulator, the more selective drugs became less efficient. **(G)** Gain as a function of the selectivity of the hypothetical allosteric modulators for a transporter operating at α = 1. At 10 μM of the modulator the relation between selectivity and the gain in substrate uptake is bell-shaped. **(H)** Effect of modulators on the transport cycle under the assumption that the slowest reaction in the transport cycle (i.e., 2 s^{-1}) is accelerated to an extent that another reaction becomes rate limiting (20 s^{-1}): the gain (in substrate uptake velocity) is plotted as a function of α for three hypothetical allosteric modulators with differing selectivity for the OF state (i.e., 10-, 100- and 1000-fold). In this instance, the attainable gain is limited, although the modulators are present at a saturating concentration.

coordinate is an intrinsic property of a reaction and not subject to change. Thus, if and to which extent a candidate solute carrier is amendable to the desired allosteric action (e.g., acceleration of substrate uptake velocity), depends on the values of these parameters.

In Figures 4C, D we show the gain of the substrate uptake velocity for an allosteric ligand that is 100 times and 1000 times more selective for the OF state over the IF state, respectively as a function of α at different ligand concentrations: a more OF-selective ligand can be an even more effective positive allosteric modulator. The maximal gain at a saturating concentration of the allosteric ligand is 100 and 1000 in Figures 4C, D, respectively (cf., lines representing ≥0.3 mM in Figure 4C, and 1 M in Figure 4D).

In Figure 4E we plotted the normalized increase in substrate uptake velocity as a function of the concentration of the hypothetical OF-selective allosteric ligands considered in Figures 4B–D. It is evident from Figure 4E that there is a right shift of the EC_{50} value for the allosteric effect with increasing OF selectivity. This is because for the more selective allosteric ligands higher concentrations are required to afford occupancy of the ligand binding site in the low-affinity state (i.e., IF state). An OF selective allosteric ligands can only support the desired positive allosteric action, if it remains bound (i.e., it must not dissociate from the IF state).

This allows for the seemingly paradoxical situation, where - at a low ambient concentration of the allosteric ligand—a less selective modulator can afford a larger gain than a more selective one. This is shown in Figure 4F, where we assumed that the allosteric modulator was present at a concentration of 10 μM. In this instance, the more selective hypothetical allosteric modulators are less effective, if α = 0.5. With α = 1 (see Figure 4G), a moderate increase in ligand selectivity for the OF state increases the gain, but the relation is bell-shaped. Hence, in this case, there is also a loss in gain, if the hypothetical allosteric modulator is too selective for the outward-facing state OF. This is to say that the optimal selectivity for the OF state (i.e., the selectivity that gives rise to the largest gain) depends on the attainable modulator concentration. Because there are inherent limits in the (plasma) concentration, which can be realistically achieved, this consideration is relevant for the design of a therapeutically useful positive allosteric modulator.

In the simulations displayed in Figures 4B–G, we assumed that the conformational transition from the inward-to the outward-facing state (Figure 4A) always remained rate-limiting, regardless of the extent to which it was accelerated upon binding of the allosteric modulator. This, however, is not a realistic scenario: if the rate-limiting reaction in the transport cycle of a solute carrier is substantially accelerated, another reaction must eventually become rate-limiting. This was explored in the simulations shown in Figure 4H. Here, we assumed that the second slowest reaction was 10 times faster than the slowest reaction (i.e., 20 s^{-1} vs. 2 s^{-1}) and that the allosteric modulators did not affect this second reaction. Plotted is the ligand-induced gain in the substrate uptake velocity as a function of α. Under these circumstances, there is little advantage in using a more state-selective modulator, even if it is applied at an unrealistic saturating concentration (e.g., 1 M).

Negative allosteric modulators

Allosteric modulators can also affect other reactions in the transport cycle of a solute carrier, e.g., the transition from the substrate-bound OF to the substrate-bound IF state. In fact, it can be argued that it is this reaction, which is targeted by the antidepressant drug vilazodone. Vilazodone is classified as a negative allosteric modulator of the serotonin transporter (SERT) based on its ability to inhibit 5-HT uptake in a non-competitive manner. A recent cryo-EM structure of SERT in complex with vilazodone revealed that this molecule bound to the S2 of SERT, rendering it likely that vilazodone and 5-HT can bind to this transporter simultaneously (Plenge et al., 2021). Thus, vilazodone is predicted to stabilize the substrate-bound OF state and to thereby slow the reaction, which carries (co)-substrate through the membrane. This reaction is depicted in the scheme shown in Figure 5A. The resulting model makes the following assumption: (i) this substrate translocation step is a partial reaction in a forwardly biased reaction loop and (ii) it proceeds at a rate, which is substantially higher than that of the slowest reaction. In the scheme of Figure 5A, the curved arrow represents all other reactions comprising the loop (including its rate-limiting step). Because the loop is biased into the forward direction the substrate-bound outward-facing (OF) state is the reactant state. Thus, in accordance with the considerations outlined above, a hypothetical allosteric modulator, which binds with higher affinity to the OF than to the IF state, is expected to reduce the rate of this reaction. For the simulation, we therefore first assumed that the substrate-bound outward- and inward-facing state bound the allosteric modulator with a K_D of 1 and 10 μM, respectively. LFER predicts that a modulator with these properties can reduce the rate of the considered reaction from 100 s^{-1} down to 10 s^{-1} if α = 1 (i.e., the transition state resembles the substrate-bound OF state). At lower values of α, the reduction is less pronounced. However, because a reaction rate of 10 s^{-1} is still considerably faster than that of the slowest reaction, the turnover rate (rate of the entire process) and thus, uptake velocity is only reduced by the modulator to a very modest extent. This is shown in Figure 5B where we plotted the inhibitory effect of a modulator with the properties described in Figure 5A on substrate uptake as a function of α for different modulator concentrations. The figure illustrates that a negative allosteric modulator, can allow for residual substrate uptake, even if it is present at a saturating concentration (≥1 mM; lines in magenta and red). Further enhancing the selectivity of the allosteric modulator for the outward-facing state to 100-fold (Figure 5C) or 1000-fold (Figure 5D) progressively reduces the level of residual substrate uptake. Figure 5E examines the concentration-dependent inhibition of substrate uptake by the three hypothetical negative allosteric modulators considered in Figures 5B–D for α = 1: the resulting concentration-response curves provide three insights: with increasing selectivity for the outward-facing state, (i) the extent of uptake inhibition is progressively augmented (Figure 5E) and (ii) the IC_{50} of the modulators shift modestly to the right (this can be readily appreciated from a replot of the data in Figure 5F; (iii) there is residual substrate uptake even at a saturating concentration of the most selective negative allosteric modulator (ratio $K_{D,OF}/K_{D,IF}$ = 1000; a green curve in Figure 5E).

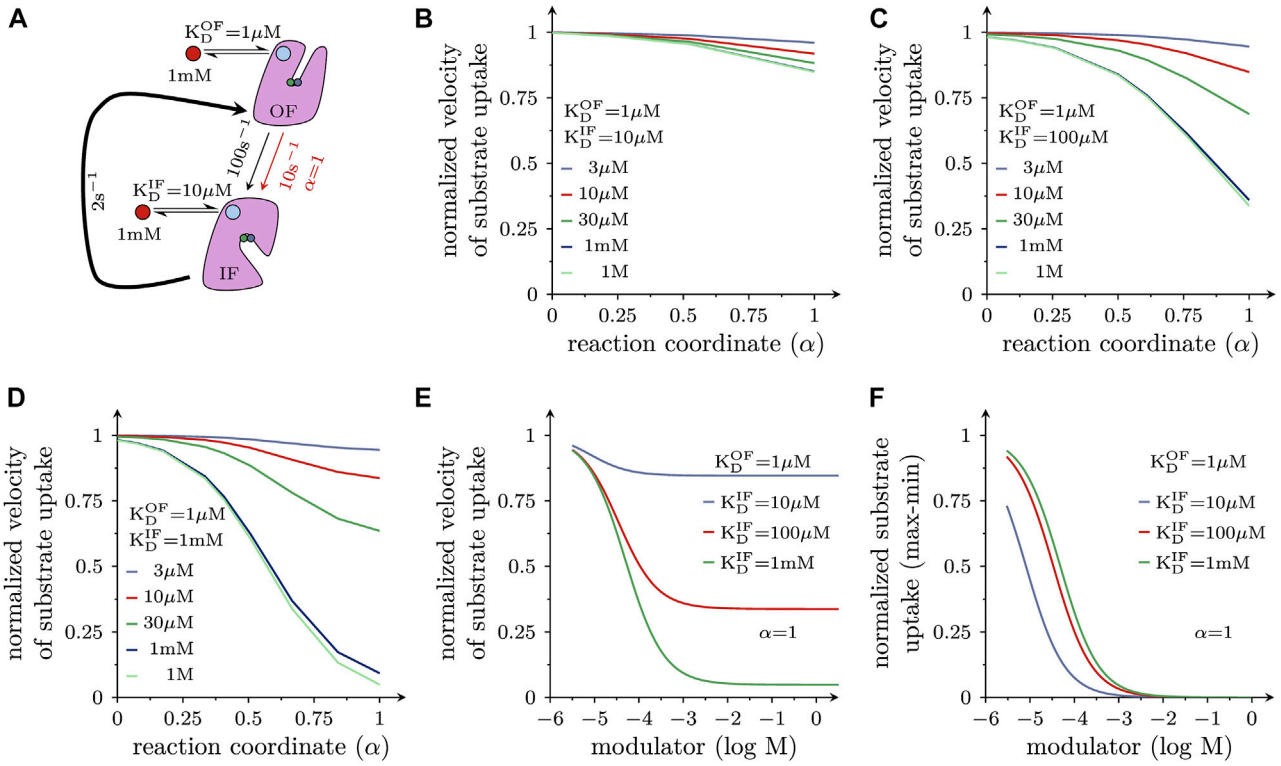

FIGURE 5
Negative allosteric modulators of solute carrier function **(A)** The scheme illustrates the reaction in the transport cycle of an SLC, which carries (co)-substrate through the membrane. This transition is a partial reaction in a forwardly biased reaction loop, because the transporter is assumed to operate under (ionic) conditions, which favor the forward cycling mode. In the absence of any (allosteric) ligand (black arrow), the rate of the transition equals 100 s^{-1}. All other reactions in the loop—including the rate-limiting step—are represented by the bold curved arrow. It is further assumed that the hypothetical negative allosteric modulator binds to the substrate-bound outward-facing (OF) state with tenfold higher affinity than to the corresponding inward-facing (IF) state (with K_D = 1 μM and 10 μM, respectively). For α is 1 and in the presence of 1 mM of the modulator, the rate of the reaction dropped from 100 s^{-1} (black arrow) to 10 s^{-1} (red arrow). **(B)** Inhibition of substrate uptake by a negative allosteric modulator is plotted as a function of α. The concentrations of the negative allosteric modulator, which has affinities for substrate-bound OF and IF state as outlined in **(A)**, were varied over the indicated range (3 μM–1 M); velocity of substrate uptake is shown as normalized value (i.e., uptake in the absence of the allosteric modulator equals 1). **(C,D)** show the same plot as in **(B)** but for negative allosteric modulators, which are more selective for the substrate-bound OF-state (i.e., 100 fold and 1000 fold, respectively). The inhibition of substrate uptake velocity depends on α and on the selectivity of the allosteric modulator for the substrate-bound outward-facing (OF) state: it progressively increases as the selectivity of the modulator is raised from 10-fold **(B)** to 100-fold **(C)** and to 1000-fold **(D)**. **(E)** Plotted is the normalized substrate uptake velocity as a function of the concentration of hypothetical negative allosteric modulators, which differ in their selectivity for the substrate-bound OF-state (α = 1). Inhibition of substrate uptake increases with the selectivity of the modulator. Negative allosteric modulators allow for residual substrate uptake when present at a saturating concentration. **(F)** The data in E were normalized (1 = no inhibition, 0 = maximal inhibition) because differences in the IC_{50} values can be more readily appreciated in this representation. With increasing selectivity the IC_{50} value of the inhibitory effect is modestly shifted to higher modulator concentrations.

The allosteric modulation of a composite reaction can be described by an apparent α (α_{app})

In the simulations summarized above, we assumed that the conformational rearrangements, which the solute carriers underwent, were elementary reactions. This, however, is a simplification: when transitioning from outward-to inward-facing (or *vice versa*), transporters must visit short-lived intermediate states. One such intermediate is the occluded state, where the binding site of the substrate is sealed off on both sides. Accordingly, isomerization from the OF- to the IF state involves at least two elementary reactions: (i) the transition from the OF to the occluded and (ii) from the occluded to the IF state. Because each reaction entails a transition state, there are now two αs which need to be considered. However, the following example shows that the multiple αs of a composite reaction can be replaced by an apparent α (α_{app}): Figure 6A illustrates a hypothetical landscape of the substrate translocation reaction, which also accounts for the occluded state. The corresponding reaction scheme is shown on top. The scheme makes the following assumptions: (i) the occluded state is short-lived (i.e., its lifetime is 10 microseconds); (ii) the value of α of each reaction (i.e., α_1 and α_2); is 0.5; (iii) the affinity of the intermediate state for the modulator lies between that of the two ground states, that is K_Ds of the (co)-substrate bound OF (T_O state in the scheme), occluded (T_{OCC}), and IF conformation (T_I)are 1, 5, and 10 μM, respectively. However, because the lifetime of the occluded state in Figure 6A is so short, it is not possible to resolve the reaction rates into and out of this state with any of the currently available methods. Observable quantities are the rate of the composite reaction in the presence and absence of the modulator and the affinity of the modulator for the two stable ground states

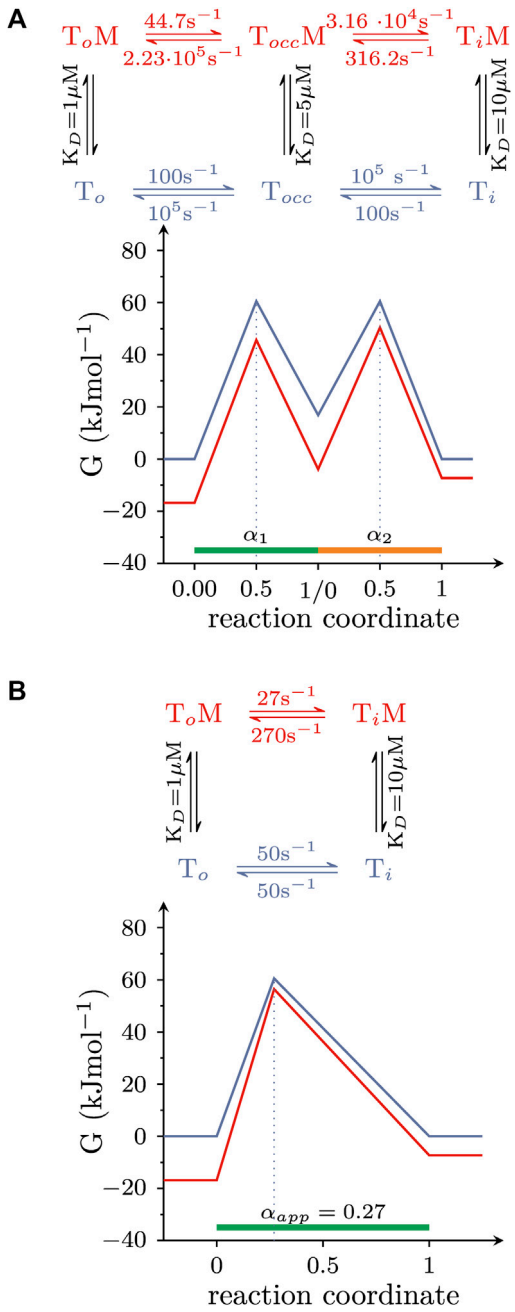

FIGURE 6
The amenability of a composite reaction by an allosteric modulator can be described by α_{app}. **(A)** Hypothetical free energy landscape of the conformational rearrangement that carries (co)-substrate through the membrane and which surpasses a short-lived occluded state (T_{Occ}). The reaction is assumed to be amenable by an allosteric modulator. Shown on top is the corresponding reaction diagram. **(B)** Equivalent free energy landscape of the reaction in **(A)**. The corresponding reaction scheme is shown on top. The scheme in **(A,B)** are indistinguishable in their ability to account for the (i) affinity of the modulator for the two stable ground states and (ii) the composite reaction rate both in the absence and presence of the modulator. These are the parameters, which can be measured in experiments.

(Hasenhuetl et al., 2015; Li et al., 2015; Bhat et al., 2023). These parameters allow for deducing the energy landscape shown in Figure 6B (the corresponding reaction scheme is shown on top). The schemes in Figures 6A, B are equivalent in their ability to account for the parameters, which are accessible to experimental determination. Thus, a value of 0.27 for α_{app} describes the overall reaction. This value of α_{app} remains a useful parameter to gauge the effect of an allosteric modulator, even if the reaction is composite. In the scheme outlined in Figure 6A, the transition states are located halfway between each pertinent reactant and product state. However, the (experimentally accessible) overall reaction shown in Figure 6B suggests that the transition state is closer to the reactant state. Thus, this comparison highlights the caveat that it is not possible to infer any structural resemblance of transition and ground states in a composite reaction (Huysmans et al., 2021). This can only be done, if the reaction is truly elementary.

Discussion

Allosteric modulation of a drug target can be attractive for pharmacotherapy; this is exemplified by the success of benzodiazepines and related compounds, which are positive allosteric modulators of $GABA_A$-receptors (Sigel and Ernst, 2018). Positive and negative allosteric modulation is not confined to cys-loop receptors and other ionotropic receptors: the calcium-sensing receptor is targeted by three approved positive allosteric modulators, cinacalcet, evocalcet, and etelcalcetide, which bind to distinct sites (Leach et al., 2020). Thus, allosteric modulation is worthwhile exploring. Transition state theory provides a theoretical framework to understand and predict the action of allosteric modulators. Here we focused on solute carriers, because they are attractive—albeit underdrugged—pharmacological targets (Wang et al., 2020; Casiraghi et al., 2021), their conformational cycle is well understood and thus amenable to kinetic modelling (Burtscher et al., 2018; Schicker et al., 2021; Schicker et al., 2022) and because allosteric modulators may remedy defects resulting from mutations (Bhat et al., 2021). We applied transition state theory by positing that—for partial reactions in the transport cycle of a solute carrier—a linear relation exists between the change in the free energy difference of reactant and product states ($\Delta\Delta G_R$; $\Delta\Delta G_P$) and its change for the corresponding transitions states ($\Delta\Delta\ G^{\ddagger}$). This structure-reactivity relation is also known as LFER (linear free energy relationship). LFER is considered a semi-empirical rule on two grounds: (i) if specific reactions are subjected to experimental scrutiny, they are usually found to conform to LFER; (ii) for some simple reactions, it is possible to derive the underlying structure-reactivity relation from first principles. However, currently, there isn't any stringent formulation of a general law, which would allow for deducing all observed LFERs (Leffler, 1963; Agmon, 1981).

LFER is not as fundamental as the law of energy preservation: this is evident from the observation that it was possible to violate LFER, while maintaining microscopic reversibility in the pertinent reaction schemes (see Figure 3). The position of the transition state on the reaction coordinate (α) is an important parameter in LFER. It is only possible to predict the effect of a given allosteric modulator, if α is known. Fortunately, experiments can be designed to determine the position of the transition state on the reaction coordinate. For this purpose, the reaction must be subjected to a perturbation that either increases or decreases its reaction rate. Partial reactions in the transport cycle of a solute carrier can be perturbed by (i) voltage

changes (if the reaction is voltage-dependent), (ii) by mutations in the coding region of the candidate SLC gene (if this leads to a change in the reaction rate) and (iii) by the use of allosteric modulators. An example of such an analysis can be found in (Huysmans et al., 2021).

Monoamine transporters are of pharmacotherapeutic relevance and they are targets of popular, illicit drugs. Accordingly, the chemical space has been amply explored for possible ligands. In fact, several hundred ligands are known to bind to monoamine transporters (Sitte and Freissmuth, 2015): these include inhibitors, which bind to the orthosteric site, full and partial substrates (Hasenhuetl et al., 2019; Niello et al., 2020), negative allosteric modulators (Niello et al., 2020) and even an uncompetitive inhibitor (Bhat et al., 2023), but surprisingly, no positive allosteric modulator other than Zn^{2+} has been identified. Our analysis provides an explanation of why it is difficult to find positive allosteric modulators: A positive allosteric modulator must bind to the product state of the slowest reaction in the transport cycle of the targeted SLC with higher affinity than to the reactant state, but it must not be too selective. This requirement is difficult to fulfill. To the best of our knowledge, Zn^{2+} and related transitional metals are the only known example of a positive allosteric modulator in the entire superfamily of SLC transporters: Zn^{2+} and other transitional metals accelerate the transport cycle of the dopamine transporter (DAT) (Li et al., 2017). DAT harbors a Zn^{2+} binding site because evolution selected this transporter for allostery. It is, therefore, tempting to speculate that the adaptive search for optimizing the rate of substrate translocation shaped the binding site of Zn^{2+} such that this transition metal can afford a maximal increase in the dopamine uptake rate (Schicker et al., 2022). This notion is supported by the observation that Zn^{2+} is only modestly selective for the OF-state over the IF-state (i.e., the affinity of Zn^{2+} for the OF-state is approximately 10 times higher than for the IF-state). If Zn^{2+} were more selective for the OF-state, a considerably higher concentration of Zn^{2+} would be required to increase the substrate uptake rate. Yet, even if it were possible to reach this high Zn^{2+} concentration, little would be gained. This is because, in a realistic scenario, another reaction in the transport cycle inevitably becomes rate-limiting. As a consequence, the extra gain afforded by a more selective ligand does not translate into a higher substrate turnover rate. In DAT, this other reaction is predicted to be the transition that carries the substrate through the membrane. The rate of this reaction is about one order of magnitude higher than that of the rate-limiting reaction (i.e., the return step of the empty transporter from the OF to the IF state). A notable shortcoming of Zn^{2+} is that it does not discriminate between substrate-free and bound OF states. Therefore, Zn^{2+} also accelerates the return step from the substrate-bound IF to the corresponding OF state (Li et al., 2017). Accordingly, if the intracellular Na^+ concentration (Na^+_{in}) is raised above 15 mM, Zn^{2+} inhibits substrate translocation (Li et al., 2015), because the substrate is released at a lower rate at elevated Na_{in}^+. This raises the abundance of the substrate-loaded IF state. As a consequence, the transporter more frequently returns in the substrate-bound form (i.e., it enters the exchange mode). Because Zn^{2+} accelerates this reaction it inhibits substrate uptake when Na_{in}^+ is high. It is possible to circumvent this issue with an allosteric ligand, which only binds to the substrate-free states. In this context, it is worth mentioning that we recently analyzed the effect of the antibody fragment 8B6 scFv on the transport cycle of SERT (Esendir et al., 2021). 8B6 scFv was produced to facilitate the crystallization of SERT (Coleman et al., 2016). Incidentally, 8B6 scFv was exquisitely selective for the substrate-free OF state over the substrate-bound OF state. This finding is encouraging because it shows that it ought to be possible to find ligands, which bind with higher affinity to substrate-free than to substrate-bound states. However, because 8B6 scFv had no appreciable affinity for the substrate-free IF state (i.e., it was too selective for the substrate-free OF state) it failed to act as a positive allosteric modulator (Esendir et al., 2021).

Another type of action is allosteric inhibition of substrate uptake. A hallmark of these compounds is their non-competitive mode of transport inhibition. To exert this effect, a negative allosteric modulator must bind with higher affinity to the reactant than to the product state of a partial reaction in the transport cycle of the candidate SLC. However, in contrast to a positive allosteric modulator, a negative allosteric modulator need not target the slowest reaction. In fact, the slowing of any reaction in the transport cycle is predicted to decrease substrate uptake. In addition, there isn't any upper limit on the selectivity of such a molecule for the high-affinity state. A higher selectivity for the reactant state solely increases the efficiency of the modulator. The larger number of possible solutions, by which this type of action can be achieved, is presumably the reason why negative allosteric modulators are not as rare as their positive counterparts. A notable insight, which we gained from our analysis, is that a negative allosteric modulator can act as a partial inhibitor, if it is not too selective for the reactant state of the targeted reaction. This property can conceivably be of value for the treatment of a disease caused by malfunctioning SLCs. A scenario can be envisaged, in which it is beneficial to clamp substrate uptake to a given level: in contrast to orthosteric inhibitors, the action of allosteric inhibitors is not overcome by rising concentrations of substrate.

Our analysis suggests that the most interesting modulatory actions (i.e., positive allosteric modulation and partial inhibition of SLC function) can be achieved by allosteric ligands, which are not too selective for either ground state of a partial reaction. The search for such compounds requires an adaption of the existing computational approaches. The present analysis provides some guidance for the design of the workflow, which ought to encompass the following steps: First, it is necessary to identify the reaction in the transport cycle of the candidate solute carrier, which is to be targeted to cause the desired effect. This, for instance, is the slowest reaction, if the goal is to find a positive allosteric modulator. Second, the structures of the corresponding reactant and product state must be searched for positions, which undergo a (modest) change. Third, (parallel) virtual screens must be conducted on these positions. The goal of this exercise is to find a ligand, which can bind to both ground states while assuming on each of them a unique binding mode. The proposed workflow can be illustrated by using SERT as an example: SERT harbors an allosteric binding site (i.e., the S2 site) to which vilazodone binds. A cryo-electron microscopy structure is available that shows vilazodone in complex with the outward open conformation of SERT (see Figure 7A). This structure corresponds to the reactant state of the reaction, which carries (co)-substrate through the membrane (cf. Figure 5). Incidentally, the structure of the corresponding product state (i.e., the substrate-bound inward-facing conformation) was also resolved (see Figure 7B) (Yang and Gouaux, 2021). In this structure, the S2 site is occupied by a second 5-HT molecule. Figures 7C, D depict the volumes (in grey) of the ortho- and allosteric binding pocket (i.e., S1 site

10.3389/fphys.2023.1166450

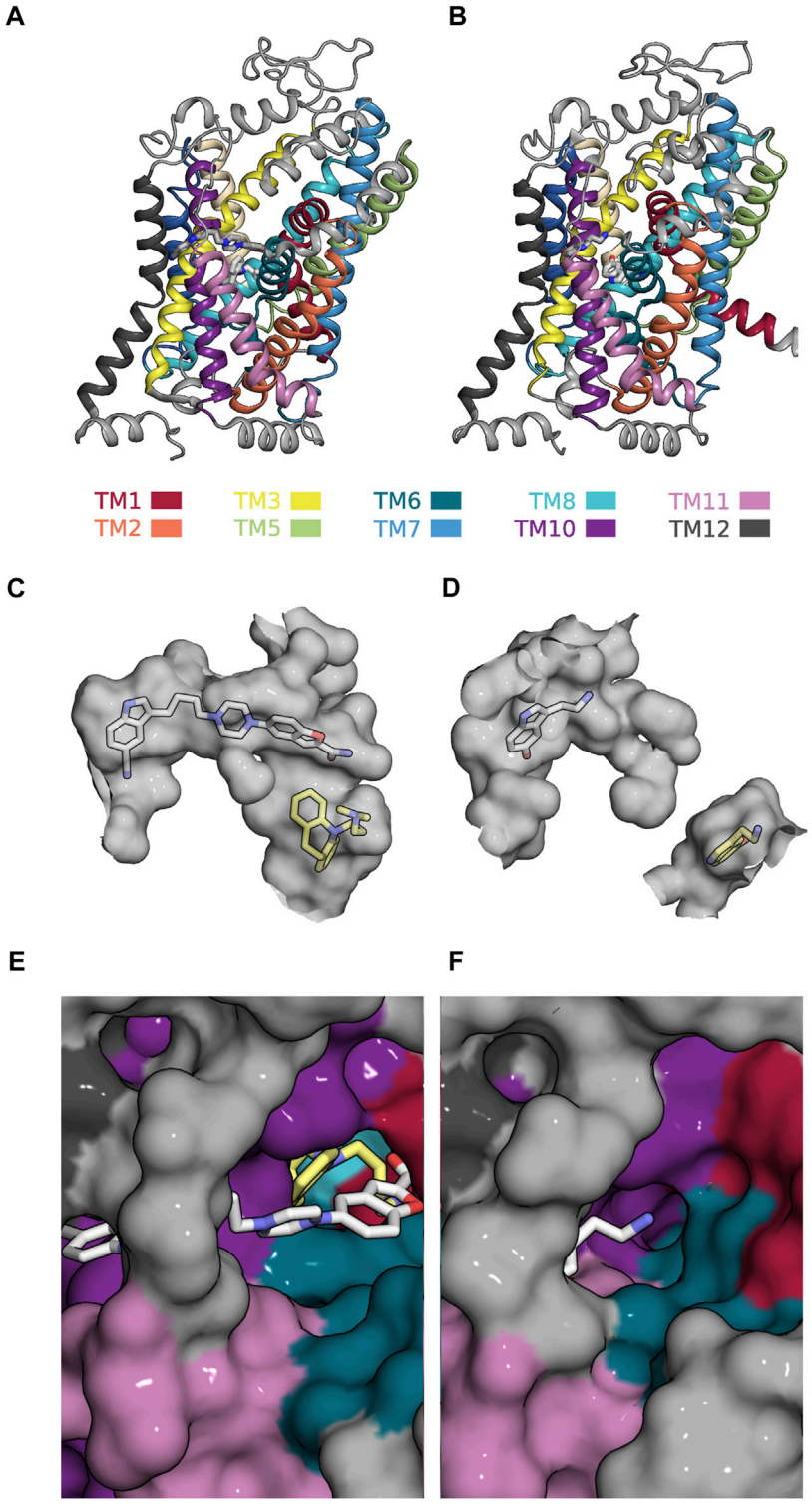

FIGURE 7
Allosteric binding site (i.e., the S2-site) in the outward- and inward-facing conformation of SERT **(A)** Side view onto the structure of SERT in the outward-facing conformation in complex with a vilazodone molecule bound to the S1- and another bound to the S2-site (PDB 7LWD) **(B)** Side view onto the structure of SERT in the substrate-bound inward-facing state, in which the S1- and S2-site are occupied with one 5-HT molecule each (PDB 7L19) **(C)** The accessible volume of the two binding pockets (S1-site and S2-site) in the outward-facing conformation. The bound vilazodone (grey carbon backbone) and imipramine molecules (yellow carbon backbone) reside in S2 and in S1, respectively. **(D)** The accessible volume of the S1- and the S2-site in the inward-facing conformation with the two bound 5-HT molecules visualized with yellow and grey carbon backbones, respectively. The S1-site is separated from the S2-site by the closed extracellular gate. **(E)** Top view onto the vilazodone molecule residing in the S2-site of the outward-facing state. The imipramine molecule residing in the S1-site is also visible. **(F)** Top view onto the 5-HT molecule bound to the S2-site of the inward-facing state.

and S2 site) in both states. In the inward-facing conformation these two binding sites are separated by the closed extracellular gate (Figure 7D). It is evident that the allosteric binding pocket is smaller in the inward-than in the outward-facing state such that the pose of vilazodone cannot be accommodated (cf. Figures 7C, D). Moreover, the path leading to the S2 site is narrower in the inward-facing conformation of SERT (Figure 7F) than in the outward-facing state (Figure 7F). This indicates a reduced accessibility to the S2 site upon transition to the inward-facing conformation. A computational search for a compound, which is not too selective for the reactant over the product state, is therefore proposed to encompass virtual screens in which each tested molecule is docked in parallel into the two binding pockets displayed in Figures 7C, D. In the selected example, only a molecule that fits into both binding pockets is likely to give rise to partial inhibition of substrate uptake. Full inhibition of substrate uptake was reported for vilazodone (Plenge et al., 2021). This is consistent with the observation that vilazodone cannot be accommodated by the S2 site of the product state (i.e., in the inward-facing conformation of SERT—cf. Figure 7D). However, it is conceivable that a slightly smaller molecule could fit into this pocket and thereby exert the desired modulatory action (i.e., partial inhibition of substrate uptake).

Another insight from our analysis is that the action of an allosteric modulator does not depend on the absolute affinities of the modulator for the reactant and product state but rather on their ratio. The ultimate goal of most docking campaigns is to find high-affinity ligands. Undoubtedly, high affinity is beneficial, because it limits off-target effects. However, we argue that the sole focus on high-affinity ligands is questionable: it may impede the discovery of allosteric ligands with useful properties.

Data availability statement

The original contributions presented in the study are included in the article/supplementary material, further inquiries can be directed to the corresponding author.

Author contributions

DB Formal analysis, writing-original draft, conceptualization. KS Formal analysis, writing-reviewing and editing, conceptualization. EH Formal analysis and editing. MF writing-reviewing and editing, conceptualization. WS writing-original draft, conceptualization, formal analysis.

Funding

This work was funded by a grant from the Austrian Science Fund/FWF (P31813 and P36667 to WS) and by a grant from the Vienna Science and Technology Fund/WWTF (LSC17-026 to MF).

Acknowledgments

We thank Lucy Forrest for her advice on the manuscript.

Conflict of interest

The authors declare that the research was conducted in the absence of any commercial or financial relationships that could be construed as a potential conflict of interest.

Publisher's note

References

Agmon, N. (1981). From energy Profiles to structure-reactivity Correlations. *Int. J. Chem. Kinet.* 13 (4), 333–365. doi:10.1002/kin.550130403

Alon, A., Lyu, J., Braz, J. M., Tummino, T. A., Craik, V., O'Meara, M. J., et al. (2021). Structures of the σ(2) receptor enable docking for bioactive ligand discovery. *Nature* 600 (7890), 759–764. doi:10.1038/s41586-021-04175-x

Ballante, F., Kooistra, A. J., Kampen, S., de Graaf, C., and Carlsson, J. (2021). Structure-based virtual screening for ligands of G protein-coupled receptors: What can molecular docking do for You? *Pharmacol. Rev.* 73 (4), 527–565. doi:10.1124/pharmrev.120.000246

Bender, B. J., Gahbauer, S., Luttens, A., Lyu, J., Webb, C. M., Stein, R. M., et al. (2021). A practical guide to large-scale docking. *Nat. Protoc.* 16 (10), 4799–4832. doi:10.1038/s41596-021-00597-z

Bhat, S., El-Kasaby, A., Freissmuth, M., and Sucic, S. (2021). Functional and Biochemical consequences of disease Variants in neurotransmitter transporters: A special Emphasis on folding and Trafficking Deficits. *Pharmacol. Ther.* 222, 107785. doi:10.1016/j.pharmthera.2020.107785

Bhat, S., El-Kasaby, A., Kasture, A., Boytsov, D., Reichelt, J. B., Hummel, T., et al. (2023). A mechanism of uncompetitive inhibition of the serotonin transporter. *Elife* 12, e82641. doi:10.7554/eLife.82641

Burtscher, V., Hotka, M., Li, Y., Freissmuth, M., and Sandtner, W. (2018). A label-free approach to detect ligand binding to cell surface proteins in real time. *Elife* 7, e34944. doi:10.7554/eLife.34944

Casiraghi, A., Bensimon, A., and Superti-Furga, G. (2021). Recent developments in ligands and chemical probes targeting solute carrier transporters. *Curr. Opin. Chem. Biol.* 62, 53–63. doi:10.1016/j.cbpa.2021.01.012

Colas, C., Ung, P. M., and Schlessinger, A. (2016). SLC transporters: Structure, function, and drug discovery. *Medchemcomm* 7 (6), 1069–1081. doi:10.1039/C6MD00005C

Coleman, J. A., Green, E. M., and Gouaux, E. (2016). X-ray structures and mechanism of the human serotonin transporter. *Nature* 532 (7599), 334–339. doi:10.1038/nature17629

Esendir, E., Burtscher, V., Coleman, J. A., Zhu, R., Gouaux, E., Freissmuth, M., et al. (2021). Extracellular loops of the serotonin transporter act as a selectivity filter for drug binding. *J. Biol. Chem.* 297 (1), 100863. doi:10.1016/j.jbc.2021.100863

Gabrielsen, M., Kurczab, R., Ravna, A. W., Kufareva, I., Abagyan, R., Chilmonczyk, Z., et al. (2012). Molecular mechanism of serotonin transporter inhibition elucidated by a new flexible docking protocol. *Eur. J. Med. Chem.* 47 (1), 24–37. doi:10.1016/j.ejmech.2011.09.056

Gabrielsen, M., Wołosewicz, K., Zawadzka, A., Kossakowski, J., Nowak, G., Wolak, M., et al. (2013). Synthesis, antidepressant evaluation and docking studies of long-chain alkylnitroquipazines as serotonin transporter inhibitors. *Chem. Biol. drug Des.* 81 (6), 695–706. doi:10.1111/cbdd.12116

Hasenhuetl, P. S., Bhat, S., Freissmuth, M., and Sandtner, W. (2019). Functional selectivity and partial Efficacy at the monoamine transporters: A Unified model of

allosteric modulation and Amphetamine-induced substrate release. *Mol. Pharmacol.* 95 (3), 303–312. doi:10.1124/mol.118.114793

Hasenhuetl, P. S., Schicker, K., Koenig, X., Li, Y., Sarker, S., Stockner, T., et al. (2015). Ligand selectivity among the dopamine and serotonin transporters specified by the forward binding reaction. *Mol. Pharmacol.* 88 (1), 12–18. doi:10.1124/mol.115.099036

Huysmans, G. H. M., Ciftci, D., Wang, X., Blanchard, S. C., and Boudker, O. (2021). The high-energy transition state of the glutamate transporter homologue GltPh. *EMBO J.* 40 (1), e105415. doi:10.15252/embj.2020105415

Katritch, V., Rueda, M., and Abagyan, R. (2011). "Ligand-guided receptor Optimization," in *Methods in molecular Biology* (Totowa, New Jersey: Humana Press), 189–205. doi:10.1007/978-1-61779-588-6_8

Klaassen, C. D., and Aleksunes, L. M. (2010). Xenobiotic, bile acid, and cholesterol transporters: Function and regulation. *Pharmacol. Rev.* 62 (1), 1–96. doi:10.1124/pr.109.002014

Kolb, P., Ferreira, R. S., Irwin, J. J., and Shoichet, B. K. (2009). Docking and chemoinformatic screens for new ligands and targets. *Curr. Opin. Biotechnol.* 20 (4), 429–436. doi:10.1016/j.copbio.2009.08.003

Kolb, P., and Irwin, J. (2009). Docking screens: Right for the right reasons? *Curr. Top. Med. Chem.* 9 (9), 755–770. doi:10.2174/156802609789207091

Kortagere, S., Fontana, A. C., Rose, D. R., and Mortensen, O. V. (2013). Identification of an allosteric modulator of the serotonin transporter with novel mechanism of action. *Neuropharmacology* 72, 282–290. doi:10.1016/j.neuropharm.2013.04.026

Kristensen, A. S., Andersen, J., Jorgensen, T. N., Sorensen, L., Eriksen, J., Loland, C. J., et al. (2011). SLC6 neurotransmitter transporters: Structure, function, and regulation. *Pharmacol. Rev.* 63 (3), 585–640. doi:10.1124/pr.108.000869

Kufareva, I., Chen, Y.-C., Ilatovskiy, A. V., and Abagyan, R. (2012). Compound Activity prediction using models of binding pockets or ligand properties in 3D. *Curr. Top. Med. Chem.* 12 (17), 1869–1882. doi:10.2174/156802612804547335

Leach, K., Hannan, F. M., Josephs, T. M., Keller, A. N., Moller, T. C., Ward, D. T., et al. (2020). International union of basic and Clinical pharmacology. CVIII. Calcium-sensing receptor Nomenclature, pharmacology, and function. *Pharmacol. Rev.* 72 (3), 558–604. doi:10.1124/pr.119.018531

Leffler, J. E. a. G. E. (1963). *Rates and equilibria of organic reactions*. New York, NY: John Wiley and Sons, Inc.

Li, Y., Hasenhuetl, P. S., Schicker, K., Sitte, H. H., Freissmuth, M., and Sandtner, W. (2015). Dual action of Zn2+ on the transport cycle of the dopamine transporter. *J. Biol. Chem.* 290 (52), 31069–31076. doi:10.1074/jbc.M115.688275

Li, Y., Mayer, F. P., Hasenhuetl, P. S., Burtscher, V., Schicker, K., Sitte, H. H., et al. (2017). Occupancy of the Zinc-binding site by transition metals decreases the substrate affinity of the human dopamine transporter by an allosteric mechanism. *J. Biol. Chem.* 292 (10), 4235–4243. doi:10.1074/jbc.M116.760140

Mayr, L. M., and Bojanic, D. (2009). Novel trends in high-throughput screening. *Curr. Opin. Pharmacol.* 9 (5), 580–588. doi:10.1016/j.coph.2009.08.004

Ngo, T., Kufareva, I., Coleman, J. L., Graham, R. M., Abagyan, R., and Smith, N. J. (2016). Identifying ligands at orphan GPCRs: Current status using structure-based approaches. *Br. J. Pharmacol.* 173 (20), 2934–2951. doi:10.1111/bph.13452

Niello, M., Gradisch, R., Loland, C. J., Stockner, T., and Sitte, H. H. (2020). Allosteric modulation of neurotransmitter transporters as a therapeutic Strategy. *Trends Pharmacol. Sci.* 41 (7), 446–463. doi:10.1016/j.tips.2020.04.006

Orry, A. J. W., Abagyan, R. A., and Cavasotto, C. N. (2006). Structure-based development of target-specific compound libraries. *Drug Discov. Today* 11 (5-6), 261–266. doi:10.1016/s1359-6446(05)03717-7

Plenge, P., Yang, D., Salomon, K., Laursen, L., Kalenderoglou, I. E., Newman, A. H., et al. (2021). The antidepressant drug vilazodone is an allosteric inhibitor of the serotonin transporter. *Nat. Commun.* 12 (1), 5063. doi:10.1038/s41467-021-25363-3

Rognan, D. (2011). "Fragment-based approaches and Computer-Aided drug discovery," in *Topics in current chemistry* (Germany: Springer Berlin Heidelberg), 201–222. doi:10.1007/128_2011_182

Rognan, D. (2017). The impact of *in silico* screening in the discovery of novel and safer drug candidates. *Pharmacol. Ther.* 175, 47–66. doi:10.1016/j.pharmthera.2017.02.034

Roth, B. L., Irwin, J. J., and Shoichet, B. K. (2017). Discovery of new GPCR ligands to illuminate new biology. *Nat. Chem. Biol.* 13 (11), 1143–1151. doi:10.1038/nchembio.2490

Rudnick, G., and Sandtner, W. (2019). Serotonin transport in the 21st century. *J. Gen. Physiol.* 151 (11), 1248–1264. doi:10.1085/jgp.201812066

Scharf, M. M., Bünemann, M., Baker, J. G., and Kolb, P. (2019). Comparative docking to distinct G protein–coupled receptor conformations Exclusively Yields ligands with Agonist Efficacy. *Mol. Pharmacol.* 96 (6), 851–861. doi:10.1124/mol.119.117515

Schicker, K., Bhat, S., Farr, C., Burtscher, V., Horner, A., Freissmuth, M., et al. (2021). Descriptors of secondary active transporter function and how they relate to partial reactions in the transport cycle. *Membr. (Basel)* 11 (3), 178. doi:10.3390/membranes11030178

Schicker, K., Farr, C. V., Boytsov, D., Freissmuth, M., and Sandtner, W. (2022). Optimizing the substrate uptake rate of solute carriers. *Front. Physiol.* 13, 817886. doi:10.3389/fphys.2022.817886

Schmidt, H., and Jirstrand, M. (2006). Systems biology Toolbox for MATLAB: A computational platform for research in systems biology. *Bioinformatics* 22 (4), 514–515. doi:10.1093/bioinformatics/bti799

Schrodinger, L. L. C. (2022). *The PyMOL molecular Graphics system*. Available at: https://pymol.org/2/support.html?.

Sigel, E., and Ernst, M. (2018). The benzodiazepine binding sites of GABA(A) receptors. *Trends Pharmacol. Sci.* 39 (7), 659–671. doi:10.1016/j.tips.2018.03.006

Singh, I., Seth, A., Billesbølle, C. B., Braz, J., Rodriguiz, R. M., Roy, K., et al. (2022). Structure-based discovery of conformationally selective inhibitors of the serotonin transporter. *bioRxiv* 2022, 495991. doi:10.1101/2022.06.13.495991

Sitte, H. H., and Freissmuth, M. (2015). Amphetamines, new psychoactive drugs and the monoamine transporter cycle. *Trends Pharmacol. Sci.* 36 (1), 41–50. doi:10.1016/j.tips.2014.11.006

Wang, W. W., Gallo, L., Jadhav, A., Hawkins, R., and Parker, C. G. (2020). The Druggability of solute carriers. *J. Med. Chem.* 63 (8), 3834–3867. doi:10.1021/acs.jmedchem.9b01237

Yang, D., and Gouaux, E. (2021). Illumination of serotonin transporter mechanism and role of the allosteric site. *Sci. Adv.* 7 (49), eabl3857. doi:10.1126/sciadv.abl3857

Zhang, Y., Zhang, Y., Sun, K., Meng, Z., and Chen, L. (2019). The SLC transporter in nutrient and metabolic sensing, regulation, and drug development. *J. Mol. Cell Biol.* 11 (1), 1–13. doi:10.1093/jmcb/mjy052

frontiers | Frontiers in Physiology

TYPE Original Research
PUBLISHED 19 July 2023
DOI 10.3389/fphys.2023.1147216

OPEN ACCESS

EDITED BY
Ossama Kashlan,
University of Pittsburgh, United States

REVIEWED BY
Elena Bossi,
University of Insubria, Italy
Christof Grewer,
Binghamton University, United States

*CORRESPONDENCE
Christoph Fahlke,
c.fahlke@fz-juelich.de

†These authors have contributed equally to this work

‡PRESENT ADDRESS
Mariia Suslova,
Institute für Neurophysiologie,
Universitätsklinikum Aachen, Aachen,
Germany

RECEIVED 18 January 2023
ACCEPTED 07 July 2023
PUBLISHED 19 July 2023

CITATION
Suslova M, Kortzak D, Machtens J-P, Kovermann P and Fahlke C (2023), *Apo* state pore opening as functional basis of increased EAAT anion channel activity in episodic ataxia 6.
Front. Physiol. 14:1147216.
doi: 10.3389/fphys.2023.1147216

Apo state pore opening as functional basis of increased EAAT anion channel activity in episodic ataxia 6

Mariia Suslova[†‡], Daniel Kortzak[†], Jan-Philipp Machtens, Peter Kovermann and Christoph Fahlke*

Institute of Biological Information Processing, Molekular-und Zellphysiologie (IBI-1), Forschungszentrum Jülich, Jülich, Germany

SLC1A2 and *SLC1A3* encode the glial glutamate transporters EAAT2 and EAAT1, which are not only the predominant glutamate uptake carriers in our brain, but also function as anion channels. Two homologous mutations, which predict substitutions of prolines in the center of the fifth transmembrane helix by arginine (P289R EAAT2, P290R EAAT1), have been identified in patients with epileptic encephalopathy (*SLC1A2*) or with episodic ataxia type 6 (*SLC1A3*). Both mutations have been shown to impair glutamate uptake and to increase anion conduction. The molecular processes that link the disease-causing mutations to two major alterations of glutamate transporter function remain insufficiently understood. The mutated proline is conserved in every EAAT. Since the pathogenic changes mainly affect the anion channel function, we here study the functional consequences of the homologous P312R mutation in the neuronal glutamate transporter EAAT4, a low capacity glutamate transporter with predominant anion channel function. To assess the impact of charge and structure of the inserted amino acid for the observed functional changes, we generated and functionally evaluated not only P312R, but also substitutions of P312 with all other amino acids. However, only exchange of proline by arginine, lysine, histidine and asparagine were functionally tolerated. We compared WT, P312R and P312N EAAT4 using a combination of cellular electrophysiology, fast substrate application and kinetic modelling. We found that WT and mutant EAAT4 anion currents can be described with a 11-state model of the transport cycle, in which several states are connected to branching anion channel states to account for the EAAT anion channel function. Substitutions of P312 modify various transitions describing substrate binding/unbinding, translocation or anion channel opening. Most importantly, P312R generates a new anion conducting state that is accessible in the outward facing *apo* state and that is the main determinant of the increased anion conduction of EAAT transporters carrying this mutation. Our work provides a quantitative description how a naturally occurring mutation changes glutamate uptake and anion currents in two genetic diseases.

KEYWORDS

neurological diseases, epilepsy, ataxia, glutamate transport, anion channel, kinetic modeling

Introduction

Glutamate is the major excitatory neurotransmitter in the mammalian brain. After release from the presynaptic nerve terminal excitatory amino acid transporters (EAATs) quickly take up glutamate into surrounding glial and neuronal cells (Rose et al., 2018). EAAT-mediated glutamate transport increases the temporal resolution of glutamatergic synaptic transmission and reduces resting glutamate concentrations. In addition to secondary active glutamate transport, the EAATs also function as glutamate-gated anion channels (Wadiche et al., 1995; Larsson et al., 1996; Machtens et al., 2015). Various cellular functions have been suggested, but the physiological importance of the EAAT anion channel function remains insufficiently understood (Untiet et al., 2017; Engels et al., 2021; Gehlen et al., 2021; Kovermann et al., 2022a).

Impaired EAAT functions have been associated with several human genetic diseases. The first EAATopathy was a genetic condition combining ataxia, hemiplegia, and seizure, called episodic ataxia type 6 (EA6), and shown to be caused by mutations in *SLC1A3*, the gene encoding the glial glutamate transporter EAAT1 (Jen et al., 2005; de Vries et al., 2009; Pyle et al., 2015; Choi et al., 2017a; Choi et al., 2017b; Iwama et al., 2017; Chivukula et al., 2020). Later, mutations in *SLC1* genes were linked to other neurological conditions such as migraine or epilepsy (Epi4K Consortium, 2016; Guella et al., 2017; Kovermann et al., 2017; Stergachis et al., 2019), as well as to psychiatric conditions such as ADHD or Tourette' syndrome (Adamczyk et al., 2011; van Amen-Hellebrekers et al., 2016).

Jen et al. (2005) reported a patient with episodic ataxia 6, who was heterozygous for a missense mutation causing the substitution of a highly conserved proline at position 290 by arginine (Figure 1A). This mutation affects both transport functions of EAAT1 in opposite ways; it reduces glutamate transport rates, but increases the EAAT1 anion conductance (Winter et al., 2012; Hotzy et al., 2013). In a transgenic animal model, the *Slc1a3*$^{P290R/+}$mouse, increased EAAT1/GLAST-mediated chloride efflux causes apoptosis of Bergmann glia in early infancy, resulting in cerebellar dysfunction via impaired glutamate reuptake and cerebellar network formation (Kovermann et al., 2020). Transgenic *Drosophila* models of this case of episodic ataxia also demonstrated pathogenic changes in EAAT anion channel function (Parinejad et al., 2016; Wu et al., 2022). Recently, the homologous mutation in *SLC1A2*, predicting P289R EAAT2, was found in patients with early-onset epilepsy and severe developmental delay (Guella et al., 2017) and was also shown to cause increased activity of EAAT2 anion channels (Kovermann et al., 2022b).

Both mutations affect a proline that is conserved in every SLC1 transporter as well as in prokaryotic and eukaryotic homologues (Figure 1B). Since the P290R/P289R mutations cause disease symptoms mainly via gain-of-anion channel function, we decided to study the mechanistic basis of this dysfunction in a related transporter that predominantly functions as glutamate-gated anion channel, in EAAT4 (Fairman et al., 1995; Melzer et al., 2003; Mim et al., 2005). We systematically evaluated the effects of substitutions of the homologous proline with various amino acids. EAAT4 has been studied extensively by our group and was shown to functionally tolerate various point mutations (Kovermann et al., 2010; Machtens et al., 2015). We expressed WT and mutant EAAT4 in mammalian cells and studied transport and anion currents. Time, substrate and voltage dependences of such currents were described with a kinetic model to identify conformational changes that are affected by those mutations.

Materials and methods

Heterologous expression of WT and mutant EAAT4 in mammalian cells

pcDNA3.1(−) *r*EAAT4 was kindly provided by Dr. J. Rothstein, Johns Hopkins University, Baltimore, MD, United States, and modified by linking the coding region of monomeric yellow fluorescent protein (mYFP) to the 5′ end of the EAAT4 coding region using PCR-based strategies (Nothmann et al., 2011). Point mutations were generated by PCR-based techniques as described (Leinenweber et al., 2011). For transient transfection of HEK293T cells, we used the $Ca_3(PO_4)_2$ technique as described (Hebeisen and Fahlke, 2005). For WT and mutant EAAT4-mYFP, two independent recombinants were examined, without obvious functional differences.

Electrophysiology

Standard whole-cell patch-clamp recordings were performed using an Axopatch 200B amplifier (Molecular Devices, San Jose, United States), with borosilicate pipettes with resistances between 1.0 to 2.0 MΩ (Garcia-Olivares et al., 2008). To reduce voltage errors, more than 80% of the series resistance was compensated by an analog procedure, and cells with current amplitudes >7 nA were excluded from analysis. Currents were filtered at 5 or 10 kHz and digitized with sampling rates of 50 kHz using a Digidata 1322A AD/DA converter (Molecular Devices, San Jose, United States). Cells were clamped to 0 mV for at least 2 s between two test sweeps. In experiments to study EAAT4 anion currents internal solutions contained either (in mM) 115 KNO_3, 2 $MgCl_2$, 5 EGTA, 10 HEPES, pH 7.4; or 115 $NaNO_3$, 2 $MgCl_2$, 5 EGTA, 10 HEPES, ±0.1 L-glutamate, pH 7.4. Bath solution contained: 140 $NaNO_3$ or CholineNO_3, 5 TEA-Cl, 4 KCl, 2 $CaCl_2$, 1 $MgCl_2$, 5 HEPES, ±0.1 L-glutamate, pH 7.4. Anion currents were determined without subtraction procedure. For rapid solution exchange to solutions, in which 140 $NaNO_3$ was substituted with KNO_3, or 140 CholineNO_3 by 140 $NaNO_3$ + 1 L-glutamate or in which 0.1 L-glutamate was added to 140 $NaNO_3$, a self-assembled piezo-driven system with a dual-channel theta glass tubing was used (Carbone and Plested, 2012). After pulling, pipette tips were reheated and bended to permit horizontal solution flow out of the mounted pipette and subsequently briefly incubated in fluoric acid to thin the theta tube filament. To decrease pipette vibration, a manually smoothed pulse was fed to the piezo amplifier. The speed of the solution exchange–estimated as 10%–90% rise times of open pipette responses–was 658 ± 53 μs (n = 56).

Glutamate transport currents were measured in cells dialyzed with (in mM) 115 K-D-gluconate, 2 Mg-D-gluconate$_2$, 5 EGTA, 10 HEPES, pH 7.4. Cells were subsequently perfused with solutions containing 140 Na-D-gluconate, 5 TEA-D-gluconate,

10.3389/fphys.2023.1147216

4 K-D-gluconate, 2 Ca-D-gluconate$_2$, 1 Mg-D-gluconate$_2$, 5 HEPES, pH 7.4, with or without 0.1 L-glutamate. Transport currents were determined as L-glutamate-sensitive currents by subtracting currents obtained in the absence of glutamate from currents measured in the presence of glutamate. For all experiments, Ag/AgCl electrodes were connected via external and/or internal agar salt bridges, made from plastic tubing filled with 3 M KCl in 1% agar. Offset potentials were determined at the end of each experiment, and junction potentials were corrected using the JPCalc software (Dr. P. Barry, University of South Wales, Sydney, Australia).

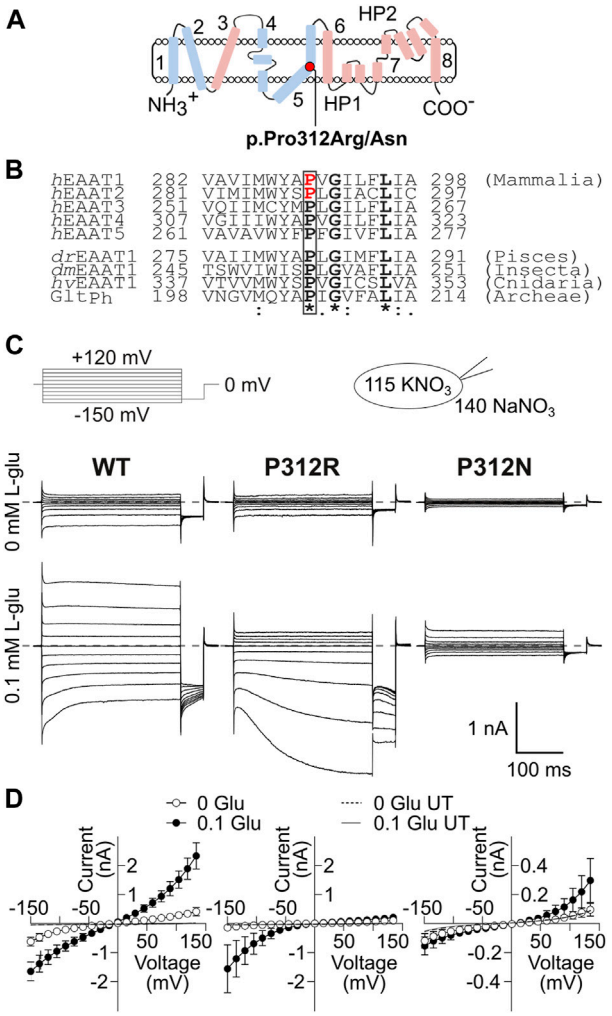

FIGURE 1
Mutations in P312 modify the time, voltage and substrate dependence of EAAT4 anion currents. **(A)** Position of P312 in an EAAT transmembrane topology model (trimerization/transport domains: blue/magenta, left panel). **(B)** Sequence alignments of mammalian EAAT isoforms and homologues from animals and bacteria illustrate the strict evolutionary conservation of a **PXGXXXL** motif in this class of transporters. Positions of missense mutations associated to human neurological diseases are indicated in red (Jen et al., 2005; Guella et al., 2017; h: *H. sapiens*, dr: *D. rerio*, dm: *D. melanogaster*, hv: *H. vulgaris*, Ph: Pyrococcus horikoshii). **(C)** Representative current recordings from HEK293T cells expressing WT (left), P312R (middle) or P312N (right) *r*EAAT4 internally dialyzed with a KNO_3-based solution and a $NaNO_3$-based external solution before (upper row) and after application of 0.1 mM L-glutamate (lower row). Zero current level is shown as grey dashed line. **(D)** Voltage dependence of mean anion current amplitudes from cells expressing WT (left), P312R (middle) or P312N (right) EAAT4 in the presence as well as in the absence of glutamate. Background currents obtained with untransfected HEK293T cells are shown as solid line in the presence of glutamate and dashed line in the absence of it. Data are given as the means ± 95% *C.I.*; $n \geq 9$.

Confocal microscopy and biochemistry

HEK293T cells were plated on poly-L-lysine coated coverslips 48 h after cell transfection and imaged with an inverted microscope (LSM 780, Carl Zeiss, Jena, Germany) using a 63*x*/1.40 NA oil immersion objective. mYFP was excited at 488 nm (argon laser), and emission was imaged between 543–549 nm, and fluorescences were analyzed with Fiji image analysis software (NIH). Transfection rates were quantified as ratios of transfected cells by the total number of cells (n = 1736/1596/788 cells; WT/P312R/P312N) with a 20*x*/1.4 NA oil immersion objective for three independent cell transfections for each construct.

For SDS-PAGEs, HEK293T cells were harvested 18 h after transfection with EAAT4-mYFP fusion proteins and lysed in phosphate buffer, supplemented with 0.4% dodecyl-maltoside for 30′ on ice. Lysates were then centrifuged for 35′ (13,000 rpm, 4°C) and equal amounts of whole cell lysates were analyzed with SDS-PAGEs (12%) and fluorescence scanning (Typhoon FLA 9500, GE Healthcare Europe GmbH, Freiburg, Germany). Each variant (WT/P312R/P312N) was tested in three independent transfections. Complex glycosylation was tested with recombinant PNGase F (New England Biolabs, Ipswich, MA, United States) at a concentration of 16.6 U/µL sample volume for 30′ at 37°C.

Kinetic modeling

Simulations of EAAT4 anion channel open probabilities were performed by solving differential equations on the basis of a modified EAAT2/Glt-1 model (Bergles et al., 2002; Machtens et al., 2011; Kovermann et al., 2017). Transitions within this kinetic scheme (Figure 7) were estimated by fitting the model predictions to experimentally determined current responses upon rapid substrate applications/removals using a genetic algorithm for minimization of squared errors as implemented in the Python package DEAP (Fortin et al., 2012). Starting values of rate constants were arbitrarily set to 1000 and for gating charges to 0.5. Parameters were "mutated" by adding a random number sampled from a normal distribution with zero mean. The size of these changes are controlled by the standard deviation of this distribution, which we adjusted over the course of fitting. Fitting started with large steps during an initial exploration phase, and steps were later restricted to 10% of the parameter value during refinement.

We initially calculated the steady-state distribution of all transporter states for each conditions before substrate application; these values subsequently serve as initial values to numerically solve a linear system of differential equations and to provide time and voltage-dependent absolute open probability $p(t, V)$. Absolute open probabilities were converted into macroscopic currents by adding occupancies of each channel

10.3389/fphys.2023.1147216

state assuming that all open-channel states exhibit same unitary conductance (Kovermann et al., 2010).

$$I(t,V) = N \cdot p(t,V) \cdot i(V)$$

with N being the number of channels in the membrane, t the time, V the voltage, $i(V)$ the single channel amplitude and $p(V)$ the absolute open probability. Dividing the current time course by current amplitudes at the end of the application provides

$$I_{norm1}(t,V) = \frac{I(t,V)}{I(t_{end},\mathrm{V})} = \frac{p(t,V)}{p(t_{end},\mathrm{V})}$$

Assuming a constant single-channel conductance (Kovermann et al., 2010), the normalization of currents to steady-state current amplitude (I_{SS}) at −150 mV (V_0) provides the voltage dependence of $p(t,V)$

$$I(t,V) = N \cdot p(t,V) \cdot i(V)$$
$$i(V) = \gamma \cdot \mathrm{V}$$
$$I_{norm2}(t,V) = \frac{I(t,V)}{I(t_{end},V_0)} = \frac{p(t,V)}{\mathrm{p}(t_{end},V_0)} \cdot \frac{V}{V_0}$$

Our fitting procedure aimed at minimizing the sum of squared residuals ($SSR1$) between experimentally determined $I_{norm1}(t,V)$ and simulated $\frac{p(t,V)}{\mathrm{p}(t_{end},\mathrm{V})}$

$$SSR1 = \sum \left(I_{norm1}(t,V) - \frac{p(t,V)}{p(t_{end},\mathrm{V})} \right)^2$$

and SSR2 between $I_{norm2}(t,V)$ and simulated $\frac{p(t,V)}{\mathrm{p}(t_{end},V_0)} \cdot \frac{V}{V_0}$

$$SSR2 = \sum \left(I_{norm2}(t,V) - \frac{p(t,V)}{p(t_{end},V_0)} \frac{V}{V_0} \right)^2$$

WT EAAT4 anion channels exhibit unitary conductances with negligible voltage dependence (Kovermann et al., 2010). We do not know how the mutations affect this unitary conductance. We therefore weighted $SSR2$ lower in mutants than in WT and allowed 20% deviation from linearity.

For plotting and error calculation, experimental currents were normalized as in I_{norm2} and plotted together with simulated traces (Figure 7). Experimental and predicted values were normalized to 1 at the end of the application of the most negative voltage. We quantified the overall error function or goodness of fit as the sum of all the individual SSRs from the different application experiments.

After optimizing fit parameters, we used a modified genetic algorithm to estimate the range of fit parameters with comparable quality of fit, as a value equivalent to a statistical error of the fit parameters (Figure 9). For this, fit parameters were randomly modified in 3000 generations of an explorative genetic algorithm to collect parameter values that impaired the goodness of fit by less than 25%.

Data analysis

Data were analyzed using a combination of Clampfit (Molecular Devices, San Jose, United States), Origin (OriginLab Corp., Northampton, MA, United States), SigmaPlot (Systat Software GmbH, Düsseldorf, Germany), Excel (Microsoft Corp., Redmont, WA, United States) and Libre office Calc (The Document Foundation, Berlin, Germany) software. All summary data are given as means ± *C.I.* (95%-confidence interval) or as box-whisker plots drawn between the first and third quartiles with whiskers providing the upper and lower 95% of the data range. Fluorescence levels of confocal images were analyzed with 2-way ANOVA with WT as controls, and Holm-Sidak *post hoc* testing, protein amounts and transfection rates were compared with one-way ANOVA, and Holm-Sidak *post hoc* testing. For comparison of dissociation constants and glutamate transport values, Kruskal–Wallis and Dunn's *post hoc* tests were used.

Results

EAAT4 functionally tolerates only few P312 substitutions

We substituted proline 312 in EAAT4 (Figure 1A) by alanine, arginine, asparagine, aspartate, cysteine, glutamate, glutamine, glycine, histidine, leucine, lysine, methionine, serine or

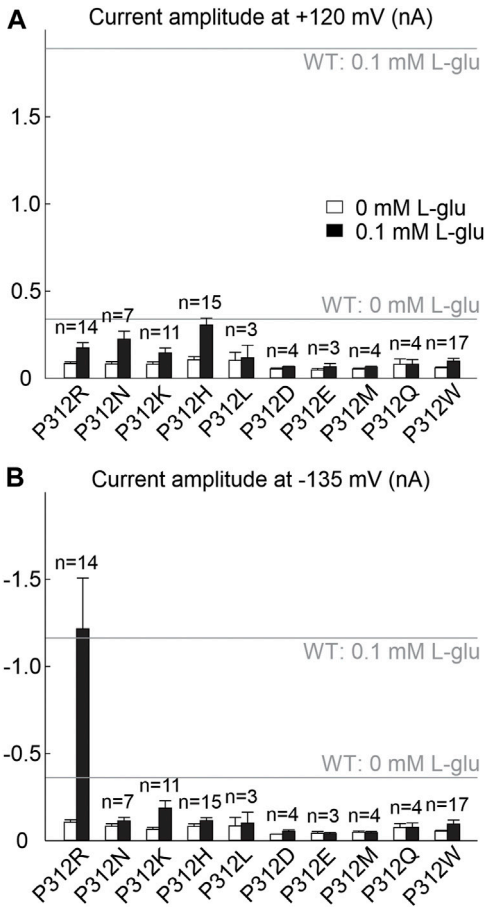

FIGURE 2
Many amino acid substitutions of P312 reduce EAAT4 anion current amplitudes. **(A, B)** Current amplitudes at +120 mV **(A)** or −135 mV **(B)** from HEK293T cells expressing WT or mutant EAAT4 with KNO_3-based internal solutions and $NaNO_3$-based external solutions after application of 0.1 mM L-glutamate (lower row). Dotted lines indicate background currents measured in untransfected cells with external glutamate.

tryptophan and expressed WT and mutant EAAT4 as mYFP fusion protein in HEK293T cells. EAATs transport three Na^+, one glutamate and one H^+ in exchange with one K^+ (Zerangue and Kavanaugh, 1996), and we therefore studied all mutants in experiments with cells dialyzed with K^+-containing solutions and externally perfused with Na^+-containing solutions with or without L-glutamate. In the following, these ionic conditions are referred to as uptake condition. NO_3^--based internal and external solutions were used to increase anion currents (Wadiche and Kavanaugh, 1998; Melzer et al., 2003). Only expression of P312H, P312K, P312N and P312R EAAT4 resulted in measurable L-glutamate-dependent anion currents under these conditions (Figures 1, 2). In cells expressing P312H and P312K EAAT4, current amplitudes were very small (Supplementary Figure S1), and we therefore restricted a detailed functional analysis to P312R and P312N EAAT4.

Figure 1C shows representative current recordings from cells expressing WT, P312R or P312N EAAT4 before (upper row) or after (lower row) L-glutamate application. Currents were small in the absence of L-glutamate, and significantly larger than background currents (given as solid lines in Figure 1D) only for WT or P312R EAAT4. For WT as well as for mutant EAAT4, anion currents were time-independent in the absence of L-glutamate, with larger conductances in the negative voltage ranges than in the positive voltage ranges. Application of L-glutamate increased current amplitudes, with distinct time and voltage dependences for WT and mutant EAAT4 in the presence of L-glutamate. WT and P312N EAAT4 anion currents showed bidirectional rectification, with macroscopic conductances increasing upon hyper- or depolarization (Figure 1D). WT EAAT4 exhibits a characteristic deactivation upon hyperpolarizing voltage steps (Kovermann et al., 2010). P312R EAAT4 anion currents increase in time and voltage-dependent manner at negative voltages. Under these ionic conditions, current amplitudes were comparable for WT and P312R EAAT4, but tenfold smaller in P312N EAAT4. Supplementary Figure S2 shows L-glutamate dependences for WT and mutant EAAT4 anion currents measured at symmetrical NO_3^-. Dose-response curves were fit with Michaelis-Menten relationships with K_M constants in the low µM range (WT: K_M = 2.9 ± 1.2 µM at −135 mV, K_M = 9.5 ± 2.6 µM at 120 mV/P312R: K_M = 0.03 ± 0.02 µM at −135 mV, K_M = 0.4 ± 0.2 µM at 120 mV/P312N: K_M = 0.03 ± 0.01 µM at −135 mV, K_M = 1.5 ± 1.0 µM at 120 mV) both strongly decrease L-glutamate K_Ms. Increased L-glutamate affinity was already described for P290R EAAT1 (Winter et al., 2012).

P312R and P312N impair EAAT4 glutamate transporter biogenesis and trafficking

Figure 3A depicts representative confocal images of cells expressing WT, P312R or P312N mYFP-EAAT4. We observed predominant surface membrane insertion for WT as well as for these mutant EAAT4, however, with large differences in total fluorescence intensities. The majority of the other mutants were retained in intracellular compartments (Figure 4). Separating fluorescences in the surface membrane from cytosolic mYFP revealed approximately tenfold lower fluorescence levels for P312R in or close to the surface membrane and twofold lower levels for P312N than for WT EAAT4 (Figure 3B). There are also lower amounts of mutant transporters in the cytosol (Figure 3B).

Resolving WT and mutant mYFP-EAAT4 fusion proteins after expression in HEK293T cells by reducing SDS-PAGE (Figure 3C) revealed triple fluorescence bands with molecular sizes of approximately 60–70 kDa. Deglycosylation with PNGase F removes the upper and the middle molecular weight bands, assigning non-, core- and complex glycosylated states to the three bands (Figure 3C). P312N and P312R both reduces complex glycosylation of EAAT4, with more pronounced effects by P312R than by P312N (Figure 3D). Integrating fluorescence amplitudes of all three bands provides averaged cellular expression levels and revealed reduced expression levels of P312R and P312N mYFP-EAAT4 (Figure 3E). In such biochemical experiments, we did not distinguish transfected from non-transfected cells, and the observed differences in protein amounts may thus be either caused by reduced cellular protein expression or by reduced percentages of transfected cells. However, no differences in transfection efficiencies were observed between transfections with WT or mutant EAAT4 (Figure 3F). We conclude that P312R and P312N reduce expression levels and surface membrane insertion of EAAT4.

P312R endows EAAT4 with a unique K^+ dependence

Our group has studied multiple EAATs using K^+-free and Na^+-based intracellular solutions (Melzer et al., 2003; Kovermann et al., 2010; Schneider et al., 2014). Under these conditions, obligate K^+-dependent retranslocation and L-glutamate transport are not possible (Kortzak et al., 2019), and EAATs are expected to accumulate in an inward-facing conformation that is inaccessible to external L-glutamate. However, we observed L-glutamate-sensitive anion currents for all tested EAATs with Na^+-based intracellular solutions (Melzer et al., 2003; Leinenweber et al., 2011; Schneider et al., 2014), possibly due to re-translocation after rebinding of L-glutamate from the internal side. Alternatively, there might exist slow Na^+-bound only translocation processes (Bergles et al., 2002). Since Na^+ binding in the absence of L-glutamate stabilizes HP2 in an open state (Alleva et al., 2020; Alleva et al., 2021), it is currently unclear how such translocations occur. Although we do not fully understand the mechanisms of anion channel activation in cells internally dialyzed with Na^+-based solutions, comparison of WT and mutant EAAT4 revealed unique properties of P312R EAAT4.

WT and mutant EAAT4 anion currents exhibit different substrate, time and voltage dependences when tested with Na^+ as major internal cation as compared to uptake conditions (Figure 5A). These changes reflect the reduced number of states the transporters can occupy in the absence of internal K^+. Anion current amplitudes were comparable in cells expressing WT or P312N EAAT4 for K^+- and Na^+-based internal solutions, but were substantially smaller under internal Na^+ conditions (Figure 5B) than under uptake conditions for P312R EAAT4 (Figure 1D). This result suggests that anion conduction within the K^+ hemicycle is especially important for gain-of-anion channel function of this mutant. Moreover, whereas anion currents were stimulated by

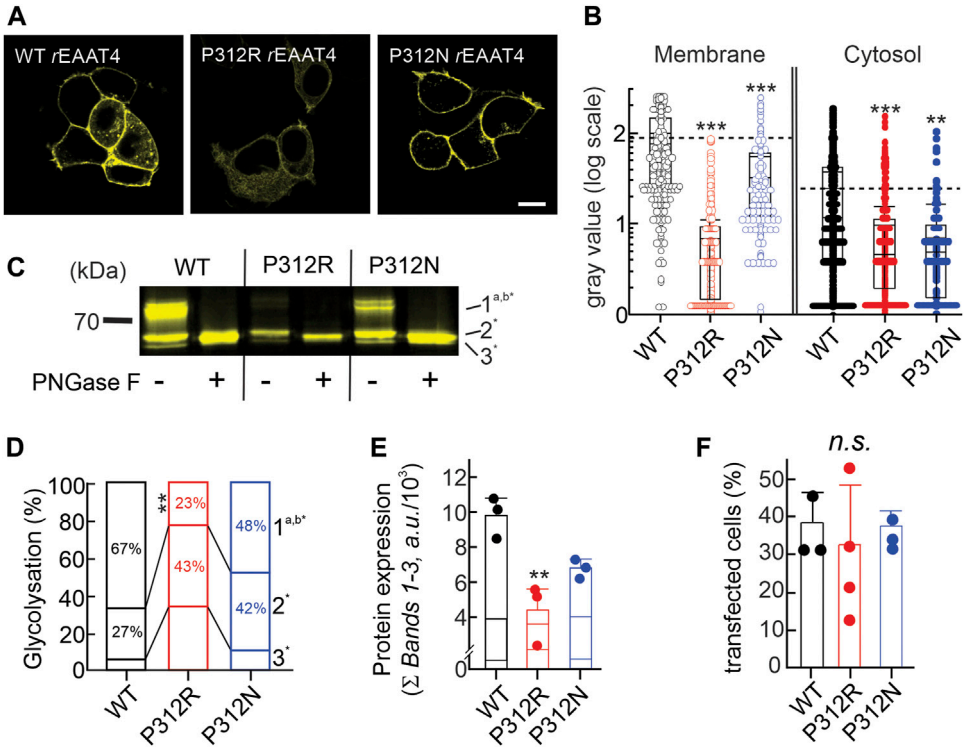

FIGURE 3
Mutating proline 312 reduces EAAT4 protein expression and modifies intracellular trafficking. **(A)** Representative confocal images of HEK293T cells expressing WT or mutant EAAT4-mYFP fusion proteins. **(B)** Box-plot analysis of fluorescence intensities from membranes and cytosolic areas. **(C)** Representative fluorescence scan of a SDS-PAGE loaded with equal amounts of whole cell lysates expressing WT or mutant EAAT4, either pretreated with PNGase F (+) or not (–). **(D)** Stacked bar graph showing the distribution of glycolysation states for WT or mutant EAAT4. **(E)** Mean protein expression levels determined from sums of fluorescence band intensities of all glycolysated fractions (Σ bands 1–3). **(F)** Transfection efficiencies given as percentages of transfected cells for three to four transfections per tested variant.

L-glutamate for WT or P312N EAAT4 with both tested internal solutions, we observed no L-glutamate-induced enhancement of P312R EAAT4 currents for cells dialyzed with Na^+-based solutions (Figure 5B).

P312N and P312R impair EAAT4 glutamate transport

EAATs mediates the stoichiometrically coupled transport of one glutamate, three Na^+ and one H^+, in exchange with one K^+. One transport cycle is therefore associated with the transport of two positive elementary charges across the membrane. Glutamate transport therefore generates a current, the so-called transport current, which can be quantified as L-glutamate-sensitive current component in internal and external solutions, in which permeant anions were completely substituted with gluconate (Figure 6A). EAAT4 is a prototypical low capacity glutamate transporter (Fairman et al., 1995; Mim et al., 2005), and EAAT4 L-glutamate transport currents are usually very small (Figure 6B). Transport currents measured approximately 30.4 ± 5.7 pA (n = 6, WT), 4.4 ± 0.6 pA (n = 5, P312R), and 1.8 ± 0.1 pA (n = 5, P312N) at −120 mV (Figure 6C). We conclude that P312R and P312N virtually abolish transport of L-glutamate.

Fast substrate application reveals changes in the glutamate transport cycle in mutant EAAT4

The effects of P312 R/N on EAAT4 anion currents under uptake and under internal Na^+ conditions as well as impaired L-glutamate uptake by mutant transporters indicate that amino acid substitutions at position 312 result in major modifications of the EAAT4 transport cycle (Figure 6A). To quantitatively describe these changes, we analyzed WT and mutant EAAT4 anion current responses to fast piezo-driven substrate applications (Franke et al., 1987; Jonas and Sakmann, 1992; Otis and Kavanaugh, 2000) for two internal solutions. Whereas L-glutamate application with internal K^+ will report on all possible anion-conducting conditions, intracellular dialysis with Na^+ + L-glutamate will restrict transitions to Na^+/L-glutamate bound translocation. Similarly, K^+-application to cells dialyzed with K^+-based internal solutions will provide insights into K^+-bound re-translocation as well as K^+-bound or *apo* state inward- or outward-facing conformations.

10.3389/fphys.2023.1147216

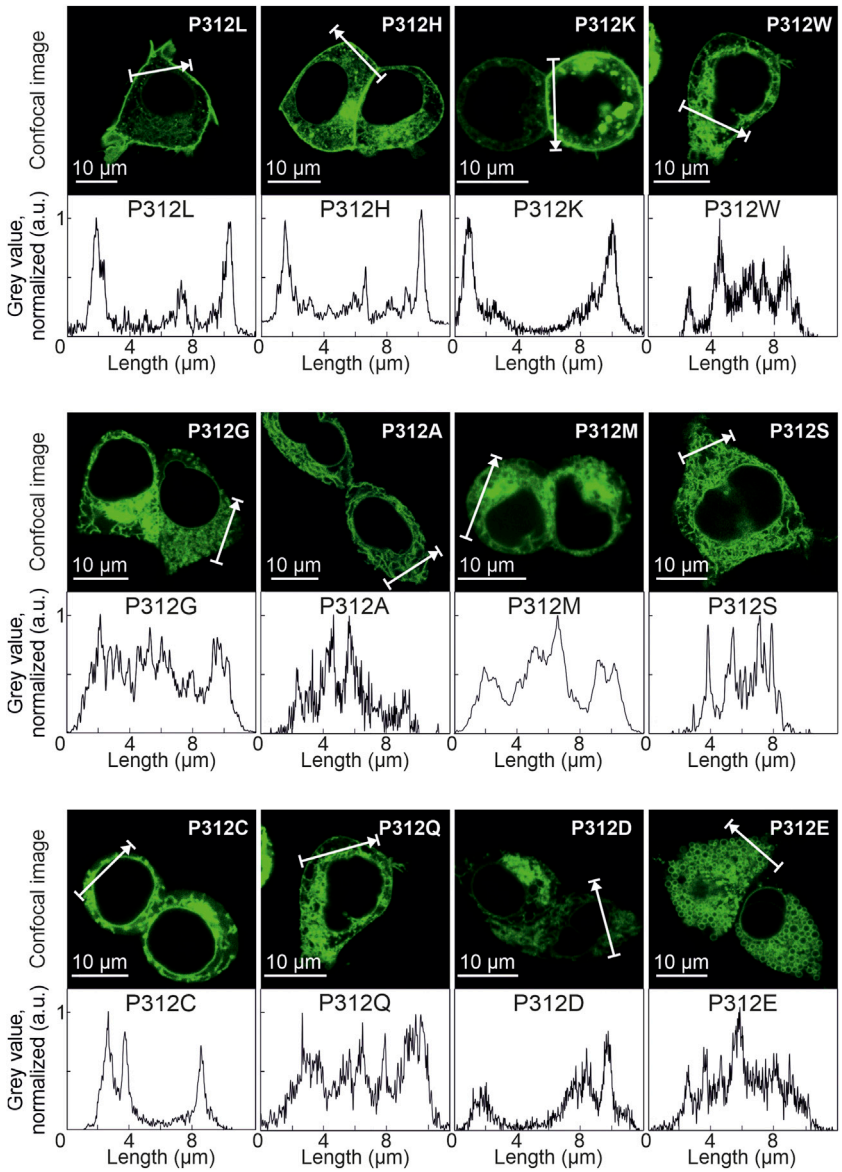

FIGURE 4
Various amino acid substitutions of P312 cause intracellular retention of EAAT4. Confocal images and corresponding intensity profiles of HEK293T cells expressing mutant mYFP-EAAT4 fusion proteins.

Figure 7 shows averaged WT, P312R and P312N EAAT4 current responses (±*C.I.*, n = 10) to fast solution exchanges. Cells were held at 0 mV, and voltage steps between −150 mV and +150 mV were applied. After reaching steady-state current amplitudes under the original ionic condition the external solution was quickly changed using a two-barreled application pipette attached to a piezoelectric bimorph (Carbone and Plested, 2012) and subsequently changed back to the original solution. The duration of solution application is given by a grey box containing the content of the perfused solution. In Figure 7B, 0.1 mM L-glutamate was applied to cells continuously perfused with a Na^+-based solution and internally dialyzed with K^+-based solutions. WT EAAT4 anion currents respond with fast increase followed by slight decrease in the positive range, and with biphasic responses consisting of fast increases and slower decreases at negative voltages, resembling earlier experiments using glutamate uncaging (Mim et al., 2005). For P312R EAAT4, current responses were inwardly rectifying; with fast activation and without deactivation at negative voltages. For P312N EAAT4, L-glutamate application results in activation to large current amplitudes at positive potentials and smaller changes in current amplitudes at negative voltages. Relative L-glutamate-induced changes in current amplitudes were larger for WT and P312R than for P312N EAAT4 currents. After removal of L-glutamate, transporters return via K^+-bound retranslocation into outward-facing conformations. For both mutant transporters,

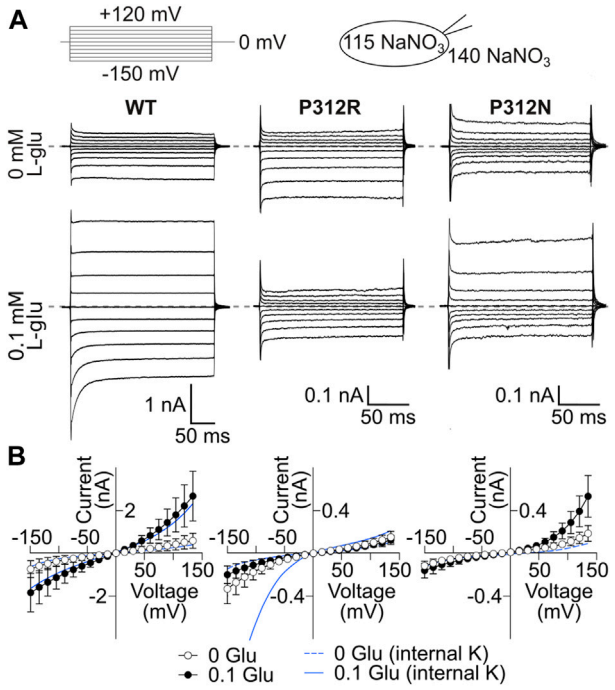

FIGURE 5
P312R makes EAAT4 anion currents glutamate-insensitive in the presence of internal Na^+. **(A)** Representative current recordings from HEK293T cells expressing WT (left), P312R (middle) or P312N (right) *r*EAAT4 with a $NaNO_3$-based internal solution and a $NaNO_3$-based external solution before (upper row) and after application of 0.1 mM L-glutamate (lower row). **(B)** Voltage dependence of mean anion current amplitudes from cells expressing EAAT4 variants obtained in cells intracellularly dialyzed with $NaNO_3$-based solutions. Data are given as the means ± *C.I.*; $n \geq 7$. Background currents obtained with untransfected HEK293T cells are shown as solid line in the presence of glutamate and dashed line in the absence of it. Blue lines provide current-voltage relationships for cells expressing WT and mutant EAAT4 and dialyzed with a K^+-based internal solution.

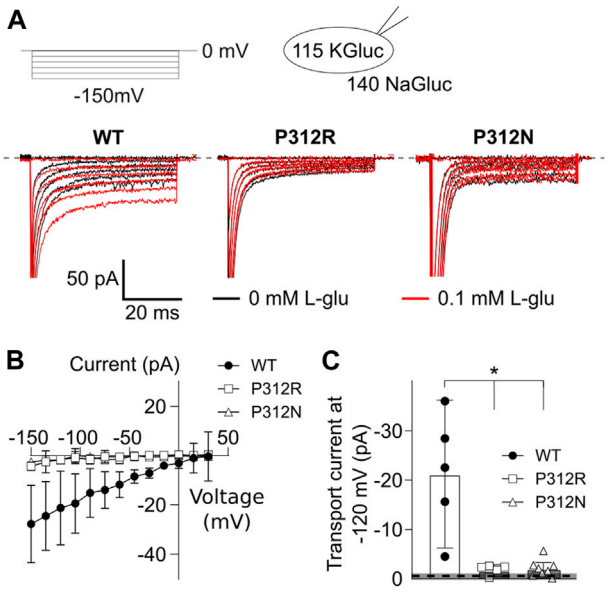

FIGURE 6
Mutations in P312 modify glutamate transport by EAAT4. **(A)** Representative current recordings from HEK293T cells expressing WT (left), P312R (middle) or P312N (right) EAAT4 with K-D-gluconate-based internal solution and Na-D-gluconate-based external solution before (black traces) and after application of 0.1 mM L-glutamate (red traces). **(B)** Voltage dependence of mean L-glutamate transport current amplitudes from cells expressing WT, P312R, or P312N EAAT4. Data are given as the means ± *C.I.*; $n \geq 4$. **(C)** Comparison of WT, P312R and P312N EAAT4 transport currents at –120 mV. Control data from untransfected cells (means ± CI) are given as grey box.

L-glutamate removal results in much slower decays of current amplitudes than for WT transporters.

Fast application of Na^+ together with L-glutamate to WT EAAT4 transporters equilibrated in choline-based solutions and dialyzed with K^+-based solutions elicits slow activation at positive as well as at negative voltages (Figure 7C), likely reflecting slow conformational changes associated with Na^+ binding to *apo* state glutamate transporters (Ewers et al., 2013; Alleva et al., 2020). Changing to a Na^+-based solution with saturating L-glutamate concentrations from a choline-based external solution resulted in comparable time courses under uptake conditions, i.e., in cells internally dialyzed with K^+ (Figure 7B), and under exchange conditions, i.e., in cells dialyzed with Na^+ + L-glutamate (Figure 7D). For P312R EAAT4, current responses were inwardly rectifying upon application of L-glutamate alone (Figure 7B) or upon application of Na^+ + L-glutamate application, under transport (Figure 7C) as well as under exchange conditions (Figure 7C). For both internal solutions, cells expressing P312R EAAT4 display currents exceeding 400 pA at external choline$^+$. Under these conditions, transporters are expected to be in the outward facing conformations. Current amplitudes clearly above background indicate anion conducting states in this conformation. Currents are comparable in external Na^+ and in external choline$^+$; with K^+-based internal solutions as well as with internal Na^+/L-glutamate. P312N EAAT4 anion currents are outwardly rectifying also for these conditions, and Na^+ application resulted in slow activation. There are substantially smaller currents with choline than with Na^+ as main external cation, indicating major contributions of P312N EAAT4 anion conducting states that can be accessed from Na^+-bound, but not from *apo* outward facing conformations.

Figure 7E depicts current responses of cells intracellularly dialyzed with K^+-based solutions to changes from K^+-free to K^+-containing solutions. Neither in cells expressing WT nor P312N EAAT4 any currents were observed under these conditions. In contrast, there exist substantial P312R EAAT4 anion currents in K^+-free solutions that were reduced upon application of external K^+. These results indicate that P312R induce a hitherto unknown open anion channel conformation that is accessible from *apo* outward facing conformation.

Kinetic modeling reveals distinct changes in substrate association and translocation as well as in anion channel opening in mutant EAAT4. To test which conformational changes are affected by the P312 mutants, we built a kinetic model (Figure 7A) and fitted simulated currents to current responses to fast substrate application (Figures 7B–E; Table 1). The model is based on a published EAAT2/Glt-1 model (Bergles et al., 2002; Machtens et al., 2011; Kovermann et al., 2017). Since we did not

10.3389/fphys.2023.1147216

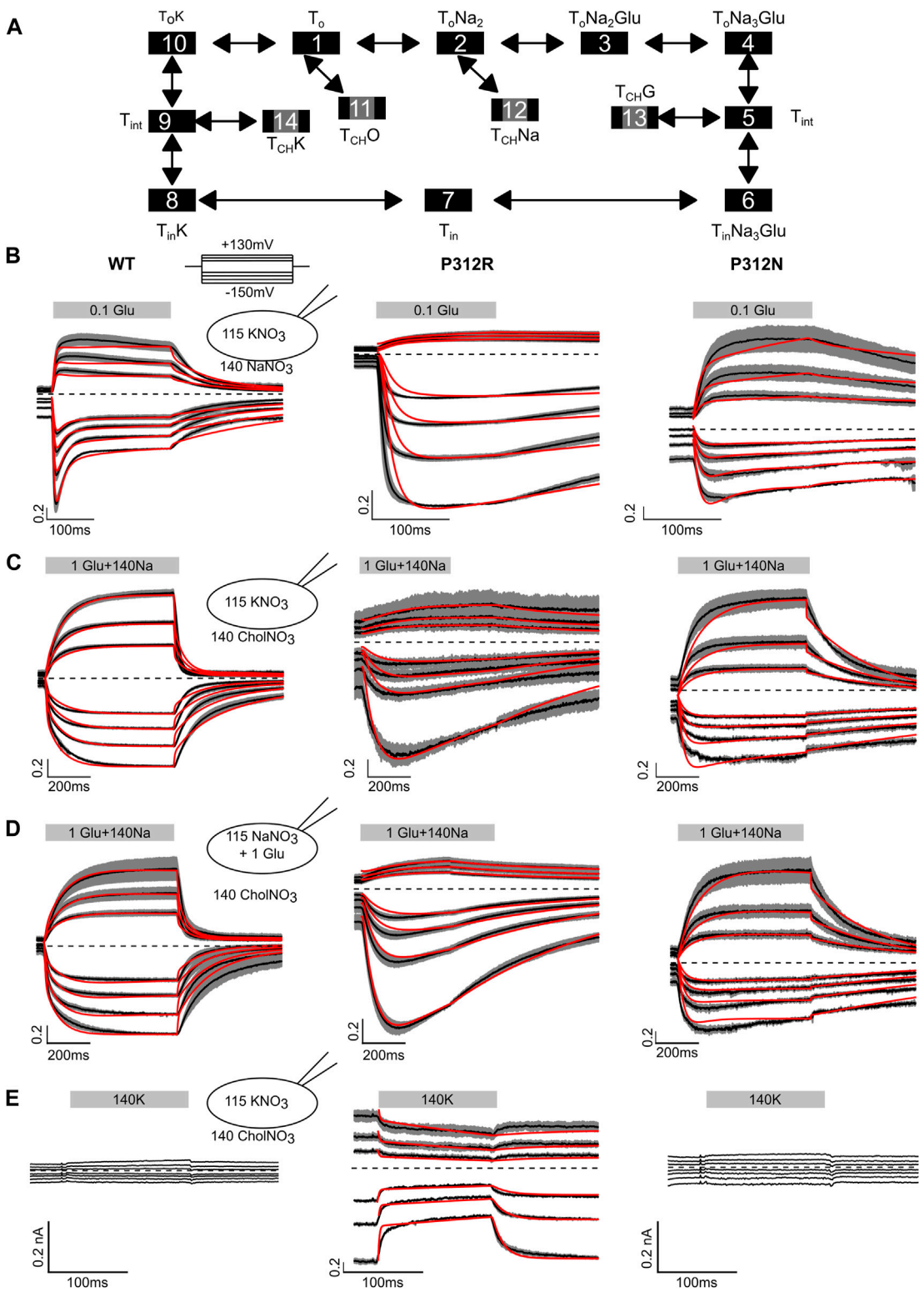

FIGURE 7
Fast application experiments with WT, P312R or P312N EAAT4. **(A)** Kinetic scheme for EAAT glutamate transport. **(B–D)** Normalized mean (black lines) of all current recordings from HEK293T cells expressing WT (left), P312R (middle) or P312N (right) EAAT4 dialyzed either with KNO_3-based **(B, C, E)** or $NaNO_3$ + L-glutamate-based **(D)** internal solution upon rapid application of L-glutamate **(B)**, Na^+ + L-glutamate **(C, D)** or K^+ **(E)**. Shaded area indicate confidence intervals, and red lines provide the time-course of simulated normalized open probabilities. Absolute WT and P312N EAAT4 currents **(E)** are indistinguishable from background; we therefore did not fit such currents.

TABLE 1 Rate constants of the transport process and of channel gating at 0 mV. Electrogenic reactions are defined by z values, which correspond to the fraction of the electric field the charge is moved across the membrane.

Transition	WT			P312R			P312N		
	Forward	Backward	z	Forward	Backward	z	Forward	Backward	z
T_o-T_oNa2	**80 $M^{-1}s^{-1}$**	**2 s^{-1}**	0.1	**80 $M^{-1}s^{-1}$**	**2 s^{-1}**	0.2	**80 $M^{-1}s^{-1}$**	12.4 s^{-1}	0.08
T_oNa2-T_oNa2Glu	**1.0•10^6 $M^{-1}s^{-1}$**	9,800 s^{-1}	0	**1.0•10^6 $M^{-1}s^{-1}$**	1400 s^{-1}	0	**1.0•10^6 $M^{-1}s^{-1}$**	8.8 s^{-1}	0
T_oNa2Glu-T_oNa3Glu	**2.5 •10^4 $M^{-1}s^{-1}$**	**1000 s^{-1}**	0.0	**2.5 •10^4 $M^{-1}s^{-1}$**	0.9 s^{-1}	0.13	277 $M^{-1}s^{-1}$	**1000 s^{-1}**	0.0
T_oNa3Glu-T_{int}	781 s^{-1}	**200 s^{-1}**	0.2	0.6 s^{-1}	**200 s^{-1}**	0.2	4,625 s^{-1}	3053 s^{-1}	0.11
T_{int}-T_{in}Na3Glu	**200 s^{-1}**	33 s^{-1}	0.07	**200 s^{-1}**	16.8 s^{-1}	0.31	5,627 s^{-1}	15 s^{-1}	0.14
T_{in}Na3Glu-T_{in}	**0.3 s^{-1}**	9.7 •10^6 M^{-3} s^{-1}	0.7	11.7 s^{-1}	780.1 $M^{-3}s^{-1}$	0.5	**0.3 s^{-1}**	9.8•10^5 $M^{-3}s^{-1}$	0.78
T_{in}-T_{in}K	**10,000 $M^{-1}s^{-1}$**	**1000 s^{-1}**	0	618 $M^{-1}s^{-1}$	2,130 s^{-1}	0	**10,000 $M^{-1}s^{-1}$**	**1000 s^{-1}**	0
T_{in}K-T_{int}	**1 s^{-1}**	0.004 s^{-1}	0.76	0.5 s^{-1}	4 s^{-1}	0.2	**1 s^{-1}**	0.123 s^{-1}	0.73
T_{int}-T_oK	**50 s^{-1}**	**1000 s^{-1}**	0.13	55 s^{-1}	**1000 s^{-1}**	0.43	**50 s^{-1}**	**1000 s^{-1}**	0.13
T_oK-T_o	**13000 s^{-1}**	**1.2•10^6 M^{-1} s^{-1}**	0	594 s^{-1}	9.9 •10^6 $M^{-1}s^{-1}$	0	**13000 s^{-1}**	**1,200,000 $M^{-1}s^{-1}$**	0
T_{int}Glu-T_{CH}F	0.77 s^{-1}	775 s^{-1}	0	925 s^{-1}	12,081 s^{-1}	0	1737 s^{-1}	19807	0
T_{int}K-T_{CH}K	0	0	0	0.4 s^{-1}	5.5 s^{-1}	0	0	0	0
T_o-T_{CH}O	0	0	0	0.1 s^{-1}	3591 s^{-1}	0	0	0	0
T_oNa2-T_{CH}Na	0.00009 s^{-1}	6.0866 s-1	0	8.6 •10^{-8} s^{-1}	2,102 s^{-1}	0	0.4 s^{-1}	7,230 s^{-1}	0

Bold values were constrained during optimization.

study effects of varying internal or external pHs, we lumped H^+-free and H^+-bound states together. Moreover, we only distinguished inward facing conformations bound to Na^+ and L-glutamate, bound to K^+ or in the *apo* state. Open anion conducting conformations (numbers marked in grey) were assumed to be accessible from intermediate conformations with bound Na^+ and L-glutamate or bound K^+, in agreement with recent MD results demonstrating that anion channels with functional properties that resemble experimental results open during lateral movements of the transport domain from intermediate positions (Machtens et al., 2015; Cheng et al., 2017). There is experimental evidence that supports branching anion channel states: rapid glutamate application results in a faster onset of EAAT3 glutamate transport currents than of anion currents (Grewer et al., 2000). Since this result is in disagreement with EAAT anion conducting states within translocation transition that were recently suggested (Chen et al., 2021), we decided not to include such states.

To account for EAAT anion conductance with external Na^+ in absence of L-glutamate an open channel state was linked to the outward-facing state with two associated Na^+ ions. To explain the inhibition of current in the K^+ application experiments of P312R, an additional channel opening from the outward-facing *apo* state was inserted. Voltage dependences were optimized by fitting current responses at different voltages. Unitary currents were assumed to changes linearly with voltage (Kovermann et al., 2010). P290R is not modifying the unitary current amplitudes of EAAT1 (Winter et al., 2012), and P290 is not contributing to forming the anion conduction pathway (Machtens et al., 2015). We therefore assumed that P312R and P312N EAAT4 anion channels also exhibit voltage-independent unitary conductances and that distinct rectification of WT and mutant EAAT4 is due to separate voltage dependent open probabilities.

We used an iterative procedure to optimize fit parameters. Initially, experimental data were fitted for each of the three constructs. Subsequently, the thus obtained parameters were individually varied, with all other parameters kept constant, and changes in the goodness of fit were calculated as function of the parameter variation (Figure 8). This analysis permits identification of the parameter interval, in which the goodness of fit is increased by less than 50% of the minimum value (the fit cutoffs are given by green lines in Figure 8). For some parameters, these intervals overlapped for two or three constructs. In such cases, we concluded that fit parameters were the same and fixed them to the mean of both values (given as arrow in Figure 8) in subsequent iterations. If forward and backward rate of one transition were identified by this criterion, we fixed only one of them. In the next fit iteration, the remaining free parameters were optimized in new fitting procedures, followed again by variation of individual parameters. These procedures were repeated three times. Parameter, which were fixed during this procedure, are provided in bold in Table 1.

We tested the accuracy of our fitting results in an additional procedure, in which all fit parameters were randomly modified. Fit parameters that decreased the goodness of fit by less than 25% were collected, providing a distribution of fit parameters that permit fitting experimental data with similar accuracy (Figure 9). This analysis demonstrated that rates of certain transitions, e.g., glutamate binding or K^+-bound translocation, are not very well defined, with a large range of parameters equally well describing the data. On the other hand, this analysis also identifies parameters, with

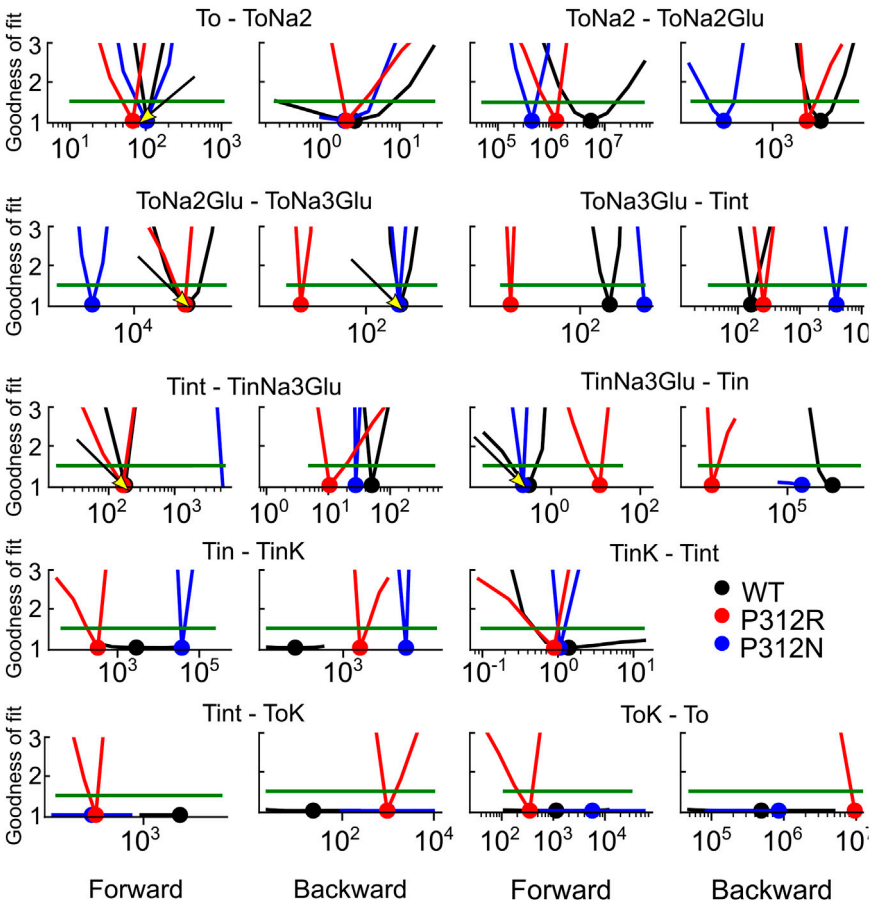

FIGURE 8
Iterative parameter optimization. Changes of the goodness of fit upon variation of individual parameters, while remaining rates were kept constant after the initial fit with no constraints. The goodness of fit was determined for fits on WT and mutant EAAT4 current traces and normalized to the minimum value. Dots indicate the position of the minimum, and green lines indicate 50% increase in the relative goodness of fit. Arrows indicate values, to which rates were constrained before starting the 2nd fitting iteration with reduced number of free parameters. This analysis was not performed for T_{int}—$T_{int}K$, because this rate is restrained by detailed balance.

mutant values that are far away from WT values and have a big impact on the fit quality. There are major alterations in both hemicycles by P312R (Table 1). P312R reduces the unbinding rate of glutamate and the third Na^+ as well as translocation rates from T_oNa_3Glu to intermediate and to inward facing states within the Na^+/L-glutamate hemicycle. Moreover, P312R impairs association of substrates to T_iNa_3GH and dissociation of K^+ from the outward-facing conformation increases K^+ binding to inward-facing conformations. P312N reduces Na^+ binding to *apo* as well as to T_oNa_2GH and L-glutamate unbinding from the outward-facing conformation. It speeds up glutamate translocation rates, but leaves translocation rates of the K+ hemicycle unaffected (Table 1; Figure 9). Whereas impaired L-glutamate bound translocation as well as K^+-bound retranslocation account for reduced L-glutamate transport by P312R EAAT4, slowed substrate release to the cytoplasm reduces P312N EAAT4 glutamate transport.

The thus optimized kinetic model correctly reproduces experimentally observed anion currents for all tested constructs (Figures 7B–E) and accounts for experimentally observed changes in L-glutamate transport (WT 2.5/s, P312N 0.05/s, P312R 10^{-6}/s). Figure 10 depicts predicted residence probabilities for transport (left panels) or anion conducting states (right panels) before and after substrate application for all internal conditions shown in Figure 5. In the presence of external glutamate, WT and P312N EAAT4 reside predominantly in the fully bound inward facing conformation. This distribution is shifted towards the outward facing fully bound and the inward-facing *apo* states in P312R EAAT4 (Figures 10A–C). Increased anion currents by P312R EAAT4 are caused by additional occupation of anion conducting states in the *apo* state; the probability of assuming the Na^+-bound only anion conducting states is decreased in P312R EAAT4 (Figures 9A–C). There are only slight modifications of anion channel occupations by P312N.

For some EAATs, absolute anion channel open probabilities can be obtained from the comparison of transport and anion currents, when absolute unitary transport rates are known (Fahlke et al., 2016; Kolen et al., 2020). Unfortunately, the absence of P312R and P312N EAAT4-mediated L-glutamate transport currents prevents application of this method for these particular mutations. Absolute open probabilities can therefore not be determined for

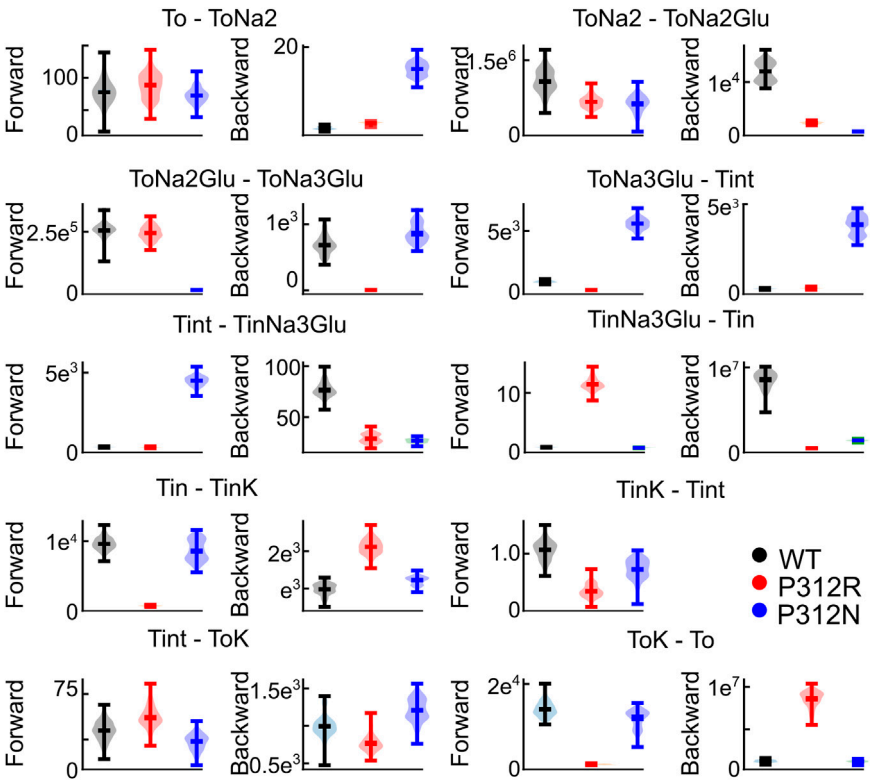

FIGURE 9
Not all fit parameter are equally well defined. Violin plots of parameters with a goodness of fit that differs by less than 25% from the optimum fit. This analysis was not performed for T_{int} - $T_{int}K$, because this rate is restrained by detailed balance.

these two mutants, and absolute current amplitudes cannot be analyzed. To test how our inability to quantify absolute open probabilities affects the outcome of modeling rates within the WT and mutant EAAT4 transport cycle, we compared predicted current time courses for WT and mutant EAAT4 upon variation of anion channel opening rates (Figure 11). Such changes resulted in dramatic alterations of absolute open probabilities, but left the time and voltage dependence of EAAT4 anion currents unchanged. We conclude that kinetic modelling of WT and mutant EAAT4 provides changes in transport rates of the transport cycle even in the absence of accurate values for absolute open probabilities. Most importantly, these results indicate that our modelling is unable to quantify anion channel opening rates.

Discussion

We here combined heterologous expression, whole-cell recording and fast ionic substitution experiments with mathematical modelling to describe the molecular basis of glutamate transporter dysfunction in two inherited human diseases. Naturally occurring mutations that predict substitution of a conserved proline in the middle of the fifth transmembrane helix by arginine were found in patients with episodic ataxia type 6 (Jen et al., 2005), EAAT1) and in patients with epileptic encephalopathy (Epi4K Consortium, 2016; Guella et al., 2017), EAAT2). These mutations cause gain-of-function of the EAAT anion channel and reduce glutamate transport rates of both isoforms (Winter et al., 2012; Hotzy et al., 2013; Kovermann et al., 2022b). The substitution of proline by arginine might affect glutamate transporter function via long range electrostatic effects or by structural alterations that affect conformational changes underlying transporter function and anion channel opening. To distinguish between these two mechanisms of dysfunction we studied multiple substitutions of the homologous proline in EAAT4 (P312).

We chose EAAT4 because of its robust and well described anion currents in transfected mammalian cells (Melzer et al., 2003; Melzer et al., 2005; Kovermann et al., 2010; Leinenweber et al., 2011; Nothmann et al., 2011; Machtens et al., 2015). Unexpectedly, expression of most of the tested EAAT4 mutants resulted in only small anion currents (Figure 2). The majority of the mutations impaired surface-membrane insertion and resulted in predominant staining of intracellular membranes (Figure 4). For this reason, we could only study the functional consequences of neutral or positive. The similarity between P312K and P312R EAAT4 suggests that the substituted positive charge plays an important role in changing the voltage dependence of mutant EAAT4 currents. Substitutions of negative charges, i.e., P312E and P312D, were studied as additional test for electrostatic interactions, however, both mutations resulted

10.3389/fphys.2023.1147216

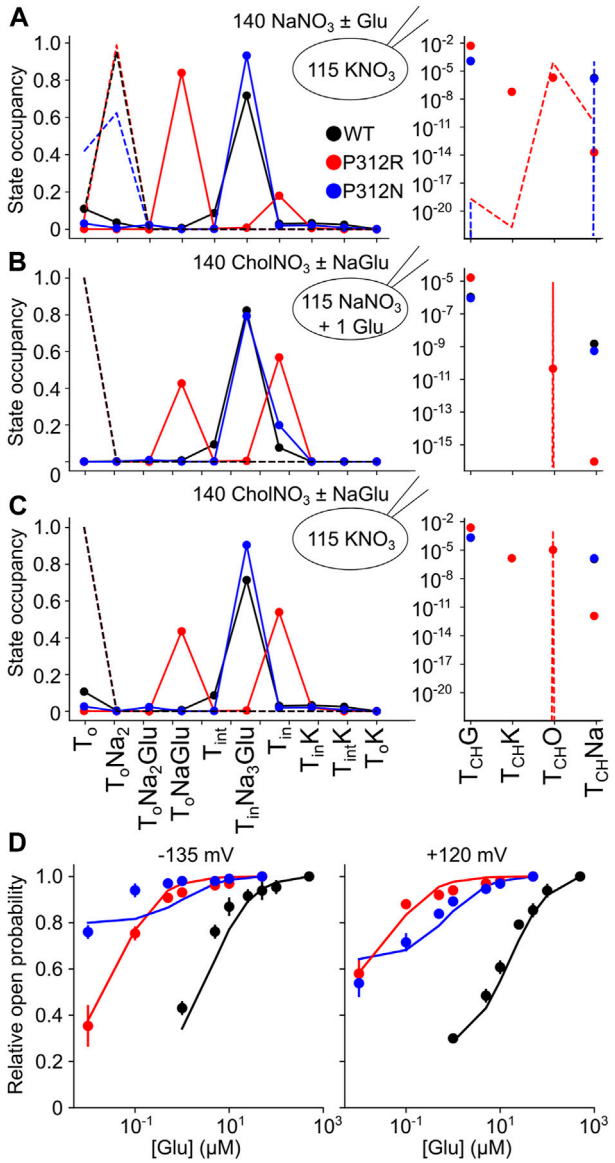

FIGURE 10
Gain-of-anion channel function of P312R EAAT4 is exclusively due to *apo* state channel opening. **(A–C)** Simulated residence probabilities for WT, P312R or P312N EAAT4 in states of the transport cycle (left) or in open anion channel (right) conformations for indicated ion and substrate conditions before (dashed lines) or after (symbols) solution exchange. **(D)** Experimental and simulated glutamate titration curves.

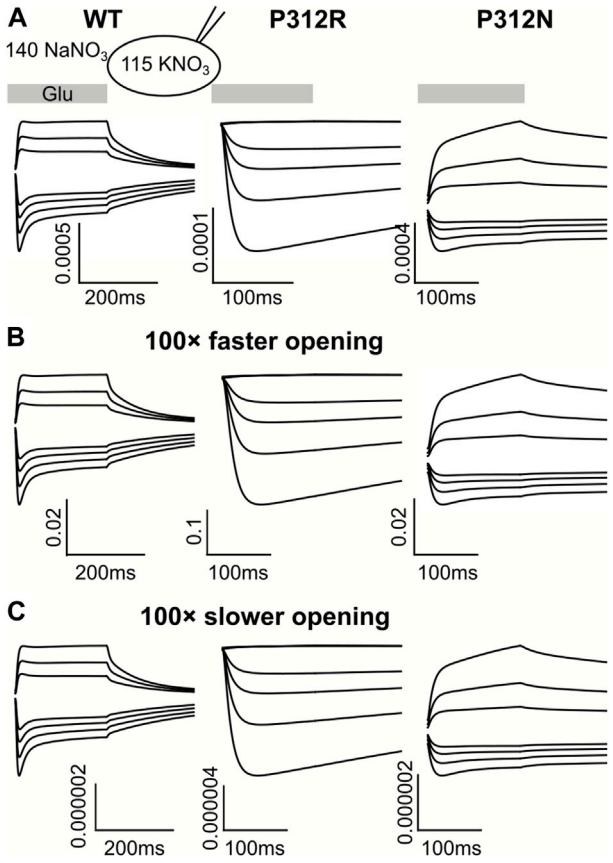

FIGURE 11
Kinetic modeling of WT and mutant EAAT4 anion currents does not require accurate knowledge of absolute anion channel open probabilities. Simulated anion currents for WT (left), P312R (middle) or P312N (right) EAAT4 with KNO_3-based internal solution upon rapid application of L-glutamate as shown in Figure 6 **(A)**, or after increasing **(B)** or decreasing **(C)** anion channel opening rates by a factor of 100.

in substantial impairment of intracellular trafficking (Figure 4), preventing functional analysis. P312N causes pronounced changes in function, indicating that not alone the charge, but also changes in transporter conformations contribute to the functional impairment of P312 mutations.

Colucci et al. recently reported the single-particle cryo-EM structure of the archaeal glutamate transporter homologue, Glt_{Tk}, carrying the homologous P208R mutation (Colucci et al., 2023). They found the structure of the fifth transmembrane helix preserved in mutant Glt_{Tk} and the inserted arginine to project into the membrane. The authors suggested that interactions with the phospholipids might cause the observed changes in transport and anion channel activity. At present, our knowledge about the conformational changes resulting in anion channel opening and their changes by these structural alterations prevents a mechanistic explanation of the functional changes of mutant transporters. It will be interesting to see structures of mutant transporters carrying this mutation in additional conformations.

P312R and P312N cause distinct changes in the time and voltage dependences of macroscopic currents (Figure 1). P312R EAAT4 anion channels activate upon hyperpolarizing voltage steps. In contrast, P312N EAAT anion currents were time-independent and outwardly rectifying. Anion channel opening can only occur from certain states of the transport cycles, and changes in transitions within the transport cycle will therefore modify the voltage dependence of anion channel opening. To identify transitions that are altered by the studied point mutations we measured current responses to rapid changes in substrate concentration and fitted current responses to a 15-state kinetic scheme, to account for the complex transport stoichiometry and the dual function of EAAT4 as L-glutamate transporter and

anion channel. The large number of states and the inability to directly measure the majority of individual rates make accurate and unambiguous determination of rate constants a complicated task. To account for this challenge, we studied WT and mutant transporters in an interative fitting procedure. After initial optimization, we tested whether fit parameters for mutant transporters differ from WT (Figure 8). If not, parameters were fixed to WT values in subsequent iterations, in order to reduce the number of variables. This procedure was three times repeated. We then tested the accuracy of our fitting results in an additional procedure, in which fit parameters were randomly modified, to define a range of values for each parameter that similarly well described the experimental data (Figure 9). This approach provided information about how well certain parameters are defined by the experimental values and our fitting procedure.

Optimization of reaction rates of the kinetic scheme demonstrated that P312R and P312N affected substrate association and dissociation, Na^+/L-glutamate and K^+-bound translocation (Table 1). Structures of mammalian EAATs and bacterial model proteins have been determined for multiple conformations, in inward and outward facing conformations (Yernool et al., 2004; Boudker et al., 2007; Reyes et al., 2009; Alleva et al., 2020) as well as in intermediate conformations (Verdon and Boudker, 2012; Chen et al., 2021). In all conformations, the residues homologous to P312, are not in close spatial proximity of any known structural determinant of Na^+ or K^+ association (Alleva et al., 2021). It thus remains unclear how P312 R/N affect cation binding/unbinding (Table 1).

Increased anion channel activity of P312R EAAT4 are caused by higher residence probabilities of existing conducting states as well as of $T_{CH}O$, an open channel state accessible from outward facing *apo* state, and $T_{CH}K$ (Figure 10). Neither WT nor P312N transporters assume $T_{CH}O$, suggesting that anion channel opening from outward-facing conformations is a direct consequence of the P312R mutation. One may imagine that increased occupation of anion channel modes that are outside the transport cycle might be the basis of the reduced transport rates. However, EAAT anion channels exhibit only very low open probabilities, and mutations that stimulate anion channel opening only minimally affected transport rates (Kolen et al., 2020). P312R and P312N reduce L-glutamate transport rates by impairing translocation (P312R) or substrate release (P312N, Table 1).

We recently employed voltage clamp fluorometry to study the functional consequences of the homologous proline by arginine mutation (P259R) on the human glutamate transporter EAAT3 (Hotzy et al., 2013). EAAT3—either carrying the P259R mutation or not–was optimized for voltage clamp fluorometry by inserting a cysteine at position 205 (M205C) and removing an endogenous cysteine at position 158 (C158S). After expression in *Xenopus* oocytes and fluorescent labeling, changes in fluorescence were evoked by voltage steps and studied for various external [Na^+] or [L-glutamate]. A kinetic analysis of fluorescence signals suggested that P259R mainly affects Na^+ binding to the glutamate-free transporter. Since two-electrode voltage clamp does not permit intracellular dialysis and thus greatly limits the analysis of translocation under distinct intracellular solution, it was impossible to identify changes in translocation or anion channel opening. Moreover, because of high anion background currents in oocytes, our earlier study was limited to the observation of fluorescence changes without analysis of anion currents. Such limitation prevented the identification of a major alteration in rate constants accessing open anion channel conformations from the *apo* state with this experimental system. In our present study, we also observed alterations of multiple Na^+ binding steps to P312R EAAT4, however, the most pronounced change was enhanced unbinding of the third Na^+, which binds after L-glutamate association and closure of HP2 (Guskov et al., 2016).

We here studied the functional consequences of disease-causing point mutations not in the affected glial EAAT isoforms, EAAT1 and EAAT2, but rather in the neuronal transporter EAAT4. This approach raises the question how our findings can help explaining the pathophysiology of episodic ataxia and epilepsy. Experiments with K^+-based solutions identified increased activity of an anion channel that is accessible in the outward facing *apo* state as main reason of gain-of-anion channel function in P312R EAAT4. Since the mechanisms of K^+ coupling are conserved in all EAATs, and since P290R EAAT1 and P289R EAAT2 share the unique K^+ dependence with P312R EAAT4 (Winter et al., 2012), this result can certainly be transferred to the glial transporters, providing novel insights into the molecular pathophysiology of the diseases. Our modelling furthermore revealed changes in various transport transitions, demonstrating that P312R impairs the EAAT4 transport cycles in multiple transporter conformations. Again, the structural conservation between EAAT isoform suggest similar changes in mutant EAAT1 and EAAT2.

In recent years, an increasing number of genetic diseases has been identified that are caused by dysfunctional ion channels and were dubbed “channelopathies”. In many cases, the linkage of human diseases helped identification of cellular roles of the affected ion channels (Adrian and Bryant, 1974; Koch et al., 1992; Barhanin et al., 1996; Sanguinetti et al., 1996; Scholl et al., 2018; Schewe et al., 2019). Disease-associated mutations were often shown to result in defined changes in ion channel function (Cannon et al., 1991; Fahlke et al., 1997) and helped understanding the molecular basis of ion channel activation and conduction. Episodic ataxia type 6 was one of the first diseases caused by genetic dysfunction of transporters (Jen et al., 2005) and continues to illustrate the complexity of this group of diseases. The P290R mutation in EAAT1 causes ataxia not because of its impaired transport function, but rather by gain-of-anion channel function that induces Bergman glial cell apoptosis and cerebellar degeneration via increased Cl^- efflux (Kovermann et al., 2020). We here demonstrate that this disease-causing dysfunction is conferred by a hitherto unknown transporter state, an anion channel conformation that opens from a conformation, which usually prevents water and anion fluxes.

Data availability statement

The original contributions presented in the study are included in the article/Supplementary Material, further inquiries can be directed to the corresponding author.

Ethics statement

All experiments were performed according to the German regulation for genetically modified organisms of Risk Group 1 (§§ 6.7 GenTG; GenTSV, Appendix 2), Aktenzeichen 53.02.01-K-1.119/15.

Author contributions

PK, J-PM, and CF conceived the project; PK and CF wrote the manuscript, with input from all co-authors; and MS, DK, PK, and J-PM performed the research and analyzed the data. All authors contributed to the article and approved the submitted version.

Funding

This work was supported by the Deutsche Forschungsgemeinschaft to J-PM. (MA 7525/1-1) and CF. (FA 301/12-1) as part of the Research Unit FOR 2518, DynIon; project P4, and the BMBF TreatIon 01GM2210D—Jülich to CF.

Acknowledgments

We would like to thank Dr. J. Rothstein for providing the expression construct for *r*EAAT4 and Dr. Andrew Plested, Humboldt Universität zu Berlin, for patiently and generously sharing his expertise on fast solution exchange systems with us. The authors gratefully acknowledge the computing time granted through JARA on the supercomputer JURECA at Forschungszentrum Jülich and the supercomputer CLAIX at RWTH Aachen University.

Conflict of interest

The authors declare that the research was conducted in the absence of any commercial or financial relationships that could be construed as a potential conflict of interest.

Publisher's note

Supplementary material

The Supplementary Material for this article can be found online at: https://www.frontiersin.org/articles/10.3389/fphys.2023.1147216/full#supplementary-material

SUPPLEMENTARY FIGURE S1
P312K and P312H cause distinct alterations in time, voltage and substrate dependences of EAAT4 anion currents.**(A)** Representative current recordings from HEK293T cells expressing P312K (left) or P312H (right) EAAT4 with a KNO_3-based internal solution and a $NaNO_3$-based external solution before and after application of 0.1 mM L-glutamate. **(B)** Voltage dependences of mean anion current amplitudes from cells expressing P312K (left) or P312H (right) EAAT4 obtained in cells intracellularly dialyzed with $NaNO_3$-based solutions. Data are given as the means ± *C.I.*; $n \geq 4$.

SUPPLEMENTARY FIGURE S2
P312R and P312N modify the glutamate dependence of EAAT4 anion currents **(A**)Representative current recordings from HEK293T cells expressing WT or mutant EAAT4 with a KNO_3-based internal solution and a $NaNO_3$-based external solution supplemented with various [L-glutamate] **(B)** Dose response curves of the L-glutamate dependence of WT or mutant EAAT current amplitudes. Data are given as the means ± *C.I.*; $n \geq 4$, solid lines provide fits with Michaelis-Menten relationships. **(C)** Statistical analysis of apparent dissociation constants from fits shown in **(B)**.

References

Adamczyk, A., Gause, C. D., Sattler, R., Vidensky, S., Rothstein, J. D., Singer, H., et al. (2011). Genetic and functional studies of a missense variant in a glutamate transporter, SLC1A3, in Tourette syndrome. *Psychiatr. Genet.* 21, 90–97. doi:10.1097/YPG.0b013e328341a307

Adrian, R. H., and Bryant, S. H. (1974). On the repetitive discharge in myotonic muscle fibres. *J. Physiol. Lond.* 240, 505–515. doi:10.1113/jphysiol.1974.sp010620

Alleva, C., Kovalev, K., Astashkin, R., Berndt, M. I., Baeken, C., Balandin, T., et al. (2020). Na^+-dependent gate dynamics and electrostatic attraction ensure substrate coupling in glutamate transporters. *Sci. Adv.* 6 (47), eaba9854. doi:10.1126/sciadv.aba9854

Alleva, C., Machtens, J. P., Kortzak, D., Weyand, I., and Fahlke, C. (2021). Molecular basis of coupled transport and anion conduction in excitatory amino acid transporters. *Neurochem. Res.* 47, 9–22. doi:10.1007/s11064-021-03252-x

Barhanin, J., Lesage, F., Guillemare, E., Fink, M., Lazdunski, M., and Romey, G. (1996). K_vLQT1 and IsK (minK) proteins associate to form the I_{Ks} cardiac potassium current. *Nature* 384, 78–80. doi:10.1038/384078a0

Bergles, D. E., Tzingounis, A. V., and Jahr, C. E. (2002). Comparison of coupled and uncoupled currents during glutamate uptake by GLT-1 transporters. *J. Neurosci.* 22, 10153–10162. doi:10.1523/JNEUROSCI.22-23-10153.2002

Boudker, O., Ryan, R. M., Yernool, D., Shimamoto, K., and Gouaux, E. (2007). Coupling substrate and ion binding to extracellular gate of a sodium-dependent aspartate transporter. *Nature* 445, 387–393. doi:10.1038/nature05455

Cannon, S. C., Brown, R. H., and Corey, D. P. (1991). A sodium channel defect in hyperkalemic periodic paralysis: potassium induced failure of inactivation. *Neuron* 6, 619–626. doi:10.1016/0896-6273(91)90064-7

Carbone, A. L., and Plested, A. J. (2012). Coupled control of desensitization and gating by the ligand binding domain of glutamate receptors. *Neuron* 74 (5), 845–857. doi:10.1016/j.neuron.2012.04.020

Chen, I., Pant, S., Wu, Q., Cater, R. J., Sobti, M., Vandenberg, R. J., et al. (2021). Glutamate transporters have a chloride channel with two hydrophobic gates. *Nature* 591, 327–331. doi:10.1038/s41586-021-03240-9

Cheng, M. H., Torres-Salazar, D., Gonzalez-Suarez, A. D., Amara, S. G., and Bahar, I. (2017). Substrate transport and anion permeation proceed through distinct pathways in glutamate transporters. *Elife* 6, e25850. doi:10.7554/eLife.25850

Chivukula, A. S., Suslova, M., Kortzak, D., Kovermann, P., and Fahlke, C. (2020). Functional consequences of SLC1A3 mutations associated with episodic ataxia 6. *Hum. Mutat.* 41, 1892–1905. doi:10.1002/humu.24089

Choi, K. D., Jen, J. C., Choi, S. Y., Shin, J. H., Kim, H. S., Kim, H. J., et al. (2017a). Late-onset episodic ataxia associated with SLC1A3 mutation. *J. Hum. Genet.* 62, 443–446. doi:10.1038/jhg.2016.137

Choi, K. D., Kim, J. S., Kim, H. J., Jung, I., Jeong, S. H., Lee, S. H., et al. (2017b). Genetic variants associated with episodic ataxia in korea. *Sci. Rep.* 7, 13855. doi:10.1038/s41598-017-14254-7

Colucci, E., Anshari, Z. R., Patiño-Ruiz, M. F., Nemchinova, M., Whittaker, J., Slotboom, D. J., et al. (2023). Mutation in glutamate transporter homologue Glt_{Tk}

provides insights into pathologic mechanism of episodic ataxia 6. *Nat. Commun.* 14, 1799. doi:10.1038/s41467-023-37503-y

de Vries, B., Mamsa, H., Stam, A. H., Wan, J., Bakker, S. L., Vanmolkot, K. R., et al. (2009). Episodic ataxia associated with EAAT1 mutation C186S affecting glutamate reuptake. *Arch. Neurol.* 66, 97–101. doi:10.1001/archneurol.2008.535

Engels, M., Kalia, M., Rahmati, S., Petersilie, L., Kovermann, P., van Putten, M., et al. (2021). Glial chloride homeostasis under transient ischemic stress. *Front. Cell Neurosci.* 15, 735300. doi:10.3389/fncel.2021.735300

Epi4K Consortium (2016). De Novo Mutations in *SLC1A2* and *CACNA1A* are important causes of epileptic encephalopathies. *Am. J. Hum. Genet.* 99, 287–298. doi:10.1016/j.ajhg.2016.06.003

Ewers, D., Becher, T., Machtens, J. P., Weyand, I., and Fahlke, C. (2013). Induced fit substrate binding to an archeal glutamate transporter homologue. *Proc. Natl. Acad. Sci. U. S. A.* 110, 12486–12491. doi:10.1073/pnas.1300772110

Fahlke, C., Beck, C. L., and George, A. L., Jr. (1997). A mutation in autosomal dominant myotonia congenita affects pore properties of the muscle chloride channel. *Proc. Natl. Acad. Sci. U. S. A.* 94, 2729–2734. doi:10.1073/pnas.94.6.2729

Fahlke, C., Kortzak, D., and Machtens, J. P. (2016). Molecular physiology of EAAT anion channels. *Pflugers Arch.* 468, 491–502. doi:10.1007/s00424-015-1768-3

Fairman, W. A., Vandenberg, R. J., Arriza, J. L., Kavanaugh, M. P., and Amara, S. G. (1995). An excitatory amino-acid transporter with properties of a ligand-gated chloride channel. *Nature* 375, 599–603. doi:10.1038/375599a0

Fortin, F. A., De Rainville, F.-M., Gardner, M., -A., Parizeau, M., and Gagne, C. (2012). DEAP: Evolutionary algorithms made easy. *J. Mach. Learn. Res.* 13, 5.

Franke, C., Hatt, H., and Dudel, J. (1987). Liquid filament switch for ultra-fast exchanges of solutions at excised patches of synaptic membrane of crayfish muscle. *Neurosci. Lett.* 77, 199–204. doi:10.1016/0304-3940(87)90586-6

Garcia-Olivares, J., Alekov, A., Boroumand, M. R., Begemann, B., Hidalgo, P., and Fahlke, C. (2008). Gating of human ClC-2 chloride channels and regulation by carboxy-terminal domains. *J. Physiol.* 586, 5325–5336. doi:10.1113/jphysiol.2008.158097

Gehlen, J., Aretzweiler, C., Mataruga, A., Fahlke, C., and Müller, F. (2021). Excitatory amino acid transporter EAAT5 improves temporal resolution in the retina. *eNeuro* 8, 0406. doi:10.1523/eneuro.0406-21.2021

Grewer, C., Watzke, N., Wiessner, M., and Rauen, T. (2000). Glutamate translocation of the neuronal glutamate transporter EAAC1 occurs within milliseconds. *Proc. Natl. Acad. Sci. U.S.A* 97, 9706–9711. doi:10.1073/pnas.160170397

Guella, I., McKenzie, M. B., Evans, D. M., Buerki, S. E., Toyota, E. B., Van Allen, M. I., et al. (2017). De novo mutations in YWHAG cause early-onset epilepsy. *Am. J. Hum. Gen.* 101, 300–310. doi:10.1016/j.ajhg.2017.07.004

Guskov, A., Jensen, S., Faustino, I., Marrink, S. J., and Slotboom, D. J. (2016). Coupled binding mechanism of three sodium ions and aspartate in the glutamate transporter homologue Glt_{Tk}. *Nat. Commun.* 7, 13420. doi:10.1038/ncomms13420

Hebeisen, S., and Fahlke, C. (2005). Carboxy-terminal truncations modify the outer pore vestibule of muscle chloride channels. *Biophys. J.* 89 (3), 1710–1720. doi:10.1529/biophysj.104.056093

Hotzy, J., Schneider, N., Kovermann, P., and Fahlke, C. (2013). Mutating a conserved proline residue within the trimerization domain modifies Na^+ binding to excitatory amino acid transporters and associated conformational changes. *J. Biol. Chem.* 288, 36492–36501. doi:10.1074/jbc.M113.489385

Iwama, K., Iwata, A., Shiina, M., Mitsuhashi, S., Miyatake, S., Takata, A., et al. (2017). A novel mutation in *SLC1A3* causes episodic ataxia. *J. Hum. Genet.* 63, 207–211. doi:10.1038/s10038-017-0365-z

Jen, J. C., Wan, J., Palos, T. P., Howard, B. D., and Baloh, R. W. (2005). Mutation in the glutamate transporter EAAT1 causes episodic ataxia, hemiplegia, and seizures. *Neurology* 65, 529–534. doi:10.1212/01.wnl.0000172638.58172.5a

Jonas, P., and Sakmann, B. (1992). Glutamate receptor channels in isolated patches from CA1 and CA3 pyramidal cells of rat hippocampal slices. *J. Physiol.* 455, 143–171. doi:10.1113/jphysiol.1992.sp019294

Koch, M. C., Steinmeyer, K., Lorenz, C., Ricker, K., Wolf, F., Otto, M., et al. (1992). The skeletal muscle chloride channel in dominant and recessive human myotonia. *Science* 257, 797–800. doi:10.1126/science.1379744

Kolen, B., Kortzak, D., Franzen, A., and Fahlke, C. (2020). An amino-terminal point mutation increases EAAT2 anion currents without affecting glutamate transport rates. *J. Biol. Chem.* 295, 14936–14947. doi:10.1074/jbc.RA120.013704

Kortzak, D., Alleva, C., Weyand, I., Ewers, D., Zimmermann, M. I., Franzen, A., et al. (2019). Allosteric gate modulation confers K^+ coupling in glutamate transporters. *EMBO J.* 38, e101468. doi:10.15252/embj.2019101468

Kovermann, P., Engels, M., Müller, F., and Fahlke, C. (2022a). Cellular physiology and pathophysiology of EAAT anion channels. *Front. Cell Neurosci.* 15, 815279. doi:10.3389/fncel.2021.815279

Kovermann, P., Hessel, M., Kortzak, D., Jen, J. C., Koch, J., Fahlke, C., et al. (2017). Impaired K+ binding to glial glutamate transporter EAAT1 in migraine. *Sci. Rep.* 7, 13913. doi:10.1038/s41598-017-14176-4

Kovermann, P., Kolobkova, Y., Franzen, A., and Fahlke, C. (2022b). Mutations associated with epileptic encephalopathy modify EAAT2 anion channel function. *Epilepsia* 63, 388–401. doi:10.1111/epi.17154

Kovermann, P., Machtens, J. P., Ewers, D., and Fahlke, C. (2010). A conserved aspartate determines pore properties of anion channels associated with excitatory amino acid transporter 4 (EAAT4). *J. Biol. Chem.* 285, 23676–23686. doi:10.1074/jbc.M110.126557

Kovermann, P., Untiet, V., Kolobkova, Y., Engels, M., Baader, S., Schilling, K., et al. (2020). Increased glutamate transporter-associated anion currents cause glial apoptosis in episodic ataxia 6. *Brain Commun.* 4, fcaa022. fcaa022. doi:10.1093/braincomms/fcaa022

Larsson, H. P., Picaud, S. A., Werblin, F. S., and Lecar, H. (1996). Noise analysis of the glutamate-activated current in photoreceptors. *Biophysical J.* 70, 733–742. doi:10.1016/S0006-3495(96)79613-3

Leinenweber, A., Machtens, J. P., Begemann, B., and Fahlke, C. (2011). Regulation of glial glutamate transporters by C-terminal domains. *J. Biol. Chem.* 286, 1927–1937. doi:10.1074/jbc.M110.153486

Machtens, J. P., Kortzak, D., Lansche, C., Leinenweber, A., Kilian, P., Begemann, B., et al. (2015). Mechanisms of anion conduction by coupled glutamate transporters. *Cell* 160, 542–553. doi:10.1016/j.cell.2014.12.035

Machtens, J. P., Kovermann, P., and Fahlke, C. (2011). Substrate-dependent gating of anion channels associated with excitatory amino acid transporter 4. *J. Biol. Chem.* 286, 23780–23788. doi:10.1074/jbc.M110.207514

Melzer, N., Biela, A., and Fahlke, C. (2003). Glutamate modifies ion conduction and voltage-dependent gating of excitatory amino acid transporter-associated anion channels. *J. Biol.Chem.* 278, 50112–50119. doi:10.1074/jbc.M307990200

Melzer, N., Torres-Salazar, D., and Fahlke, C. (2005). A dynamic switch between inhibitory and excitatory currents in a neuronal glutamate transporter. *Proc. Natl. Acad. Sci. U. S. A.* 102, 19214–19218. doi:10.1073/pnas.0508837103

Mim, C., Balani, P., Rauen, T., and Grewer, C. (2005). The glutamate transporter subtypes EAAT4 and EAATs 1-3 transport glutamate with dramatically different kinetics and voltage dependence but share a common uptake mechanism. *J. Gen. Physiol.* 126, 571–589. doi:10.1085/jgp.200509365

Nothmann, D., Leinenweber, A., Torres-Salazar, D., Kovermann, P., Hotzy, J., Gameiro, A., et al. (2011). Hetero-oligomerization of neuronal glutamate transporters. *J. Biol. Chem.* 286, 3935–3943. doi:10.1074/jbc.M110.187492

Otis, T. S., and Kavanaugh, M. P. (2000). Isolation of current components and partial reaction cycles in the glial glutamate transporter EAAT2. *J. Neurosci.* 20, 2749–2757. doi:10.1523/JNEUROSCI.20-08-02749.2000

Parinejad, N., Peco, E., Ferreira, T., Stacey, S. M., and van Meyel, D. J. (2016). Disruption of an EAAT-mediated chloride channel in a Drosophila model of ataxia. *J. Neurosci.* 36, 7640–7647. doi:10.1523/jneurosci.0197-16.2016

Pyle, A., Smertenko, T., Bargiela, D., Griffin, H., Duff, J., Appleton, M., et al. (2015). Exome sequencing in undiagnosed inherited and sporadic ataxias. *Brain* 138, 276–283. doi:10.1093/brain/awu348

Reyes, N., Ginter, C., and Boudker, O. (2009). Transport mechanism of a bacterial homologue of glutamate transporters. *Nature* 462, 880–885. doi:10.1038/nature08616

Rose, C. R., Ziemens, D., Untiet, V., and Fahlke, C. (2018). Molecular and cellular physiology of sodium-dependent glutamate transporters. *Brain Res. Bull.* 136, 3–16. doi:10.1016/j.brainresbull.2016.12.013

Sanguinetti, M. C., Curran, M. E., Zou, A., Shen, J., Spector, P. S., Atkinson, D. L., et al. (1996). Coassembly of K_vLQT1 and minK (IsK) proteins to form cardiac I_{Ks} potassium channel. *Nature* 384, 80–83. doi:10.1038/384080a0

Schewe, J., Seidel, E., Forslund, S., Marko, L., Peters, J., Muller, D. N., et al. (2019). Elevated aldosterone and blood pressure in a mouse model of familial hyperaldosteronism with ClC-2 mutation. *Nat. Commun.* 10, 5155. doi:10.1038/s41467-019-13033-4

Schneider, N., Cordeiro, S., Machtens, J. P., Braams, S., Rauen, T., and Fahlke, C. (2014). Functional properties of the retinal glutamate transporters GLT-1c and EAAT5. *J. Biol. Chem.* 289, 1815–1824. doi:10.1074/jbc.M113.517177

Scholl, U. I., Stolting, G., Schewe, J., Thiel, A., Tan, H., Nelson-Williams, C., et al. (2018). CLCN2 chloride channel mutations in familial hyperaldosteronism type II. *Nat. Genet.* 50, 349–354. doi:10.1038/s41588-018-0048-5

Stergachis, A. B., Pujol-Giménez, J., Gyimesi, G., Fuster, D., Albano, G., Troxler, M., et al. (2019). Recurrent *SLC1A2* variants cause epilepsy via a dominant negative mechanism. *Ann. Neurol.* 85, 921–926. doi:10.1002/ana.25477

Untiet, V., Kovermann, P., Gerkau, N. J., Gensch, T., Rose, C. R., and Fahlke, C. (2017). Glutamate transporter-associated anion channels adjust intracellular chloride concentrations during glial maturation. *Glia* 65, 388–400. doi:10.1002/glia.23098

van Amen-Hellebrekers, C. J., Jansen, S., Pfundt, R., Schuurs-Hoeijmakers, J. H., Koolen, D. A., Marcelis, C. L., et al. (2016). Duplications of *SLC1A3* associated with ADHD and autism. *Eur. J. Med. Genet.* 2016. doi:10.1016/j.ejmg.2016.06.003

Verdon, G., and Boudker, O. (2012). Crystal structure of an asymmetric trimer of a bacterial glutamate transporter homolog. *Nat. Struct. Mol. Biol.* 19, 355–357. doi:10.1038/nsmb.2233

Wadiche, J. I., Amara, S. G., and Kavanaugh, M. P. (1995). Ion fluxes associated with excitatory amino acid transport. *Neuron* 15, 721–728. doi:10.1016/0896-6273(95)90159-0

Wadiche, J. I., and Kavanaugh, M. P. (1998). Macroscopic and microscopic properties of a cloned glutamate transporter/chloride channel. *J. Neurosci.* 18, 7650–7661. doi:10.1523/JNEUROSCI.18-19-07650.1998

Winter, N., Kovermann, P., and Fahlke, C. (2012). A point mutation associated with episodic ataxia 6 increases glutamate transporter anion currents. *Brain* 135, 3416–3425. doi:10.1093/brain/aws255

Wu, Q., Akhter, A., Pant, S., Cho, E., Zhu, J. X., Garner, A., et al. (2022). Ataxia-linked *SLC1A3* mutations alter EAAT1 chloride channel activity and glial regulation of CNS function. *J. Clin. Invest.* 132, e154891. doi:10.1172/jci154891

Yernool, D., Boudker, O., Jin, Y., and Gouaux, E. (2004). Structure of a glutamate transporter homologue from Pyrococcus horikoshii. *Nature* 431, 811–818. doi:10.1038/nature03018

Zerangue, N., and Kavanaugh, M. P. (1996). Flux coupling in a neuronal glutamate transporter. *Nature* 383 (6601), 634–637. doi:10.1038/383634a0

Frontiers in Physiology

Understanding how an organism's components work together to maintain a healthy state

The second most-cited physiology journal, promoting a multidisciplinary approach to the physiology of living systems - from the subcellular and molecular domains to the intact organism and its interaction with the environment.

Discover the latest Research Topics

See more →

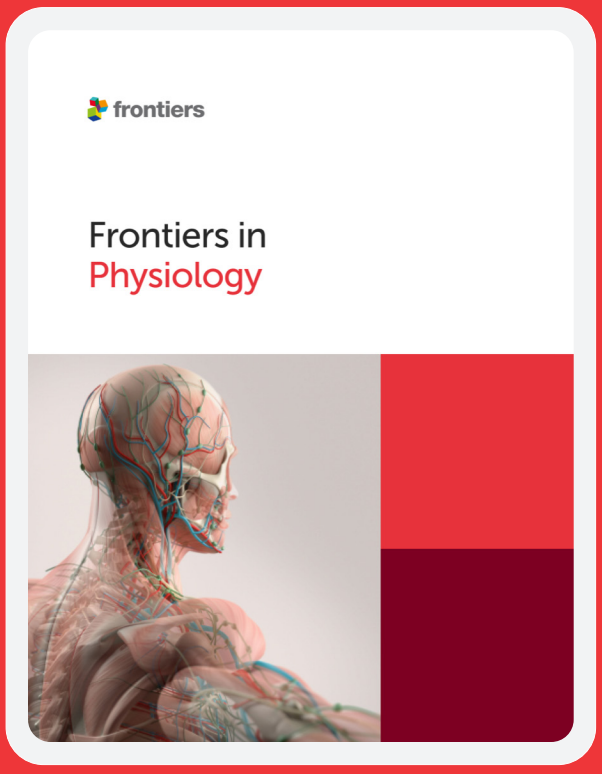

Frontiers

Avenue du Tribunal-Fédéral 34
1005 Lausanne, Switzerland
frontiersin.org

Contact us

+41 (0)21 510 17 00
frontiersin.org/about/contact